

Georgia Water Resources Institute Annual Technical Report FY 2004

Introduction

The GWRI mission is to foster the creation of partnerships, resources, and knowledge base necessary to address current water resources challenges in the state of Georgia, the U.S., and the world. Specific GWRI goals include:

- a) Develop new research methods and scientific knowledge to support sustainable river basin planning and management;
- b) Educate scientists, engineers, and water professionals in state-of-the-science methods and their potential applications; and
- c) Disseminate useful information to policy makers, water managers, industry stakeholders, citizen groups, and the general public.

In keeping with the above-stated mission and goals, during Fiscal Year 2004, the Georgia Water Resources Institute (GWRI) was involved in a wide range of activities at the state, national and international levels. The following sections summarize these activities as they pertain to research, education, technology transfer, and professional and policy impact.

RESEARCH PROJECTS:

1. Seismic Imaging of Fractured Systems in Crystalline Rock; sponsored by GWRI/USGS104B; 2. Bio-geochemical Cycling of Arsenic at the Sediment-Water Interface of the Chattahoochee River; sponsored by GWRI/USGS104B; 3. Reductive Biotransformation of Polychloronitrobenzenes under Iron-Reducing Conditions; GWRI/USGS104B; 4. Decision Support For Georgia Water Resources Planning and Management; sponsored by GWRI/USGS104G; 5. INFORM: Integrated Forecast and Reservoir Management System for Northern California; sponsored by NOAA, California Energy Commission, and CalFed; 6. Remote Sensing of Precipitation Combining Geostationary and TRMM Satellite Data; sponsored by NASA.

EDUCATION AND TECHNOLOGY TRANSFER:

1. USGS Graduate Student Internship, Groundwater Modeling for Coastal Aquifers; 2. Hydrologic Engineering for Dam Design; continuing education course; 3. Advanced Technical Seminar: Seepage for Earthen Dams; continuing education course; 4. Savannah River Basin Workshop; regional workshop (Georgia and South Carolina); 5. Georgia Water Resources Conference; Biennial state water resources conference.

PROFESSIONAL AND POLICY IMPACT:

GWRI's continued involvement with the INFORM project brings together all relevant agencies and stakeholder groups associated with the Sacramento and American Rivers in Northern California and provides opportunities for significant policy impact. Participating agencies include the National Weather Service, the US Army Corps of Engineers, the US Bureau of Reclamation, the Sacramento Flood Control Authority, US EPA, California Department of Water Development, and the California Energy Commission. The project aims at developing the institutional framework and technical tools necessary to support integrated river basin management.

At the state level, the GWRI workshop on the Savannah River brought together stakeholders and state officials and planners in a preliminary effort to develop a shared vision strategy for the management of the Savannah River. As a result, the Governors of the two states agreed to form a Committee of Experts and begin considering various compact issues and alternatives.

Research Program

Seismic imaging of fracture systems in crystalline rock

Basic Information

Title:	Seismic imaging of fracture systems in crystalline rock
Project Number:	2004GA56B
Start Date:	3/1/2004
End Date:	2/28/2005
Funding Source:	104B
Congressional District:	5
Research Category:	Not Applicable
Focus Category:	Groundwater, None, None
Descriptors:	
Principal Investigators:	Leland Timothy Long

Publication

Final Report
Project G-35-B99
Covering period: March 2004 through February 2005

Seismic imaging of fracture systems in crystalline rock.

Sponsored by:
Georgia Water Research Institute

Principal investigator:

Dr. Leland Timothy Long,
Professor of Geophysics
Georgia Institute of Technology
School of Earth and Atmospheric Sciences
Atlanta, GA 30332-0340
(404) 894-2860 (Office) (404) 894-5638 (FAX)

Graduate Assistant:

Tatiana Toteva
Georgia Institute of Technology
School of Earth and Atmospheric Sciences

Seismic imaging of fracture systems in crystalline rock

Executive Summary

A critical need in understanding open or fluid filled fractures in crystalline rock is the ability to reliably identify fractures and to characterize their source zones. This research is directed toward testing two advanced seismic imaging techniques that have not been used previously in hydrology. One technique is scattering inversion, which is a three-dimensional extension of CDP (common depth point) stacking and tomography. The other technique is surface wave inversion to monitor changes in the water content in shallow soils. Together, these two techniques could image the fracture systems and surface source zones characteristic of the Piedmont province. The tests were performed in the Panola Mountain Research Watershed, a watershed typical of the Piedmont Province.

For the shallow source aquifers above the crystalline rock we compared seismic traces over time to identify changes in seismic response related to changes in water content. In the Rhodes-Jordan Well Field (RHWF) near Lawrenceville, GA we observed significant changes in the seismic signature when comparing data obtained during pumping and without pumping of water out of the fractures. However, the cause and location of the perturbation could not be uniquely defined.

At the Panola Mountain Research Watershed (PMRW) we tested the capability of trace differences (using identical sources, recording sites and instruments) to monitor soil moisture content. The surface wave data from a line parallel to the streambed in the valley floor showed significant variations in character with time. The analysis can thus be used as a water content monitor if calibrated against water level data.

At the PMRW we also established an array of sensors on the exposed rock. In the area of exposed rock, we have preliminary results from a modified formulation of the scattering inversion. The data suggest that we will be able to identify and map fractures and surface features.

These two techniques when applied to appropriate areas could be important tools for the evaluation of water resources in crystalline rocks. We have demonstrated that they have the potential of providing quantitative data on the fractures and the near-surface water sources.

The research results have contributed in whole or in part to 6 talks at national and regional meetings. Two papers describing the techniques are in preparation. The next step in developing these as viable exploration and monitoring techniques is to refine the techniques with further tests, more carefully define the types of areas where they can be applied and establish a protocol for their application.

Seismic imaging of fracture systems in crystalline rock

Statement of critical regional water problem

In areas like the Georgia Piedmont, that are underlain by fractured and unweathered crystalline rock, water resources are limited to surface reservoirs and shallow wells. Because surface reservoirs are approaching full development, and because new large surface reservoirs are difficult to site, the water needs of the expanding suburban and urban areas in central Georgia will have to come from alternate sources. These sources include conservation and ground water. In crystalline areas the near-surface ground water supplies, usually exploited by shallow wells, have a capacity that is limited by thin soils, but there exist fracture systems in the crystalline rocks that can supply significant amounts of water because they draw from a wide area and from many near-surface shallow aquifers. These fractures and their supply system offer a mechanism for efficient pumping of water for municipal water supplies. Fracture systems with production potential are difficult to locate and evaluate, and, hence, are underutilized. A growing need exists for methods to detect and characterize open productive fracture zones in the metamorphic and igneous rocks of the Georgia Piedmont. Some communities, for example Lawrenceville, have successfully tapped such fracture zones as a supplement to surface reservoirs. An increasing number of Counties and local governments are evaluating ground water in fractures as a primary or supplemental source to their existing surface water systems because in periods of drought, surface reservoirs and shallow wells will be depleted before deep fractures. A more important aspect of productive fracture zones is to understand the geometry of the productive fractures and their relation to near-surface water sources. A quick and non-intrusive method to locate and evaluate fracture zones that are productive could save on drilling exploration techniques and expand available water resources.

Nature, scope, and objectives of the research.

In this work we tested the ability of new seismic analysis methods to image and evaluate fractured rock aquifer systems. The fractured rock aquifer system studied in this research consisted of a fracture zone in crystalline rock and the shallow storage or collection zones at the surface. This is a system that would be typical for well fields in crystalline rock, such as those found at the Rhodes-Jordan Well Field in Lawrenceville, GA, or the Panola Mountain Research Watershed (PMRW). Figure 1 is a simplified cross section of the PMRW, which served as the primary test area for seismic techniques.

Our hypothesis is that new seismic analysis methods can image and quantify fractured rock aquifer systems. We hypothesize that the fractures can be imaged using high-frequency scattered or reflected waves using scattering inversion, a technique analogous to the stacking process in reflection seismic data analysis or pre-stack migration. Furthermore, we hypothesize that the near-surface source aquifer can be imaged and monitored using surface waves. Most importantly, we hypothesize that the addition or withdrawal of water from these aquifers can be monitored by observing slight changes in the waveform over time. Specifically, we proposed to evaluate coda envelope inversion in an area of known fracture zones in order to assess whether

fractures can be detected on a scale of 100 meters. And, we proposed to test the differential surface wave technique for monitoring variations in water content in a surface aquifer.

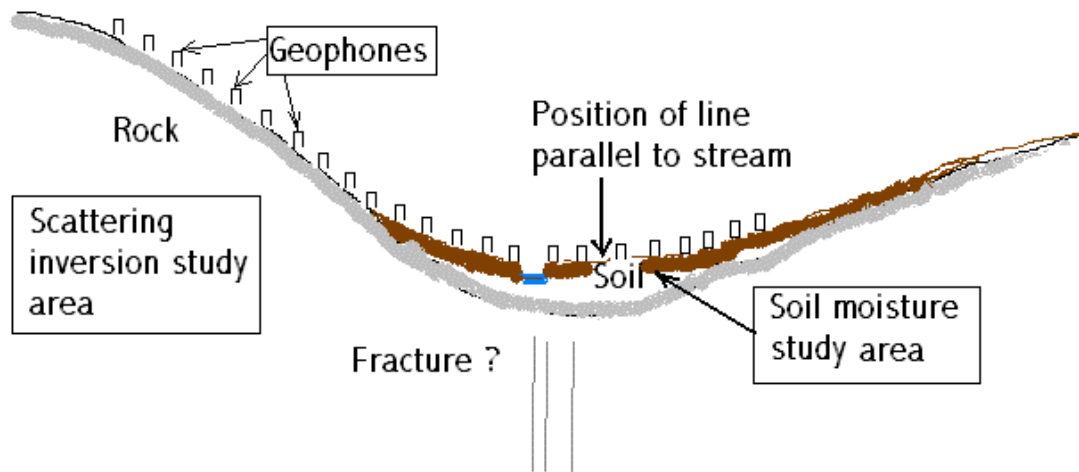


Figure 1. Cross section of the Panola Mountain Research Watershed showing proposed locations of geophones.

The PMRW is a small watershed that is a model for many similar watersheds in the Piedmont Province of Georgia. The advantage of the PMRW for this research is that it is small and has been extensively studied. The small scale is an advantage for seismic data acquisition because smaller non-destructive sources can be used. The disadvantage is the attenuation of the higher frequencies needed to resolve details. The exposed rock portion of the study area (left side of figure 1) is where the scattering inversion experiment was performed to attempt to detect a possible fault/fracture zone below the axis of the valley. The lack of soils greatly reduced the attenuation of high frequency seismic waves. The PMRW provided a clean rock surface to test the scattering inversion without interference from surface sediments. However, the location and extent of fractures in the crystalline rock is only partially documented at the PMRW. The Rhodes-Jordan Well Field in Lawrenceville was studied as a site where the fractured rock is below a layer of sediment or fill, but where the fractures have been documented by geophysical logs from numerous test wells.

At the PMRW the soil fill in the valley were used to test the ability of surface waves to monitor water content. We used surface waves to measure the velocity structure of the shallow soil layer before and after a significant rain event. By comparing the seismic velocity perturbations with stream flow and soil moisture measurements (from independent USGS data) we proposed to determine the effectiveness of surface wave perturbation measurements to monitor water content in the soil aquifer. Conventional seismic refraction and surface wave interpretation were used to determine the thickness and structure of the soil layer.

Specific objectives and summary of results:

Objective 1: The first two objectives relate to the Rhodes-Jordan Well Field (RJWF). First, we proposed to obtain at least two new sets of data in order to improve the array design for sensitivity to reflections and their perturbations under different pumping rates. In a field trip

during December 2003, we obtained data for the analysis of shallow structures. In a later field trip on October 8, 2004, we used modified field measurement techniques and a more repeatable source to attempt to obtain temporal perturbations in reflections from the known fractures.

Objective 2: We proposed to complete an analysis of the shallow structure in order to assist in the interpretation of temporal changes in scattering. The details of this analysis are given in Appendix I. The analysis used conventional stacking (averaging) techniques to enhance arrivals from the depths of the fractures identified in well logs provided by the US Geological Survey. The analysis showed that the cessation of pumping produced measurable changes in the seismic response. We were not able to determine in this case whether the change was due to changes in water pressure within the fracture or to changes in water content in the sediments. A significant limitation at the RHWF was that the surface waves dominated the record in the time window expected for arrival of many of the waves scattered off of the fractures. Hence, a coda sufficiently clean for scattering inversion could not be obtained at this site. Also, the frequency response of the geophones located in near-surface soils could not be tested for frequencies above 400 Hz, and those frequencies are needed for a reliable scattering inversion.

Objective 3: We had demonstrated a need to improve the high-frequency content and repeatability of our source. Consequently, we have designed a modified weight drop mechanism that produces the repeatable and relatively small signals needed in this work. The amplitudes of the signals generated need not be large because we are operating at comparatively short distances, typically less than 30 meters.

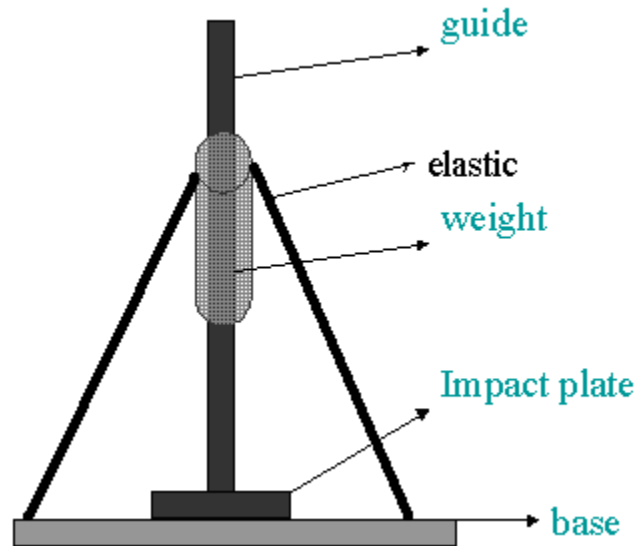


Figure 2. Simplified diagram of controlled source.

The source consists of a weight that slides down a guide. The impact plate on the bottom produces the high-frequency source function and the base, which is weighted or attached to the ground, transmits the signal into the ground. The elastic bands serve to accelerate the mass to provide a stronger strike within a short distance. The guide and impact plate design assure that

the signal for each shot is similar. The trigger is placed on the base. An additional elastic band was attached later to prevent multiple signals caused by a bouncing of the weight.

Objective 4: In the PMRW, we will lay out two repeatable seismic lines, one parallel to the valley and one perpendicular. We have set up two orthogonal lines of 16 geophones each in the valley. The first line is parallel to the stream. The second line starts at the center of the first line and extends up hill, forming a “T” configuration. The upstream end of the first line is shown in Figure 3. The area was chosen because it is populated with many water level monitoring pipes placed into the ground.



Figure 3. Picture of the first line parallel to the streambed (to the right of the figure).

Objective 5 and 6: We proposed to take sets of surface wave measurements along the lines during periods of similar rainfall and at different times to obtain data during different phases of significant rain events. We have obtained numerous sets of data on the line parallel to the streambed and the results are illustrated in Appendix II. The data in Appendix II show that changes on the order of 5 percent can be expected in the surface wave velocities when comparing records obtained before and after significant changes in water level in soils. The technique can resolve velocity changes of less than 1 percent.

Objective 7: By moving the source over many sites on the crystalline rock outcrop we proposed to provide data for a scattering inversion to identify fractures in the surrounding rock. The scattering inversion will be performed using arrays of geophones on the outcropping unweathered rock. This has the advantage of not attenuating the source and will allow excitation of more high-frequency energy. The results of this analysis are in preparation for presentation at the American Geophysical Union meeting in May 2005. The preliminary details of this analysis are given in Appendix III. A significant problem in measuring seismic vibrations on hard rock is

the coupling of the geophones to the rock. This was made more difficult by the fact that we needed to record frequencies in the range of 500 to 1000 Hz. At these frequencies, the geophones must be very tightly coupled to the rock. We tried making mounts with cement and screwing the geophones into the mounts and the traditional technique of weighting the geophones with sand bags. Neither of these worked satisfactorily. The most successful technique was to mold the geophones into the rock face with modeling clay and use the sand bags to help maintain contact.

Objective 8: We proposed to perform a comparison of the seismic interpretation with data from water monitoring sites provided by the USGS. Because of the character of these measurements, we did not consider this a significant comparison. The data available from the USGS close to the test site is obtained at the upper weir. Unfortunately, this weir does not block water flow in the valley sediments, and a significant portion of the water outflow is not registered. The fate of the water was one aspect studied, but not solved by the Georgia Tech environmental field methods course EAS4610. We also obtained refraction data from the upper weir to our test site to assist Dr. Marc Stieglitz in his investigation of the water budget of the smaller watershed. Dr. Stieglitz is making a detailed study of the USGS water flow data.

Statements of Collaboration:

The field research has been designed to supplement research performed by the U.S. Geological Survey. Personnel familiar with the Lawrenceville and Panola Mountain sites have visited our field site and suggested areas of potential additional work. The seismic techniques have proven valuable in identifying underground structures. The surface wave technique is effective in determining depth to basement and locating anomalous structures in profiles. We plan to continue development of these techniques. The preliminary results of scattering inversion on the hard rock suggest that this technique could be very effective in identifying fractures.

As part of our collaborative efforts, we have obtained a line of data extending from the upper weir to our test line. This data was designed to help Marc Stieglitz in understanding the fate of water bypassing the upper weir.

Training Activities

One Ph.D. student, Tatiana Toteva, in geophysics was partially supported by this research. The results of the scattering inversion will contribute to her Ph.D. thesis. Two undergraduate students, Chris Keiser and Michael Chen, received partial support working on this research. Chris Keiser assisted in some of the fieldwork and Michael Chen assisted in computer programming.

The Panola Mountain Research Watershed during spring semester, 2005, was made the topic for the capstone senior course, environmental field methods. The course included 14 students who obtained field data and analyzed the data as part of their studies. The topics ranged from atmospheric pollution to water temperature. One student used seismic data in a seismic reflection experiment and another student used seismic data in a refraction study. A third student interpreted ground penetrating radar data obtained as part of the course. The results of these

studies were written up in a final report and presented at a class symposium. Copies of the report have been given to the U.S. Geological Survey, water resources division, in Atlanta.

One MS thesis will be the direct result of studies in the Panola Mountain Research Watershed. Gabriel Hebert has obtained data and will be writing his M.S. thesis on a comparison of ground penetrating radar and seismic techniques. The study area brackets the trench area extensively studied by the U.S. Geological Survey and associated scientists. The thesis is directed to, first, an evaluation of the advantages of the two techniques and, second, to solving problems related to flow of water down slope. The significant question to be answered by this analysis is whether fractures can be found that contribute to diverting fluid from the soil.

Information Transfer

Final report: The contributions of this research are summarized in this final report.

Talks at professional meetings: The research results have contributed in whole or in part to 6 talks at national and regional meetings. The titles and abstracts for these talks are listed below

Toteva, Tatiana, and L.T. Long. Differential coda imaging of fractures, American Geophysical Union Meeting, San Francisco, December 2003.

Abstract: Coda waves have been extensively used to characterize the scattering and attenuation properties of the earth interior. Their sensitivity to earth's heterogeneity makes them a potential tool for mapping fractures within the earth crust and monitoring changes in their properties. Some lab experiments (Sneider, 2002) show that small change in the temperature can lead to very subtle change in the velocity, which is detectable in the coda waves and not in the direct arrivals. We used a finite difference coda to generate acoustic waves, traveling in a fractured medium. A small change in the velocity within the fractures is not visible on the seismogram. The effect of that change becomes obvious if one takes the difference in the seismograms. In the case of elastic medium such differences should be even more prominent. One possible application of this differential coda imaging technique is detection and monitoring of open productive fracture zones. These fracture zones may offer larger flow rates and capacity than shallow surface wells. Use to monitor changes in water pressure associated with initiation or stopping on pumping on production wells.

Long, L.T., and Toteva, Tatiana. Differential surface wave analysis: a technique to monitor changes in fluid flow in shallow aquifers. American Geophysical Union Spring Meeting, Montreal, Canada. May 2004

Abstract: The objective of differential surface-wave analysis is to identify temporal perturbations in the shear-wave velocity, and hence ultimately to monitor water saturation and/or water pressure in shallow soils. We directly measure perturbations in velocity by a comparison of seismic traces obtained before and after a change in the water saturation. Perturbations in phase velocity are measured as a function of frequency in the frequency domain of the difference of normalized traces. The perturbed structure can then be computed relative to a reference structure that need only approximate the actual structure.

Michael Chen, Processing the perturbation method. 76th Annual Meeting, Eastern Section Seismological Society of America, Virginia Polytechnic Institute and State University, Blacksburg, Virginia. October 31 to November 1, 2004.

Abstract: A software implementation of a perturbation method for shear-wave velocity inversion from surface waves is presented. Signals from Seismic Unix data files are extracted and processed with the multiple-filter technique. The dispersion curves are then treated as perturbations to the reference dispersion from a library of pre-computed curves. Finally, the corresponding reference velocity profile is perturbed in the equivalent way to yield the shear-wave profile. Orthogonal functions of velocity with respect to depth are used as the perturbation functions. The software's code will be freely available under an open-source license.

Tatiana Toteva, and L.T. Long, Differential Approach for Detecting Temporal Changes in Near-Surface Earth Layers, 76th Annual Meeting, Eastern Section Seismological Society of America, Virginia Polytechnic Institute and State University, Blacksburg, Virginia. October 31 to November 1, 2004.

Abstract: The physical parameters (shear wave velocity, density, porosity, etc.) of near-surface soils and weathered rocks have been extensively studied for the purposes of geotechnical engineering, hydrology, oil and gas exploration etc. The possibility of using geophysical techniques for monitoring changes within this upper layer has gained big popularity within the recent years. The objective of this study is to develop a differential technique for detecting subtly velocity changes within the soil layer. The differential technique is based on a study of the difference between two normalized traces taken at successive time intervals. The differences are interpreted as perturbations to a structure. This study has applied the differential technique to Rayleigh waves. We hypothesized that fluid penetration due to natural causes (rainfall) or pumping of fluids, would lead to changes in the shear wave velocity, which could be detected on the differential seismograms. In the traditional approach the soil layer is studied by inverting the phase velocity dispersion curve for the velocity structure. Instead of the phase velocity we use group velocity for inversion curve. Group velocity depends on phase velocity and the change of the phase velocity with frequency. Hence, we hypothesized that group velocity would be more sensitive to subtle changes in the velocity structure. The technique was tested for two different types of soil perturbations. We acquired data before and after heavy rain in the Panola Mountain Research Watershed to test the effect of variations in water table and soil moisture. At a second site, we tested a more controlled perturbation by pumping water into the soil at a depth of about 1.0 meter. Important factors in the acquisition of this data were the use of a repeatable weight-drop source and a secure and repeatable geophone placement. Our results show that the fluid penetration in the soil causes phase changes and time shifts, detectable on the differential seismograms.

Tatiana Toteva and L.T. Long, ESSSA

Tatiana Toteva, A differential Approach for detecting subtle changes in the near-surface earth layer, Graduate Student Symposium, School of Earth and Atmospheric Sciences, November, 2004.

Abstract: The near-surface earth layer includes the soil layer and the near-surface rocks. Its physical parameters (shear wave velocity, density, porosity etc.) have been extensively studied for the purposes of geotechnical engineering, hydrology, oil and gas exploration etc. The idea of developing techniques for monitoring changes within this upper layer has gained big popularity within the recent years. The objective of this study is to develop a differential technique for detecting subtle velocity changes within the soil layer. We are targeting the upper few meters. The technique utilizes Rayleigh waves. We hypothesized that fluid penetration due to natural causes (rainfall) or pumping of fluids, would lead to changes in the shear wave velocity, which could be detected on the differential seismograms. In the traditional approach the soil layer is studied by inverting the phase velocity dispersion curve for the velocity structure. Instead of using the phase velocity we used group velocity inversion curve. Group velocity depends on phase velocity and the change of the phase velocity with frequency. We hypothesized that group velocity would be more sensitive to subtle changes in the velocity structure. The technique was tested at two different soil sites. We acquired data before and after heavy

rain in Panola Mnt., GA and during fluid pumping at the ATL site (Atlanta, GA). We used a repeatable weight-drop source and 16 geophones (central frequency 16 Hz). Our results show that the fluid penetration in the soil causes phase changes and time shifts, detectable on the differential seismograms.

Toteva, Tatiana, and L. T. Long. A scattering inversion experiment to identify fractures on a granite outcrop. American Geophysical Union Meeting, New Orleans, May, 2005.

Abstract: A critical need in understanding open or fluid filled fractures in crystalline rock is the ability to identify these fractures, to characterize their source zones, to map flow paths within the fractures, and to assess residence time of water in the system. Fractures are an important component in the water resources of areas where crystalline rocks crop out at the surface. We have attempted to use scattered waves to identify and map fractures in a crystalline rock. Our research was conducted at the Panola Mountain Research Watershed (PMRW), GA. The scattering technique was tested in an area of exposed rock. We used 16 geophones, 100Hz each, placed in a circular array with diameter of 16m. A major effort was taken towards suppressing resonances in the geophones at high frequency. We used clay to better attach the geophones to the outcrop and sand bags to weight the instruments down to suppress the high frequency resonance. A small weight drop source was designed to generate high frequency input signal. The source provides signals in the 300 to 800 Hz range. The source was moved about the array in distance ranges of 5 to 60 meters. The recorded signals were highly filtered to pass only waves above 500 Hz. In processing the data, the distance is obtained from the travel time and direction to the scattering fracture is obtained by using apparent velocity across the array. The technique provides a theoretical way to map positions of varying scattering efficiency and hence the location of fractures.

(note: the analysis for this paper is in preparation. Background information and draft version are given as part of Appendix III)

Publications: We plan to prepare two papers on data from this study. The first will be an analysis of the scattering inversion from data obtained on the exposed rock. The second will be the analysis of temporal changes in the velocity along the test line parallel to the streambed in the Panola Mountain Research Watershed. The first will document the technique for identifying fractures and the second will propose this as a means to document and monitor ground water. Depending of the results, the M.S. thesis by Gabriel Hebert could lead to a publication on the comparison of seismic and ground penetrating radar techniques.

Appendix I.

Analysis of reflection data from the Rhodes-Jordan Well Field

Introduction

The Rhodes-Jordan Well Field is operated by the city of Lawrenceville, Ga. It is located in Gwinnett County, Georgia (Figure 1.0). The basement rocks are metamorphosed igneous and sedimentary rocks of the Piedmont province of central Georgia. In this area they are relatively unweathered and of granitic composition.

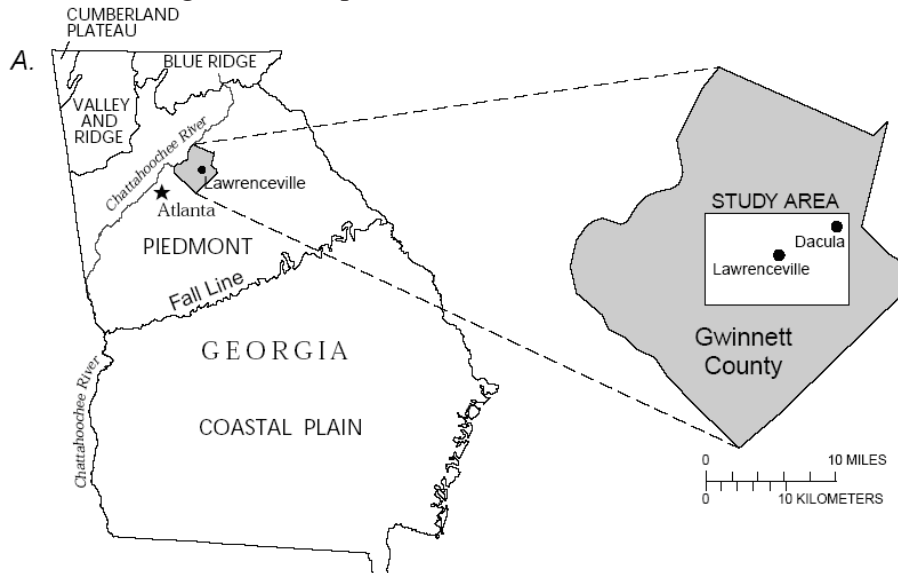


Figure 1. The Rhodes Jordan wellfield study area is located in Gwinnett County, GA. in the Piedmont Physiographic province (Figure from U.S. Geological Survey, Water Resources Division, Atlanta, GA)

The wells in the well field form a tight cluster downstream of the Lawrenceville City Lake (Figure 2). Multiple wells were drilled and studied for documentation of depth of joints. The jointing is typical of the crystalline Piedmont province. The joints sets are the conventional near-vertical orthogonal sets of joints with nearly horizontal stress release joints, which decrease in frequency with increased depth. The locations of the principal joints and their depths are identified in Figure 3.

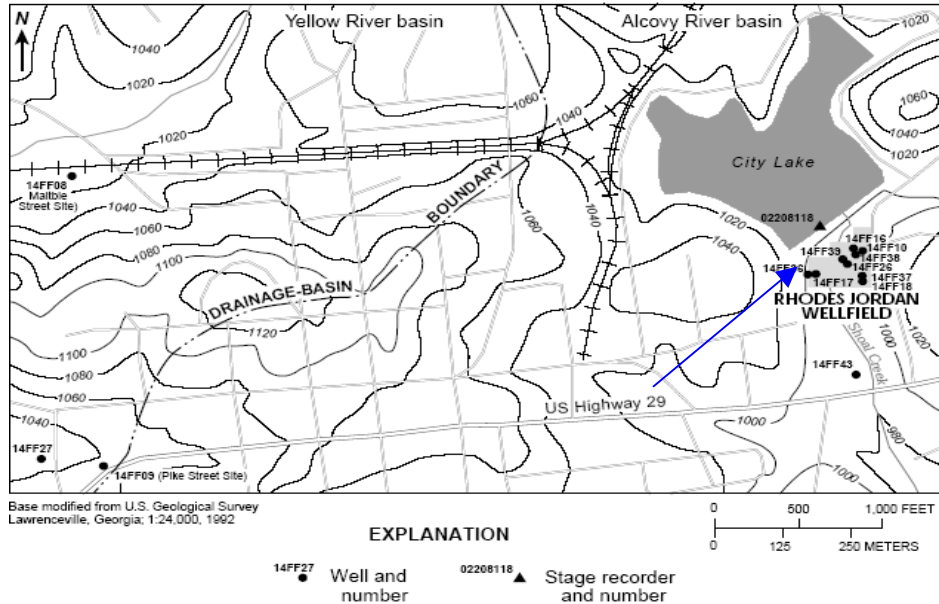


Figure 2. Observation wells in Lawrenceville, GA. The blue arrow points towards the well which was used to delineate fractures. (Figure from U.S. Geological Survey, Water Resources Division, Atlanta, GA)

Delineation of borehole fractures in well 14FF16

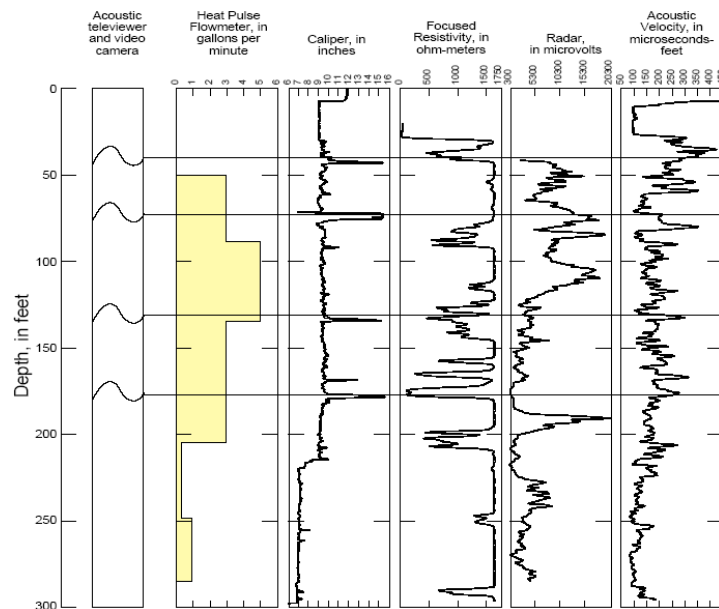


Figure 3. Delineation of fractures for well 14FF16. Two fractures were targeted in this study. First fracture is at 41.76ft (12.73m) and the second fracture is at 73.08ft (22.27m). (Figure from U.S. Geological Survey, Water Resources Division, Atlanta, GA)

Data analysis for shallow structure.

The seismic refraction technique was used to define the thickness of the soil layer. The data were collected in the fall of 2003. The geophones were spaced at 1 meter and the source was located a distance of 1m (at 4 meters) from first geophone. The travel times for direct and refracted waves are picked from the recorded seismograms and are shown on Figure 4.

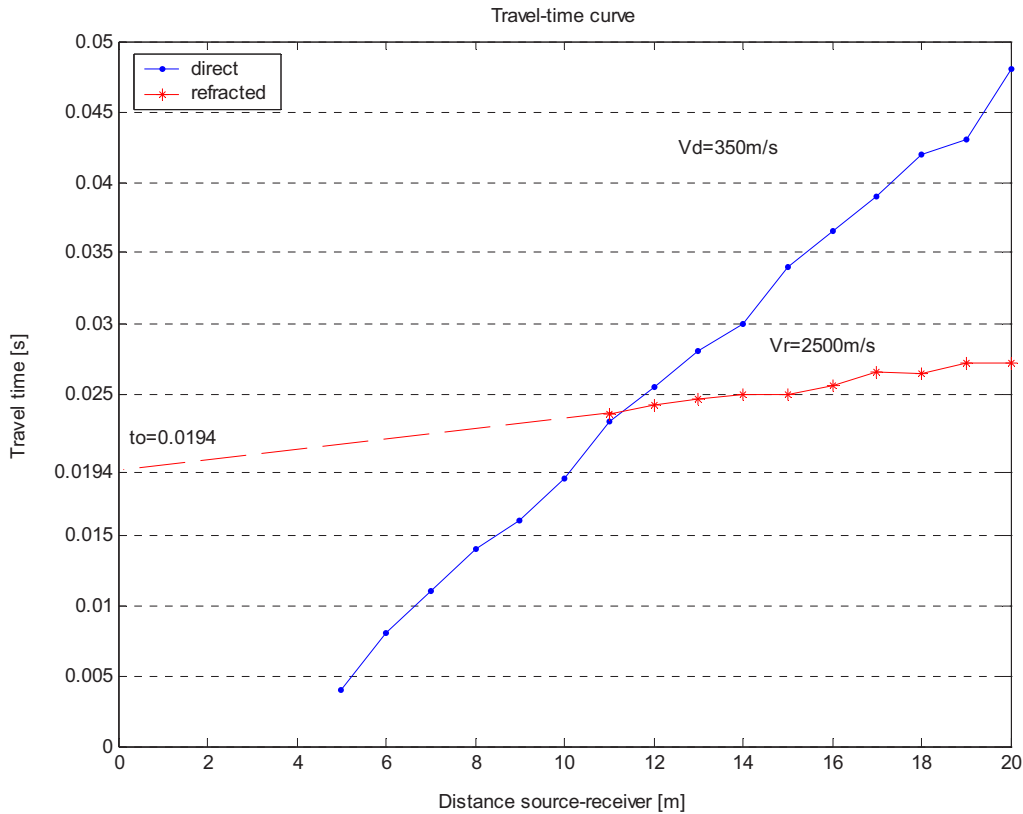


Figure 4. Travel time curves for direct and refracted wave. Velocities are calculated as the slopes of the two curves – $V_{\text{direct}}=V_{\text{soil}}=350\text{m/s}$ and $V_{\text{refracted}}=V_{\text{rock}}=2500\text{m/s}$. The intercept time t_i is found to be 0.0194s. The computed depth to soil layer for this line is 3.4 m.

The depth of the soil layer was calculated from the equation:

$$h = \frac{t_o}{2} \frac{V_{\text{rock}} V_{\text{soil}}}{\sqrt{(V_{\text{rock}}^2 - V_{\text{soil}}^2)}} = 3.4\text{m}$$

We would expect there to be measurable variations in the thickness of the sediments, but do not believe this variation is sufficient to affect our results.

In order to obtain more information on the thickness of the sediments, we also performed a dispersion analysis of the surface waves. The observed dispersion for the data is shown on Figure 5.

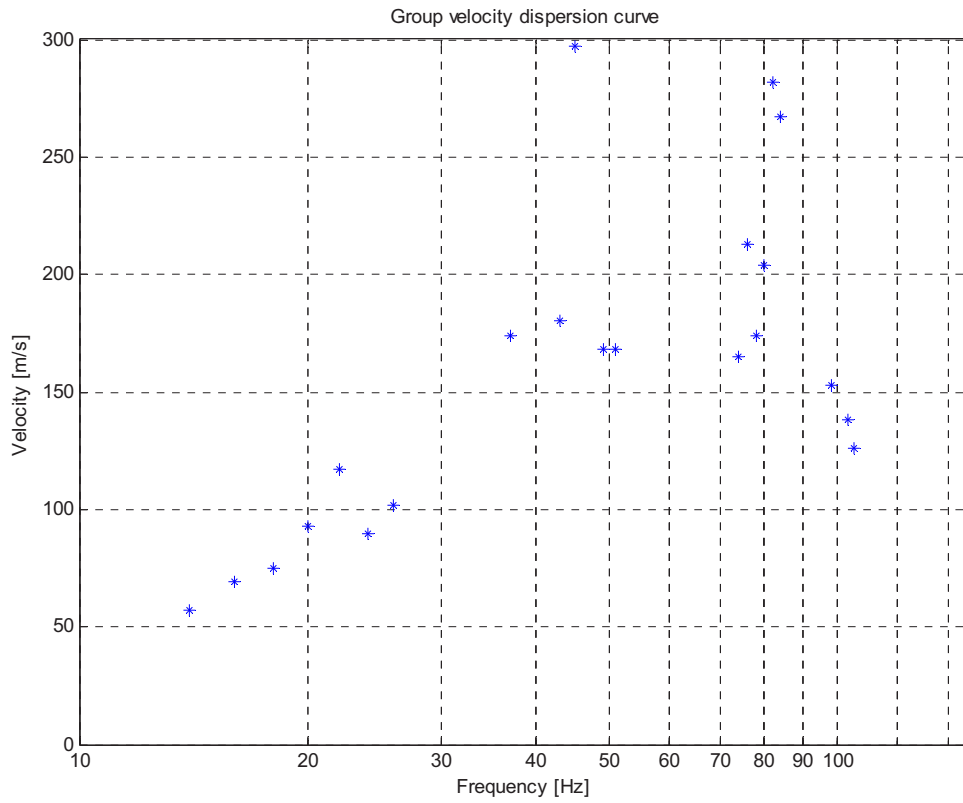


Figure 5. Observed group velocities of Rayleigh waves.

In order to find the structure, we used the forward modeling technique. In the forward modeling technique, a synthetic dispersion curve is found by varying the velocities and thicknesses of the soil until a fit to the observed data is found. The resulting velocity and layer structure is listed in Figure 6. The group velocity tends to increase with frequency, a phenomena often referred to as reversed dispersion. Reversed dispersion can be caused either by a low velocity zone at depth, by a sharp increase in velocity with depth, or both. In this case we were able to fit the dispersion curve with a structure with a low velocity zone and a sharp increase in velocity with depth. The low-velocity zone is very likely the depth of significant increase in water content. Also, the near surface soils contained many rock fragments suggesting that the surface had been reworked and likely contained a significant amount of unweathered crushed rock that could, in a dry packed condition lead to a higher near-surface velocity. These rocks in many cases made it difficult to plant the geophones because the spikes could not be pushed into the ground. The soil thickness of 3.5 m is approximately the same as that estimated from the refraction analysis.

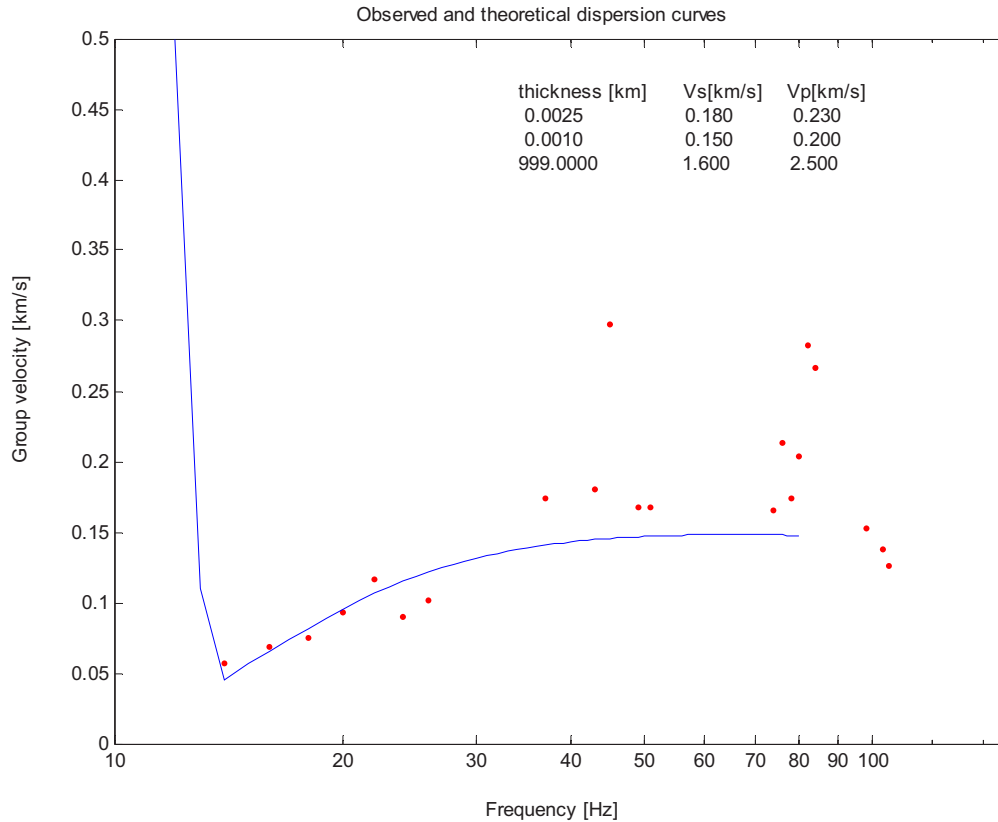
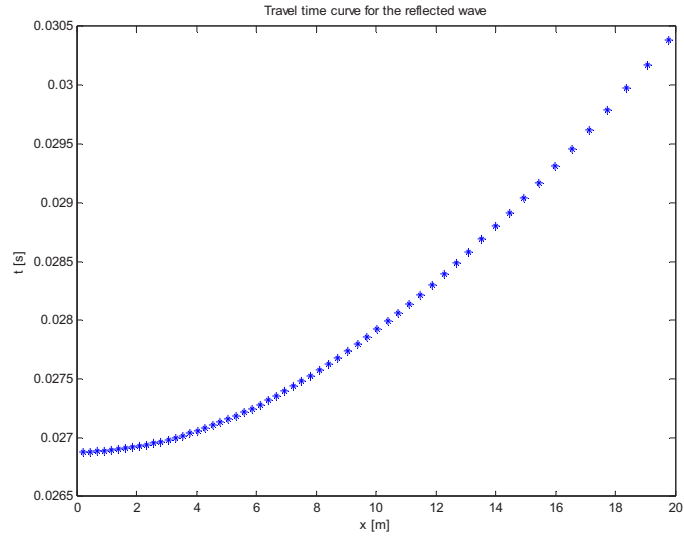


Figure 6. Observed (dots) and theoretical (line) dispersion curve.

Data Stacking for reflections

Data reduction in conventional seismic reflection processing includes the stacking of seismic traces that have reflected from the same reflector. In stacking, the time for the arrival from a given reflector is identified on each record trace and the traces are time shifted so that the reflection arrives at the same time on each trace and the traces are added. With proper time shift, the reflections on each trace will be coherent and will add, while noise and other reflections will be incoherent and tend to cancel out. The reflections are enhanced and made easier to identify.

In order to stack the traces on the expected times of the reflections from the fractures it is necessary to compute the expected times of the reflections. The times of the reflections increase with increased distance from the source. This is the normal move out, or NMO. Using the velocity profile defined by the refraction analysis, we calculated the NMO corrections for the fracture depths obtained from the down-hole well logs. The values assumed are; a soil velocity of $V_{\text{soil}}=340\text{m/s}$, a thickness of the soil layer $h=3.4\text{m}$, and a velocity of rock $V_{\text{rock}}=2500\text{m/s}$. With these data, the travel-time (Figure 7a) and the x^2-t^2 curve was generated (Figure 4b) for an assumed fracture depth of 12m.



a)

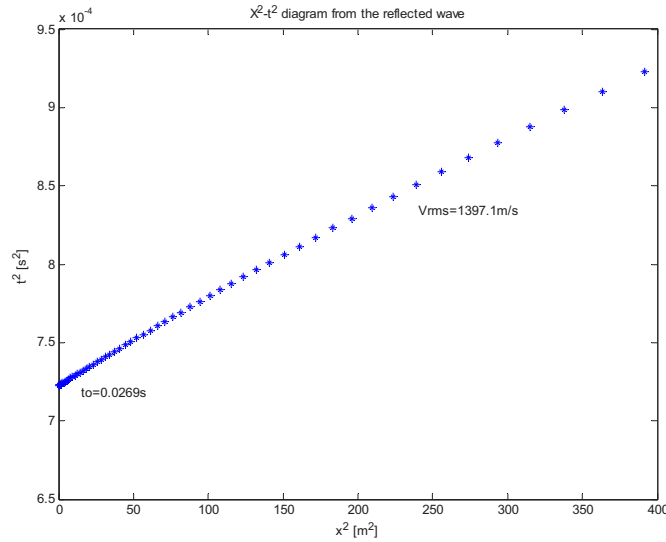
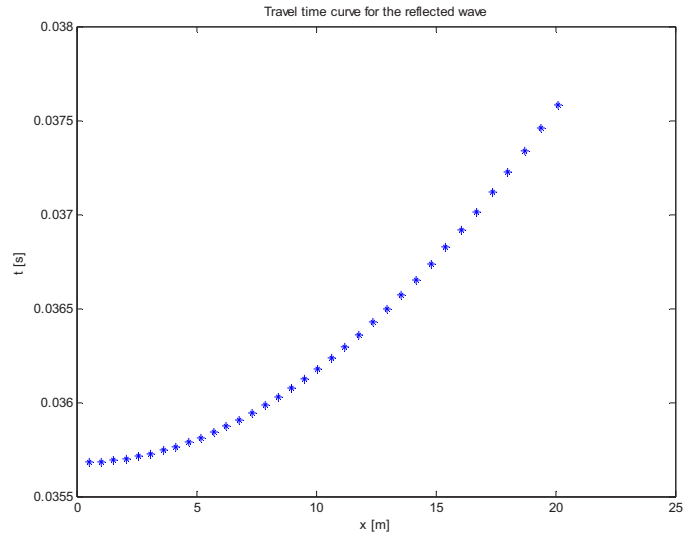
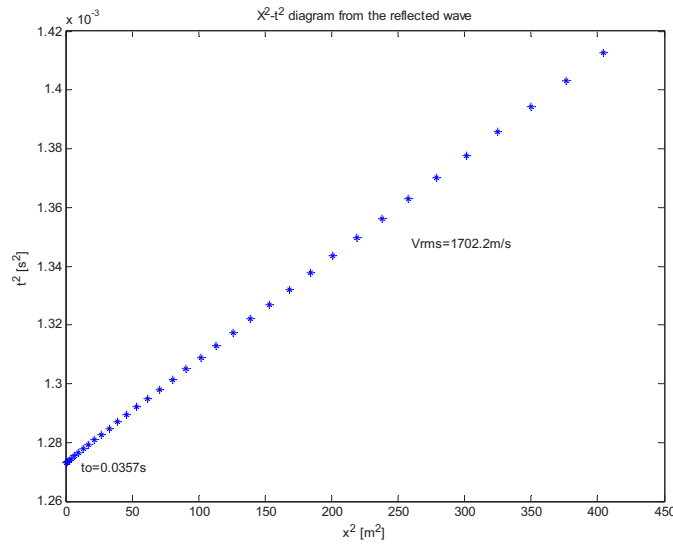


Figure 4. a) travel-time curve for the reflected wave; b) x^2-t^2 curve for the reflected wave. The rms velocity is defined to be 1397.1m/s and the intercept time is $t_0=0.0269$ s.

The same computations were performed for the fracture at 23m and are shown in Figure 8.



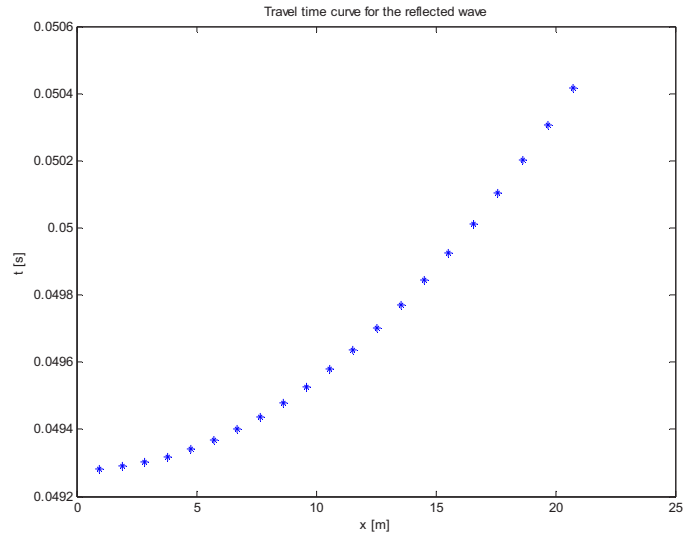
a)



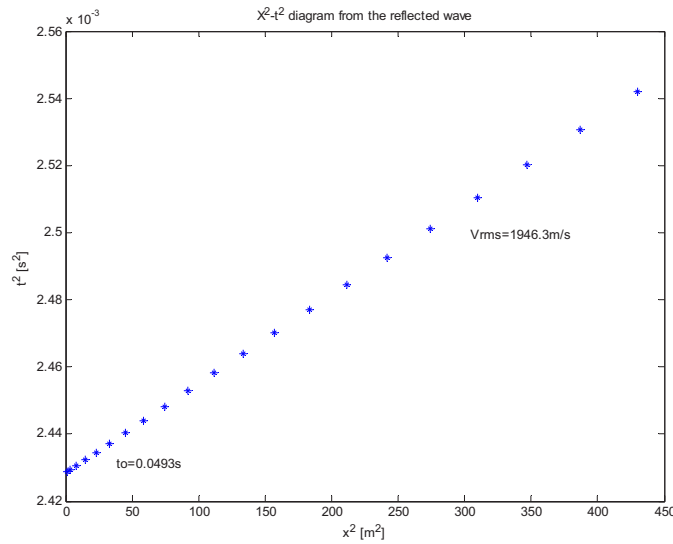
b)

Figure 8. a) travel-time curve for the reflected wave; b) x^2-t^2 curve for the reflected wave. The rms velocity is defined to be 1702.2m/a and the intercept time is $t_0=0.0357s$.

The computations were repeated again for the 40m fracture and the results are shown in Figure 8.



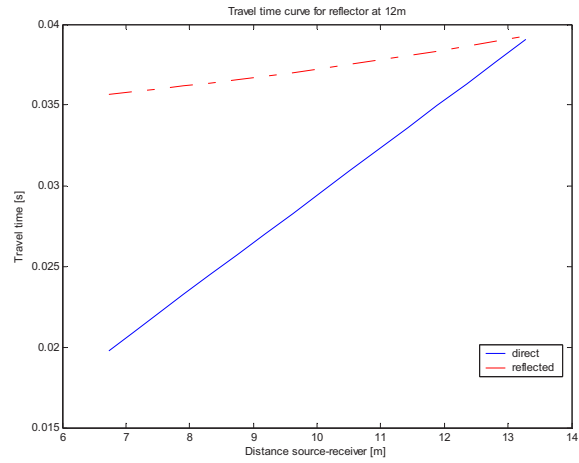
a)



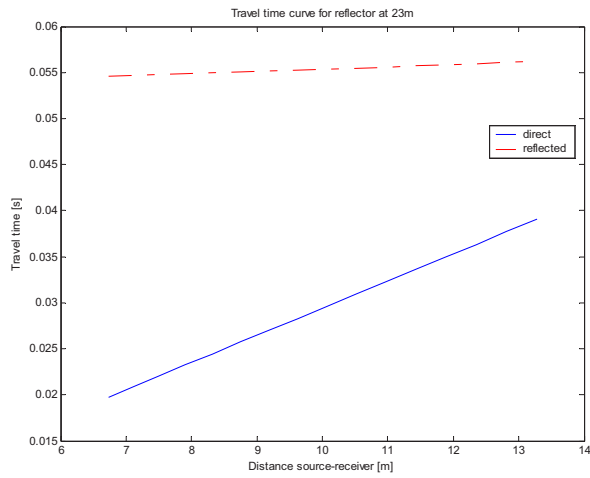
b)

Figure 9. a) travel-time curve for the reflected wave; b) x^2-t^2 curve for the reflected wave. The rms velocity is defined to be 1946.3m/s and the intercept time is $t_0=0.0493$ s.

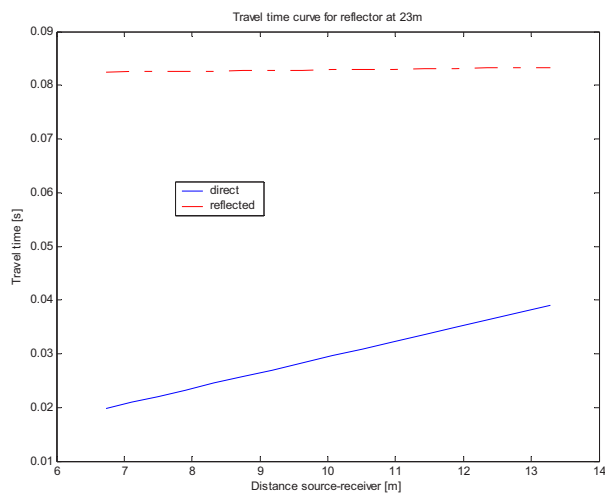
Arrival times were generated for the direct waves and reflected waves for the fractures at 12, 23, 40m depth in Figure 10a, Figure 10b, and Figure10c, respectively,



a)



b)

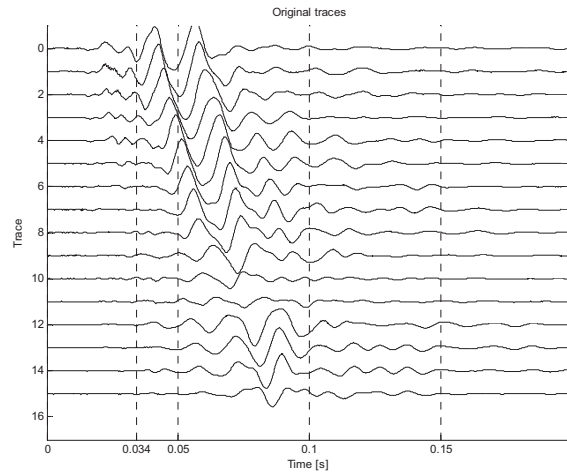


c)

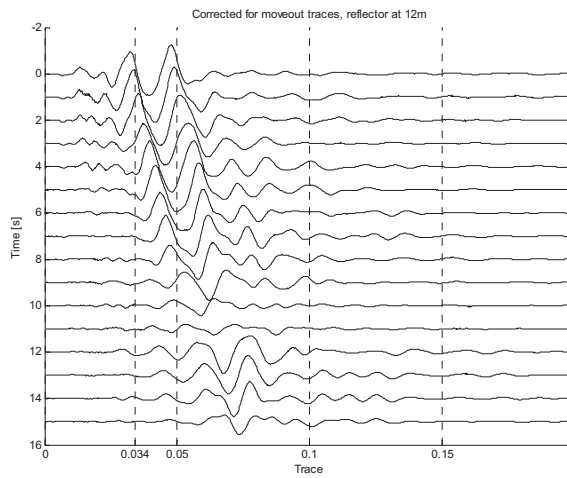
Figure 10. Travel time curves for direct and reflected waves for a) 12m deep fracture; b) 23m deep fracture; c) 40m deep fracture.

The travel times in Figure 10 are the NMO corrections. These NMO corrections were applied to each trace and then the traces were added together. Figure 11a shows the original traces and their variation with distance from the shot. Figure 11b shows the traces after application of the NMO correction. Figure 11c is the stacked trace. The objective of stacking is to amplify coherent arrivals, the reflections, and cancel out non-coherent arrivals such as those from surface waves. The data in Figure 11 show the application of NMO for the 12m fracture. Figure 12 shows the application of NMO for the 23m fracture. Figure 13 shows the application of NMO for the 40m fracture.

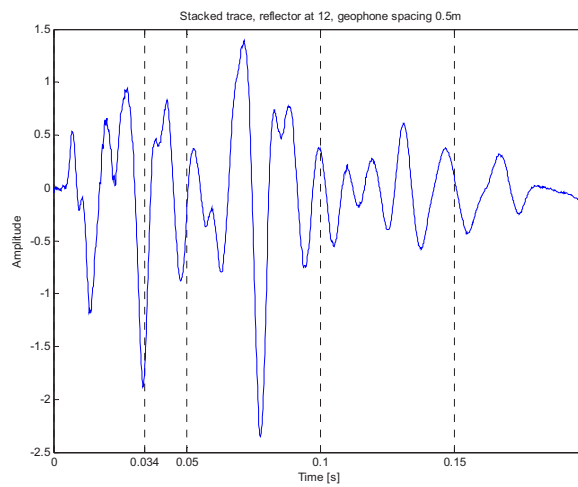
The stacking was done for two wet records (during pumping) and two dry records (15min after pumping stopped). Comparison of records taken under similar conditions is a measure of the repeatability of our measurement of the seismic waves. Figure 14 shows how the amplitude of the stacked traces differs between dry and wet records. Figure 14 a shows the direct comparison of two shots before pumping and during wet conditions. Figure 14b shows the direct comparison of two shots when pumping had stopped, during dry conditions. Figure 14, shows a comparison of the seismic signal for wet and dry conditions. Because the comparison is not as great, we computed differences in the traces. Figure 14d shows the comparison of the differences in these traces. There is a clear difference in the traces with the difference exceeding twice the noise level as determined by differences between traces obtained under similar conditions. Figure 15 shows the repeat of the analysis for the fractures at 23m and 40m.



a)

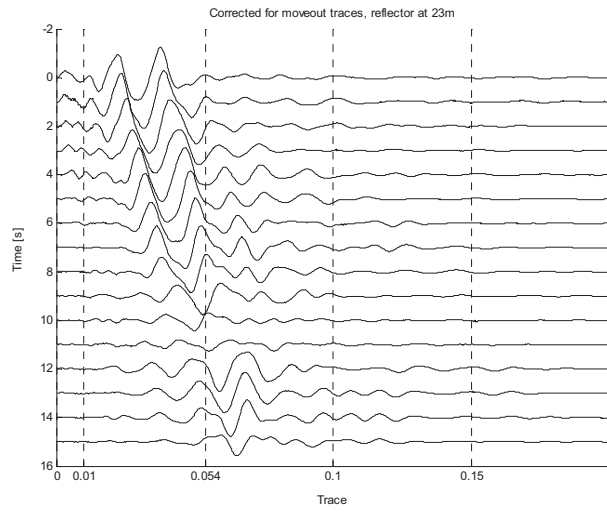


b)

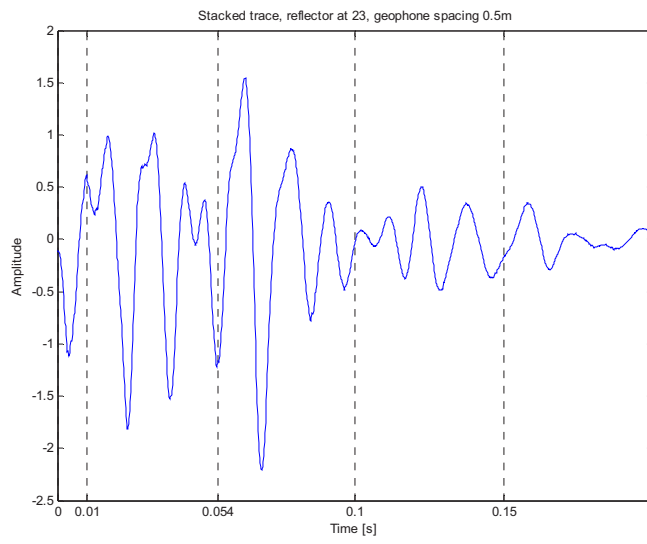


c)

Figure 11. a) original traces; b) corrected for nmo traces; c) stack trace, the fracture is nicely delineated at 0.034s.

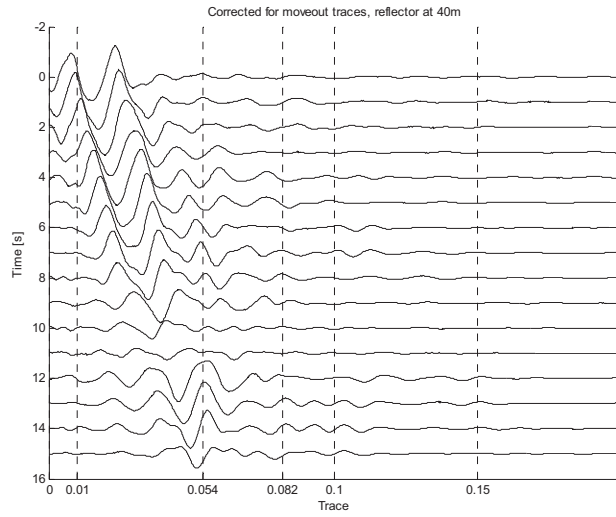


a)

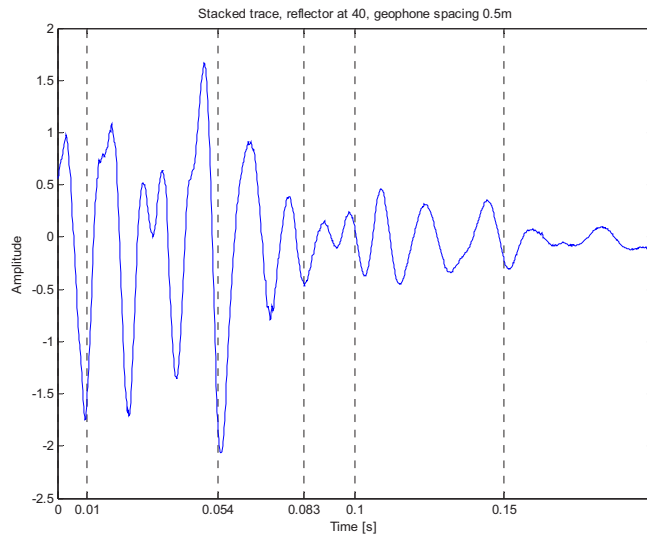


b)

Figure 12. a) NMO traces; b) stack trace delineates the fracture at 23m

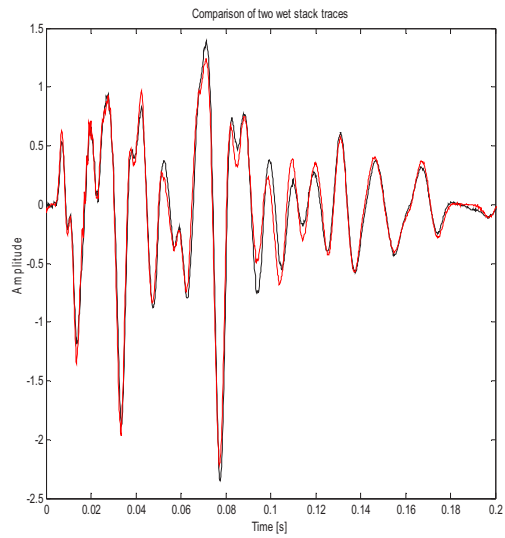


a)

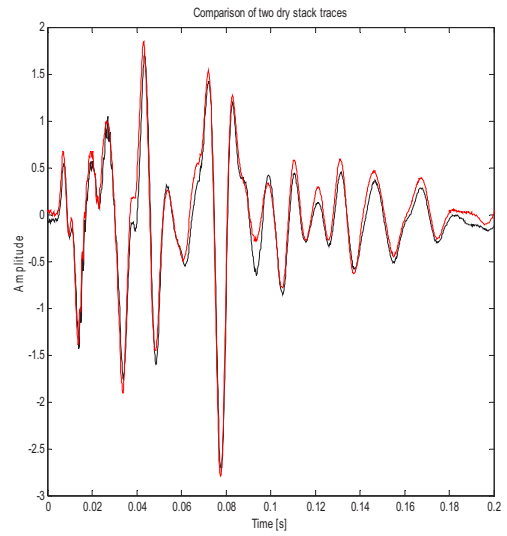


b)

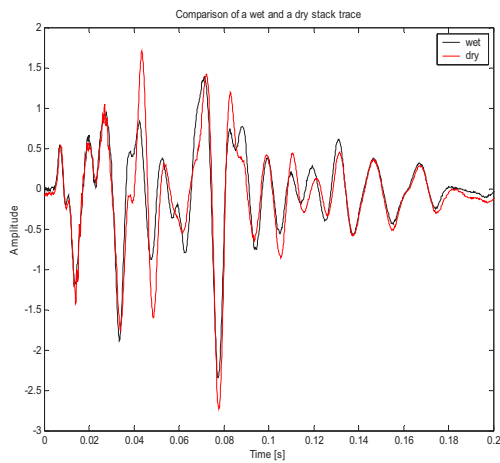
Figure 13. a) NMO traces, b) stack trace, the 40m fracture is at 0.082s, although the reflection is quite weak. The 23m fracture is even more noticeable here.



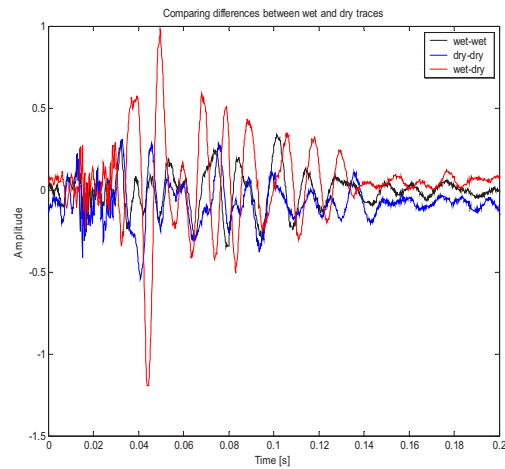
a)



b)

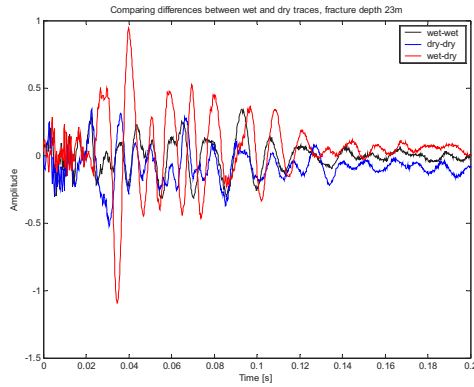


c)

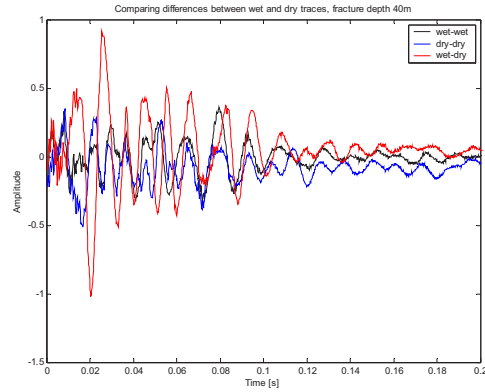


d)

Figure 14. Differential analysis for the 12m fracture. a) comparison of the stack trace of two wet records; b) comparison of the stack trace of two dry records; c) comparison of the stack trace of a wet and a dry records; d) comparison of the difference between two wet (black line), two dry (blue line) and a wet and a dry (red line) trace.



a)



b)

Figure 15. Comparison of the differences between wet and dry records for a) 23m deep fracture; b) 40m deep fracture.

The resulting difference traces are similar, as might be expected because the move out functions are similar, but shifted in time. There is a distinct change in seismic properties under the different pumping conditions. It is not entirely clear that these changes are due to changes in the reflections from the fractures or to changes in water content in the shallow soil. More signal analysis may resolve the source of the anomalies.

Chapman, Melinda J. Thomas J. Crawford, and W. Todd Tharpe (1996). *Geology and Ground-water Resources of the Lawrenceville area, Georgia*, Water-Resources Investigations Report 98-4233, U.S. Geological Survey, Denver, CO, 56pp.

Appendix II

A Differential Approach for Detecting Temporal Changes in Near-Surface Earth Layers

Based on the presentation by Tatiana Toteva, and L.T. Long, at the 76th Annual Meeting, Eastern Section Seismological Society of America, Virginia Polytechnic Institute and State University, Blacksburg, Virginia. October 31 to November 1, 2004.

Abstract: The physical parameters (shear wave velocity, density, porosity, etc.) of near-surface soils and weathered rocks have been extensively studied for the purposes of geotechnical engineering, hydrology, oil and gas exploration etc. The possibility of using geophysical techniques for monitoring changes within this upper layer has gained big popularity within the recent years. The objective of this study is to develop a differential technique for detecting subtly velocity changes within the soil layer. The differential technique is based on a study of the difference between two normalized traces taken at successive time intervals. The differences are interpreted as perturbations to a structure. This study has applied the differential technique to Rayleigh waves. We hypothesized that fluid penetration due to natural causes (rainfall) or pumping of fluids, would lead to changes in the shear wave velocity, which could be detected on the differential seismograms. In the traditional approach the soil layer is studied by inverting the phase velocity dispersion curve for the velocity structure. Instead of the phase velocity we use group velocity for inversion curve. Group velocity depends on phase velocity and the change of the phase velocity with frequency. Hence, we hypothesized that group velocity would be more sensitive to subtle changes in the velocity structure. The technique was tested for two different types of soil perturbations. We acquired data before and after heavy rain in the Panola Mountain Research Watershed to test the effect of variations in water table and soil moisture. At a second site, we tested a more controlled perturbation by pumping water into the soil at a depth of about 1.0 meter. Important factors in the acquisition of this data were the use of a repeatable weight-drop source and a secure and repeatable geophone placement. Our results show that the fluid penetration in the soil causes phase changes and time shifts, detectable on the differential seismograms.

Introduction

The objective of this study is to demonstrate a differential technique for detecting subtle velocity changes, particularly those occurring within the near-surface soil layer. We hypothesized that fluid penetration due to natural causes (rainfall) or the pumping of fluids would lead to changes in the shear wave velocity, which in turn could be detected by the group velocity dispersion curve. Subtle changes in seismic velocity can be expressed as subtle time shifts in seismograms. Hence, we obtain seismic data with the same source and receiver positions at sequential times in order to monitor the change in velocity.

Surface Wave Analysis:

Conventional surface wave analysis uses either the phase velocity or group velocity to determine the dispersion curve in a specific area. In this study, we will do this along a line, obtaining dispersion relations for phase and/or group velocity as a function of position along the line. The standard procedure is to use the dispersion relation to find a layered velocity structure under the area with the dispersion curve.

Instead of mapping variations in structure (note, the structure could be provided as a separate analysis) in differential surface-wave interpretation we look for time variations in the dispersion curves (as indicated by time variations in the seismic trace) induced by changes in

fluid content. The reference or average structure is no longer critical to the analysis so long as a reasonable approximation is available to generate appropriate theoretical differences in dispersion induced by known perturbations in the structure. For the differential approach, the reference is not the pre-test velocity structure, which is generally unknown in detail, but is the seismic trace from the unperturbed structure, which is available from an earlier survey. In the differential approach, we measure the differences in the dispersion for waves traveling the same path by direct comparison of two seismic traces recorded at different times. The direct comparison gives the time shift.

The time shift between two phases can be expressed as the difference between the phases of the two traces by the equation,

$$\delta t = \frac{\Delta \varphi}{2 \pi f}$$

where for angles less than 45 degrees,

$$\Delta \varphi = \sin^{-1} \left(\frac{A_{ref} - A}{A} \right)$$

and the A's are the amplitudes of the reference trace and the perturbed trace.

Data for this study were collected at the Panola Mountain Research Watershed using 15 Hz geophones on the established line. A linear array of geophones with one meter spacing was used for the recording of the data. The line was marked with permanent concrete geophone mounts. The data taken after each hurricane represent wet saturated ground. The weight-drop source was placed 5m from the first geophone. Measurements were taken before and one day after each of two major hurricanes –hurricane Frances and hurricane Jeane. On comparison (Figure 1.) the phase arrival times look similar for the two events.

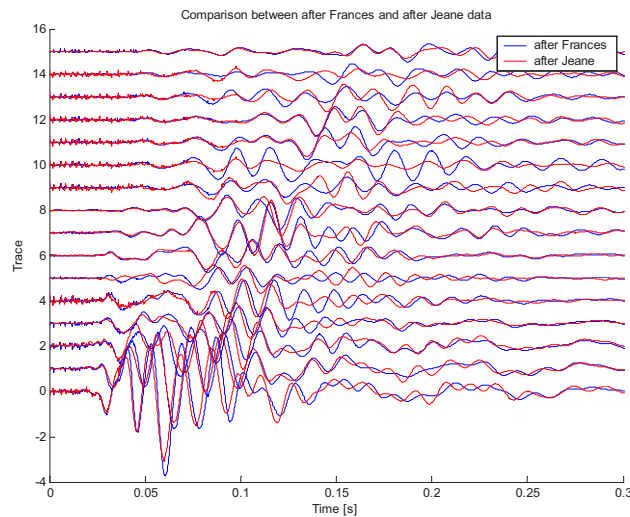
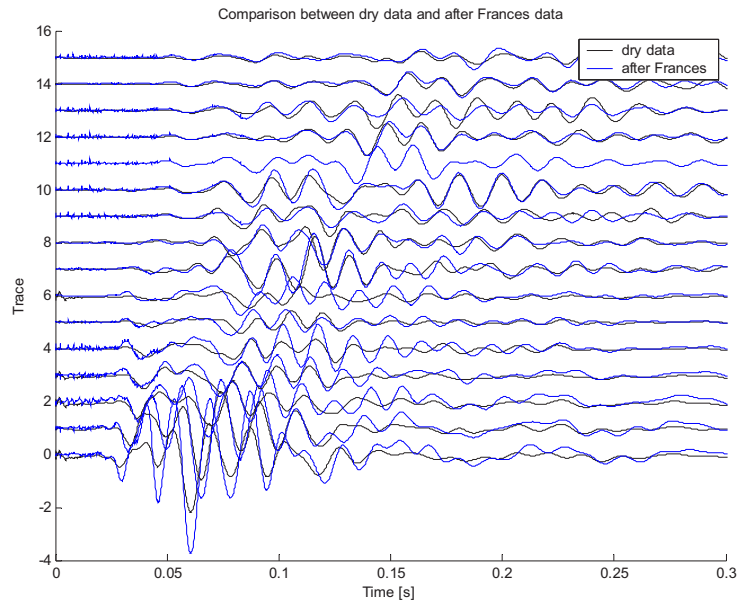


Figure 1. Comparison of data recorded during wet periods after two storms.

However, in Figure 1, the amplitudes vary along the line. In contrast, both the amplitudes and the phases appear to vary when comparing data between dry and wet periods (Figure 2).

Figure 2. Comparison between records recorded during dry periods before the storms and wet



period after the storms.

In all tests we showed that the tests over a short time period were repeatable, giving in all cases almost identical signatures. The differences represent variations in the velocity structure with time. In order to quantify these changes, we have computed group velocities from the data and for filtered data we have computed the phase shifts. The group velocities are shown in figure 3. In the 20 to 30 Hertz range, which is appropriate for a reasonable sampling of the top meter of soil and rock, the velocities following the two hurricanes were distinctly lower. Reduced velocity would be expected for the increased density associated with a higher water table

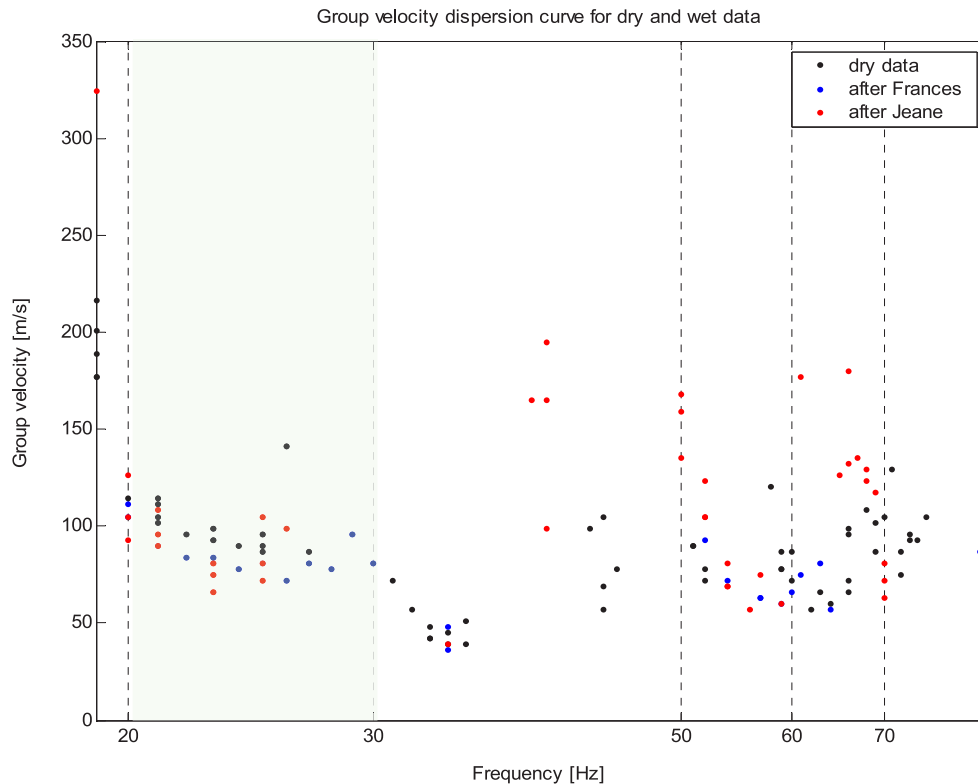


Figure 3. Group velocities observed before and after major storms and associated changes in water saturation.

In order to compute actual changes in arrival times for particular phases, we used a multiple filter technique. The filtered data for 30 Hz is shown in Figure 4. The traces showed that the amplitudes were higher when water content was higher than they were during dry periods. While the phase shifts for the hurricane data were similar, there were significant shifts in phase relative to the dry recording periods. Figure 5 shows the computed time differences in the arrival of various phases. The reference is the record during the dry period. The dry trace line in Figure 5 indicates that the source is stable in the first half of the line and becomes increasingly unstable at the most distant geophones. The progressive increase in time in the short distances, with increasing times with distance, suggests that the velocity has been reduced by increased water content. The velocity decrease amounts to about 5 percent.

Conclusions

The very good repeatability of the source allows detection of subtle time shifts in dispersed surface waves. In particular, soils with higher water content, such as following a significant rain event, have lower group velocity than data obtained when the soils are dry. We were able to detect time differences comparable to the sampling interval by measuring the phase shift defined over a few cycles of wave motion.

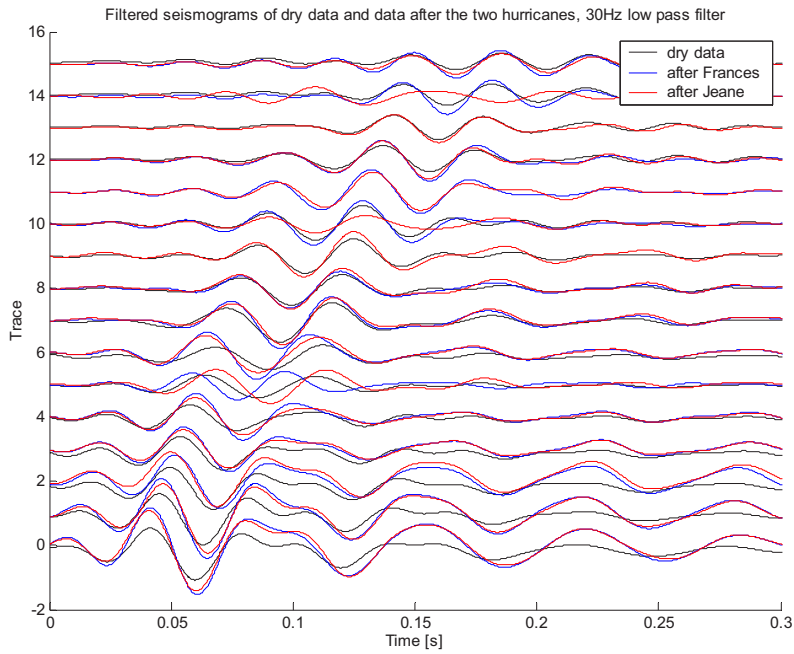


Figure 4. Data filtered at 30 Hertz showing comparison of data during dry periods and following hurricanes Frances and Jeane.

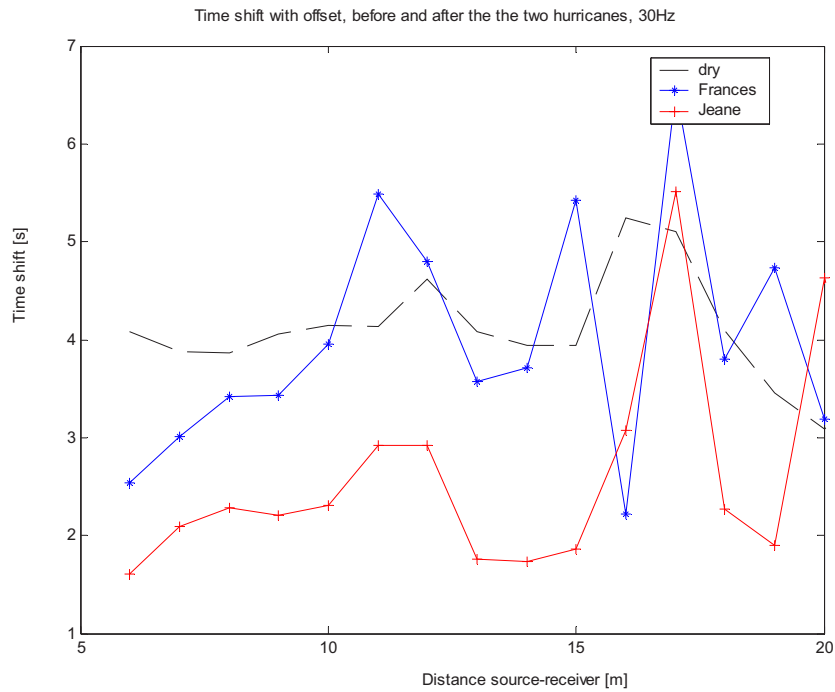


Figure 5. Computed time shifts for 30 Hertz.

Appendix III

A scattering inversion experiment to identify fractures on a granite outcrop

Tatiana Toteva and L. T. Long.

Abstract: A critical need in understanding open or fluid filled fractures in crystalline rock is the ability to identify these fractures, to characterize their source zones, to map flow paths within the fractures, and to assess residence time of water in the system. Fractures are an important component in the water resources of areas where crystalline rocks crop out at the surface. We have attempted to use scattered waves to identify and map fractures in a crystalline rock. Our research was conducted at the Panola Mountain Research Watershed (PMRW), GA. The scattering technique was tested in an area of exposed rock. We used 16 geophones placed in a circular array with diameter of 16m. The free period of the geophones is 100Hz. A major effort was taken towards suppressing resonances of the geophones at high frequency. We used clay to better attach the geophones to the outcrop and sand bags to weight the instruments down to suppress the high frequency resonance. A small weight-drop source was designed to generate a high-frequency input signal. The source provided signals in the 300 to 800 Hz range. The source was moved to shot points in the distance range of 5 to 60 meters from the recording array. The recorded signals were high-pass filtered to allow only waves above 500 Hz. Analysis of the data gave independent estimates of the velocities of surface waves on the rock and shear and compressional wave velocities in the rock. In processing the data, the distance of travel of a scattered wave was obtained from the travel time. The direction to the scattering fracture is obtained by interpreting maximum the semblance as a function of apparent velocity and direction of propagation. The technique provides a theoretical way to map positions of varying scattering efficiency and hence the location of fractures.

Introduction to scattering inversion for fracture detection

Scattering inversion is a form of the 3-dimensional migration used in processing seismic reflection data in industry. The basis for the scattering inversion we propose has been described in detail by Chen and Long, (2000a). By combining a two dimensional array of geophones and sources, the sites of reflections can be located in a 3 dimensional spatial grid. As in the study by Chen and Long (2000a) the inversion can be improved by performing the stacking by using the Algebraic Reconstruction Technique (ART). However, in this study we have used beam focusing with an array of geophones to give the direction of arrival of scattered waves. This refinement to the Algebraic Reconstruction Technique is a significant improvement because it strongly limits the source zone of the reflection.

Summary of scattering inversion: The generally accepted model for the seismic coda is a superposition of wavelets scattered back from many structures (Aki, 1969, Aki and Chouet 1975). This coda model has been refined in order to relate coda decay to the scattering and attenuation properties of the earth's crust (Sato, 1977; Frankel and Wennerberg, 1987; Revenaugh, 2000). A fundamental assumption of the coda model is that intrinsic absorption and

the distribution of structures causing scattering is uniform. As a result of this assumption, all these models predict that the seismic coda should decay smoothly and that the coda decay rate should be independent of the hypocenter. However, in most recordings of seismic events the rate of decay deviates from this prediction. As is well known from reflection seismic methods, the seismic coda does not always decay smoothly, often containing anomalous amplitudes from waves reflected from structures at depth. These observations suggest that the assumptions concerning the uniform distribution of structures that scattered wave energy or the uniform distribution of intrinsic absorption may be violated. This conclusion should have been expected because the structures that scatter seismic energy are rarely distributed uniformly in the earth's crust. For example, open fractures that can scatter significant seismic energy are clustered near fault zones and are more prevalent at shallow depths where the lithostatic pressure is too low to close joints or fractures.

In the past decade, several studies have attempted to characterize the distribution of structures that scatter seismic waves. One approach is to apply frequency-wavenumber (F-K) analysis to the data from dense seismic arrays (e.g. Furumoto *et al.*, 1990). Studies based on this approach have identified waves scattered from geological structures and topographic relief near the recording stations. Our approach is the coda envelope inversion technique (Ogilvie, 1988; Nishigami, 1997; Chen and Long, 2000a, Revenaugh, 2000). One advantage of this approach over the F-K analysis is that coda envelope inversion does not require a dense array of stations. An advantage over the Kirchhoff depth-imaging method (Sun *et al.*, 2000) is the reduction in required data processing. Coda envelope inversion is appropriate when the coda is long compared to the period of the waves. For shallow scattering, Kirchhoff depth imaging methods may be required. Part of this research is to define the conditions under which Kirchhoff migration and coda envelope inversion techniques work best.

The effectiveness of coda envelope inversion can be illustrated by results from Chen and Long (2000a). Figure 3 shows the distribution of scattering coefficients surrounding the Norris Lake Community seismicity. The epicenters of the many earthquakes of this swarm are located near the center of the image. The 5 to 7 stations recording the small earthquakes surround the epicentral zone.

The areas of greater relative scattering coefficients are closely associated with the epicentral zone in the center, and near some geologic structures along the east border of the image area. The distribution relative scattering coefficients showed that fracture density decreased rapidly with depth. One important observation is that the shallow scattering coefficients are strongly frequency dependent, indicating scattering from fractures rather than from velocity contrasts that would be frequency dependent.

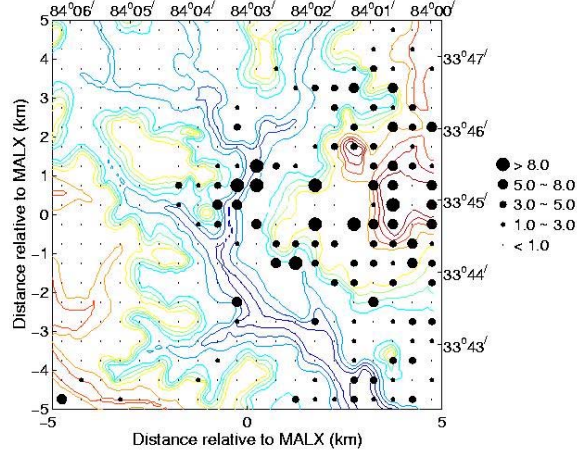


Figure 3. Relative scattering coefficients at 17 Hz for a depth of 0.25 km.

The theoretical model for the scattered waves in the coda is given in the paper by Chen and Long (2000a) and can be summarized as follows. The coda energy level at lapse time t is a function of the source radiation pattern, the numerous velocity anomalies and discontinuities that scatter seismic energy, and the propagation properties of the medium. Most investigations (Aki and Chouet, 1975; Sato, 1977) assume that the propagation may be represented by statistical methods. To obtain information about a non-uniform distribution of scattering coefficients, deterministic methods such as those of Ogilvie (1988), and Nishigami (1997) must be used. In the coda envelope inversion of this study, we take advantage of the simple expressions of the statistical method to find the master curve of coda decay. Then a deterministic method is used to find the scattering strength of individual structures relative to the master curve of coda decay. Relative scattering coefficients are the ratio of the actual scattering coefficient of a scattering structure to the average scattering coefficient of the region. In statistical methods, uniform and random distributions of scattering structures, spherical radiation of energy from the source, isotropic scattering and homogeneous velocity structure are usually assumed. Furthermore, if the scattering does not contain converted phases, and the medium takes up the whole three-dimensional space, then the mean energy density of scattered waves at frequency ω can be found by the single isotropic scattering theory of Sato (1977),

$$E_0(r, t | \omega) = \frac{Wg_0}{4\pi V^2 t^2} K\left(\frac{t}{t_s}\right) \exp\left(-\frac{\omega t}{Q_c}\right) \quad (1)$$

where W is the total energy radiated from the source at frequency ω , g_0 is the average scattering coefficient of the random medium, Q_c is the coda quality factor, V is the velocity of the S wave, t is the lapse time of coda waves measured from the earthquake origin, t_s is the travel time of direct S wave, and $K(t/t_s) = (t_s/t) \ln[(t+t_s)/(t-t_s)]$. Here we put a subscript 0 for both E and g to denote that both parameters hold the average value and that they are derived for a uniform distribution of scattering objects.

From the deterministic point of view, the medium consists of discrete scattering structures at defined locations. If the phases of scattered waves are randomly distributed, we may assume that the scattered waves can be regarded as incoherent. Then, the energy of the scattered waves contained within the lapse time window $[t_j - \delta t/2, t_j + \delta t/2]$ will be equal to the summation of the individually scattered waves arriving within this window. In a constant-velocity medium the scattered waves that meet this travel time condition are contained in an ellipsoidal shell whose foci are located at the source and receiver. For a source and receiver in close proximity, the shell is approximated by a sphere whose inner radius is $V(t_j - \delta t)/2$, and whose thickness is $V\delta t/2$. If the scattering cross section of each scattering structure takes the average value σ_0 , and if the total number of scattering structures falling into the shell is N_j , then the energy contained in the lapse time window $[t_j - \delta t/2, t_j + \delta t/2]$ is approximated (Aki and Chouet, 1975; Sato, 1977) by,

$$E_0(t_j)\delta t = \frac{WN_j\sigma_0}{(4\pi)^2(Vt_j)^4} \exp\left(-\frac{\omega t_j}{Q_c}\right) \quad (2)$$

For the uniform distribution of scattering coefficients and the homogeneous distribution of Q_c , equation (2) predicts that the coda wave amplitude will decay smoothly with lapse time and be random. However, fluctuations in the coda decay are caused by the non-uniform distribution of scattering coefficient and/or intrinsic absorption. For a non-uniform distribution of scattering cross sections, we assume that the scattering cross section of each structure is unique. In this case, the scattering cross section for structure i can be written as $\sigma_i = \chi_i \sigma_0$, where χ_i is called the relative scattering coefficient. The energy contained in the coda waves in a lapse time window becomes

$$E(t_j)\delta t = \frac{W\sigma_0}{(4\pi)^2(Vt_j)^4} \exp\left(-\frac{\omega t_j}{Q_c}\right) \sum_{i=1}^{N_j} \chi_i \quad (3)$$

Here the relative scattering coefficient χ_i measures the ratio of the scattering strength of an individual scattering object to the average scattering strength of the medium.

Following the method of Nishigami (1997) and divided equation (3) by equation (2), we finally get

$$\frac{E(t_j)}{E_0(t_j)} = \frac{1}{N_j} \sum_{i=1}^{N_j} \chi_i \quad (4)$$

Equation (4) indicates that the ratio of observed energy density displayed in individual coda to the average energy density is independent of the source response and path effects. Also, equation (4) indicates that the ratio is equal to the average of the relative scattering coefficients of those structures responsible for the generation of this part of the coda.

For each seismogram, the coda is divided into small time windows, each of which gives an equation based on equation (4). For these equations, the scattering objects contributing to each time window are contained in a series of ellipsoidal shells. The number of scatterers can be large, over 13500 in the Chen and Long (2000a) study. Equation 4 leads to a very large but sparse matrix.

For monitoring the change in scattering coefficients from fractures (4) should be modified by replacing the vector of the ratio $e_j = E(t_j)/E_0(t_j)$ with its change δe_j and the vector of the relative scattering coefficients with $\Delta\chi_i$.

The coda-envelope-inversion is conventional tomography, in which conventional matrix inversion methods are not practical. In this study, the iterative Algebraic Reconstruction Technique (ART) is used to find a solution for equation (4) (Humphreys *et al.*, 1984; Nakanishi, 1985). We first make an arbitrary initial guess at the solution. In this study we assign a value of one to all χ_i 's so that the initial solution represents average background level of scattering coefficients. We examined other starting solutions but found that we obtained the same solution for each. We applied a relaxation parameter to control the rate of convergence and a constraint that all relative scattering coefficients remain positive. In this formulation successive iterations of the ART algorithm converge to a constrained and damped least square error solution (Kak and Slaney, 1988, pp280-281). In our study, the relaxation parameter was given a value of 0.1 and the iterations were truncated when the model parameters change less than 5% for additional iterations.

The use of an array of geophones provides a significant advantage in performing the scattering inversion. The array can be analyzed for velocity and direction of approach of the scattered waves by computing the semblance for an array of apparent velocities and directions.. Semblance is a measure of multichannel coherence. Semblance is computed from

$$S(t) = \frac{\sum_{j=t-N/2}^{t+N/2} \left[\sum_{i=1}^M F_{ij} \right]^2}{M \sum_{j=t-N/2}^{t+N/2} \sum_{i=1}^M (f_{ij})^2}$$

where M channels are summed. The coefficient for time t is evaluated for a window of width N. The time at the center of the window, t, is adjusted for each trace to correspond to a direction of approach and apparent velocity across the array. An example of semblance analysis for one shot at the PMRW is shown in Figure 4.

Figure 4 is a plot of semblance as a function of apparent velocity and angle of approach. The arrival of surface waves, shear waves and compressional waves is indicated by high semblances at appropriate velocities. The surface waves show consistent peaks at velocities near 2300m/s. The surface of the granite is relatively unweathered and the surface waves do not show significant dispersion. This condition is a clear advantage for recording scattered waves because there are no dispersed surface waves to interfere with the scattered waves. For both the compressional and shear waves, the apparent velocity varies, depending on the angle of emergence. The angle of emergence is the angle between the ray path and the horizontal. The angle of emergence for shear waves varies from 0 degrees (horizontal propagating waves) at the shear wave velocity of about 3200m/s to about 55 degrees at the compressional wave velocity of 5500m/s. The compressional wave arrivals show velocities of 5500m/s or above, depending on angle on their angle of emergence. There are apparent velocities in the range of 5500m/s and above where both shear and compressional waves can give measurable semblances. However, shear waves at near vertical angles of emergence are not recorded strongly on vertical seismometers and the near vertical compressional waves would be expected to be strong arrivals

on the vertical geophones. We have assumed that the waves travel their entire path as either surface waves, shear waves or compressional waves. It is very likely that some portion of the arrivals at the array represent converted waves. That is, waves that start as a shear wave and on reflection at a fracture are converted to compressional waves and detected as compressional waves at the array. These are fortunately not coherent and would not accumulate at one reflection location as a strong reflection. Hence, converted waves may contribute to the noise background, but would not interfere with the detection of fractures.

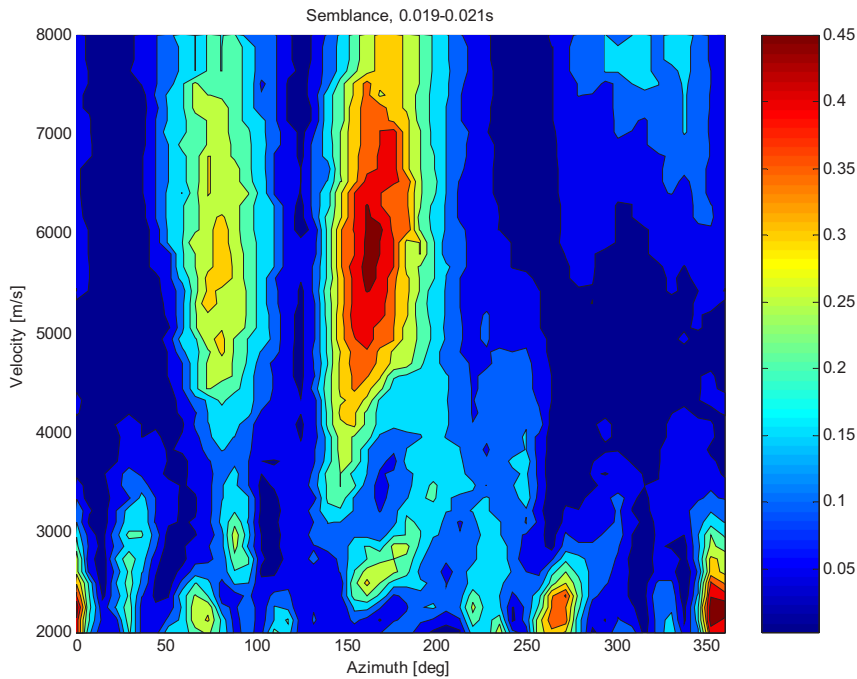


Figure 4. is a semblance plot showing a strong compressional wave arrival at 160 degrees. A shear wave arrival can be seen at 90 degrees and surface wave arrivals appear at 70, 270, and 360 degrees.

Because the semblance plots give tightly constrained angles of approach for both compressional and shear waves, iteration with the ART algorithm is not needed to locate fractures. Iteration would be needed to quantify the strength of scattering from the fracture. In this analysis we have computed the semblance for multiple times in the coda for about 14 shot point locations on the granite. The 14 shot point locations were in the shape of a rectangle. In order to test the imaging program and its ability to locate sources of signals, we applied it to the time window containing the direct surface wave arrival. The surface wave arrival should point back to the origin, and correspond to the shot point. The results of this first test are shown in Figure 5. The only shot points not clearly imaged are those on the left in Figure 5. The background noise appears as circles surrounding the origin of the recording array.

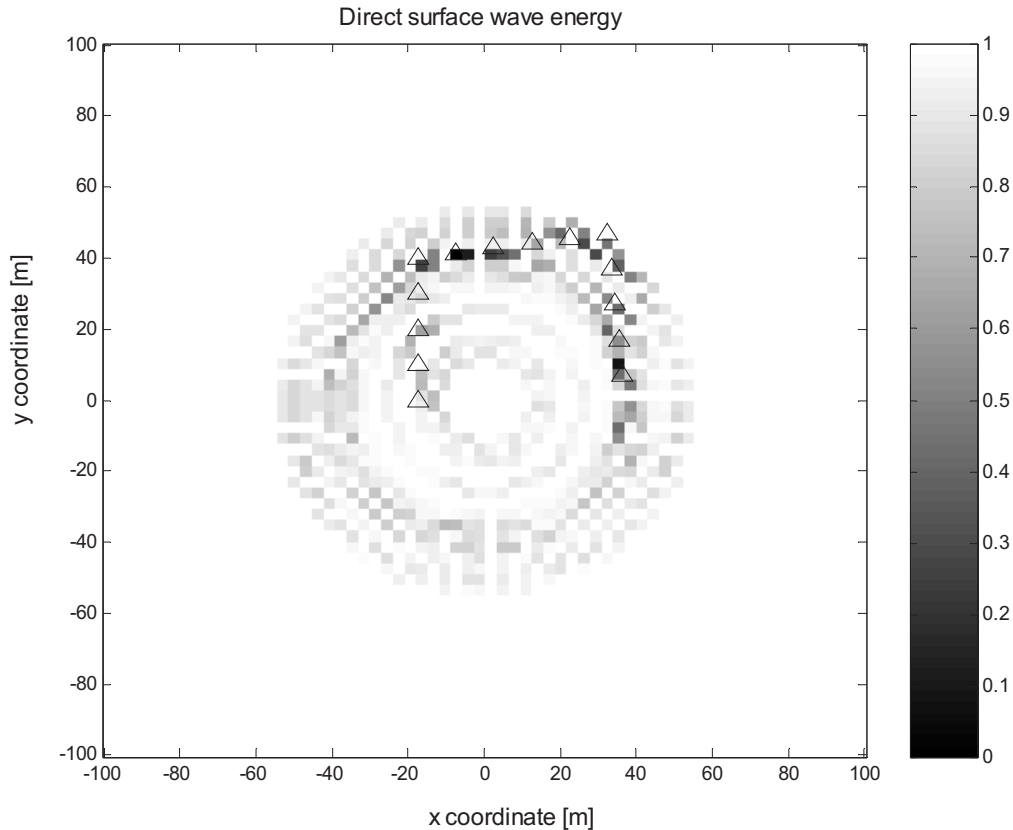


Figure 5. Inversion for sources using only windows in the arrival time of the surface wave. The triangles show the actual locations of the shots, the bright squares, particularly those on the top and right, are indicated sources of the signals.

Bibliography

- Aki, K.(1969). Analysis of the seismic coda of local earthquakes as scattered waves, *J. Geophys. Res.*, **74**, 615-631.
- Aki, K. and B. Chouet (1975). Origin of coda waves: source, attenuation and scattering effects. *Journal of Geophysical Research*, **80**, 3322-3342.
- Chen, Xiuqi, and L.T. Long (2000a). Spatial distribution of relative scattering coefficients determined from microearthquake coda. *Bulletin. Seismological Society America*, 90, 2, pp 512-524.
- Frankel, A. and L. Wennerberg (1987). Energy-flux model of seismic coda: separation of scattering and intrinsic attenuation, *Bull. Seism. Soc. Am.* **77**, 1223-1251.
- Furumoto, M., T. Kunitomo, H. Inoue, I. Yamada, K. Yamaoka, A. Ikami, and Y. Fukao (1990). Twin source of high-frequency volcanic tremor of Izu-Oshima Volcano, Japan. *Geophysical Research Letters*, **17**, 25-27.
- Humphreys, E., R. W. Clayton, and B. H. Hager (1984). A tomographic image of mantle structure beneath southern California. *Geophysical Research Letters*, **11**, 625-627.
- Kak, A. C. and M. Slaney (1988). *Principles of computerized tomographic imaging*. IEEE Press, New York.

- Nakanishi, I. (1985). Three-dimensional structure beneath the Hokkaido-Tohoku region as derived from a tomographic inversion of P-arrival times. *Journal Physics of the Earth*, 33, 241-256.
- Nishigami, K. (1997). Spatial distribution of coda scatterers in the crust around two active volcanoes and one active fault system in central Japan: inversion analysis of coda envelope. *Physics of the Earth and Planetary Interiors*, 104, 75-89.
- Ogilvie, J. S. (1988). Modeling of seismic coda, with application to attenuation and scattering in southeastern Tennessee, *M.S. Thesis*, Georgia Institute of Technology, Atlanta, Georgia.
- Sato, H. (1977). Energy propagation including scattering effects: single isotropic scattering approximation. *J. Phys. Earth*, 25, 27-41.
- Sun, Yonghe, F. Qin, S. Checkles, and J. P. Leveille, (2000). A beam approach to Kirchhoff depth imaging, *The Leading Edge*. 19, 1168-1173.
- Revenaugh, J., (2000). The relation of crustal scattering to seismicity in southern California, *Journal of Geophysical Research*, 105, 25,403-25,422.

Decision Support for Georgia Water Resources Planning and Management

Basic Information

Title:	Decision Support for Georgia Water Resources Planning and Management
Project Number:	2004GA57B
Start Date:	3/1/2004
End Date:	2/28/2005
Funding Source:	104B
Congressional District:	12
Research Category:	None
Focus Category:	Management and Planning, None, None
Descriptors:	None
Principal Investigators:	Kathryn J. Hatcher

Publication

PROGRESS REPORT FOR YEAR 1

Project Title: Decision Support for Georgia Water Resources Planning and Management

Duration: March 1, 2004 - February 28, 2006 (24 months)

Principal Investigator: Kathryn J. Hatcher
Institute of Ecology Tel: 706-542-3709
University of Georgia, Athens, Georgia 30602-2202

Executive Summary

The ninth biennial Georgia Water Resources Conference was held April 25-27, 2005, to provide a forum for discussion of Georgia water resources and information relevant to the state's initiative to prepare a comprehensive statewide water resources management plan. Over 25 government, professional, and citizen organizations served to co-sponsor the conference and organize sessions and panels with over 250 speakers in these general tracks: state water plan and policy, Atlanta area water issues, water conservation, instream flow and restoration, watershed protection and TMDLs, flood mapping and stormwater, groundwater, coastal water issues, and river basins including Savannah, Etowah, Flint, and Chattahoochee Rivers. The 2005 conference proceedings with 240 papers is available on CD and as printed volumes.

The conference included panels to discuss five state water policy issues selected by the Georgia EPD director: (1) protection of instream and downstream flows, (2) water quantity allocation/reallocation among users, (3) minimum aquifer levels protection policy, (4) water quality allocation (TMDL allocation policy), and (5) water conservation/efficiency and reuse policy.

The third day of the conference provided five all-day training courses on these topics: (1) Shared Vision Planning Approach – Linking Participation and Water Planning through a Technical Systems Model (by USACE-IWR), (2) ArcHydro – GIS for Water Resources, (3) Introduction to the Clean Water Act for Watershed Stakeholders (by USEPA-Region 4), (4) Water Quality Modeling using WASP software (by USEPA-ERL), and (5) Stormwater Management using Locally-Based Planning and Management Tools (by UGA-Engr); as well as (6) a workshop on government programs with technical assistance and/or funding for water resources planning and management (hosted by USACE-SAM).

Over 40 students from UGA and Georgia Tech provided assistance for the conference sessions, policy panels and training courses.

Main Project Elements

Georgia Water Resources Conference

The ninth biennial Georgia Water Resources Conference was held April 25-27, 2005, at the Georgia Center for Continuing Education, Athens, Georgia. In addition to its traditional purpose of providing a biennial forum for presentation and discussion of major water projects, issues, programs and research in Georgia, the 2005 conference was designed with an additional purpose -- to provide information relevant to the state's initiative to prepare a comprehensive statewide water resources management plan by 2008. The conference steering committee, which sets the goals and theme for the conference, consisted of representatives from the 5 main sponsors including USGS, NRCS, UGA, the director of the Georgia Water Resources Institute and the director of the Georgia Environmental Protection Division. The EPD director selected the conference theme, "Creating Georgia's Sustainable Water Future," and gave the plenary session presentation on Georgia's initiative to develop a comprehensive statewide water resources

management plan. Governor Sonny Perdue gave the keynote conference address on Georgia water resources.

In addition to the five main sponsors, the conference was supported by over 20 co-sponsoring organizations and a program committee of co-sponsor representatives, who organized 36 of the 70 sessions and panels presented at the conference, and provided exhibits and conference promotion. The conference agenda included over 250 speakers in 70 sessions, with sessions on the Etowah River, Savannah River, Chattahoochee River Basin, Flint River Basin, and Coastal Georgia. The session and panel topics, each with 3-5 speakers, are listed below with the session organizer indicated:

TRACK 1. STATE WATER PLAN AND POLICY

- + Water Allocation Legal Issues
- + Regional Water Plans in Georgia (GaEPD)
- + Plenary Session: Carol Couch, GaEPD Director
- + Panel: Perspectives on State Water Plan Process (GWC)
- + Panel: Policy on Water Allocation/Reallocation (UGA)
- + Poster and Exhibit Session (USDA-NRCS)
- Low Impact Development
- Integrated Water Resources Planning
- Legislative Update and Water Law
- Panel: Indicators of Sustainability (GaDNR-P2AD)
- Conflict Resolution
- ^ Technical and Financial Assistance Programs (USACE-SAM)
- ^ Technical and Financial Assistance Programs II (USACE-SAM)
- ^ Adopt-A-Stream Monitoring field demonstrations (GaEPD)

TRACK 2. ATLANTA AREA WATER ISSUES

- + Public Education and Awareness (ARC)
- + Atlanta Area Stream Quality
- + Metro District Water Plans Development (MNGWPD)
- + Metro District Water Plans Implementation (MNGWPD)
- Panel: ACF River Federal Water Requirements
- ACF River Basin Water Negotiations
- Sustainable Mgt w/Lake Lanier Reuse (GW&PCA)
- Atlanta Water Supply Issues
- Sewage Overflow and Infrastructure
- ^ Full-day Course on Basin Planning (USACE-IWR)

TRACK 3. INSTREAM FLOW AND RESTORATION

- + Instream Flow Guidelines for Georgia (TNC)
- + Instream Flow Studies (Entrix Inc.)
- + Panel: Policy on Instream/Downstream Flow Protection (UGA)
- + Streamflow vs Fish Distribution
- Aquatic Ecosystems
- Imperiled Aquatic Species (USFWS)
- Etowah River Habitat Conservation Plan (USFWS)
- Stream Restoration (USACE-SAD)
- Ecosystem Restoration
- ^ Full-day Course on Clean Water Act (USEPA Region4)

TRACK 4. FLOOD MAPPING, WATER CONSERVATION

- + Floodplain Mapping using GIS (AWRA-Ga)
- + GIS Applications in Water Resources (GaEPD)
- + River Flood Forecasting (NWS-SERFC)
- + Watershed Assessment
- Georgia Sustainability Initiative (GaDNR-P2AD)
- Water Conservation in Landscape (GWWC)
- Water Conservation
- Potable Water Reuse (GW&PCA)
- Panel: Policy on Water Conservation and Reuse (UGA)
- ^ Full-day Course on GIS Use for Water Resources (GaEPD)

TRACK 5. WATERSHED PROTECTION

- + Stream Riparian Buffers
- + Runoff Impacts to Stream Quality
- + Stream Quality Studies
- + Stream Data for TMDL Models
- Watershed Alliances and Education
- Watershed Management (USEPA Region4)
- Water Quality Permit Trading
- Panel: Policy on TMDL Allocation/Reallocation (UGA)
- TMDL Plans Development (USEPA Region4)
- ^ Full-day Course on Water Quality Modeling (USEPA-ERL)

TRACK 6. STORMWATER, SAVANNAH RIVER

- + Stream Channel Restoration
- + Adequacy NPDES Stormwater Regulations
- + Panel: Erosion & Sediment Control (ASCE-Ga)
- + BMPs for Runoff Control (ASCE-Ga)
- Gwinnett County Stormwater Program I (Gwinnett Co)
- Gwinnett County Stormwater Program II (Gwinnett Co)
- Savannah River Basin Models (USACE-SAV)
- Panel: Savannah River Basin Water Use GA/SC (USACE-SAV)
- ^ Full-day Course on Stormwater Management (UGA-Engr)

TRACK 7. GROUND WATER ISSUES

- + Conservation Tillage (SWCS-Ga)
- + Piedmont Ground Water Supply I (GGWA)
- + Piedmont Ground Water Supply II (GGWA)
- Education for Private Well Owners I (UGA-CES)
- Education for Private Well Owners II (UGA-CES)
- Irrigation Water Use in Georgia
- Flint River Basin Models
- ^ Surface and Ground Water Interactions
- ^ Coastal Ground Water Levels and Management
- ^ Panel: Policy on Minimum Ground Water Levels (UGA)
- ^ Savannah Harbor Dredging Effects on Ground Water
- ^ Ground Water Contamination

Workshops and Training Courses

The third day of the conference consisted of workshops and one-day training courses:

- * Workshop on Multiple Agency Programs with Technical Assistance and Funding for Water Resources Planning and Management, hosted by US Army Corps of Engineers-Mobile District.
- * Workshop on Adopt-A-Stream Monitoring (field demonstrations), by Georgia Environmental Protection Division, Adopt-A-Stream program www.riversalive.org/aas.htm
- * Course on the Shared Vision Planning Approach - Linking Participation and Water Planning through a Technical Systems Model, by US Army Corps of Engineers, Institute for Water Resources www.iwr.usace.army.mil
- * Course on ArcHydro: GIS for Water Resources, with application for the Upper Ocmulgee watershed in Georgia, by Dr. David Maidment, University of Texas, and Jack Hampton, PBSJ [48 seats in computer lab] Organized by Georgia Environmental Protection Division. <http://www.ce.utexas.edu/prof/maidment/>
- * Course on Introduction to Clean Water Act for Watershed Stakeholders, by US Environmental Protection Agency Region IV. www.epa.gov/r5water/cwa.htm
- * Course on Water Quality Modeling using WASP software package, by US EPA Environmental Research Laboratory, Athens. www.epa.gov/AthensR/research/modeling/wasp.html
- * Course on Stormwater Management using Locally-Based Planning and Management Tools, by University of Georgia, Biological and Agricultural Engineering Department.

Conference Co-Sponsors

The conference is sponsored by: U.S. Geological Survey, Georgia Department of Natural Resources, University of Georgia, Georgia Tech – Georgia Water Resources Institute, and USDA Natural Resources Conservation Service.

Additional co-sponsors include Georgia offices of:

- American Society of Civil Engineers
- American Water Resources Association
- American Water Works Association
- Association County Commissioners of Georgia
- Georgia Municipal Association
- Georgia Department of Community Affairs
- Georgia Forestry Commission
- Georgia Soil and Water Conservation Commission
- Georgia Pollution Prevention Assistance Division
- Georgia Water & Pollution Control Association
- Georgia Ground Water Association
- Georgia Lake Society
- Georgia Water Wise Council
- National Weather Service, SE River Forecast Center
- Natural Resources Conservation Service (SCS)
- Soil and Water Conservation Society

- Soil Science Society of Georgia
- The Georgia Conservancy
- Upper Chattahoochee River Keeper
- Water Environment Federation
- U.S. Army Corps of Engineers, Mobile/Atlanta/Savannah
- U.S. Environmental Protection Agency, Region 4
- U.S. Environmental Protection Agency, ERL
- U.S. Fish and Wildlife Service

Policy Panels

The conference program plans, which were outlined by the steering committee in summer 2004 to support the state's comprehensive water plan process, were modified in fall 2004 after Governor Perdue expressed his wish that the state water plan process would emphasize resolving state water policy issues that were discussed leading up to the legislation mandating the state water plan. To adjust to this new direction, the conference agenda added five water policy panels to cover several of the key state water policy issues:

1. Protection of Instream and Downstream Flows
2. Water Quantity Allocation/Reallocation among Users
3. Minimum Aquifer Levels Protection Policy
4. Water Quality Allocation (TMDL allocation policy)
5. Water Conservation/Efficiency and Reuse Policy

These five topics were selected for the conference by the chair of the Georgia Water Council (the EPD director), responsible for developing the state water plan (www.georgiawatercouncil.org). Each panel consisted of five panelists: a DNR-EPD representative (nominated by the EPD director) to summarize Georgia's current policy and procedures; three panelists representing diverse interest groups to summarize their group's desired policy choice and view of the pros/cons for the policy choices; and a technical or legal expert. The purpose of the panels was to begin a policy dialogue and provide information useful as background for the Georgia Water Council in considering several of the key state water policy issues facing Georgia. The panels were not intended to reach consensus or to make recommendations, only to provide useful background information about the difficult water policy issues, the policy choices available, and the pros/cons of each choice from the perspectives of the major groups concerned with the issue. The five panels discussions were held during the conference, with four of the interim panel papers included in the conference proceedings (see list under publications). The policy discussions will be continued with the major stakeholders, and extended versions of policy analysis papers for the five topics will be provided for the Georgia Water Council (www.georgiawatercouncil.org) in the second year of this project.

Student Participation

Over 40 students from the University of Georgia and Georgia Institute of Technology provided volunteer assistance to the conference. Thirty-six students served as moderator assistants during the conference sessions, operating the A/V equipment and lighting. Three students provided technical and computer assistance for the all-day training course on the ArchHydro software. Ten students provided research assistance during spring semester for the five water policy panels. The student chapter of American Water Resources Association organized the Monday evening event with speaker for the conference, and also organized the team of students who served as moderator assistants. One graduate student, funded by a research assistantship, helped with editing and peer reviewer correspondence for 200+ papers published in the conference proceedings.

Publications

Hatcher, Kathryn J. (editor), Proceedings of the 2005 Georgia Water Resources Conference, Volumes I and II, April 25-27, 2005, Athens, Georgia; sponsored by U.S. Geological Survey, Georgia Department of Natural Resources, USDA Natural Resources Conservation Service, Georgia Institute of Technology – Georgia Water Resources Institute, and The University of Georgia, Athens GA, 931 pages.

Bomar, Robert, Joel Cowan, Ciannat Howett, Kevin Farrell, David Newman, Kathryn Hatcher, “State Water Policy Alternatives for Water Allocation and Reallocation,” in: Proceedings of the 2005 Georgia Water Resources Conference, The University of Georgia, Athens GA, pp. 37-43.

Biagi, John, Jerry Ziewitz, Brian Richter, Bob Scanlon, Billy Turner, Kathryn Hatcher, “State Water Policy Alternatives for Instream and Downstream Flow Protection,” in: Proceedings of the 2005 Georgia Water Resources Conference, The University of Georgia, Athens, GA, pp. 270-278.

Keyes, Alice Miller, Cindy Daniel, Shana Udvardy, Brian Skeens, David Bennett, Kathryn Hatcher, “State Water Policy Alternatives for Water Conservation/Efficiency and Reuse,” in: Proceedings of the 2005 Georgia Water Resources Conference, The University of Georgia, Athens GA, pp. 459-468.

Williams, Vince, Curry Jones, Shana Udvardy, Bill White, Matt Harper, Candace Connell, Kathryn Hatcher, “State Water Policy Alternatives for TMDL Allocation and Reallocation,” in: Proceedings of the 2005 Georgia Water Resources Conference, The University of Georgia, Athens GA, pp. 567-575.

Tasks for Year 2:

Task 1: As a follow-up to the 2005 Georgia Water Resources Conference, the electronic version of the full conference proceedings (over 200 papers) has been provided to the Georgia Water Resources Institute for uploading to the GWRI website. The complete Table of Contents (1989-2005) for the Georgia Water Resources Conference will be updated; this is searchable by author, organization and keyword in a paper’s title. Authors for the 2003 and 2005 conferences will be provided the opportunity to add a web link to their papers in the Table of Contents for readers who wish to read about new developments on the paper’s topic. The electronic version of all back volumes of the conference proceedings (1989-2005) will be provided for the Georgia Water Resources Institute.

Task 2: Review of the state sediment and erosion control program and 319 grant program, with recommendations to the state EPD director for improving the program and for coordinating this program with the state’s existing river basin plans and the pending Statewide Comprehensive Water Plan.

Task 3: The work on the five water policy panel topics, selected by the EPD director, will be continued with further discussions with the major stakeholder groups to help them define their preferred policy alternatives. Extended versions of the policy analysis papers for the five panel topics will be provided for the Georgia Water Council in the second year of this project. The panels were not intended to reach consensus or to make recommendations, only to provide useful background information about the difficult water policy issues, the policy choices available, and the pros/cons of each choice from the perspectives of the major groups concerned with the issue.

Task 4: A survey and summary of information and training needs of water resources professionals in Georgia will be provided. A website will be set up to provide guidance and training materials for comprehensive water resources planning and management, both water quantity and quality, including examples of best practices.

Biogeochemical Cycling of Arsenic at the Sediment-Water Interface of the Chattahoochee River

Basic Information

Title:	Biogeochemical Cycling of Arsenic at the Sediment-Water Interface of the Chattahoochee River
Project Number:	2004GA58B
Start Date:	3/1/2004
End Date:	2/28/2005
Funding Source:	104B
Congressional District:	5
Research Category:	None
Focus Category:	None, Sediments, Water Quality
Descriptors:	None
Principal Investigators:	Martial Taillefert

Publication

Biogeochemical Cycling of Arsenic at the Sediment-Water Interface of the Chattahoochee River

Martial Taillefert

School of Earth and Atmospheric Sciences
Georgia Institute of Technology, Atlanta GA

May 16, 2005

1.0 Executive Summary

In a previous study, elevated dissolved arsenic concentrations were detected in the Chattahoochee River (GA) and decreased in concentration with increasing distance from a suspected point-source, suggesting that arsenic could be scavenged by particles and settle to the sediment-water interface (SWI). In this study, we investigated the cycling of arsenic in the sediment of the Chattahoochee River to determine if arsenic is accumulated in the sediment downstream from two coal-fire power plants and how arsenic is biogeochemically transformed in these sediments. To realize these objectives, a combination of state-of-the-art analytical techniques - ICP-MS and voltammetry - with other conventional techniques was used to determine, with a high spatial resolution, the distribution of arsenic between particulate and dissolved phase, the redox speciation of arsenic in the dissolved phase, and the distribution of other redox species (O_2 , SO_4^{2-} , NO_3^- , Fe(II), Mn(II), and ΣH_2S) in the first 10 centimeters of four sediment cores. Depth profiles suggest that iron oxides scavenge arsenic in the form of arsenate in the water column and settle to the SWI where they are reduced by iron reducing bacteria. As a result of microbial iron reduction, dissolved arsenic, in the form of As(V) only, is released and accumulates in the porewaters near the sediment-water interface, where it can diffuse back to the overlying waters, with fluxes ranging between 20 and 200 nM/cm² yr. Sediment slurry incubations conducted to determine the mechanisms and rate of arsenic biogeochemical transformations in these sediments confirm that any arsenate added to these sediments is immediately adsorbed and later released during the reductive dissolution of iron oxides. Incubations in the presence of low concentrations of arsenate verified that microbial iron reduction occurs in these sediments and that arsenate is not concomitantly reduced during this process. Incubations with higher initial arsenate concentrations indicate that the microbial processes in these sediments may be affected by high inputs of arsenic. Finally, differences between high discharge rates and base-flow conditions in the Chattahoochee River do not seem to affect the biogeochemical processes involved in iron and arsenic cycling but may enhance fluxes across the sediment-water interface.

This investigation was part of the Ph.-D. dissertation of Stephanie Chow and has contributed to the training of several other undergraduate (Jimmy Elsenbeck, Jennifer King, Dian Putrasahan, Farhana Yasmin) and graduate (Gwendolyn Bristow, Elizabeth Carey, Judson Partin) students working under Dr. Taillefert's direction. These students either participated in field trips or performed some of the reported chemical analyses. This project resulted in the publication of one peer-reviewed paper (35), two presentations at professional meetings (American Chemical Society), one presentation at a local symposium (Georgia Tech), and one seminar (Savannah River Ecology Laboratory, UGA). Other abstracts and publications will follow in 2005.

2.0 Introduction

The adverse human health effects of arsenic have been known for several centuries. The toxicity and biochemical behavior of arsenic depends on its chemical form. In natural environments, arsenite (H_3AsO_3) is not only more mobile but can be greater than 60 times more toxic than arsenate (ΣAsO_4^{3-}), or organoarsenic compounds (1, 2). Reported regions impacted by elevated arsenic concentrations are Bangladesh, China, India, England, Thailand, and within the United States (e.g., New Hampshire, New Mexico, Massachusetts, Maine, Michigan, California, and Oregon). Arsenic input in the natural environment is mainly due to natural sources and coal-fire power plants because of its ubiquitous presence in coal (3). Coal-fire power plants release arsenic and other metalloids in the atmosphere during burning. However, the ashes are usually stored in ponds that may be episodically flooded during storm events and represent significant sources of arsenic for aquatic systems, especially nearby rivers which are often used for cooling purpose. Once in rivers, arsenic may be removed by adsorption onto sediments or travel downstream in solution (3).

In high concentrations, the most toxic fraction, arsenite, may affect ecosystems and can also present a risk for human health as these waters will eventually recharge water tables and/or lakes used for the supply of drinking water. The problem of arsenic is a main concern of the Georgia Environmental Protection Division of the Department of Natural Resources (<http://www.ganet.org/dnr/environ/>) and largely recognized in major cities, as part of the heavy metal class. However, it is equally important to evaluate locations where arsenic exists at low concentration due to its potential impact on drinking water resources.

Most environmental arsenic problems are a result of mobilization and reduction of arsenic regulated by biogeochemical processes at redox interfaces (4). In oxic conditions, authigenic iron, manganese, and aluminium oxides, clays, and particulate organic matter (POM) can remove metals by sorption or precipitation (5). The adsorption of arsenic in natural waters is mainly controlled by solid-solution interactions with iron oxides (1, 6-8) because their charge, in contrast to POM and manganese and aluminum oxides, is slightly positive at circumneutral pH (9), while arsenate is negatively charged (7, 10-12). As a result, arsenate mobility and bioavailability is limited in oxic conditions. In suboxic conditions, manganese and iron oxides are reductively dissolved during organic matter remineralization, potentially releasing trace metals including arsenate (4), in the dissolved phase. It is also suggested that arsenate may be simultaneously reduced during the reduction of iron oxides (13), thus turning arsenic-contaminated sediments into a persistent toxic source. However, little evidence of the simultaneous reduction of iron and arsenate has been found in natural systems.

In anoxic conditions, arsenate may be reduced to arsenite microbially (14-16) or chemically by dissolved sulfide (17) and Fe^{2+} (18, 19) though both chemical reactions are usually slow. Arsenite is neutral at circumneutral pH and is less susceptible to adsorption onto metal oxides (7, 10, 11). In the presence of dissolved sulfide produced by sulfate-reducing bacteria, arsenite may form thioarsenite complexes (20) and eventually precipitate as arsenosulfide minerals (21, 22) or, alternatively, adsorb onto iron sulfide minerals (22). These thioarsenite complexes have yet to be identified in natural waters but, if they exist, the solubility of arsenite may be enhanced in the presence of H_2S , providing a source of toxic compound in the natural environment.

Finally, arsenite can be rapidly reoxidized in the presence of dissolved oxygen (23) or

manganese oxides (24, 25). Thus, desorption and remobilization of arsenic from sediments is influenced by pH, the activity of microorganisms, and the concentrations of dissolved oxygen, sulfide and iron in interstitial waters (8, 10, 22, 28-31). In addition, phosphate, bicarbonate, silicate and organic matter all compete with arsenic for adsorption sites, enhancing arsenic desorption and thus mobility (31).

3.0 Objectives

It is clear that arsenic is subject to several complex transformations in aquatic systems. As the sediment is usually the ultimate repository of trace metals and metalloids, it is necessary to determine quantitatively the fate of arsenic in these systems. In this project, we proposed to investigate the cycling of arsenic in the sediment of the Chattahoochee River to determine if and by what mechanism arsenic is accumulated in the sediment downstream from two coal-fire power plants and how arsenic is biogeochemically transformed in these sediments. The specific questions we proposed to answer in this project were the following:

1/ Does arsenic accumulate in the sediment, is remobilized, and diffuse back into the water column episodically after storm events?

2/ What are the main biogeochemical process regulating the transformation of arsenic in these iron-rich riverine sediments?

To answer question 1, we proposed to monitor in situ the depth profiles of dissolved oxygen, Mn(II), Fe(II), and $\Sigma\text{H}_2\text{S}$ at one site in the sediment of the Chattahoochee River downstream from the suspected arsenic source before, during, and after a storm. Unfortunately, deployment of our in situ instrument presented logistical problems. We could not find a boat that could deploy our heavy instrumentation on the Chattahoochee River. We therefore decided to collect sediment cores and use a non-invasive ex situ approach to monitor depth profiles of the main redox species involved in arsenic cycling at different sites along the river. After completion of the ex situ measurements, sediment porewaters were extracted, and the concentration of dissolved arsenic (As_d) and arsenite as well as the major ions involved in the cycling of arsenic were determined. Finally, solid phase extractions were performed to quantify amorphous iron oxides and total extractable arsenic (As_t).

To answer question 2, sediments were collected at the monitoring points according to their chemical characteristics and sediment slurries manipulated in batch reactor experiments. The slurries were analyzed as a function of time for arsenite, As_d , Fe(II), Mn(II), and $\Sigma\text{H}_2\text{S}$. Manipulations consisted in providing arsenate to the sediment slurries and following the evolution of the reactants and products over time to determine the reaction kinetics.

4.0 Sampling Site

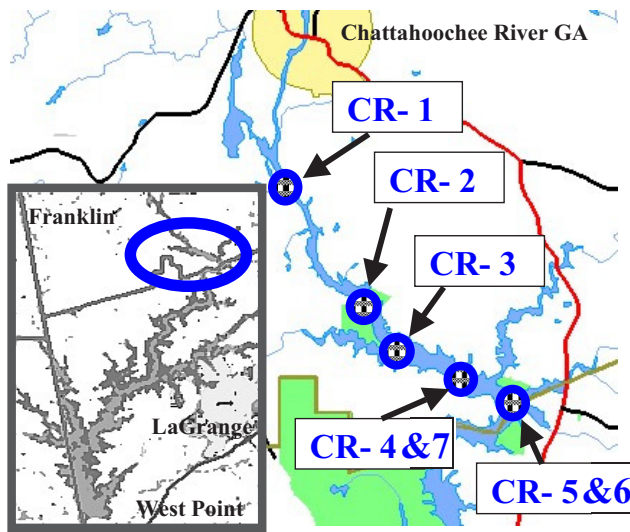


Figure 1. Study Location in the Chattahoochee River upstream from West Point Lake (GA). Seven sediment cores, numbered CR-1 to -7, were collected along the Chattahoochee River during this study. Their locations are provided on the map.

We selected our field site in the Chattahoochee River near West Point Lake, downstream from a point-source of arsenic in the water column (3). West Point Reservoir (inset Figure 1) is a 25,900-acre mainstream Chattahoochee River impoundment located an hour southwest of Atlanta (GA). West Point Lake lies on a 35 mile stretch of the Chattahoochee River between Franklin and West Point (GA). The lake has a shoreline of more than 500 miles and runs along and across the Georgia/Alabama State line. The lake is controlled by the Army Corps of Engineers and was impounded in 1974 to provide drinking water, flood control, hydroelectric power, navigation, wildlife development, and general recreation for Southwest Georgia.

TABLE 1. Water Levels (feet) and Discharge (cfs) Measured in the Chattahoochee River at West Point, GA (USGS Station #02339500) Around the Time of Sampling During Three Consecutive Years (2002, 2003, 2004).

Date	Time	Water Level	Discharge
		[feet]	[cfs]
6/11/2002	7:10	2.28	647
6/25/2002	8:15	2.24	816
9/5/2002	8:25	2.1	748
5/9/2003	10:54	21.42	65500
5/9/2003	19:26	20.64	63600
5/10/2003	11:05	19.75	60300
5/12/2003	13:25	8.88	16990
8/6/2003	10:45	5.16	6850
4/5/2004	8:50	6.16	9210
12/1/2004	14:33	5.84	7995

Seven sediment cores (Figure 1) were collected from the outfall of the Chattahoochee River north of the drinking water reservoir of West Point Lake in LaGrange (GA) based on elevated total dissolved arsenic concentrations detected in the water column (3). Our study focused in an area approximately 60 km away from the suspected arsenic source where total dissolved arsenic was depleted from the water column. The sediment cores were collected in July 2003, three weeks

after Tropical Storm Bill brought approximately 20 foot crests through the study location, and in May 2004, when the Chattahoochee River was at base-flow conditions (Table 1).

5.0 Methods

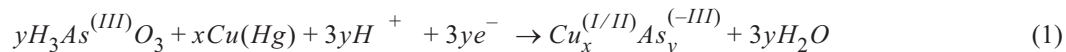
Sediment samples were collected with 60 cm long and 10 cm diameter polycarbonate core liners. Approximately 10 cm of overlying water was collected with each core to maintain the integrity of the sediment-water interface and minimize exposure to the atmosphere during transport to the laboratory. To answer question 1, we determined depth profiles of redox geochemical species at a millimeter resolution in selected sediment cores with gold-mercury (Au/Hg) voltammetric microelectrodes (32). Voltammetric techniques are attractive to measure chemical species in sediments because they can detect several analytes at once, they have low detection limits, and generally do not suffer from matrix problems (e.g., high salinity). Voltammetric microelectrodes have been successfully built and are routinely utilized in our group for field deployments (33, 35) or laboratory investigations (34). High resolution voltammetric and potentiometric profiles of $O_{2(aq)}$, Fe^{2+} , Mn^{2+} , ΣH_2S (H_2S , HS^- , S^0 , S_x^{2-}), organic- $Fe^{(III)}_{(aq)}$, $FeS_{(aq)}$, and pH were obtained by lowering an Au/Hg voltammetric microelectrode and a pH minielectrode (Diamond General Corp.), in millimeter increments, into each sediment core with a micro-manipulator (Analytical Instrument Systems, Inc.).

Voltammetric and pH measurements were conducted with a DLK-100A potentiostat that includes a voltmeter for combination measurements (Analytical Instrument Systems, Inc.). Dissolved oxygen was measured cathodically by linear sweep voltammetry, while Fe^{2+} , Mn^{2+} , organic- $Fe^{(III)}_{(aq)}$, ΣH_2S , and $FeS_{(aq)}$ were detected by cathodic square wave voltammetry. Prior to each scan, a conditioning step was applied at -0.1 V for 10 s to clean the microelectrode. Scan rates of 200 mV/s were used for all measurements (32). The pH was calculated using the Nernst Law after recording the potential and sample temperature at the minielectrode (36). By using microelectrodes, a suite of constituents could be measured with a high spatial resolution without sediment handling, thus minimizing contamination while maximizing the volume of porewater for other analyses.

Immediately following completion of the electrochemical profiles, the sediments were sectioned and centrifuged under $N_{2(g)}$ atmosphere, and porewaters were filtered (Norm-Ject sterile Teflon syringe and Puradisc 0.2 μ m Whatman filter) and acidified with Trace Metal Grade HCl or HNO_3 (Fisher) as needed for preservations and analysis. All porewaters were extracted and maintained in a $N_{2(g)}$ atmosphere and kept at 4°C until analysis of As(III), total dissolved arsenic (As_d), chloride, nitrate, sulfate, total dissolved orthophosphate, and total dissolved silica within 24 hours.

All solutions were prepared with 18 MW-cm Reverse Osmosis (RO) water (Barnstead). All plasticware and glassware used for trace metal analyses were acid-washed in 2% Trace Metal Grade HNO_3 (Fisher) for one week and rinsed thoroughly with RO water. For As(III) analysis, standards were made from an As(III) stock solution prepared daily by dissolving As(III) oxide (Alfa Aesar) in NaOH then acidifying with 12 N HCl (37). Voltammetric measurements for As(III) were performed with a HMDE using the VA 663 multi-mode mercury drop electrode stand (Metrohm) coupled to the PGSTAT 12 Autolab potentiostat (Ecochemie). The reference electrode was an Ag/AgCl/KCl (3 M) with a 0.2 M NaCl glass bridge, and a glassy carbon rod acted as the

counter electrode. The solutions were thoroughly degassed with ultra high purity $N_{2(g)}$ in between each As(III) measurement to prevent reoxidation by dissolved oxygen. As(III) concentrations were determined by amending the sample with 0.7 mM Cu(II) ($CuCl_2 \cdot 2H_2O$ Aldrich) and 1 M HCl. A potential was applied at -0.4 V for 10 seconds to form an arseno-copper complex (Eq. 1 - deposition step) (37).



The potential was then scanned cathodically (from -0.4 V to -1.2 V) at 300 Hz using square wave voltammetry to reduce $Cu^{(I/II)}$ from the arseno-complex to Cu^0 and allow the indirect measurement of As(III) (Eq. 2 - stripping step).

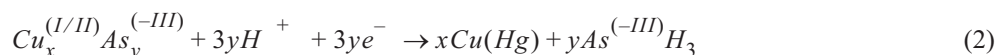


Figure 2 shows a triplicate raw data scan of a 1 nM As(III) standard. The detection limit of the method was 0.25 nM As(III) (at 3σ of the blank).

Total dissolved arsenic concentrations (As_d) were determined in triplicate with an Agilent - 7500a ICP-MS. Standards were prepared from a 1,000 ppm in 5% HNO_3 As stock solution (Aldrich). An internal standard of 1 ppb germanium, prepared from 1,000 ppm stock solution (Aldrich) was added to standards and samples to correct for internal drift of the instrument. For quality control, As_d standards were inserted every 10 samples. The detection limit of As_d was found to be 0.25 nM.

Total dissolved phosphate and silica were determined by spectrophotometry (38, 39). Sulfate, nitrate, and chloride were measured by Ion Chromatography (Dionex Model 300X) with a bicarbonate buffer as eluent. Amorphous iron oxides were extracted in triplicate in selected samples using ascorbate reagent (40). Fe(II) produced during the extraction was analyzed with the Ferrozine Method (41). Total extractable arsenic (As_t) was obtained from aqua regia digestions for 8h at $80^\circ C$ (42).

Sediment slurry incubations with sediments from the CR-4 and CR-5 cores were used to determine the mechanisms of accumulation of dissolved arsenic and iron in the porewaters. These sediments were incubated in overlying water from the sites. A first set of incubations was conducted with sediments from three different depths in CR-4 and CR-5 to reflect the microbial community changes that may occur with depth in sediments. This first set of incubations was amended with a low constant concentration of 100 nM arsenate to reflect the porewater composition at these sites. A second set of incubations was conducted with the first 10 cm of sediments from CR-4 and CR-5 but with three different initial concentrations of arsenate to mimic a pollution event. All incubations were performed in sealed 25 ml Dellco

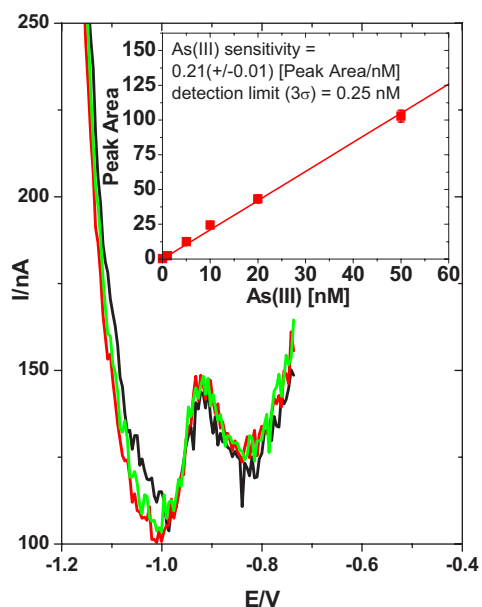


Figure 2. Reproducibility of triplicate HMDE voltammetric measurements of a 1 nM As(III) standard. The inset shows a typical calibration curve. The method has a detection limit of 0.25 nM at three standard deviations from the blank

Hungate tubes to maintain anaerobic conditions. The tubes and rubber stoppers (septa) were acid washed, rinsed, dried, and autoclaved to avoid contaminations. The slurries consisted of 5 g of sediment in each tube, to which 17 ml of autoclaved overlying water from the Chattahoochee River was added. Each reactor was degassed for 30 minutes before being sealed permanently with rubber stoppers and aluminum caps. They were kept in the dark and at room temperature but gently and constantly rotated to homogenize the slurries. At regular time intervals, 2 ml of porewaters were sampled through the rubber septa with a sterile polypropylene syringe. All sample extractions were performed under a nitrogen atmosphere to avoid oxidation of reduced metabolites. Subsamples were immediately analyzed for As(III) by HMDE (see above) and Fe(II) with the Ferrozine method. The remaining sample was acidified with 0.1 N HNO₃ (Fisher) and analyzed at a later stage for total dissolved As by ICP-MS. Abiotic control slurries were added to ensure that no oxygen penetrated the Hungate tubes and that no microbes were present in the autoclaved overlying water from the Chattahoochee River.

6.0 Results

The sediment cores collected in July 2003 were both anoxic, with dissolved oxygen decreasing from approximately 280 μM in the overlying water to undetectable levels just below the sediment-water interface (Figure 3a and Figure 4a). As illustrated on Figure 3b, the pH decreased from 6.4 just below the SWI to 6.1 at 20 mm, then stabilized until 50 mm where it decreased again to reach 5.8 at 80 mm. Fe(II) rose from undetectable levels ($< 5 \mu\text{M}$) within 10 mm from the SWI to a maximum of 940 μM in CR-4 (Figure 3a) and 540 μM in CR-5 (Figure 4a). It then stabilized around these values until 40 mm in both CR-4 and CR-5. While Fe(II) abruptly increased in CR-5 to a maximum of 550 μM before decreasing regularly to a minimum of 100 μM at 80 mm, it oscillated between 500 and 900 μM below 40 mm in CR-4. Mn(II) concentrations displayed similar behaviors in both CR-4 and CR-5, except that Mn(II) was produced at 5 mm below the SWI in CR-4 and directly at the interface for CR-5. It increased to reach a maximum of 590 μM between 45 and 55 mm in CR-4 (Figure 3a) and 470 μM between 20 and 30 mm in CR-5 (Figure 4a). Below these depths, Mn(II) decreased in both cores to approximately 100 μM . No $\Sigma\text{H}_2\text{S}$ (detection limit $< 0.2 \mu\text{M}$) were detected in these sediments. Chloride concentrations were approximately 130 μM in the first 10 cm of the sediment then slightly decreased to 100 μM . Nitrate (Figure 3c) was detected in the overlying water only, at a concentration of 27 μM . Sulfate concentrations were highest at 47 μM in the overlying water then diminished regularly to below the detection limit of 2 μM at 43 mm in CR-4 (Figure 3c).

Total dissolved phosphate and total dissolved silica (data not shown) were below detection limit in both cores. As(III) was not detected in the extracted porewaters using HMDE, even after increasing the deposition time from 60 to 600 s to improve the detection limit. We therefore conclude that total dissolved arsenic (As_d) profiles (Figure 3d and Figure 4b) are indicative of arsenate only. In both cores, the concentration of As(V) was significant at the sediment-water interface, 25 nM in CR-4 and 75 nM in CR-5, and increased deeper to a maximum of 156 nM between 15 and 25 mm in CR-4 and 107 nM between 55 and 68 mm in CR-5. As(V) then decreased to a minimum of 15 nM between 125 and 135 mm in CR-4 and 20 nM between 95 and 105 mm in CR-5.

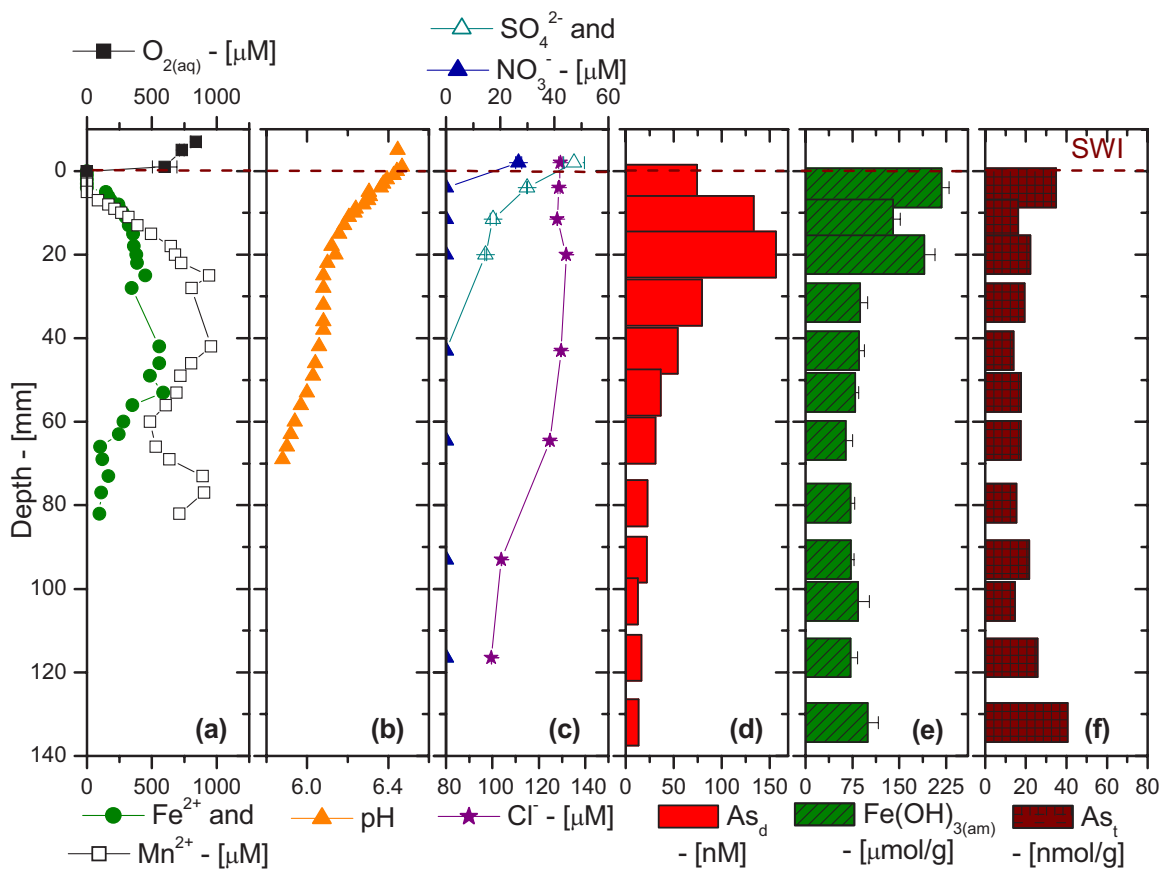


Figure 3. Depth Profiles of: dissolved oxygen, Fe(II), and Mn(II) (a); pH (b); sulfate, nitrate and chloride (c); total dissolved arsenic (d); amorphous iron oxides (e); and total extractable arsenic (f) in CR-4 collected in July 2003 in the Chattahoochee River. $\Sigma\text{H}_2\text{S}$ was below detection limit.

The concentration of amorphous iron oxides, as determined by the ascorbate extraction, decreased with depth in CR-4, from $170 \pm 6 \mu\text{mol/g}$ in the top 5 mm to $75 \pm 8 \mu\text{mol/g}$ below 20 mm (the depth depicting the highest dissolved As(V) in the porewaters - Figure 3d and e). CR-5 results displayed a more variable profile with concentrations of amorphous iron oxides ranging between $108 \pm 25 \mu\text{mol/g}$ in the first 50 mm and $78 \pm 30 \mu\text{mol/g}$ between 60 mm (depth depicting the highest As(V) concentration - Figure 4b) and 120 mm. The concentration of total extractable arsenic followed the trends displayed by iron oxides in both cores, with concentrations ranging between 20 and 40 nmol/g in both cores (Figure 3f and Figure 4d). These data suggest that arsenic is adsorbed onto iron oxides and released in solution when iron oxides are reductively dissolved.

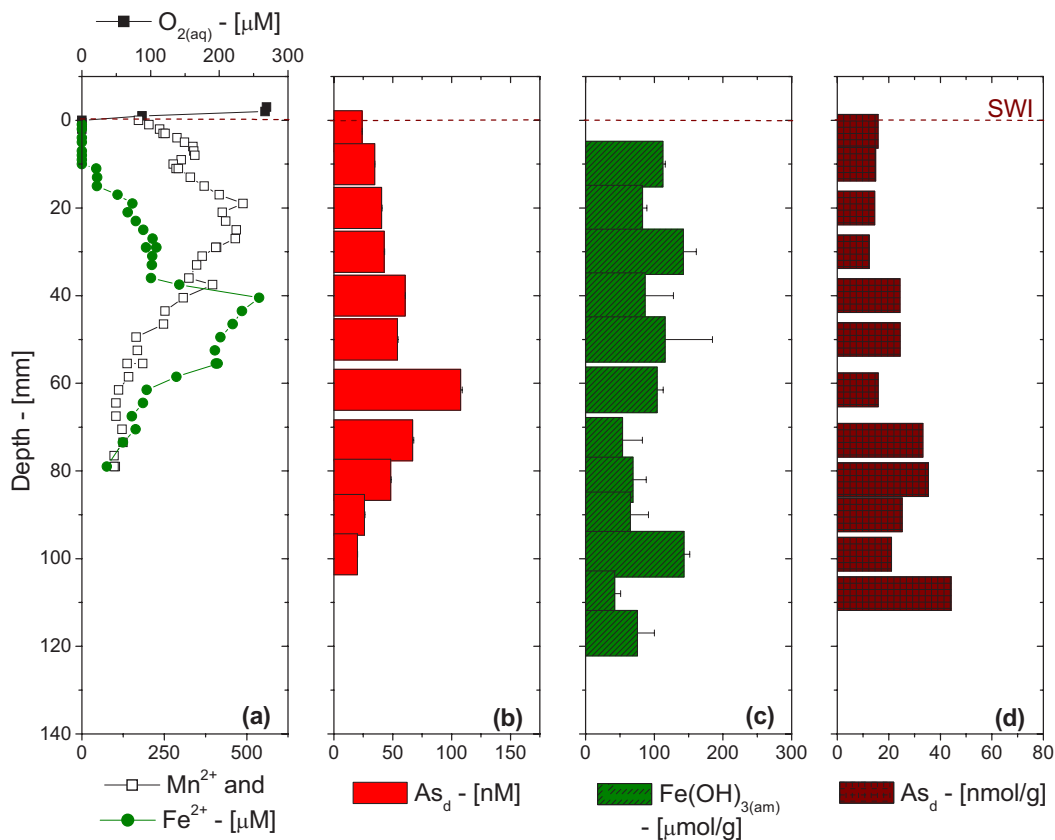


Figure 4. Depth Profiles of: dissolved oxygen, Fe(II), and Mn(II) (a); total dissolved arsenic (b); amorphous iron oxides (c); and total extractable arsenic (d) in CR-5 collected in July 2003 in the Chattahoochee River. $\Sigma\text{H}_2\text{S}$ was below detection limit.

The sediment cores collected in May 2004 were, in a similar fashion, both anoxic, with dissolved oxygen decreasing from approximately 100-150 μM in the overlying water to undetectable levels just below the sediment-water interface (Figure 5a and Figure 6a). In both cores, the pH decreased just below the sediment-water interface (Figure 5b and Figure 6b), indicating that respiration and denitrification were both ongoing in the first 10 mm of these sediments. Fe(II) was produced below the pH minimum in both cores and reached concentrations as high as 1 mM at about the same depth (30 mm) before decreasing to below detection limit at 70 mm in CR-6 (Figure 5a) and 500 μM in CR-7 (Figure 6a). Mn(II) was detected in CR-6 but not in CR-7. Interestingly, both cores displayed new features not seen the previous year. First, soluble organic-Fe(III) was detected below the onset of Fe(II) in both cores (Figure 5b and Figure 6b). The voltammetric currents for these soluble complexes of Fe(III) were similar, with maximums around 100 nA. While soluble organic-Fe(III) was maintained at high levels in CR-7, it decreased to 50 nA below 50 mm in CR-6. Second, sulfur species were detected in both cores (Figure 5b and Figure 6c). In CR-6, a distinct voltammetric signal for $\Sigma\text{H}_2\text{S}$ ($= \text{H}_2\text{S} + \text{HS}^- + \text{S}^{2-} + \text{S}^{(0)} + \text{S}_x^{2-}$) was detected about 5 mm below the onset of Fe(II) and soluble organic-Fe(III), reached a maximum as high as 25 μM at 25 mm, and stabilized deeper around 15 μM . In CR-7, $\text{FeS}_{(\text{aq})}$, instead of $\Sigma\text{H}_2\text{S}$, was detected at the onset of Fe(II) and soluble organic-Fe(III) and reached a steady value around 30 nA below 25 mm. These features suggest that sulfide may be involved in arsenic cycling.

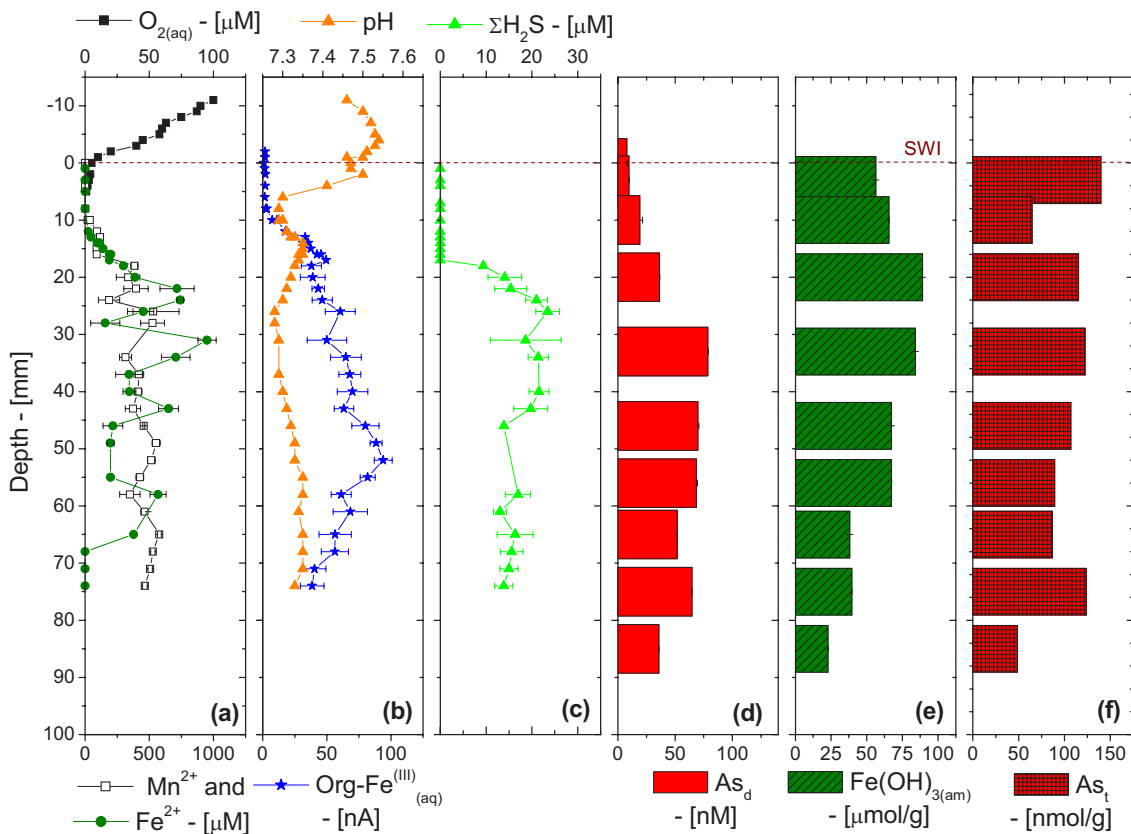


Figure 5. Depth Profiles of: dissolved oxygen, Fe(II), and Mn(II) (a); pH and Org-Fe^(III)_(aq) (b); ΣH₂S (c); total dissolved arsenic (d); amorphous iron oxides (e); and total extractable arsenic (f) in CR-6 collected in May 2004 in the Chattahoochee River.

Total dissolved arsenic (As_d) in both cores fell in the range of concentrations detected the previous year (compare Figure 3d, Figure 4b, Figure 5d, and Figure 6c), and, likewise, arsenite was never detected. Therefore, dissolved arsenic was probably under the form of arsenate in these porewaters. In general, the dissolved arsenic depth profiles of both cores displayed similar trends. As_d increased below the sediment-water interface in both cores and reached a maximum of 75 nM at 35 mm in CR-6 (Figure 5d) and 115 nM at 65 mm in CR-7 (Figure 6c). Both profiles coincided with the onset of Fe(II) in these porewaters, suggesting that arsenate was released during the reductive dissolution of iron oxides.

Amorphous iron oxides behaved differently in both cores. CR-6 contained 50 $\mu\text{mol/g}$ iron oxides just below the sediment-water interface and displayed a maximum of 87 $\mu\text{mol/g}$ at 20 mm before decreasing regularly to 25 $\mu\text{mol/g}$ at 85 mm (Figure 5e). In contrast, amorphous iron oxides was more variable in CR-7, with concentrations as high as $166 \pm 34 \mu\text{mol/g}$ (Figure 6d). Total extractable arsenic displayed the exact opposite. It was variable in CR-6, with concentrations ranging around $100 \pm 30 \text{ nmol/g}$, but CR-7 contained high background concentrations around $200 \pm 30 \text{ nmol/g}$ at the surface and displayed a maximum of 550 nmol/g arsenic at 40 mm in the region where Fe(II) reached its maximum. Below 40 mm, it decreased back to the high background concentrations observed at the surface.

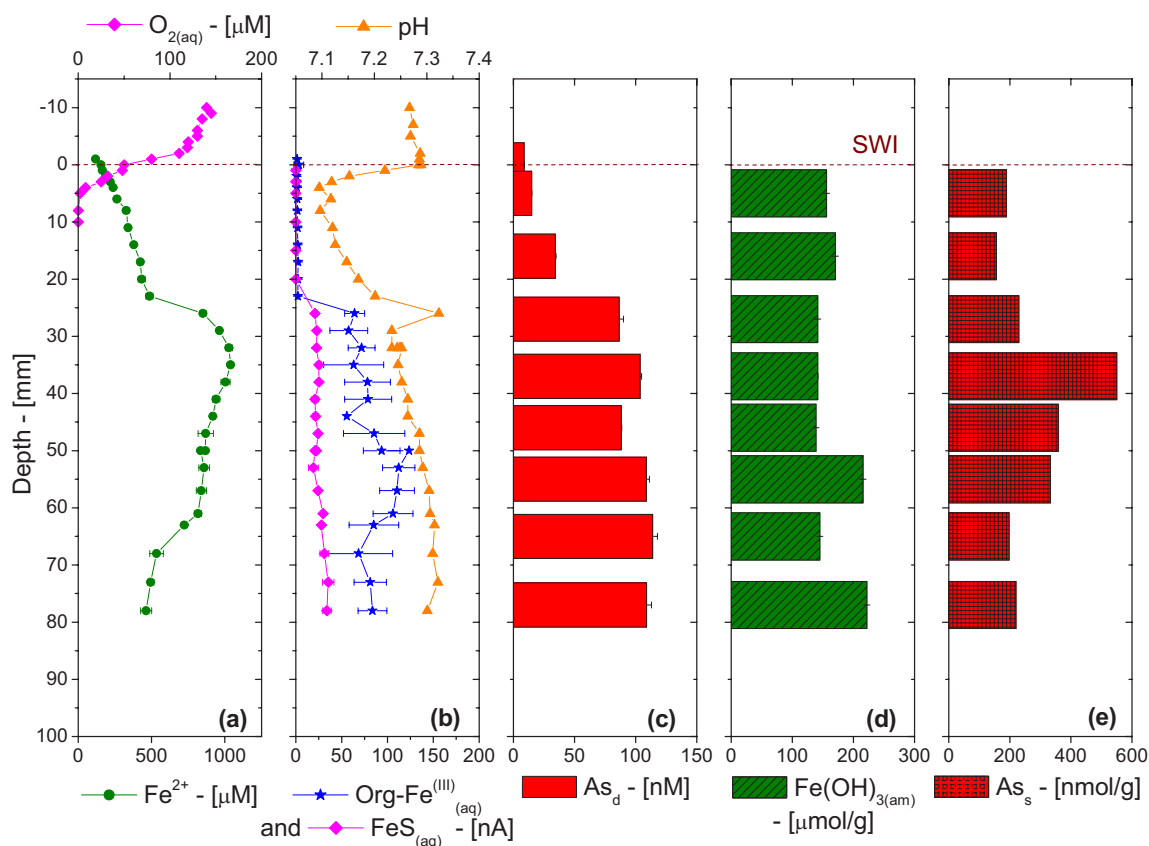


Figure 6. Depth Profiles of: dissolved oxygen and Fe(II) (a); pH, $Org-Fe^{(III)}_{(aq)}$, and $FeS_{(aq)}$ (b); total dissolved arsenic (c); amorphous iron oxides (d); and total extractable arsenic (e) in CR-7 collected in May 2004 in the Chattahoochee River. ΣH_2S and Mn(II) were below detection limit.

The first set of incubations was conducted with sediments from CR-4 and CR-5 in the presence of a low concentration of arsenate (100 nM) to mimic the maximum concentration of dissolved arsenic measured in the porewaters (Figure 3d and Figure 4b). These incubations were conducted using sediments from the surface (0-15 mm in CR-4 and 5-25 mm in CR-5), intermediate depths (15-38 mm in CR-4 and 55-78 mm in CR-5), and deep depths (71-98 mm in CR-4 and 94-112 mm in CR-5) to reflect the fact that the microbial communities responsible for the transformation of iron and arsenic may be different at these locations. All the incubations showed that iron oxides were reduced and produced much higher Fe(II) concentrations than measured in the porewaters samples. Iron reduction rates were similar between the surface and the intermediate-depth sediments in both cores (Figure 7a, b, d, and e). In turn, incubations with the deepest sediments at both sites showed a phase lag of about 60 days before iron reduction took place. These data logically suggest that microbial communities were much more difficult to activate in the deeper sediments. Interestingly, about 50% of the arsenate initially added to the slurries was instantaneously removed from the porewaters, and only a fraction of the total amendment was recovered in the porewaters during these incubations. Speciation measurements in the dissolved phase of these samples revealed that arsenite was never produced during these incubations.

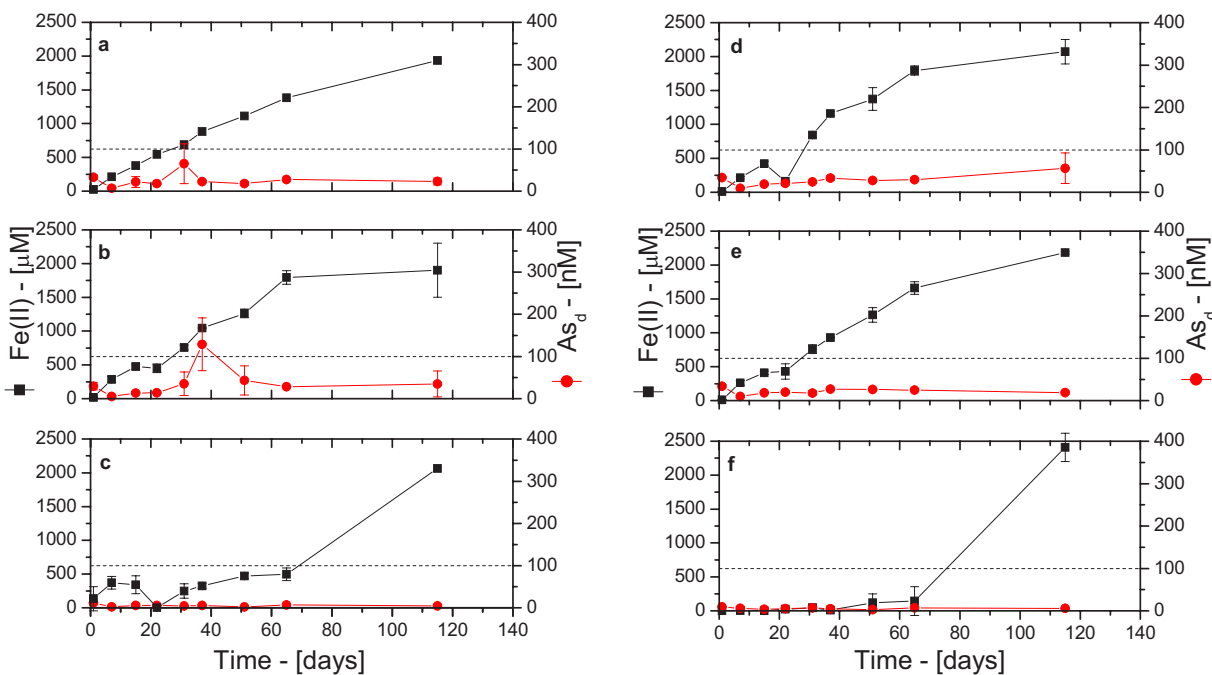


Figure 7. Fe(II) and total dissolved arsenic (As_d) produced during sediment slurry incubations amended with 100 nM arsenate in West Point Lake overlying water: surface sediment from CR-4 (a); CR-4 sediment from intermediate depths (b); deep sediment from CR-4 (c); surface sediment from CR-5 (d); CR-5 sediment from intermediate depths (e); and deep sediment from CR-5. The dash line represents the initial concentration of arsenate added to each slurry (right axis).

A second set of incubations was conducted to simulate the effect of a contamination by arsenate. This time, the sediments from the surface and intermediate depths of CR-4 and CR-5 were respectively mixed into two large samples, and three treatments for each sediment were selected, with respective amendments of 0, 1, and 10 μM arsenate. These incubations are still ongoing but already show interesting results (Figure 8). First, the control slurries (no amendment) show significant release of dissolved arsenic into the porewaters (Figure 8a and d), with concentrations reaching that measured in the sediment cores (Figure 3d and Figure 4b). The accumulation of dissolved arsenic is accompanied by the accumulation of Fe(II), with concentrations in the same range as measured in the porewaters (Figure 3a and Figure 4) and during the first 30 days of the first set of incubations (Figure 7). These results suggest that these incubations are reproducible. It is also interesting to observe that the incubations performed with the 1 μM arsenate amendments (Figure 8b and e) very rapidly produce in both sediments higher concentrations of Fe(II) than the no amendment controls (Figure 8a and d). Simultaneously, dissolved arsenic, which was almost completely removed from the porewaters initially, is produced in much higher concentrations during the course of the incubations than in the no amendment controls. In turn, the highest arsenic amendment incubations in both CR-4 and CR-5 sediments (Figure 8c and f) release the same Fe(II) concentrations as in the no amendment controls (Figure 8a and d), while dissolved arsenic, initially completely removed from the porewaters, is slowly produced in higher concentrations than both the no amendment controls and the 1 μM amendment. These incubations show that only a fraction of the total arsenate added has been released in the porewaters. They will be pursued until 100% recovery is reached.

Preliminary speciation measurements indicate that As(III) can be detected in both the 1 and 10 μM arsenic amendments after 30 days, suggesting that arsenate reduction must occur in these sediments.

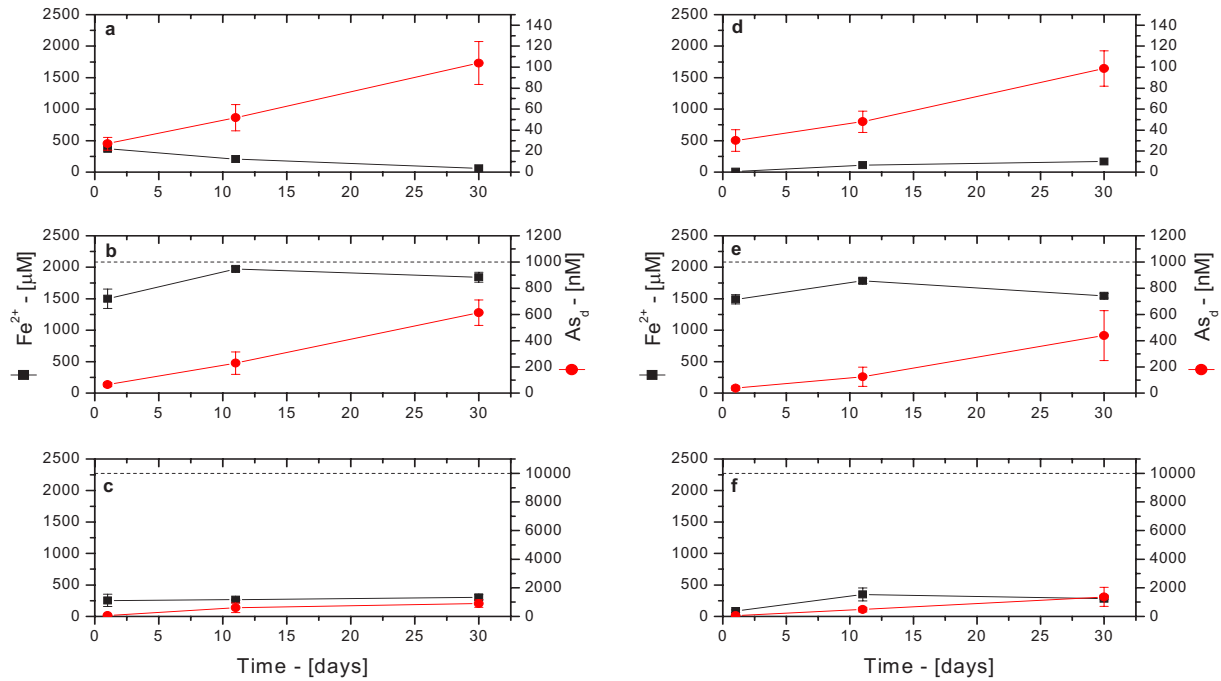
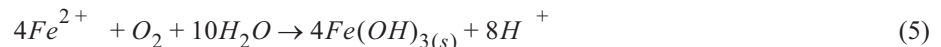
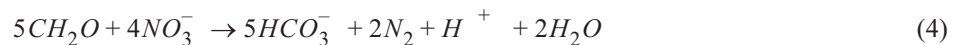


Figure 8. Fe(II) and total dissolved arsenic (As_d) produced during sediment slurry incubations amended with different initial arsenate concentrations in West Point Lake overlying water: CR-4 sediment with no amendment (a); CR-4 sediment amended with 1 μM As(V) (b); CR-4 sediment amended with 10 μM As(V) (c); CR-5 sediment with no amendment (d); CR-5 sediment amended with 1 μM As(V) (e); and CR-5 sediment amended with 10 μM As(V). The dash line represents the initial concentration of arsenate added to each slurry (right axis).

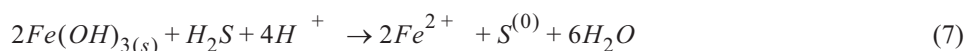
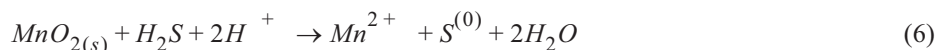
7.0 Discussion

Altogether, the chemical profiles provide a clear picture of the processes regulating the cycling of arsenic near the sediment-water interface. The rapid decrease in dissolved oxygen close to the SWI in each sediment core analyzed indicates that these sediments are anoxic. The generally low concentration of Fe(II), the absence of nitrate, and the decrease in pH near the SWI suggest that a combination of aerobic respiration (Eq. 3), denitrification (Eq. 4), and chemical oxidation of Fe(II) (Eq. 5) occur within the first centimeter of these sediments:

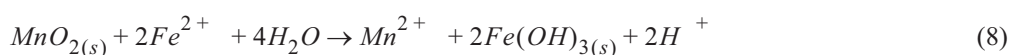


Iron oxidation is confirmed by the high concentration of amorphous iron oxides detected in the upper sediment of CR-4 and CR-6. Additionally, manganese and iron oxide reduction is demonstrated with the production of Mn(II) and Fe(II) within the first 3 to 4 cm of these sediments (Figure 3a to Figure 6a). The occurrence of metal reduction leads to a subsequent

stabilization of the pH in the sediment porewaters (Figure 3b, Figure 5b, and Figure 6b) because these reactions consume protons (36). Chemical reduction of manganese and iron oxides by dissolved sulfide (Eq. 6 and Eq. 7) may occur in sediments. However, the maximum concentration of dissolved sulfide available from the sulfate present in these freshwater sediments (i.e. 50 μM) is not high enough to account for all the Mn(II) and Fe(II) produced (compare maximum sulfate to maximum Mn(II) and Fe(II) concentrations in Figure 3 and Figure 4 for example).



Similarly, the chemical reduction of manganese oxides by Fe(II) is also possible (Eq. 8) but is usually slow above pH 4 (43).



It can therefore be concluded that most of the reduction of manganese and iron oxides is microbial in these sediments. Interestingly, Mn(II) reaches the sediment-water interface in core CR-5, suggesting that it diffuses out of the sediment at this location. This feature is well known and due to the slow oxidation kinetics of Mn(II) at circumneutral pH in the presence of oxygen (44). The disappearance of sulfate within the first 40 mm of CR-4 (Figure 3c) and the occurrence of $\Sigma\text{H}_2\text{S}$ and $\text{FeS}_{(\text{aq})}$ in CR-6 (Figure 5c) and CR-7 (Figure 6b), respectively, suggest that sulfate reduction proceeds in these sediments. In the sediments where dissolved sulfide was not detected in the porewaters, it must have been removed by precipitation as FeS. Interestingly, thermodynamic calculations with MINEQL+ using an average pH of 6.1, Fe(II) concentration of 800 μM and assuming 50 μM H_2S (i.e. the maximum sulfate measured) produced in these sediments indicate that the solubility product of FeS_{am} and mackinewite are not exceeded. At this point, it is not clear if the system is not at equilibrium or if the thermodynamic database is inaccurate. Nevertheless, these profiles indicate that H_2S is produced episodically in these sediments and must have a significant impact on the cycling of arsenic.

Arsenic is thought to enter the Chattahoochee River upstream of the study location and is transported in the oxic river water in the form of As(V) (3). As As(V) flows downstream, it may adsorb onto colloidal and particulate matter contained in the river and settle to the sediment-water interface. The data indicate that this sediment is not a natural source of arsenic, since the concentration of dissolved arsenic in all sediment cores, except for CR-7 (Figure 6c), is higher near the SWI and depleted at depth. Therefore, these data support earlier hypothesis that the anthropogenic input of arsenic is significant in the Chattahoochee River (3).

The role of manganese and iron on the arsenic cycle has been investigated extensively (8, 10-12, 17-19, 22, 24-26, 30). In these sediments, adsorption of arsenic should dominate in the upper sediments which contain the highest concentration of amorphous iron oxides. The adsorption of arsenic is also affected by the degree of crystallization of the iron oxides because the density of adsorption sites decreases as the minerals are more crystallized (45). To determine the extent of adsorption of As(V) onto iron oxides in the first centimeters of these sediments, we implemented a double-layer surface adsorption model with MINEQL+ using parameters from the literature (45). The model assumes a specific surface area of 600 m^2/g for amorphous iron oxides and two types of binding sites: high affinity sites with a density of 5 mmol/mol Fe and low affinity sites

with a density of 0.2 mol/mol Fe. The input concentrations used in the model are based on the data of Figure 3 and Figure 4 (pH = 6.4; $[\Sigma\text{AsO}_4^{3-}] = 150 \text{ nM}$; $[\text{Cl}^-] = 130 \text{ }\mu\text{M}$; $[\text{Fe}^{2+}] = 10 \text{ }\mu\text{M}$; $[\text{SO}_4^{2-}] = 50 \text{ }\mu\text{M}$) or are estimated from previous work in the area (i.e. DIC = 300 μM). Assuming a sediment density varying between 0.98 and 0.87 g/cm³ in clayey and silty sediments (46), the molar concentration of amorphous iron oxides is ca. 0.05 M. The model calculation predicts that 97% of the arsenate in our system is adsorbed onto iron oxides.

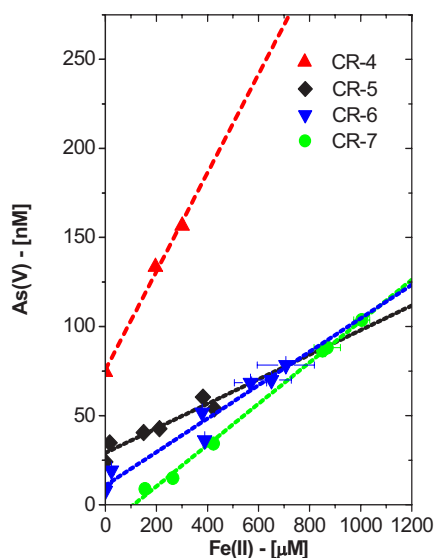
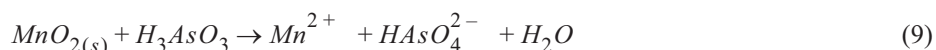


Figure 9. Correlation between Fe(II) and As(V) between 0 and 25 mm in CR-4, 40 mm in CR-5, 65 mm in CR-6, and 47 mm in CR-7.

As(V) is produced simultaneously with Fe(II) in the first few centimeters of each sediment investigated (Figure 3 to Figure 6). A positive correlation exists between Fe(II) and As(V) in all the cores, though with different slopes (Figure 9). From the slopes, a As:Fe(II) ratio of 3:10,000 in the top 25 mm of CR-4, 6:100,000 in the top 40 mm of CR-5, and 1:10,000 in the top 65 and 47 mm of, respectively, CR-6 and CR-7 were found. These data indicate that adsorbed arsenic may be released during the reduction of iron oxides, thus confirming the significant role of iron in the arsenic cycle. These data also indicate that more arsenate is scavenged onto iron oxides in CR-4 than any of the other cores. Silicates and phosphate were below the detection limit in all cores, suggesting they probably do not significantly effect arsenic mobilization in this system.

their involvement with arsenic is not evident. First, adsorption is not favored because at circumneutral pH, manganese oxides are negatively charged (9) while As(V) is mainly deprotonated (4). It is also known that manganese oxides oxidize arsenite to arsenate (25-27) according to:



However, there is an inconsistent correlation between Mn(II) and As(V) in all the cores (not shown). The lower adsorption affinity of As(V) onto manganese oxides at circumneutral pH along with the poor correlation between Mn(II) and As(V) suggest that manganese oxides play a minor role in the arsenic cycle in these sediments.

As previously mentioned, sulfate disappears in these porewaters suggesting that sulfate reduction may occur in these sediments. It has been shown recently that dissolved sulfide may slowly reduce As(V) and complex As(III) in the form of electrochemically inactive AsO_xS_y (20, 21) that could then undergo precipitation. Our measurements, however, could not detect any As(III) in solution in these sediments. We ruled out the possible oxidation of our samples after porewater extraction since the sediment cores were sectioned, centrifuged, filtered, acidified, and stored at 4°C under a $\text{N}_{2(g)}$ atmosphere until As(III) analysis, which was conducted within 24 hours after collection. In addition, the arsenosulfide complexes, if present, should be dissociated in the acidic conditions of the As(III) analysis (pH 1) and detected electrochemically.

The fact that the sediment is reduced but arsenic is oxidized may be due to the dynamic nature of the system studied. The first two surficial sediments evaluated in this study (CR-4 and CR-5) were most likely deposited after the passage of Tropical Storm Bill, which impacted the site three weeks prior to this investigation. It is possible that the kinetically slow reduction of As(V) had not occurred so soon after deposition, while microbial iron reduction released As(V) in solution. Finally, the presence of As(V) and Fe(II) at deeper locations in CR-5 as compared to CR-4 is probably due to the more turbulent river flow at CR-5 which may bring dissolved oxygen to the sediment and increase erosion. This process is evidenced by a general decrease in both the Fe(II) and amorphous iron oxide concentrations in the sediment of CR-5 compared to CR-4 (Figure 3 and Figure 4). Interestingly, the last two sediment cores investigated in this study were obtained at base-flow conditions for the Chattahoochee River (Table 1). Yet our speciation measurements did not evidence any As(III), though conditions in these sediments were more reducing, with the occurrence of both dissolved sulfide (Figure 5c) and $\text{FeS}_{(\text{aq})}$ (Figure 6b), a precursor of $\text{FeS}_{(\text{s})}$ precipitation (36).

Diffusive fluxes were calculated for each core using Fick's Law with the molecular diffusion coefficient of phosphate as a proxy for that of arsenate ($9.1 \times 10^{-5} \text{ cm}^2/\text{sec}$ for H_2PO_4^-). According to these calculations, approximately 20 to 200 nM/cm²yr of arsenic may be diffusing into the overlying water column from the sediment depending on the flow conditions in the Chattahoochee River. Although the arsenic concentrations detected in the porewaters are not considered high compared to contaminated sites, the data suggest that arsenic is remobilized and may impact the drinking water reservoir located downstream.

The sediment incubations show that arsenate spiked to the sediment is initially very rapidly removed from the porewaters, most likely by adsorption onto iron oxides. These incubations also show that iron reduction occurs in these sediments and that dissolved arsenic is released concomitantly with the production of Fe(II). Our speciation measurements reveal that arsenic is under the form of arsenate only when the initial concentration of arsenic is in the range of that found in the porewaters, suggesting that arsenate reduction does not occur in the sediments of the Chattahoochee River. The second set of incubations show that when the initial concentration of arsenic injected to the sediment is elevated, some reduction may occur, though more data are needed at this point. In addition, it appears that microbial iron reduction is affected by elevated concentrations of total dissolved arsenic (Figure 8). Arsenic is a toxic compound that, in high concentration, may inhibit microbial processes.

The first set of incubations was used to calculate the rate of iron reduction assuming a first order with respect to iron oxides and zero order with respect to the reductant (Eq. 10). The reductant could either be dissolved sulfide, if its concentration is high enough, or natural organic matter if iron-reducing bacteria are involved in the transformation of iron oxides. From our field measurements, we can conclude that the involvement of dissolved sulfide in the production of Fe(II) is not significant. Therefore, these rates likely represent rates of microbial iron reduction in these sediments. The rate law of iron reduction is:

$$\frac{d}{dt}[\text{Fe}^{2+}] = k[\text{Fe}(\text{OH})_{3(\text{s})}] = k([\text{Fe}(\text{OH})_{3(\text{s})}]^0 - [\text{Fe}^{2+}]) \quad (10)$$

where k is the rate constant (d^{-1}), $[\text{Fe}(\text{OH})_{3(\text{s})}]^0$ is the initial concentration of iron oxides (μM) in these sediments. This rate law has an analytical solution that was used to fit the rate constant k to

the data of Figure 7 using a least-square fitting procedure. The initial concentration of iron oxides was calculated from the sediment extraction measurements (Figure 3e and Figure 4c) assuming a sediment density of 0.78 g/cm³ (46). Table 2 reports the rate constants determined for each incubation described in Figure 7, except for the deep depths, which displayed a phase lag, as there was not enough data to provide accurate rate constants. From these calculations, it is obvious that the rate of reduction increases with depth in these sediments. So far, the incubations cannot be used to provide rates of release of arsenate in the porewaters. These ongoing incubations will provide this information at a later time.

TABLE 2. Sediment Depths Used in the First Set of Incubations (Figure 7), Initial Concentration of Amorphous Iron Oxides Measured in these Sediments and Used in the Model, and First Order Rate Constant (k) Determined in Each of these Incubations. ND = not determined.

Core	Depth Incubated [mm]	[Fe(OH) _{3(s)}] ⁰ [μmol/g]	k [1/d]
CR-4	0-15	178.8	0.0198
CR-4	15-38	120.8	0.0203
CR-4	71-98	73.01	ND
CR-5	5-25	97.7	0.0164
CR-5	55-78	90.0	0.0251
CR-5	94-112	83.6	ND

8.0 Conclusions

This study successfully combined several analytical techniques to determine the profiles of major redox species and the speciation of As(III) and As(V) with a high spatial resolution (i.e., < 10 cm) from four sediment cores collected a year apart at two locations in the Chattahoochee River. Results provide evidence of the accumulation of dissolved arsenic close to the sediment-water interface at both locations and at both time periods. Depth profiles also display a substantial correlation between the diagenetic processes involving iron and arsenic in these sediments. They suggest that iron oxides scavenge arsenic in the form of arsenate in the water column and settle to the sediment-water interface where they are reduced by iron reducing bacteria. As a result of microbial iron reduction, As(V) is released and accumulates in the porewaters near the sediment-water interface, where it can diffuse back to the overlying waters. Interestingly, As(III) was never found in the porewaters, suggesting that the reduction of As(V) is a slow process that was not occurring in these sediments. Incubations with sediment slurries conducted in the presence of low concentrations of arsenate verified that microbial iron reduction occurs in these sediments and that arsenate is not concomitantly reduced during this process. Incubations of the same sediments but amended with higher initial arsenate concentrations indicate that the microbial processes in these sediments may be affected by high inputs of arsenic, including those necessary for remediation or natural attenuation. Finally, differences between high discharge rates and base-flow conditions in the Chattahoochee River do not seem to affect the biogeochemical processes involved in iron and arsenic cycling but may enhance fluxes across the sediment-water interface.

9.0 References

1. Ferguson, F.; Gavis, J. *Wat. Res.* 1972, 6, 1259-1274.
2. Ryu, J.; Gao, S.; Dahlgren, R.A.; Zierenberg, R.A. *Geochim. Cosmochim. Acta* 2002, 66, 2981-2994.
3. Lesley, M.P.; Froelich, P.N. Proceedings of 2003 Georgia Water Resources Conference.
4. Smedley, P.L.; Kinniburgh, D.G. *Appl. Geochem.* 2002, 17, 517-568
5. Buffle, J. *Complexation Reactions in Aquatic Systems an Analytical Approach*; Halsted Press: a division of Wiley: New York, NY, 1988; p 692.
6. Cullen, W.; Reimer, K.J. *Chem. Rev.* 1989, 89, 713-764.
7. Jain, A.; Raven, K.P.; Loeppert, R.H. *Environ. Sci. Technol.* 1999, 33, 1179-1184.
8. Kneebone, P.E.; O'Day, P.A.; Jones, N.; Hering, J.G. *Environ. Sci. Technol.* 2002, 36, 381-186.
9. Stumm, W. *Chemistry of the Solid-Water Interface*; John Wiley and Sons, Inc.; New York, 1992.
10. Pierce, M.L.; Moore, C.B. *Wat. Res.* 1982, 16, 1247-1253.
11. Belzile, N.; Tessier, A. *Geochim. Cosmochim. Acta* 1990, 54, 103-1039.
12. Mucci, A.; Boudreau, B.; Guignard, C. *Appl. Geochem.* 2003, 18, 1011-1026.
13. Guo, T.; DeLaune, R.D.; Patrick Jr., W.H. *Environ. Intern.* 1997, 23, 305-316.
14. Ahmann, D.; Krumholz, L.R.; Hemond, H.F.; Lovley, D.R.; Morel, F.M.M. *Environ. Sci. Technol.* 1997, 31, 2923-2930.
15. Harrington, J.M.; Fendorf, S.E.; Rosenzweig, R.F. *Environ. Sci. Technol.* 1998, 32, 2425-2430.
16. Oremland, R.S.; Dowdle, P.R.; Hoefft, S.; Sharp, J.O.; Schaffer, J.K.; Miller, L.G; Blum, J.S; Smith, R.L; Bloom, N.S; Wallschlaeger, D. *Geochim. Cosmochim. Acta* 2000, 64, 3073-3084.
17. Rochette, E.A.; Bostick, B.C.; Li, G.C.; Fendorf, S. *Environ. Sci. Technol.* 2000, 34, 4714-4720.
18. Appelo, C.A.J.; Van Der Weiden, M.J.J.; Tournassat, C.; Charlet, L. *Environ. Sci. Technol.* 2002, 36, 3096-3103.
19. Charlet, L.; Bosbach, D.; Peretyashko, T. *Chem. Geol.* 2002, 190, 303-319.
20. Wilkin, R.T.; Wallschlaeger, D.; Ford, R.G. *Geochem. Trans.* 2003, 4, 1-7.
21. Sadiq, M. *Mar. Chem.* 1997, 31, 285-297.
22. Bostick, B.C.; Fendorf, S. *Geochim. Cosmochim. Acta* 2003, 67, 909-921.
23. Johnson, D.L.; Pilson, M.E.Q. *Environ. Lett.* 1975, 8, 157-171.
24. Scott, M.J.; Morgan, J.J. *Environ. Sci. Technol.* 1995, 29, 1898-1905.
25. Manning, B.A.; Fendorf, S.E.; Goldberg S. *Environ. Sci. Technol.* 1998, 32, 2383-2388.
26. Chiu, V.Q.; Hering, J.G. *Environ. Sci. Technol.* 2000, 34, 2029-2034.

27. Driehaus, W.; Seith, R.; Jekel, M. *Wat. Res.* 1995, 29, 297-305.
28. Andreae, M.O. *Limnol. Oceanogr.* 1979, 24, 440-452.
29. Xu, H.; Allard, B.; Grimvall, A. *Water Air Soil Pollut.* 1988, 57, 269-278.
30. Mok, W. A.; Wai, C.M. *Environ. Sci. Technol.* 1990, 24, 102-108.
31. Meng, X.K.; Guo, P.; Bang, S.; Bang, K.W. *Toxicol. Letters* 2002, 133, 103-111.
32. Brendel, P. J.; Luther, G. W.; III. *Environ. Sci. Technol.* 1995, 29(3), 751-761.
33. Bull, D. C.; Taillefert, M. *Geochem. Trans.* 2001, 13, 1-8.
34. Carey, B.; Taillefert, M. *Limnol. Oceanogr.* 2005, In Press.
35. Chow, S. S.; Taillefert, M. 2005. In: *Advances in arsenic research: Integration of experimental and observational studies and implications for mitigation* (O'Day, P. V., D.; Meng, X.; Benning, L. G., Eds.), ACS Symposium Series, Vol. 915, In Press.
36. Taillefert, M.; Rozan, T. F.; Glazer, B.T.; Herszage, J.; Trouwborst, R. E.; Luther III, G. W. 2001. In: *Environmental Electrochemistry: Analyses of Trace Element Biogeochemistry* (M. Taillefert; T. F. Rozan, Eds.). ACS Symposium Series, Vol. 811, Washington, D.C. 247-264.
37. Li, H.; Smart, R. B. *Anal. Chim. Acta* 1996, 325, 25-32.
38. Murphy J.R.; Riley J.P. *Anal. Chim. Acta* 1962, 27, 31-36.
39. Strickland, J.D.H. *J. Amer. Chem. Soc.* 1952, 74, 862-876.
40. Kostka, J.E.; Luther III, G.W. *Geochim. Cosmochim. Acta* 1994, 58, 1701-1710.
41. Stookey, L.L. *Anal. Chem.* 1970, 42, 779-782.
42. Tessier, A.; Campbell, P. G. C.; Bisson, M. *Anal. Chem.* 1979, 51, 844-851.
43. Postma, D. *Geochim. Cosmochim. Acta* 1985, 49, 1023-1033.
44. Stumm, W.; Morgan, J.J. 3rd Ed. *Aquatic Chemistry Chemical Equilibria and Rates in Natural Waters*, John-Wiley and Sons, Inc.; New York; 1996.
45. Dzombak, D.A.; Morel, F.M.M. *Surface Complexation Modeling: Hydrous Ferric Oxide*. John Wiley and Sons, Inc.; New York; 1990.
46. Kastler, J.A.; Wilberg, P.L. *Estuar. Coastal Shelf Sci.* 1996, 42, 683-700.

REDUCTIVE BIOTRANSFORMATION OF POLYCHLORO-NITROBENZENES UNDER IRON-REDUCING CONDITIONS

Basic Information

Title:	REDUCTIVE BIOTRANSFORMATION OF POLYCHLORO-NITROBENZENES UNDER IRON-REDUCING CONDITIONS
Project Number:	2004GA59B
Start Date:	3/1/2004
End Date:	2/28/2005
Funding Source:	104B
Congressional District:	5
Research Category:	None
Focus Category:	Agriculture, Hydrogeochemistry, Toxic Substances
Descriptors:	None
Principal Investigators:	Spyros G. Pavlostathis

Publication

Project Report

**REDUCTIVE BIOTRANSFORMATION OF
POLYCHLORONITROBENZENES UNDER IRON-REDUCING
CONDITIONS**

By

**Spyros G. Pavlostathis, Principal Investigator
Didem Okutman-Tas, Graduate Research Assistant
School of Civil and Environmental Engineering
Georgia Institute of Technology
Atlanta, GA 30332-0512**

For

**Georgia Water Resources Institute
Georgia Institute of Technology
Atlanta, GA 30332-0355**

May 2005

TABLE OF CONTENTS

	<u>Page</u>
EXECUTIVE SUMMARY	3
1. INTRODUCTION	4
2. BACKGROUND	5
3. RESEARCH METHODOLOGY	7
3.1. Target Compounds	7
3.2. Scope/Hypothesis	7
3.3. Research Objectives	9
3.4. Materials and Methods	9
3.4.1. Culture development	9
3.4.1.1. Iron-reducing enrichment cultures (Cultures A, B, and C)	9
3.4.1.2. Fermentative/methanogenic enrichment culture (Culture D)	10
3.4.2. PCNB biotransformation assays	10
3.4.3. Assessment of the effect of iron reduction on PCA dechlorination	10
3.4.4. Analytical methods	11
4. RESULTS AND DISCUSSION	12
4.1. Iron-reducing enrichment cultures	12
4.1.1. Development and activity of iron-reducing enrichment cultures (Cultures A, B, and C)	12
4.1.2. PCNB biotransformation in an iron-reducing enrichment culture (Culture A)	16
4.2. Fermentative/methanogenic enrichment cultures	17
4.2.1. PCNB biotransformation by the fermentative/methanogenic enrichment culture (Culture D)	17
4.2.2. Effect of iron reduction on PCA dechlorination by the fermentative/ methanogenic enrichment culture (Culture D)	18
5. CONCLUSIONS	22
6. DISSEMINATION OF PROJECT RESULTS	23
7. REFERENCES	23

EXECUTIVE SUMMARY

Persistent anthropogenic, hydrophobic organic compounds in the environment pose a chronic threat to the health and safety of humans and wildlife. Despite the fact that chloronitroaromatics are extensively used synthetic compounds in industry and agriculture (e.g., pesticides, fungicides, pharmaceuticals, dyes) and found worldwide in surface and subsurface soils, as well as streambed sediments, studies on their fate and transformation, especially for polychloronitro-substituted compounds, have been rare as compared to either chlorinated or nitroaromatic compounds. To address and explore this paucity of information, the focus of this research was to elucidate the reductive biotransformation of polychloronitrobenzenes, and their corresponding chloroanilines (CAs) under iron-reducing conditions. Several of these compounds are classified as either carcinogenic, potentially carcinogenic, or as methemoglobinemia-causing chemicals. The main parent compound used in the present research was pentachloronitrobenzene (PCNB), a powerful organochlorine fungicide commonly used to combat phytopathogenic fungi. Although PCNB is used in several States, most of its usage is found in the Southeastern US because of its effectiveness against phytopathogenic fungi associated with crops predominantly found in this region.

Our research hypothesis was that reductive dehalogenation of polychlorinated organic compounds under iron-reducing conditions may take place co-metabolically where both Fe(III) and the chlorinated organic compounds merely serve as electron acceptors (primary and secondary electron acceptors, respectively), and/or abiotically, using biologically produced Fe(II) as the terminal electron donor (i.e., as a reductant). The specific objectives of this study were to: a) assess the potential for the microbial reductive transformation of PCNB and CAs under dissimilatory iron-reducing conditions; b) evaluate the effect of iron bioavailability on the amination/dechlorination process; and c) assess the role of humic substances in the iron reduction and PCNB biotransformation processes.

Overall, the results of this study indicate that biotransformation of PCNB to pentachloroaniline (PCA) is very fast under both methanogenic and iron reducing conditions. Reduction of the nitro-group of PCNB and production of PCA also takes place under abiotic, reductive conditions. However, the rate of this conversion is highly enhanced under biotic conditions. Further dechlorination of PCA under abiotic, reductive conditions, e.g., in the presence of sulfide and/or Fe(II), was not observed in the present study. Under biotic conditions, the rate of PCNB to PCA biotransformation was higher under methanogenic conditions as compared to iron-reducing conditions. PCA dechlorination did not take place when Fe(III)-EDTA was reduced at a relatively fast rate under biotic conditions. In contrast, PCA dechlorination and iron reduction took place simultaneously when the iron source was less bioavailable (e.g., FeOOH). Addition of anthraquinone 2,6-disulfonate (AQDS), a humic acid model compound, to the culture, increased the rate and extent of FeOOH reduction, which in turn resulted in a significant decrease of the rate and extent of PCA dechlorination. Thus, fast iron reduction suppresses and delays the onset of the reductive dechlorination of PCA.

The results of this study have significant implications relative to the fate and biotransformation of PCNB and PCA under anoxic/anaerobic conditions encountered in most subsurface soil and sediment environments. Based on the observed fast and facile conversion of PCNB to PCA, PCNB is not expected to be persistent in natural systems. However, the bioavailability of iron in natural systems, which in turn is controlled by soluble humic material, has a pronounced effect on the rate and extent of PCA dechlorination and thus on its persistence in natural systems.

1. INTRODUCTION

Persistent anthropogenic, hydrophobic organic compounds in the environment pose a chronic threat to the health and safety of humans and wildlife. Despite the fact that chloronitroaromatics are extensively used synthetic compounds in industry and agriculture (e.g., pesticides, fungicides, pharmaceuticals, dyes) and found worldwide in surface and subsurface soils, as well as streambed sediments, studies on their fate and transformation, especially for polychloronitro-substituted compounds, have been rare as compared to either chlorinated or nitroaromatic compounds. To address and explore this paucity of information, the focus of this research was to elucidate the reductive biotransformation of polychloronitrobenzenes (polyCNBs), and their corresponding chloroanilines (CAs) under iron-reducing conditions. Several of these compounds are classified as either carcinogenic, potentially carcinogenic, or as methemoglobinemia-causing chemicals. The main parent compound used in this research was pentachloronitrobenzene (PCNB). PCNB ($C_6Cl_5NO_2$), a powerful fungicide commonly used to combat phytopathogenic fungi, is a registered organochlorine fungicide used as a seed dressing or soil treatment to control a wide range of fungi species in crops such as cotton, potatoes, wheat, onions, lettuce, tomatoes, tulips, garlic, and others, as well as on grass, lawn flowers, ornamental crops, shrubs and in gardens (EXTOXNET, 1996; U.S. EPA, 2003). PCNB is included in U.S. EPA's toxicity class III and is among the thirty chemicals included in the U.S. EPA's list of "Waste Minimization Priority Chemicals". The U.S. EPA has classified PCNB as a possible cancer causing substance (U.S. EPA, 2003).

During 2000 alone, 23,500 pounds of PCNB were used in six participating States (CA, FL, MI, OR, PA, and TX) in nursery and floriculture, whereas, 5,400 pounds were used in 2002 in the production of a single vegetable (fresh snap beans) in five participating States (FL, GA, NY, NC, and TN) (USDA, 2002; USDA, 2003). Although PCNB is used in several States, most of its usage is found in the Southeastern US because of its effectiveness against phytopathogenic fungi associated with crops predominantly found in this region. For example, in 2000, from the total reported PCNB usage of 543,500 lbs of active ingredient, 331,100 lbs (i.e., 61%) were used in seven States in the region (Table 1).

Table 1. PCNB Use for Two Selected Crops in the Southeastern U.S.
(active ingredient in lbs; 2000 data; NASS, 2003)

State	Snap Fresh Beans	Cotton Upland
Alabama	NA	74,000
Florida	6,900	NA
Georgia	7,200	NA
Louisiana	NA	48,000
Mississippi	NA	109,000
North Carolina	NA	17,000
South Carolina	NA	NA
Tennessee	NA	69,000
Total	> 14,100	> 317,000

NA, data not available

PCNB is extensively used as a fungicide for the prevention and control of certain soil borne diseases on golf courses, sod farms, home lawns and institutional areas where turf is grown. In a recently published report by the USGS on the occurrence of semivolatile organic compounds in streambed sediments of twenty major river basins across the United States, PCNB

was detected at a maximum concentration of 180 $\mu\text{g}/\text{kg}$ (Lopes and Furlong, 2001). Therefore, as the above-mentioned, PCNB-related activities are more intense in the Southeastern US, the fate of PCNB and its biotransformation products is of regional interest.

2. BACKGROUND

Polyhalogenated organic compounds tend to be resistant to biodegradation in aerobic environments. Such compounds are more oxidized than their nonhalogenated counterparts due to the presence of highly electronegative halogen substituents, which provide molecular stability. Therefore, as the degree of halogenation increases, reduction of these compounds is more likely to occur than oxidation (Pavlostathis *et al.*, 2003). However, polyhalogenated compounds can be used as electron acceptors in thermodynamically favorable reactions (Dolfing and Beurskens, 1995; Fantroussi *et al.*, 1998; Fetzner and Lingens, 1994; Fetzner, 1998; Middeldorp *et al.*, 1999; Häggblom *et al.*, 2000). Under anaerobic conditions, the reductive transformation of nitroaromatic compounds proceeds with the reduction of one or more aryl nitro groups ($-\text{NO}_2$) and the formation of aryl amines.

Nitrate, sulfate, and carbonates are alternative electron acceptors commonly considered for anaerobic subsurface processes (i.e., nitrogen reduction, sulfate reduction, and methanogenesis) and bioremediation applications. Relatively recent studies however have demonstrated the significant role of iron and manganese reducing bacteria in the cycling of organic matter and the biotransformation of organic contaminants (Lovley, 1991). The role of dissimilatory iron-reducing bacteria in the reduction of nitrobenzenes has been elucidated (Heijman *et al.*, 1995; Klausen *et al.*, 1995). This transformation involves two coupled reactions, one biotic and mediated by the iron-reducing bacteria, the other abiotic, where reduced iron [Fe(II)] serves as the intermediate electron donor and nitrobenzenes serve as the electron acceptor. The interdependence between the reduction of the organic pollutants and microbial iron reduction in aquifers was demonstrated. The biotic iron reduction step -- which provides the required reducing power for the transformation of the contaminants -- was found to be the rate-limiting process. On the other hand, the reduction of the contaminants leads to a continuous regeneration of the relatively limited, microbially-available Fe(III) pool.

Based on published reduction potentials of key redox couples of Fe(III)/Fe(II) and organic compounds (Haderlein and Schwarzenbach, 1995), polychlorinated organic compounds can be reduced by a number of Fe(II)-bearing compounds. Iron-mediated, abiotic dechlorination has been demonstrated for compounds such as carbon tetrachloride and chloroform (Matheson and Tratnyek, 1994; Kriegman-King and Reinhard, 1992; Kriegman-King and Reinhard, 1994). Microbial dechlorination under iron-reducing conditions has been reported for a number of halogenated compounds, including carbon tetrachloride (Picardal *et al.*, 1993), monochlorinated isomers of phenol, and benzoate (Kazumi *et al.*, 1995a; Kazumi *et al.*, 1995b), and vinyl chloride (Bradley and Chapelle, 1996).

Despite the fact that chloronitroaromatics are extensively used synthetic compounds in industry and agriculture (e.g., pesticides, fungicides, pharmaceuticals, dyes) and found worldwide in surface and subsurface soils, as well as streambed sediments, studies on their fate and transformation, especially for polychloronitro-substituted compounds, have been rare as compared to either chlorinated or nitroaromatic compounds. An exhaustive literature review did not reveal any information on the definitive reductive dechlorination of polyCNBs under iron-reducing conditions which was the focus of this research. To address and explore this paucity of information, the focus of this research was to elucidate the reductive biotransformation of polyCNBs, and their corresponding chloroanilines (CAs).

We have developed methanogenic, mixed cultures from a sediment historically contaminated with chlorinated benzenes and hexachloro-1,3-butadiene (Prytula and Pavlostathis, 1996; Booker and Pavlostathis, 2000; Yeh and Pavlostathis, 2001) as well as dissimilatory iron-reducing, mixed cultures from a non-contaminated soil sample and the contaminated sediment (Doikos, 1998). Iron was provided in the form of ferric-EDTA in order to circumvent limitations related to iron bioavailability. Research carried out in our laboratory with the iron-reducing cultures on the reductive dechlorination of hexachlorobenzene revealed a low rate and extent of dechlorination as compared to those achieved with methanogenic cultures (Doikos, 1998). These results may be an outcome of competition for available electrons by the two simultaneous processes, namely, iron-reduction and dechlorination, or due to complexation of Fe(II) with EDTA and possible inhibition of the dechlorination process. The proposed research expanded the scope of the previously conducted research by the use of PCNB as well as different forms of Fe(III).

The role of humic substances has been recognized in electron-transfer reactions in general and more specifically in the biotransformation of recalcitrant compounds (Bradley *et al.*, 1998; Lovley *et al.*, 1998; Scott *et al.*, 1998). Humics could serve as carbon and energy sources in mixed, dissimilatory iron-reducing cultures, as electron-transfer mediators between Fe(II) and halogenated organic compounds (Haderlein and Schwarzenbach, 1995), as well as electron shuttles in the microbial reduction of insoluble Fe(III) compounds (He and Sanford, 2003; Komlos and Jaff , 2004). The role of humic substances in the biotransformation process of PCNB and PCA under dissimilatory, iron-reducing conditions was also assessed in this study.

Most of the early studies on the biodegradation of PCNB focused on using fungi and were conducted under aerobic/anoxic conditions. Production of extracellular phenoloxidases by a number of fungal strains was not correlated with their capacity to degrade PCNB (Seiglemurandi *et al.*, 1992; Steiman *et al.*, 1992; Guiraud *et al.*, 1999). Removal of more than 50% of 100 mg/L PCNB by three fungal species was attributed to biosorption and subsequent biodegradation (Lièvreumont *et al.*, 1996a). The best PCNB degradation by the fungal species *Sporothrix cyanescens* was observed under carbon and nitrogen limitation (Lièvreumont *et al.*, 1996b). During the biotransformation of PCNB by four soil micromycetes, six metabolites were identified according to three metabolic pathways (Mora Torres *et al.*, 1996): PCNB → pentachloroaniline (C₆Cl₅NH₂) → tetrachloroaniline (C₆Cl₄HNH₂); PCNB → pentachlorothiophenol (C₆Cl₅SH) → pentachlorothioanisole (C₆Cl₅SCH₃); and PCNB → pentachlorophenol (C₆Cl₅OH) → pentachloroanisole (C₆Cl₅OCH₃).

PCNB degradation was observed in a large number of soil samples screened for microorganisms capable of degrading PCNB, irrespective of previous application of PCNB to the field. An isolate with a relatively fast PCNB degradation rate was identified as *Pseudomonas aeruginosa*. This isolate degraded PCNB best under anoxic conditions and the principal metabolic product of PCNB was pentachloroaniline, thus demonstrating that in anoxic soil environments the main degradation pathway of PCNB is its reduction to pentachloroaniline (Tamura *et al.*, 1995). Co-metabolic mineralization of monochloronitrobenzenes was achieved by a coculture of *Pseudomonas putida* and a *Rhodococcus* sp. The former species converted the chloronitrobenzenes to chloro-hydroxyacetanilides by partial reduction and subsequent acetylation, and the later species mineralized the chloro-hydroxyacetanilides to CO₂, NH₄⁺ and Cl⁻ (Park *et al.*, 1999). Sequential dehalogenation of CAs in microcosms developed with aquifer material was achieved under methanogenic, but not sulfidogenic conditions. Dechlorination at the *para* and *ortho* position of 2,3,4,5-TeCA resulted in the formation of 2,3,5-TrCA and eventually 3,5-DCA, whereas 3,4-DCA was transformed to 3-CA (Kuhn and Suflita, 1989).

Chloronitrobenzenes (3-CNB, 3,4-DCNB, 2,3,4-TrCNB, and PCNB) were transformed in anaerobic, sulfidogenic estuarine sediments with pseudo-first order rate constants ranging from 0.216 to 0.866 day⁻¹. Their transformation proceeded with reduction of the nitro group resulting in the formation of the corresponding chloroanilines, which were further transformed via *ortho* and *para* dechlorination pathways (Susarla et al., 1996). In contrast, chloroanilines were sequentially dechlorinated in the same estuarine sediments with pseudo-first order rate constants ranging from 0.005 to 0.012 day⁻¹ (Susarla et al., 1997). The degradation of 3,4-dihaloanilines by an anaerobic enrichment culture and *Rhodococcus* sp. strain derived from this culture under nitrate reducing conditions was recently reported to proceed by reductive deamination and formation of 1,2-dihalobenzene (Travkin et al., 2002). Further dehalogenation of the produced dihalobenzene was also observed.

3. RESEARCH METHODOLOGY

3.1. Target Compounds

As mentioned above, the focus of this research was primarily on the biotransformation of PCNB and its transformation products (i.e., CAs). The following compounds can theoretically be produced as a result of the sequential reductive dechlorination of pentachloroaniline: tetrachloroanilines (3); trichloroanilines (6); dichloroanilines (6); monochloroanilines (3); and aniline (see Figure 1). Reduction of the nitro group and formation of the electron-donating amino group will lead to electronic and steric effects, which in turn are expected to affect the reductive dechlorination of CAs. It has been shown that substitution of an electron-withdrawing nitro group by an electron-donating amino group strongly decreases the formation of electron donor-acceptor complexes by nitroaromatic compounds (Haderlein et al., 2000).

3.2. Scope/Hypothesis

Our research hypothesis was that reductive dehalogenation of polychlorinated organic compounds under iron-reducing conditions may take place by either one or both of the following mechanisms (Figure 2):

- a) Co-metabolic biotransformation: both Fe(III) and the chlorinated organic compounds merely serve as electron acceptors (primary and secondary electron acceptors, respectively)(Mechanism I, Figure 2);
- b) Abiotic transformation: the reductive dechlorination is mediated abiotically, using Fe(II) as the terminal electron donor (i.e., as a reductant) which is biotically produced from the reduction of Fe(III)(Mechanism II, Figure 2).

The difference between these two mechanisms is that in the first one, Fe(III) is reduced to Fe(II) without regeneration of Fe(III), whereas, according to the second mechanism, the reduction of the chlorinated organic contaminant(s) regenerates and continuously provides microbially available Fe(III) (see Figure 2). In the case of humic substances involvement in the reductive biotransformation process, these substances may serve as an electron shuttle between Fe(II) and the target chloroorganic compound, especially if the Fe(II) is surface-bound. In addition, humic substances may accelerate the biological reduction of amorphous Fe(III) oxyhydroxide. Such possible effects were assessed in the present study.

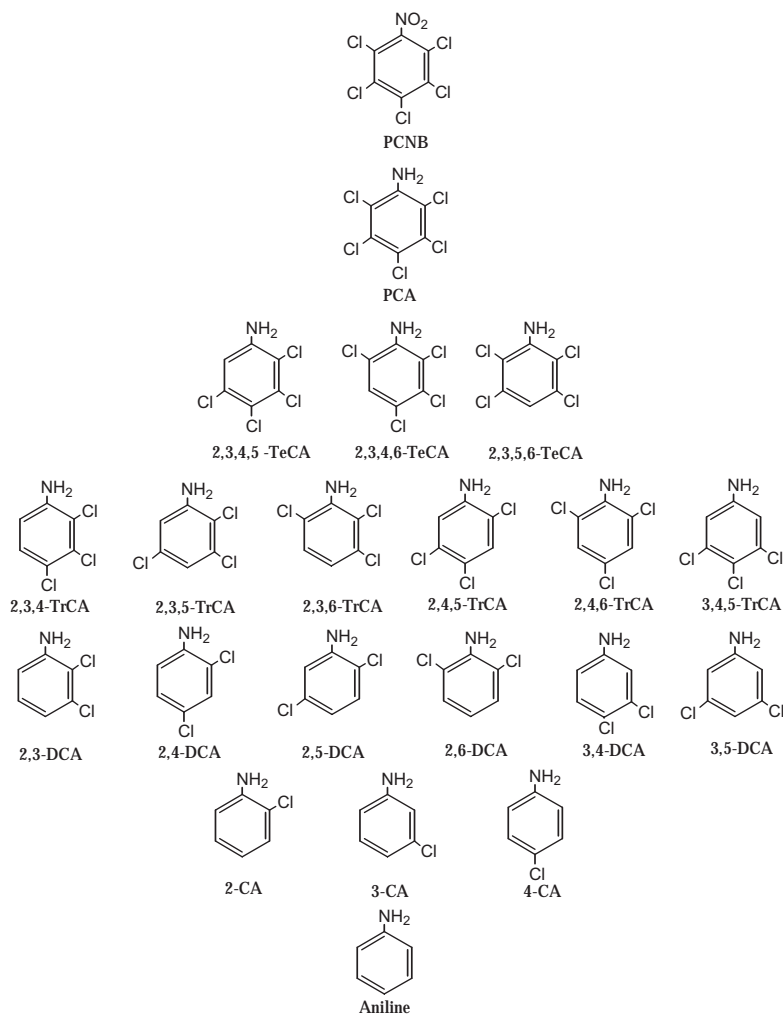


Figure 1. Possible compounds formed by the reductive transformation of PCNB.

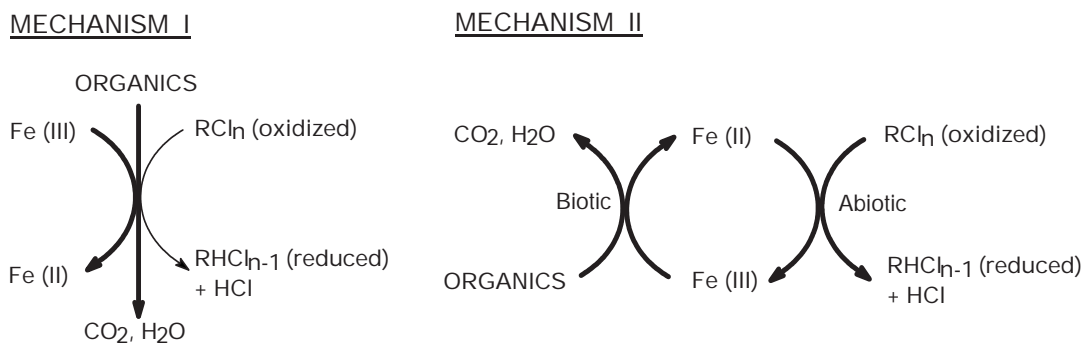


Figure 2. Mechanisms potentially involved in the reductive dechlorination of polychlorinated organic compounds under iron-reducing conditions.

3.3. Research Objectives

The specific objectives of this study were to:

1. Assess the potential for the microbial reductive transformation of PCNB and CAs under dissimilatory iron-reducing conditions.
2. Evaluate the effect of iron bioavailability on the amination/dechlorination process.
3. Assess the role of humic substances in the iron reduction and PCNB biotransformation processes.

3.4. Materials and Methods

3.4.1. Culture development

In order to meet the above-stated research objectives, a number of cultures were developed using a contaminated estuarine sediment as inoculum and monitored for various parameters over several feeding cycles (Table 2). Acetate or glucose and methanol were used as electron donors and Fe(III)-EDTA, Fe(III)-citrate, amorphous ferric hydroxide (FeOOH) and PCNB or PCA were used as electron acceptors.

Table 2. Enrichment cultures and their characteristics.

Culture	Electron acceptor-Target Compound	Electron donor	Iron form
A	Fe(III)	Acetate	Fe(III)-EDTA
B	Fe(III)	Acetate	Fe(III)-citrate
C	Fe(III)	Acetate	FeOOH
D	Fermentative/methanogenic-PCNB & PCA	glucose/methanol	None

The contaminated sediment was obtained from Bayou d'Inde, a tributary of Calcasieu River near Lake Charles, Louisiana, USA. Industrial wastes, including petroleum hydrocarbons, polycyclic aromatic hydrocarbons, and polychlorinated aromatic and aliphatic organic compounds have been discharged into this canal. The pH of the sediment sample was 6.6 and the total organic carbon was 5.74 ± 0.02 (expressed as % on a dry weight basis). The location of sediment and details on the sediment sampling have been reported elsewhere (Prytula and Pavlostathis, 1996; Gess and Pavlostathis, 1997). All cultures were developed and incubated in a constant temperature room at 22°C in the dark to better simulate natural conditions and were mixed once a day by hand.

3.4.1.1. Iron-reducing enrichment cultures (Cultures A, B, and C)

Three iron-reducing cultures were setup in 500 mL serum bottles as follows. Sediment samples (16 g wet basis) were added to the serum bottles, which were capped with butyl rubber stoppers, flushed with N₂ and the sediment sample was then diluted to 400 mL with iron-reducing culture mineral media. The media had the following composition (in mg/L): KH₂PO₄, 1000; NH₄Cl, 500; CaCl₂·2H₂O, 100; MgSO₄·7H₂O, 200; MgCl₂·6H₂O, 100; MnCl₂·4H₂O, 100; NaHCO₃, 2,500. Also, 0.2 mL/L vitamin stock solution (Wolin et al., 1963) and 1 mL/L trace metal stock solution (Mah and Smith, 1981) were added to the media. The cultures were fed with acetate (5 mM) as an electron donor and yeast extract (20 mg/L) and three different iron sources (Fe-citrate, Fe-EDTA and FeOOH) with a Fe(III) concentration of 25 mM. The pH in each culture

was kept between 6 and 7 with the addition of NaHCO_3 . A volume of each culture was wasted once a week and replaced with fresh media, and an aliquot of electron donor and Fe(III) was added, resulting in a culture retention time of 52 days. Microbial activity in these cultures was monitored by measuring total gas and gas composition, acetate, Fe(II) and total iron concentration. After several feeding cycles, sediment-free cultures were developed by diluting 50 mL of the first generation culture with 1.5 L mineral media in a nitrogen-flushed 2-L glass flask reactor (second generation culture). Because of the complexity of the process, as discussed in the Results and Discussion section, the Fe-citrate fed culture was not transferred to a new reactor.

3.4.1.2. Fermentative/methanogenic enrichment culture (Culture D)

This enrichment culture had been developed from the above-mentioned contaminated estuarine sediment as follows. A sediment sample (80 g wet basis) was added and diluted with 1.8 L of mineral media in a N_2 -flushed, 2-L glass flask reactor, capped with a Teflon-lined stopper. The media had the following composition (in mg/L): K_2HPO_4 , 900; KH_2PO_4 , 500; NH_4Cl , 500; $\text{CaCl}_2 \cdot 2\text{H}_2\text{O}$, 100; $\text{MgCl}_2 \cdot 6\text{H}_2\text{O}$, 200; $\text{FeCl}_2 \cdot 4\text{H}_2\text{O}$, 100; $\text{Na}_2\text{S} \cdot 9\text{H}_2\text{O}$, 500; NaHCO_3 , 1,200; resazurin (redox indicator), 2. Also, 0.2 mL/L vitamin stock solution (Wolin et al., 1963) and 1 mL/L trace metal stock solution (Mah and Smith, 1981) were added to the media. The culture was fed weekly with glucose and a PCNB/methanol solution. Glucose and methanol served as the carbon source and electron donor. At the beginning of each seven-day feeding cycle, glucose, yeast extract, and PCNB in methanol were added resulting in initial concentrations of 333 mg/L, 17 mg/L, 0.089 μM and 53 mg/L, respectively. The culture was kept in the dark in a 22°C constant temperature room, was stirred once a day using a Teflon-coated stirring bar over a magnetic stir plate, and its pH was kept around 7 with NaHCO_3 addition. After several feeding cycles, a culture transfer took place by diluting 100 mL of the first generation culture in 1.8 L mineral media in a N_2 -flushed, 2-L glass flask reactor (second generation culture). Finally, after several weekly wasting/feeding cycles, a similar culture transfer took place in 2 L of mineral media in a N_2 -flushed, 9-L glass reactor, and its contents were gradually increased up to 6 L (third generation culture). The retention time of this enrichment culture was 84 d. All batch experiments with the fermentative/methanogenic culture reported here were performed with the sediment-free, third generation mixed culture.

3.4.2. PCNB biotransformation assays

The biotransformation of PCNB by the enriched cultures was investigated using 160 mL serum bottles amended with acetate (300 mg/L), yeast extract (20 mg/L) and methanol (246 mg/L). The enriched culture D was able to quickly transform PCNB to PCA and further dechlorinate PCA to predominantly dichloroanilines under methanogenic conditions. Because of the relatively fast transformation of PCNB to PCA under both methanogenic and iron reducing conditions, in subsequent batch experiments, PCA dechlorination rather than PCNB biotransformation was investigated.

3.4.3. Assessment of the effect of iron reduction on PCA dechlorination

The impact of Fe(III) on the reductive dechlorination of PCA was investigated using the sediment-derived, third generation mixed culture developed under fermentative/methanogenic conditions (culture D). Fe(III)-EDTA (25 mM) and FeOOH (25 mM) were used as a source of iron in order to assess the rate and extent of PCA dechlorination and iron reduction. Aliquots of culture D were anaerobically transferred to 160 mL serum bottles which were previously capped with Teflon-lined septa and flushed with N_2 . The cultures were amended with 0.5 μM PCA

dissolved in methanol. The Fe(III)-EDTA amended cultures were fed twice with acetate in order to avoid lack of electron donor during the prolonged incubation. Possible inhibitory effects of EDTA (25 mM) and sodium (50 mM) resulting from the disodium salt of EDTA ($\text{Na}_2\text{-EDTA}$) were also tested. AQDS (200 μM), a humic acid model compound was added to some iron-amended cultures in order to increase the availability and thus the reduction rate of ferric iron. Another control was set up to test for any possible effect of AQDS on the reductive dechlorination of PCA in the absence of iron. Because of the potential of several culture media components (i.e., sulfide, Fe(II), vitamin B_{12}) to abiotically mediate the reductive transformation of PCA, two additional controls were setup, one with only autoclaved culture media and another with autoclaved media plus 25 mM ferrous iron ($\text{FeCl}_2\cdot 4\text{H}_2\text{O}$), which matched the iron concentration in the culture series amended with either Fe(III)-EDTA or FeOOH (see above).

3.4.4. Analytical methods

Liquid/liquid extraction was performed to analyze and quantify PCNB and its biotransformation products. Aliquots of 10 mL samples were extracted in glass tubes with 2 mL isooctane which contained 0.5 mg/L 1,3,5-tribromobenzene (TBB) as an internal standard. The tubes were capped with Teflon-lined stoppers and aluminum crimps, mixed vigorously for 2 min and centrifuged at 3000 rpm for 20 min. The solvent phase was transferred to amber glass autosampler vials, and sealed with Teflon-lined septa and aluminum crimps. The efficiency of the solvent extraction procedure was assessed at a concentration range of 0.03-40 μM PCNB, PCA and the less chlorinated anilines for 2 min, 1 h, 1 d and 3 d extraction period. It was determined that the efficiency was greater than 90% and did not change between 2 min and 3 days extraction period. Analysis of PCNB and biotransformation products was performed with an HP 6890 Series gas chromatograph (GC) equipped with an electron capture detector (ECD) and a 75-m 0.53-mm ID column (J&W Scientific, Folsom, CA, USA). The temperature program used was as follows: 100°C for 4 min, increased by 2°C/min up to 210°C and held for 60 min. Nitrogen was used as the carrier gas at a constant flow rate of 10 mL/min. The detection limits for PCNB, PCA and less chlorinated anilines were as follows: PCNB, 7 nM; PCA, 4 nM; tetrachloroanilines, 9 nM; trichloroanilines, 25 nM; dichloroanilines, 0.15 μM ; monochloroanilines 16 nM. Because of the structural similarity which led to coelution, 2,5-DCA and 2,4-DCA could not be separated during the GC/ECD analysis.

Because of detection limitations in GC/ECD, aniline, monochlorinated and dichlorinated anilines were also measured with a high performance liquid chromatography (HPLC) unit (Hewlett Packard Model 8453, Hewlett Packard Co., Palo Alto, CA) which was equipped with a Zorbax SB-C18 column (3 x 250 mm, 5 μm) (Agilent Technologies, New Castle, DE). The column compartment temperature was set at 40°C and the injection volume was 10 μL . The eluent mixture was an aqueous solution of 25 mM phosphate buffer (pH = 2.5) (52%) and methanol (48%) and the flow rate was 0.35 mL/min. Spectrometric detection was set at 203 nm. Samples used in HPLC analyses were filtered through 0.20 μm PTFE syringe filters (Cole-Parmer, Vernon Hills, IL) using glass syringes. The detection limits in HPLC for dichlorinated and monochlorinated anilines were 4 μM . 2,5-DCA and 2,4-DCA could also be separated during HPLC analysis.

Gas production was measured by connecting the culture headspace via a needle to an acid-brine solution filled graduated buret and recording the volume of displaced solution, after correcting to atmospheric pressure. Gas composition was determined by a gas chromatography (GC) unit equipped with a thermal conductivity detector. Methane was separated with a 25 m Chrompack Molsieve 5A fused silica 0.53 mm ID column and carbon dioxide was separated

with a 25 m Chrompack PoraPlot Q fused silica 0.53-mm ID column. Both columns were operated with helium as the carrier gas with a constant flow rate of 5 mL/min. The 10:1 split injector was maintained at 150°C and the detector temperature was set at 150°C. H₂ was measured with a GC (HP 5980 Series) equipped with a thermal conductivity detector and a 10 m Chrompack Molsieve 5A fused silica 0.53-mm ID column. The carrier gas was N₂ at a constant pressure of 70 psi. All gas samples were analyzed by injecting a 100 µL gas sample.

Methanol and acetate were measured in culture samples filtered through 0.20 µm syringe filters (PVDF-Whatman, Springfield Mill, England) using an HP 5890 Series II GC equipped with a flame ionization detector (FID) and a 35 m Stabilwax-DA 0.53-mm ID column (Restek, Bellefonte, PA, USA). Glucose was measured with a HP Series 1050 HPLC (Hewlett Packard, Palo Alto, CA) equipped with an Aminex HPX-87H-resin packed column (Bio-Rad, Richmond, CA). The column was maintained at 65°C in an external column heater. The eluent was 0.01 N H₂SO₄ and the flow rate was 0.6 mL/min.

The oxidation-reduction potential (ORP) was measured following the procedure outlined in *Standard Methods* (APHA, 1995) using an Orion Research digital pH/milivolt meter model 611 in conjunction with a Sensorex electrode (platinum electrode with an Ag/AgCl reference in a 3.5 M HCl gel). The meter was calibrated prior to use with a shorting lead to establish meter reading at zero millivolts and by using Light's standard solution [Fe(NH₄)₂(SO₄)₂·6H₂O, 0.1 M; H₂SO₄, 1 M]. Fe(II) was quantified with a modification of the method described by Kazumi et al. (1995a, b). Aliquots of 1 mL well-mixed culture were added to 20 mL 0.5 N HCl in 28 mL serum tubes. After 10 min of acidification, an aliquot of 100 µL was filtered and added to a serum tube containing 5 mL of ferrozine solution [1 g/L in 50 mM HEPES (N-2-hydroxyethylpiperazine-N'-2-ethanesulfonic acid) buffer (pH = 7)]. This solution was vortexed for 10 s to develop the characteristic magenta color of the Fe(II)-ferrozine complex. The absorbance of this solution was measured using an HP 8453 UV-Visible spectrophotometer (Hewlett Packard, Palo Alto, CA) with DI water as a blank.

4. RESULTS AND DISCUSSION

4.1. Iron-reducing enrichment cultures

4.1.1. Development and activity of iron-reducing enrichment cultures (Cultures A, B, and C)

These cultures were fed with acetate (5mM) and yeast extract (20 mg/L) and three different iron sources (Fe-citrate, Fe-EDTA and FeOOH). The initial Fe(III) concentration was 25 mM which served as the electron acceptor. Development of the enrichment cultures took place without any contaminant (i.e., PCNB, or PCA) amendment. Significant gas production was observed during the development of the Fe-citrate and Fe-EDTA amended cultures (Figure 3A and 3B). After 25 days of incubation, methane was observed in the Fe-citrate amended culture, which also used citrate as an electron donor after a few days of incubation, resulting in significant acetate accumulation (Figure 4A). Significant carbon dioxide and methane production was not observed in the reactor amended with FeOOH (Figure 3A and 3B), although after 65 days of incubation, traces of methane were observed. Significant consumption of acetate was not observed in the culture amended with FeOOH (Figure 4A).

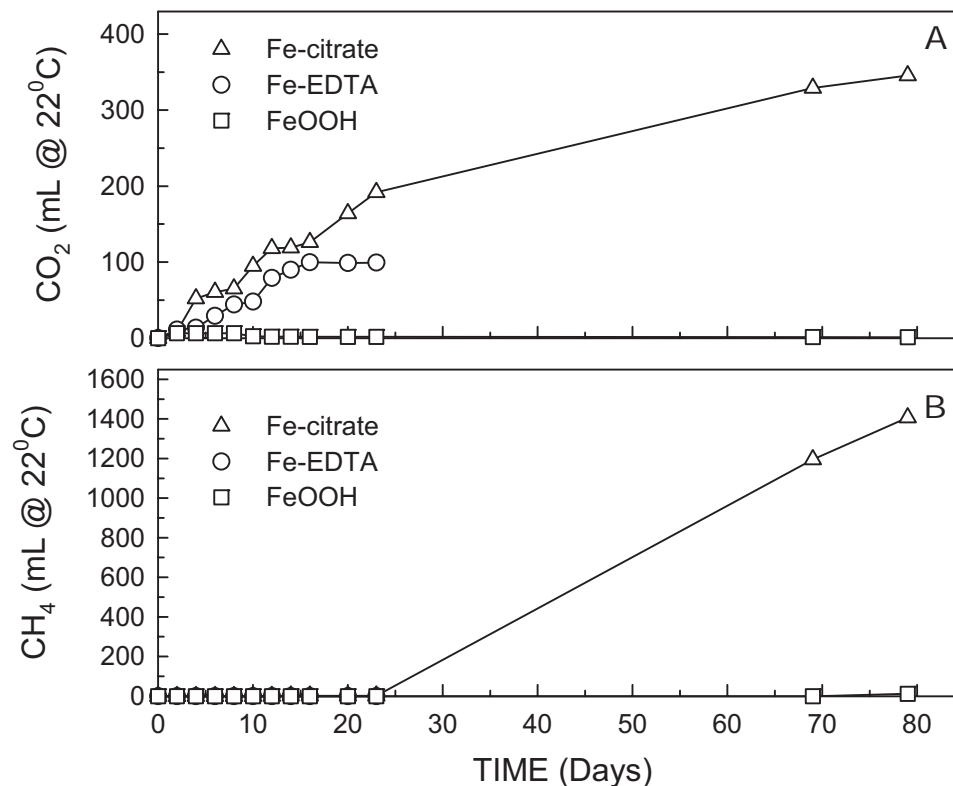


Figure 3. Cumulative gas production and composition: CO₂ (A) and CH₄ (B) in the sediment-derived, iron-reducing cultures (first-generation; multiple feeding cycles).

During all feeding cycles, the pH in the Fe-EDTA amended culture remained between 5 and 7. After feeding, the pH increased up to 6.5-7, as a result of media and alkalinity addition and gradually decreased due to the reduction of the newly added Fe(III) (Figure 4B). The pH drop can be explained by the following stoichiometric equation of iron reduction and acetate oxidation: $\text{CH}_3\text{COO}^- + 8 \text{Fe}^{3+} + 3 \text{H}_2\text{O} \rightarrow \text{CO}_2 + \text{HCO}_3^- + 8 \text{Fe}^{2+} + 8 \text{H}^+$. In the FeOOH amended culture, the pH increased from 7 to 8 over 23 days of incubation, which also indicates that iron reduction was very slow in this culture (Figure 4B).

Iron reduction in all three cultures was monitored by the measurement of Fe(II). Fast Fe(III) reduction was observed in both the Fe-citrate and Fe-EDTA amended cultures. However, Fe(III) reduction was much slower in the FeOOH amended culture (Figure 4C and 4D). Fe(III) reduction was the fastest in the Fe-EDTA amended culture. Because of the observed consumption of citrate and accumulation of a high concentration of acetate in the Fe-citrate amended culture, this culture was not transferred to create a second generation culture. After several feeding cycles, 50 mL inocula from the Fe-EDTA and FeOOH amended cultures were transferred to 2-L glass reactors and were maintained with the same feeding procedure. Headspace gas analysis showed production of CO₂ in the Fe-EDTA amended culture, but gas production was not observed during all feeding cycles in the second generation, FeOOH amended culture (Figure 5A). Similar to the first generation culture, the pH increased in the FeOOH amended culture during the incubation. After 15 days of incubation, although the pH was adjusted to 7, CO₂ production did not increase in the FeOOH amended culture (Figure 5B).

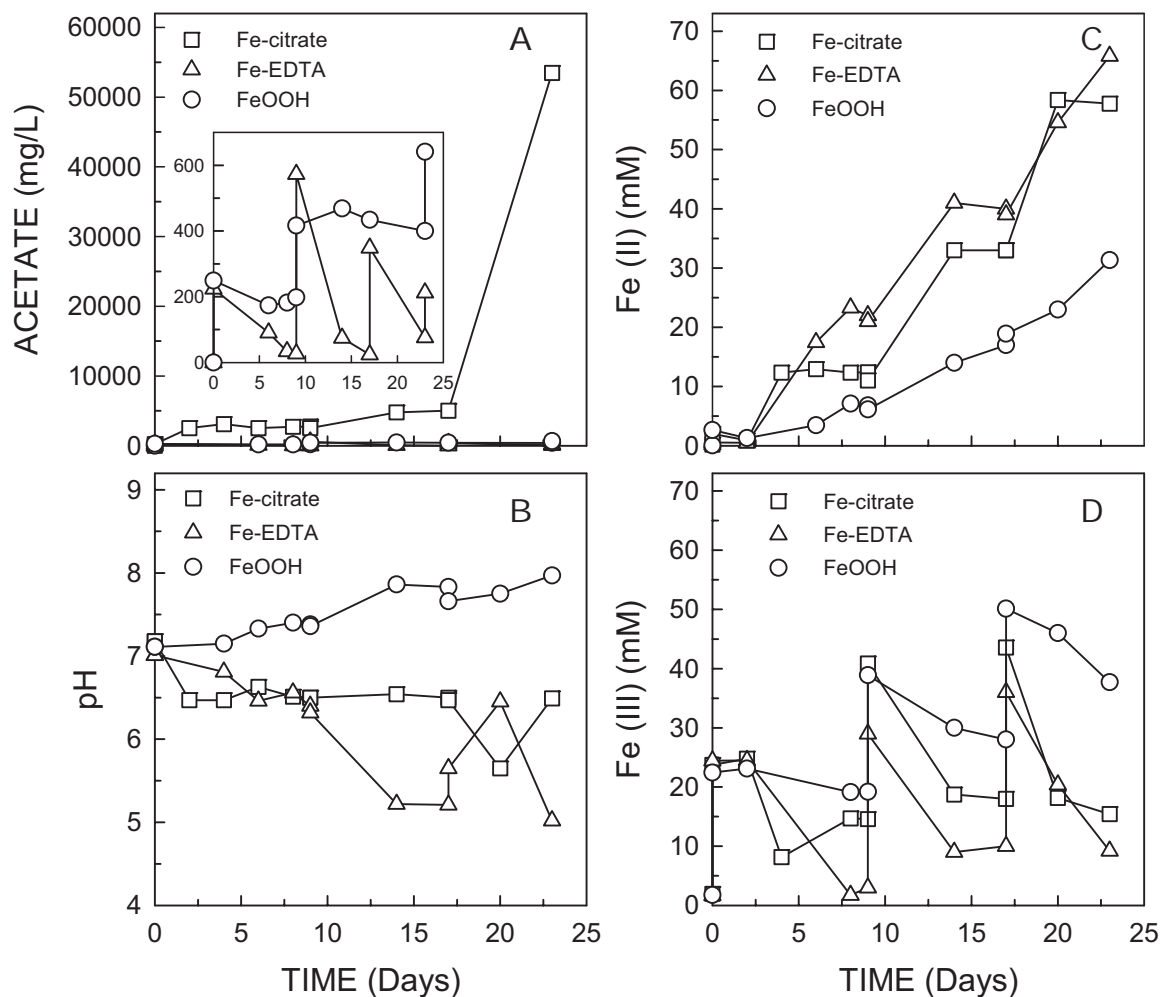


Figure 4. Acetate consumption (A), pH variation (B), Fe(II) production (C), and Fe(III) reduction (D) in the sediment-derived, iron-reducing cultures (first-generation; multiple feeding cycles).

Acetate consumption was much slower in the second generation FeOOH amended culture as compared to the Fe-EDTA amended culture (Figure 5C), which combined with the observed very low gas production, indicates very low microbial activity when the electron acceptor was FeOOH. In contrast, acetate consumption was much faster in the second generation Fe-EDTA amended culture (Figure 5C) and Fe(III) reduction approached almost 100% in all feeding cycles (Figure 5D). In contrast, the rate and extent of iron reduction in the FeOOH amended culture was much lower (Figure 5D). After pH adjustment of the FeOOH amended culture, a modest increase in the iron reduction rate was observed. In order to assess the effect of iron concentration on iron reduction in FeOOH-amended cultures, two batch cultures were setup with inoculum taken from the second generation FeOOH-reducing culture. In this setup, the initial Fe(III) concentrations of 40 mM and 80 mM were 1.6 and 3.2 times higher than the normal culture feeding conditions. After 7 days of incubation, about 45% of initially added FeOOH was reduced in both cultures (Figure 6). A higher iron reduction rate was observed in the 80 mM amended culture as compared to the 40 mM amended culture. Magnetite (Fe_3O_4) production was observed in the culture amended with 80 mM FeOOH.

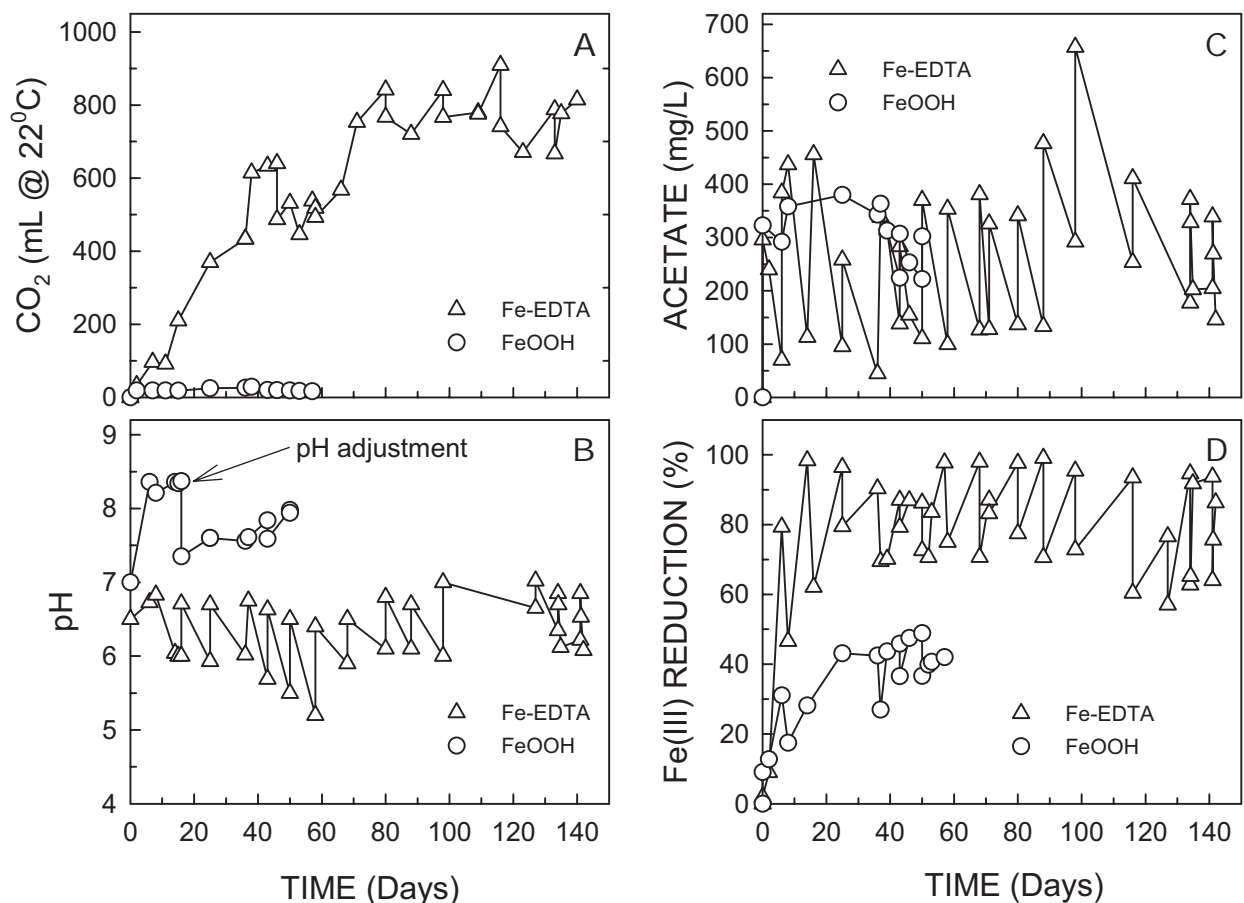


Figure 5. Cumulative CO₂ production (A), pH profile (B), acetate consumption (C), and extent of iron reduction (D) in the sediment-derived, iron-reducing cultures (second-generation; multiple feeding cycles).

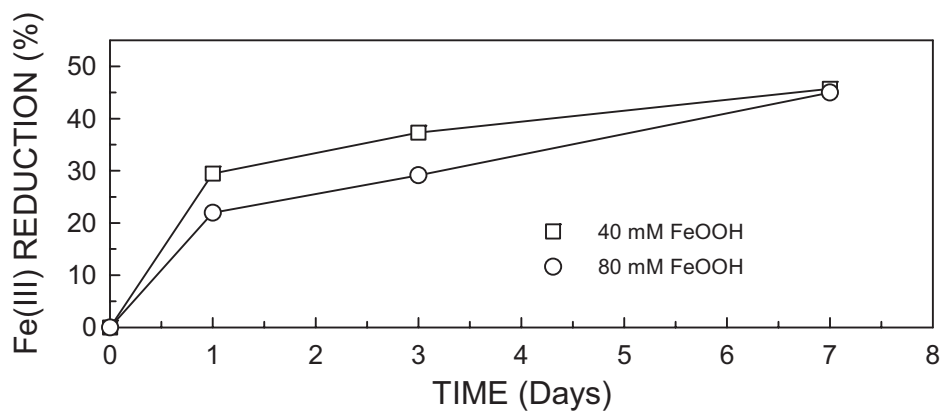


Figure 6. Extent of iron reduction in sediment-derived, FeOOH-amended, second generation, batch cultures.

4.1.2. PCNB biotransformation in an iron-reducing enrichment culture (Culture A)

A batch PCNB biotransformation assay was conducted with the sediment-derived, second generation culture developed under iron reducing conditions (Fe-EDTA). Two sub-cultures were developed: one with Fe(III)-EDTA addition and one without any new iron addition. About 78 mM Fe(II) was present in these cultures at the beginning of the incubation contributed by the inoculum (Figure 7A and 7D). A delay in the transformation of PCNB to PCA was observed in the culture amended with Fe(III)-EDTA. In contrast, PCNB to PCA transformation was complete within 2 days in the culture that was not amended with any Fe(III). In both cultures, PCA was sequentially transformed to TeCAs and TrCAs (Figure 7A and 7D). However, the observed transformation rates in both cultures were significantly slower compared to those observed with the mixed methanogenic, PCNB-dechlorinating enrichment culture (see Section 4.2.1, below). After 10 days of incubation, methane production was observed in both cultures (Figure 7C and 7F). Acetate consumption and CO₂ production was higher in the culture amended with Fe(III), compared to that in the culture which was not amended with Fe(III). Transformation of PCNB to PCA was not observed during the 43-day of incubation period in the abiotic control which was setup with autoclaved iron-reducing culture media (data not shown).

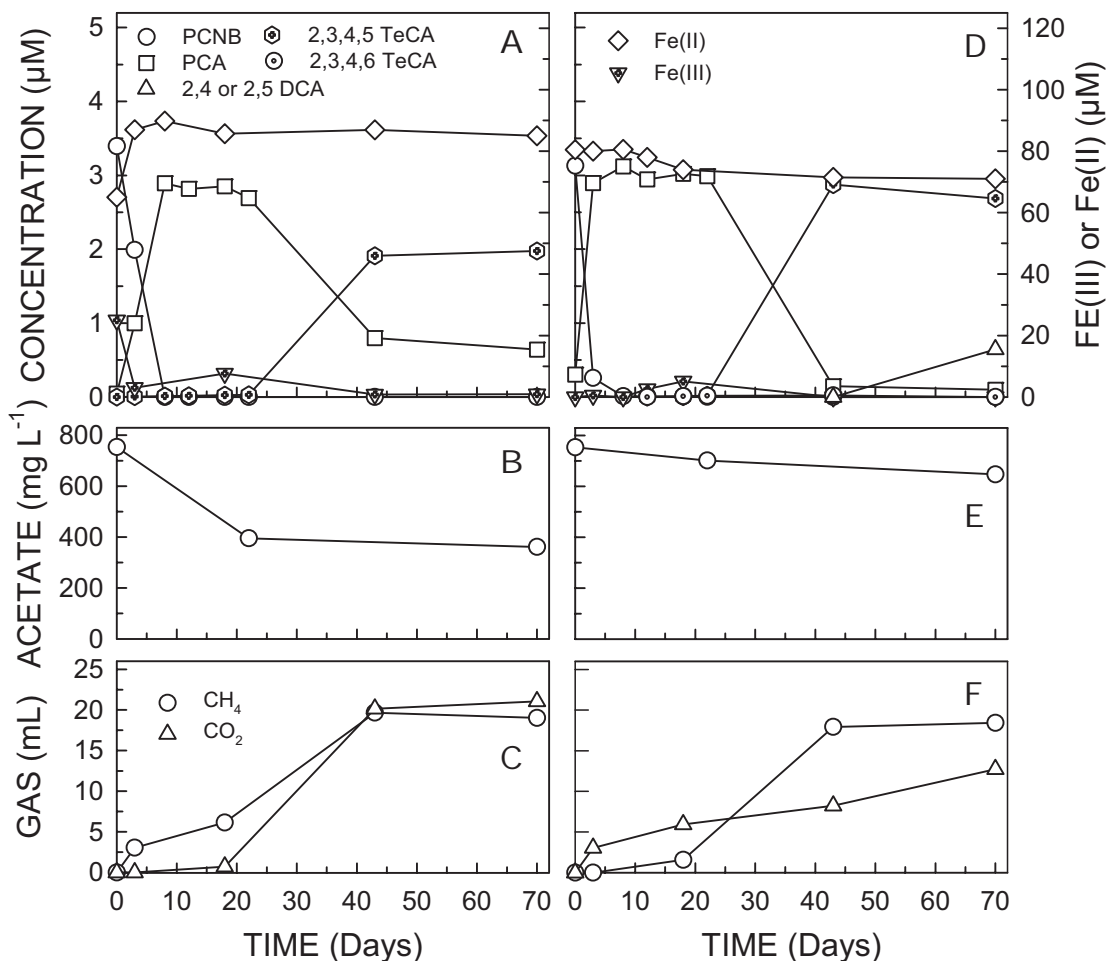


Figure 7. PCNB transformation, acetate consumption and gas production (at 22°C) in the sediment-derived, second generation Fe-EDTA reducing cultures (A, B, and C: culture with Fe(III)-EDTA amendment; D, E, and F: culture without Fe(III)-EDTA amendment).

4.2. Fermentative/methanogenic enrichment culture

4.2.1. PCNB biotransformation by the fermentative/methanogenic enrichment culture (Culture D)

Complete transformation of PCNB to PCA in the sediment-free, fermentative/methanogenic culture occurred in less than one day (Figure 8). Batch assays performed with the sediment-free enrichment culture resulted in the biotransformation of PCNB to PCA, which was then sequentially dechlorinated as follows: PCA \rightarrow 2,3,4,5- and 2,3,5,6-tetrachloroaniline (TeCA) \rightarrow 2,4,5- and 2,3,5-trichloroaniline (TrCA) \rightarrow 2,4-, 2,5- and 3,5-dichloroaniline (DCA) \rightarrow 3- and 4-chloroaniline (CA) (low levels). The predominant end product was 2,5-DCA (Figure 9).

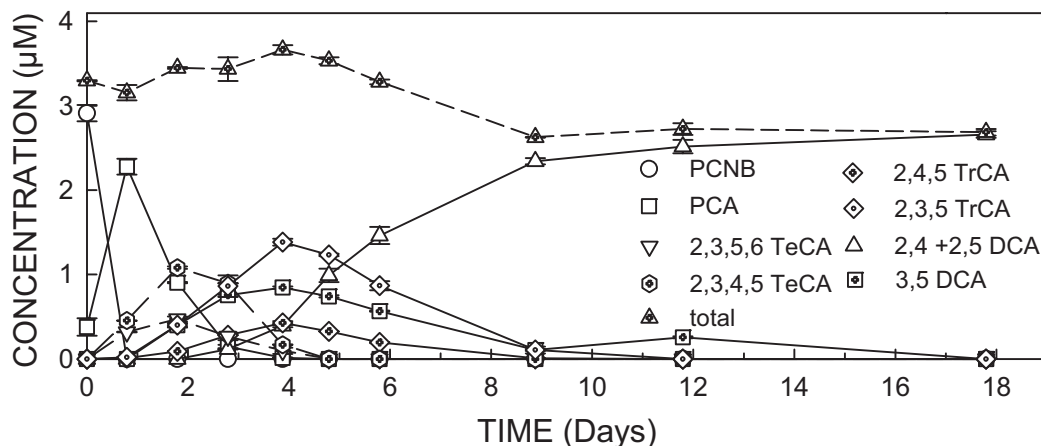


Figure 8. Time course of PCNB and its biotransformation products during a typical batch biotransformation assay conducted with the PCNB-enriched, mixed methanogenic culture (Error bars represent mean values \pm one standard deviation).

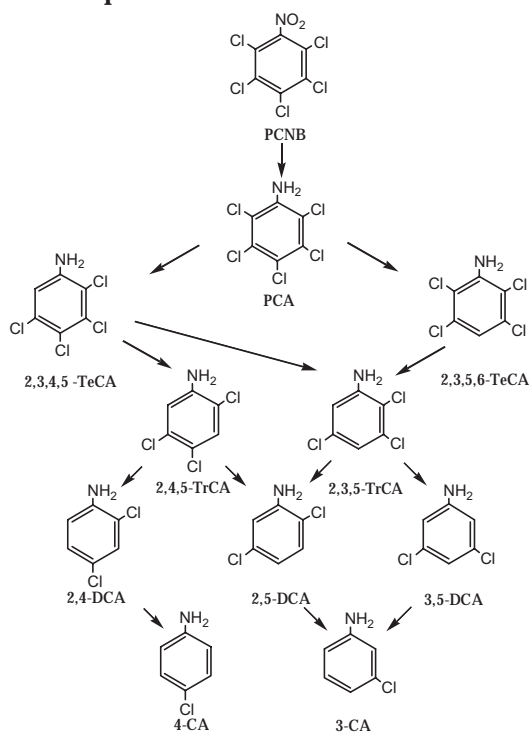


Figure 9. PCNB biotransformation products observed in the fermentative/methanogenic enrichment culture.

4.2.2. Effect of iron reduction on PCA dechlorination by the fermentative/methanogenic enrichment culture (Culture D)

As mentioned in the Materials and Methods section, above, complete and fast PCNB transformation to PCA was observed under any anoxic/anaerobic conditions. Therefore, all subsequent assays were conducted with PCA as opposed to PCNB. The initial biomass concentration in all cultures in this assay was 310 ± 20 mg C/L (measured as particulate organic carbon). The pH and ORP values in the iron-free, control culture were 7.0 ± 0.3 and -170 ± 5 mV, respectively (mean \pm standard deviation; $n = 3$). The initial and final ORP values in the cultures amended with Fe(III)-EDTA or FeOOH were $+138 \pm 2$, -120 ± 4 mV, and -60 ± 14 , -120 ± 70 mV, respectively. The higher decrease in the ORP value of the Fe(III)-EDTA amended cultures was mainly due to the exhaustion of Fe(III). Fetzner and Conrad (1993) found no inhibition of methanogenesis at ORP values as high as $+420$ mV. Therefore, inhibition of methanogenesis due to the relatively high redox potential seems unlikely in all of these cultures. The initial and final pH values in the Fe(III)-EDTA amended cultures were similar to those of the control culture. However, the pH increased from 7.2 ± 0.1 to 8.1 ± 0.4 in the FeOOH amended cultures within 60 days of incubation. The increase in pH was also observed in the sediment-derived FeOOH reducing cultures as mentioned above.

PCA was dechlorinated to 3,5 DCA and 2,4+2,5 DCA and all acetate was consumed in the iron-free, control culture under methanogenic conditions within 10 days of incubation without any delay (Figure 10). However, dechlorination of PCA was not observed in the cultures amended with either Fe(III)-EDTA or Fe(III)-EDTA and AQDS until 30 days of incubation when more than 90% of the added Fe(III) was reduced (Figure 11). The PCA dechlorination pathway was similar to that of the control culture after 30 days of incubation in both the Fe(III)-EDTA and Fe(III)-EDTA plus AQDS amended cultures (Figure 11A and 11B). On the other hand, PCA dechlorination as well as acetate consumption were not observed during 60 days of incubation in the culture amended with $\text{Na}_2\text{-EDTA}$ (Figure 12C). Therefore, EDTA had an inhibitory effect on the dechlorinating and methanogenic culture. In contrast, the presence of iron in the case of Fe-EDTA eliminated the inhibitory effect of EDTA, more likely because of binding with the resulting Fe(II). Straub et al. (2001) suggested that the inhibitory effect of EDTA could be because of its interaction with divalent cations such as Ca^{2+} or Mg^{2+} , causing an imbalance in the supply of these ions. Such interactions may be detrimental, especially for gram-negative bacteria, which depend on such cations in their outer membranes. PCA dechlorination was not observed in the presence of only culture media or culture media amended with 25 mM ferrous iron (Figure 12A and 12B). PCA dechlorination and acetate consumption in the culture which was amended with 50 mM Na^+ proceeded as in the iron-free, control culture without any inhibitory effect (Figure 13A and 13B). AQDS did not have any inhibitory or stimulatory effect on the dechlorination of PCA in the absence of an iron source (Figure 13B).

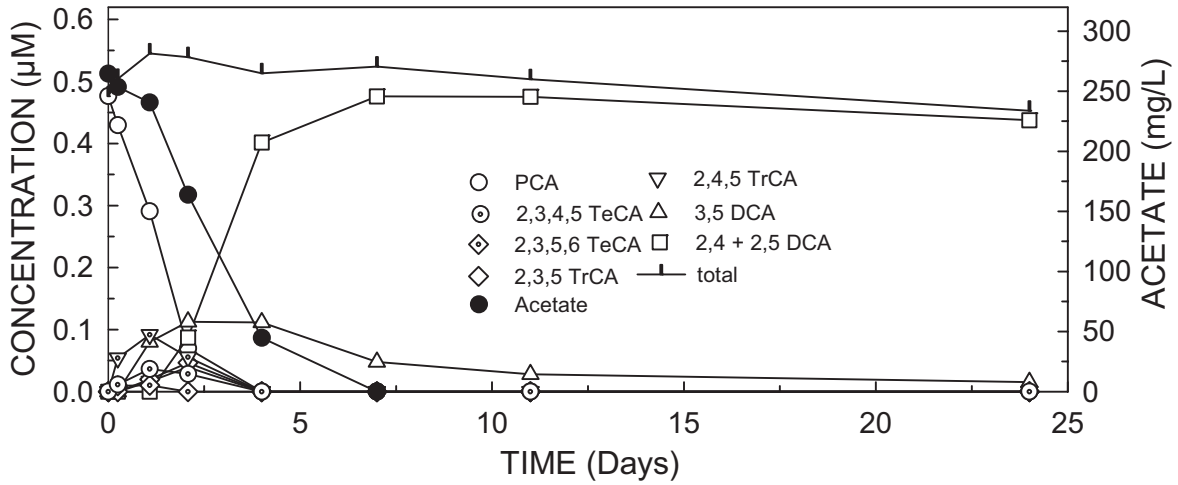


Figure 10. Time course of PCA and its dechlorination products, as well as acetate consumption in the iron-free, control methanogenic culture (sediment-free culture)

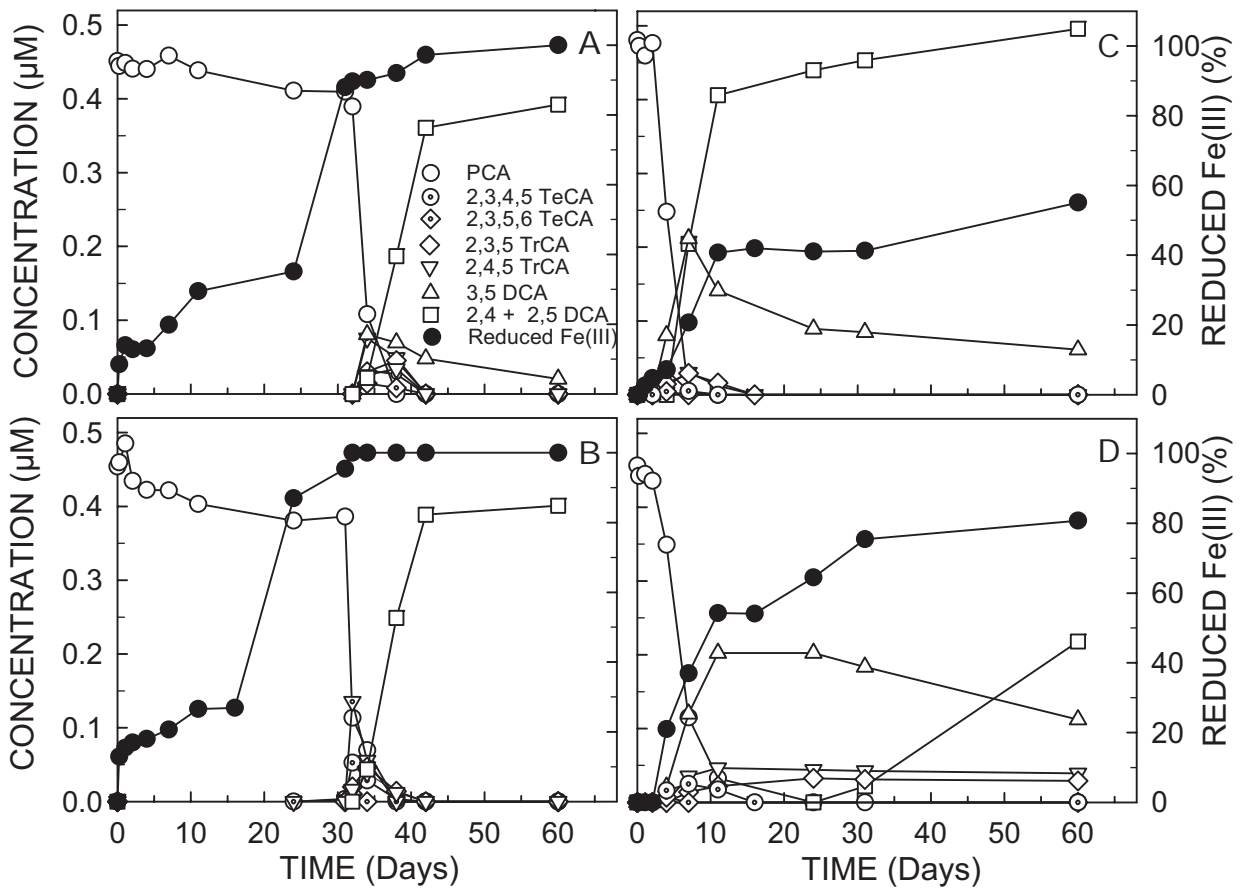


Figure 11. Iron reduction and PCA dechlorination in cultures amended with Fe(III)-EDTA (A), Fe(III)-EDTA and AQDS (B), FeOOH (C), FeOOH and AQDS (D).

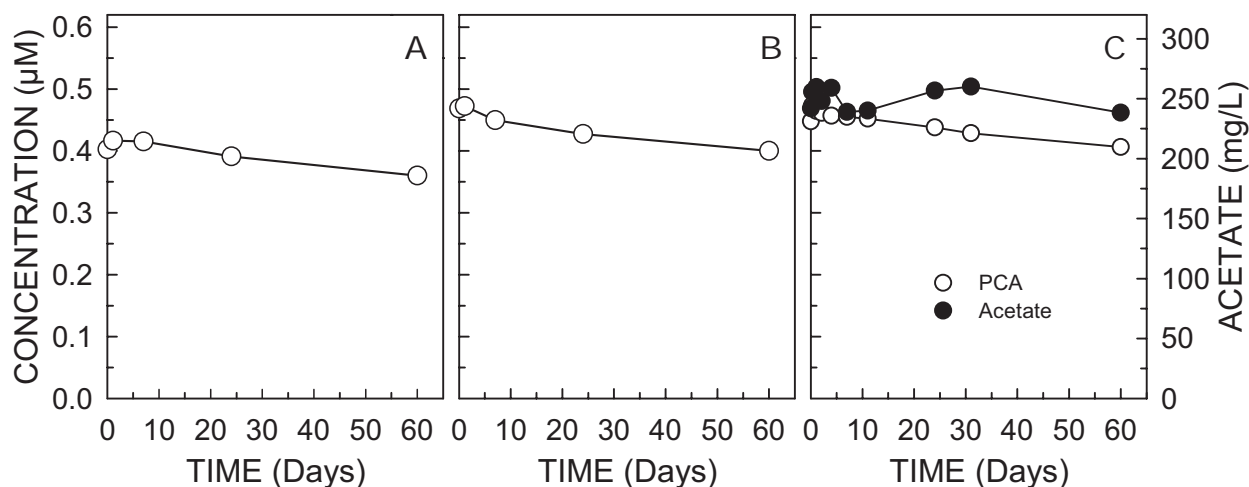


Figure 12. PCA in culture media (A), culture media amended with Fe(II) (B), and methanogenic culture amended with Na₂-EDTA (C).

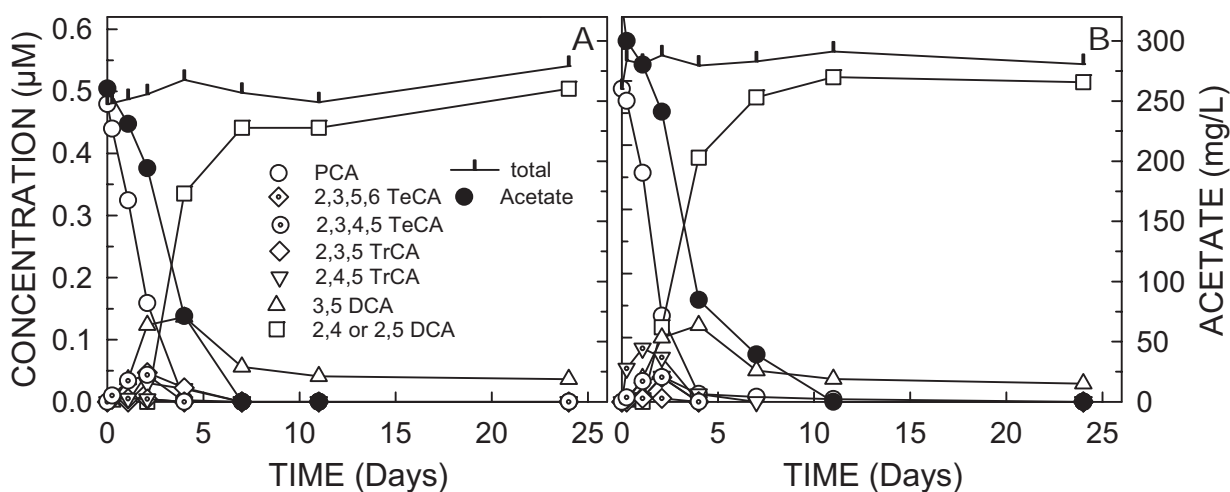


Figure 13. PCA dechlorination and acetate consumption in methanogenic cultures amended with either Na⁺ (A) or AQDS (B).

Dechlorination of PCA started after 2 days of lag period in the culture amended with FeOOH (Figure 11C), but the dechlorination rate was lower than that observed in the control culture. Dechlorination of PCA was slower in the FeOOH and AQDS amended culture (Figure 11D) as compared to the culture amended with only FeOOH. Lovley et al. (1998) showed that the humics analog, AQDS, can be reduced by microorganisms to anthrahydroquinone-2,6-disulfonate (AHQDS) which then abiotically reduces Fe(III). Similar to our results, He and Sanford (2003) reported inhibition of 2-chlorophenol dechlorination by the *Anaeromyxobacter dehalogenans* strain 2CP-C when the iron source was soluble (ferric pyrophosphate), whereas insoluble FeOOH did not have a significant effect on the dechlorination of 2-chlorophenol.

Gas production by all cultures during the incubation period is shown in Figure 14. AQDS did not have any inhibitory or stimulatory effect on the methane production of the dechlorinating, mixed fermentative/methanogenic culture. A slight decrease in the rate and

extent of methane production was observed in the culture amended with sodium chloride. An earlier study reported sodium concentrations ranging from 150 to 240 mM to be moderately and 347 mM to be strongly inhibitory to methanogens at mesophilic temperatures (McCarty, 1964). In another study, sodium chloride concentrations over 15.2 mM were inhibitory for *Methanobacterium thermoautotrophicum* (Patel and Roth, 1977). Similar to the dechlorination activity, methane production was observed after a lag period of 2 days in the cultures amended with FeOOH. Very low methane production and relatively high carbon dioxide production was observed in the cultures amended with Fe(III)-EDTA until 30 days of incubation. However, significant methane production and PCA dechlorination was observed after 30 days of incubation when more than 90% of Fe(III) was reduced to Fe(II). High carbon dioxide production shows that iron-reduction was the main metabolic process in these cultures. The cumulative carbon dioxide production was very similar in the two Fe(III)-EDTA amended cultures. Methane production was lower in the culture amended with both FeOOH and AQDS compared with that of the culture amended with only FeOOH. van Bodegom et al. (2004) reported direct inhibition of methanogenesis in the presence of ferric iron, and found that methanogens grown on H₂/CO₂ were more sensitive to ferric iron than methanogens grown on acetate. A relatively low carbon dioxide production was observed in the cultures amended with FeOOH compared to the Fe(III)-EDTA amended cultures. Both methane and carbon dioxide production was very low in the culture amended with Na₂-EDTA, showing very low biological activity in this culture.

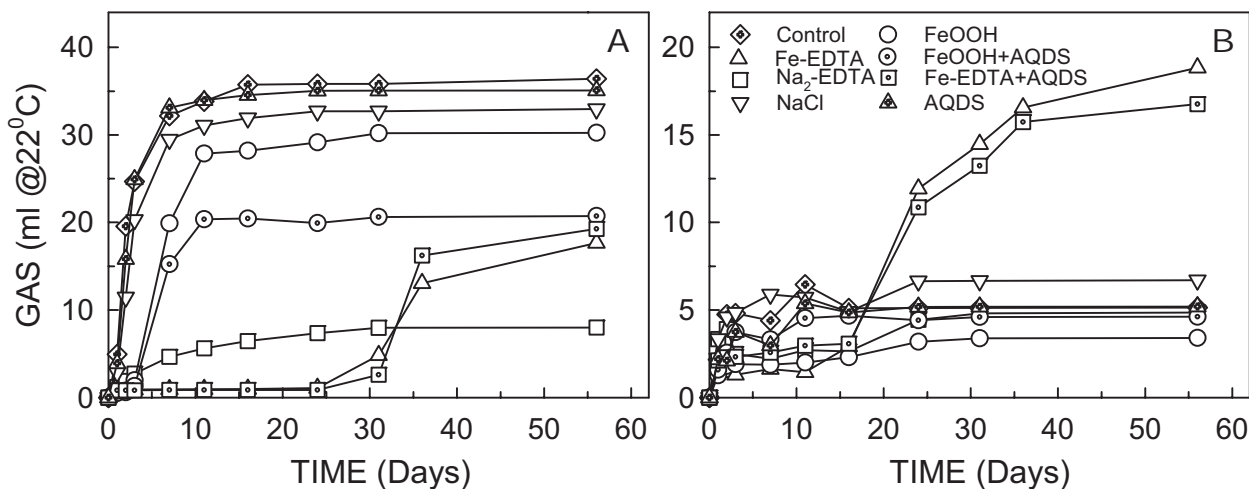


Figure 14. Gas production in all PCA-amended cultures. (A) methane; (B) carbon dioxide.

AQDS addition increased the Fe(III) reduction rate to some degree in the Fe(III)-EDTA amended culture, but the Fe(III) reduction rate was considerably increased in the FeOOH amended culture (Figure 15). Complete iron reduction was observed in the Fe(III)-EDTA plus AQDS amended culture after 30 days of incubation, whereas complete iron reduction in the culture without AQDS amendment was observed after 60 days of incubation (Figure 15A). Iron reduction was not observed for the first two days of incubation in the culture amended with FeOOH and AQDS, but after 10 days of incubation, the extent of Fe(III) reduction was significantly higher than in the culture without AQDS amendment (Figure 15B). Similar to our findings, Lovley et al. (1996) reported acceleration of the reduction of amorphous Fe(III) oxyhydroxide by the presence of a very low concentration of AQDS. The role of the humic acid analog AQDS as an electron shuttle provides a strategy for Fe(III) reducers to access insoluble

Fe(III) compounds (Lovley et al., 1996). Complete iron reduction was not observed in the cultures amended with FeOOH (Figure 15B). Similarly, it has been demonstrated that even the most available iron oxide -- amorphous hydrous ferric oxide -- cannot be totally consumed during microbial iron reduction (Lovley and Phillips, 1986a and b; Roden and Zachara, 1996).

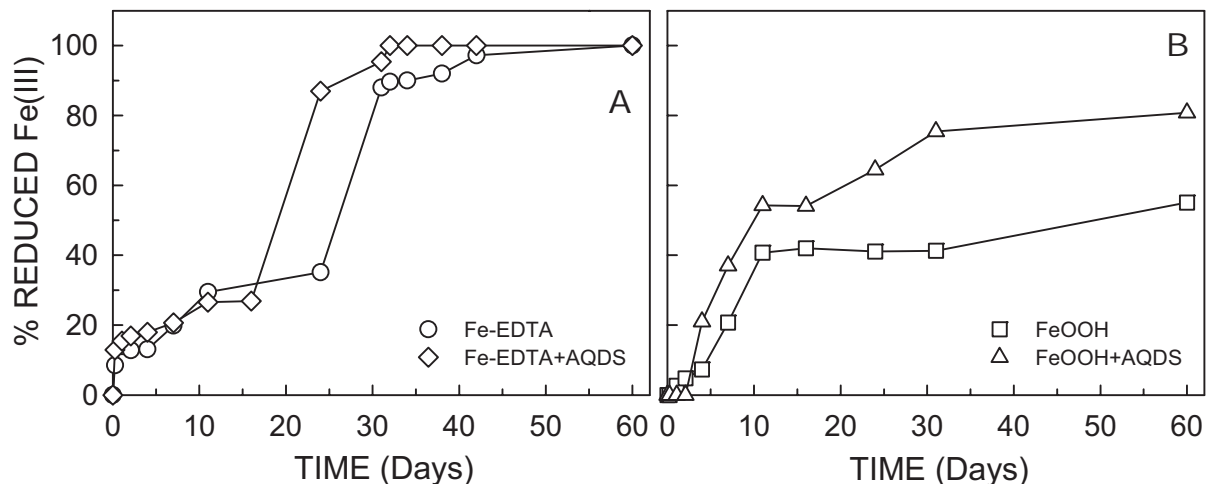


Figure 15. Iron reduction in cultures amended with Fe-EDTA (A) and FeOOH (B) (The effect of AQDS on the rate and extent of iron reduction is also shown).

5. CONCLUSIONS

Based on the results of the present study, the following conclusions are drawn:

- 1) Enrichment of dissimilatory, iron-reducing cultures using amorphous Fe(III) oxyhydroxide as an electron acceptor is extremely slow as compared to cultures enriched with either Fe(III)-citrate or Fe(III)-EDTA. Thus, the bioavailability of Fe(III) oxyhydroxide at circumneutral pH values is very low.
- 2) Reduction of the nitro-group of PCNB and production of pentachloroaniline (PCA) is taking place under both abiotic and biotic, reductive conditions. However, the rate of this conversion is highly enhanced under biotic conditions. Under biotic conditions, the rate of PCNB to PCA biotransformation was higher under methanogenic conditions as compared to iron-reducing conditions.
- 3) Dechlorination of PCA under abiotic, reductive conditions, e.g., in the presence of sulfide and/or Fe(II), was not observed in the present study.
- 4) PCA dechlorination did not take place when Fe(III)-EDTA was reduced at a relatively fast rate by an enriched, PCA-dechlorinating methanogenic culture, but dechlorination took place after iron reduction was almost complete. The PCA dechlorination pathway was similar to that of the iron-free, control culture.
- 5) PCA dechlorination and iron reduction took place simultaneously when the iron source was less bioavailable (e.g., FeOOH). However, addition of anthraquinone 2,6-disulfonate (AQDS), a humic acid model compound, to the culture, increased the rate and extent of

FeOOH reduction, which in turn resulted in a significant decrease of the rate and extent of PCA dechlorination. Thus, fast iron reduction suppresses and delays the onset of the reductive dechlorination of PCA.

The results of this study have significant implications relative to the fate and biotransformation of PCNB and PCA under anoxic/anaerobic conditions encountered in most subsurface soil and sediment environments. Based on the observed fast and facile conversion of PCNB to PCA, PCNB is not expected to be persistent in natural systems. However, the bioavailability of iron in natural systems, which in turn is controlled by soluble humic material, has a pronounced effect on the rate and extent of PCA dechlorination and thus on its persistence in natural systems.

6. DISSEMINATION OF PROJECT RESULTS

The results of this project are being disseminated as follows:

Okutman-Tas, D. and S. G. Pavlostathis. Microbial Reductive Transformation of Pentachloronitrobenzene under Methanogenic Conditions. Manuscript submitted to *Environmental Science and Technology*.

Okutman-Tas, D. and S. G. Pavlostathis. Microbial Reductive Transformation of Pentachloronitrobenzene under Nitrate-reducing Conditions. Abstract to be presented at the 105th General Meeting, American Society for Microbiology, Atlanta, GA, June 5-9, 2005.

Okutman-Tas, D., and S. G. Pavlostathis. The Influence of Iron Reduction on the Reductive Biotransformation of Pentachloronitrobenzene. Paper to be presented at the Third European Bioremediation Conference, Chania, Greece, July 4-7, 2005.

Okutman-Tas, D. and S. G. Pavlostathis. The Influence of Iron Reduction on the Sequential Microbial Reductive Dechlorination of Pentachloroaniline. Manuscript in preparation.

7. REFERENCES

- American Public Health Association (APHA); American Water Works Association; and Water Environment Federation. 1998. *Standard Methods for the Examination of Water and Wastewater*, 20th Ed., Washington, D.C.
- Booker, R. S. and Pavlostathis, S. G.. 2000. Microbial reductive dechlorination of hexachloro-1,3-butadiene in a methanogenic enrichment culture. *Water Res.* 34:4437-4445.
- Bradley, P.M., and F.H. Chapelle. 1996. Anaerobic mineralization of vinyl chloride in Fe(III)-reducing, aquifer sediments. *Environ. Sci. Technol.* 30:2084-2086.
- Bradley P.M., F.H. Chapelle and D.R. Lovley. 1998. Humic acids as electron acceptors for anaerobic microbial oxidation of vinyl chloride and dichloroethene. *Appl. Environ. Microbiol.* 64:3102-3105.
- Doikos, P. *Investigation of the Potential for Microbial Reductive Dechlorination of Hexachlorobenzene under Iron-Reducing Conditions*. MS Thesis, Georgia Institute of Technology, 1998.
- Dolfing, J. and Beurskens, J.E.M. 1995. The microbial logic and environmental significance of reductive dehalogenation. In: *Advances in Microbial Ecology*, Vol. 14, Jones, J.G. (ed.), Plenum Press, New York, NY.

- Extension Toxicology Network (EXTOXNET). 1996. Pesticide Information Profiles (<http://ace.ace.orst.edu>).
- Fantroussi, S. El, Naveau, H. and Agathos, S.N. 1998. Anaerobic dechlorinating bacteria. *Biotechnol. Prog.* 14:167-188.
- Fetzner, S. 1998. Bacterial dehalogenation. *Appl. Microbiol. Biotechnol.* 50:633-657.
- Fetzer, S. and R. Conrad. 1993. Effect of redox potential on methanogenesis by *Methanosarcina barkeri*. *Arch. Microbiol.* 160:108-113.
- Fetzner, S. and Lingens, F. 1994. Bacterial dehalogenases: biochemistry, genetics, and biotechnological applications. *Microbiol. Rev.* 58:641-685.
- Gess, P., and Pavlostathis, S.G. 1997. Desorption of chlorinated organic compounds from a contaminated estuarine sediment. *Environ. Toxicol. Chem.* 16:1598-1605.
- Guiraud, P., Steiman, R., Ait-Laydi, L., and Seigle-Murandi, F. 1999. Degradation of phenolic and chloroaromatic compounds by *Coprinus* spp. *Chemosphere* 38:2775-2789.
- Haderlein, S. B., and R. P. Schwarzenbach. 1995. Environmental processes influencing the rate of abiotic reduction of nitroaromatic compounds in the subsurface. In *Biodegradation of Nitroaromatic Compounds*; Spain, J. C. (Ed.); Plenum Press, New York, pp 199-225.
- Haderlein, S. B., Hofstetter, T. B., and Schwarzenbach, R. P. 2000. Subsurface chemistry of nitroaromatic compounds. In: *Biodegradation of Nitroaromatic Compounds and Explosives*, J.C. Spain, J.B. Hughes, and H-J. Knackmuss (eds), Lewis Publishers, Boca Raton, Florida, USA, pp. 311-356.
- Hägglom, M. M., Knight, V. K., and Kerkhof, L. J. 2000. Anaerobic decomposition of halogenated aromatic compounds. *Environ. Pollut.* 107:199-207.
- He, Q., and R. A. Sanford. 2003. Characterization of Fe(III) reduction by chlororespiring *Anaeromyxobacter dehalogenans*. *Appl. Environ. Microbiol.* 69:2712-2718.
- Heijman, C. G., E. Grieder, C. Holliger, and R. P. Schwarzenbach. 1995. Reduction of nitroaromatic compounds coupled to microbial iron reduction in laboratory aquifer columns. *Environ. Sci. Technol.* 29:775-783.
- Kazumi, J., M.M. Hägglom, and L.Y. Young. 1995a. Diversity of anaerobic microbial processes in chlorobenzoate degradation: nitrate, iron, sulfate and carbonate as electron acceptors. *Appl. Microbiol. Biotechnol.* 43:929-936.
- Kazumi, J., M.M. Hägglom, and L.Y. Young. 1995b. Degradation of monochlorinated and nonchlorinated aromatic compounds under iron-reducing conditions. *Appl. Environ. Microbiol.* 61:4069-4073.
- Klausen, I., S. P. Tröber, S. B. Haderlein, and R. P. Schwarzenbach. 1995. Reduction of substituted nitrobenzenes by Fe(II) in aqueous mineral suspensions. *Environ. Sci. Technol.* 29:2396-2404.
- Komlos, J., and P. R. Jaff . 2004. Effect of iron bioavailability on dissolved hydrogen concentrations during microbial iron reduction. *Biodegradation* 15:315-325.
- Kriegman-King, M. R., and M. Reinhard. 1992. Transformation of carbon tetrachloride in the presence of sulfide, biotite, and vermiculite. *Environ. Sci. Technol.* 26:2198-2206.
- Kriegman-King, M. R., and M. Reinhard. 1994. Transformation of carbon tetrachloride by pyrite in aqueous solution. *Environ. Sci. Technol.* 28:692-700.
- Kuhn, E. P., and Suflita, J. M. 1989. Sequential reductive dehalogenation of chloroanilines by microorganisms from a methanogenic aquifer. *Environ. Sci. Technol.* 23:848-852.
- Lièvremon, D., SeigleMurandi, F., BenoitGuyod, J. L., and Steiman, R. 1996a. Biotransformation and biosorption of pentachloronitrobenzene by fungal mycelia. *Mycol. Res.* 100:948-954.
- Lièvremon, D., SeigleMurandi, F., and BenoitGuyod, J. L. 1996b. Effects of culture parameters on pentachloronitrobenzene removal by *Sporothrix cyanescens*. *Chemosphere* 32:361-375.

- Lopes, T. J., and Furlong, E. T. 2001. Occurrence and potential adverse effects of semivolatile organic compounds in streambed sediment, United States, 1992-1995. *Environ. Toxicol. Chem.* 20:727-737.
- Lovley, D. R. 1991. Dissimilatory Fe(III) and Mn(IV) reduction. *Microbiol. Rev.* 55:259-287.
- Lovley, D. R. and E. J. P. Phillips. 1986a. Organic matter mineralization with reduction of ferric iron in anaerobic sediments. *Appl. Environ. Microbiol.* 51:683-689.
- Lovley, D. R. and E. J. P. Phillips. 1986b. Availability of ferric iron for microbial reduction in bottom sediments of the freshwater tidal Potomac River. *Appl. Environ. Microbiol.* 52:751-757.
- Lovley, D. R., and E. J. P. Phillips. 1988. Novel mode of microbial energy metabolism: Organic carbon oxidation coupled to dissimilatory reduction of iron or manganese. *Appl. Environ. Microbiol.* 54:1472-1480.
- Lovley, D.R. and J.C. Woodward. 1996. Mechanisms of chelator stimulation of microbial Fe(III)-oxide reduction. *Chem. Geol.* 132:19-24.
- Lovley, D.R., J.D. Coates, E.L. Blunt-Harris, E.J.P. Phillips and J. C. Woodward. 1996. Humic substances as electron acceptors for microbial respiration. *Nature* 382:445-448.
- Lovley, D.R., J.L. Fraga, E.L. Blunt-Harris, L.A. Hayes, E.J.P. Phillips, and J.D. Coates. 1998. Humic substances as a mediator for microbially catalyzed metal reduction. *Acta Hydroch. Hydrob.* 26:152-157.
- Lovley, D.R. and E.L. Blunt-Harris. 1999. Role of humic-bound iron as an electron transfer agent in dissimilatory Fe(III) reduction. *Appl. Environ. Microbiol.* 65:4252-4254.
- Mah, A. R., and M. R. Smith. 1981. The methanogenic bacteria. In: *Prokaryotes: A Handbook of Habitats, Isolation and Identification of Bacteria*, Starr, M. P., Ed., Springer-Verlag: New York, NY; pp. 948-977.
- Matheson, L. J., and P. G. Tratnyek. 1994. Reductive dehalogenation of chlorinated methanes by iron metal. *Environ. Sci. Technol.* 28:2045-2053.
- McCarty, P.L. 1964. Anaerobic waste treatment fundamentals, part III: Toxic materials and their control. *Public Works* 95:91-94.
- Middeldorp, P.J.M., Luijten, M.L.G.C., van de Pas, B.A., van Eekert, M.H.A., Kengen, S.W.M., Schraa, G., and Stams, A.J.M. 1999. Anaerobic microbial reductive dehalogenation of chlorinated ethenes. *Bioremediation J.* 3:151-169.
- Mora Torres, R. M., Grosset, C., Steiman, R., and Alary, J. 1996. Liquid chromatography study of degradation and metabolism of pentachloronitrobenzene by four soil micromycetes. *Chemosphere*, 33:683-692.
- National Agricultural Statistics Service (NASS). 2003. NASS Database. U.S. Department of Agriculture, Washington, D.C. (http://www.pestmanagement.info/nass/act_dsp_statcs2_state.cfm).
- Park, H. S., Lim, S. J., Chang, Y. K., Livingston, A. G., and Kim, H. S. 1999. Degradation of chloronitrobenzenes by a coculture of *Pseudomonas putida* and a *Rhodococcus* sp. *Appl. Environ. Microbiol.* 65:1083-1091.
- Patel, G.B. and L.A. Roth. 1977. Effect of sodium chloride on growth and methane production of methanogens. *Can. J. Microbiol.* 23:893-7.
- Pavlostathis, S. G., and M. Prytula. 2000. Kinetics of the sequential microbial reductive dechlorination of hexachlorobenzene. *Environ. Sci. Technol.* 34:4001-4009.
- Pavlostathis, S. G., Prytula, M. T., and Yeh, D. H. 2003. Potential and limitations of microbial reductive dechlorination for bioremediation applications. *Water, Air, & Soil Pollution: Focus* 3(3):117-129.

- Picardal, F.W., R.G. Arnold, H. Couch, A.M. Little, and M.E. Smith. 1993. Involvement of cytochromes in the anaerobic biotransformation of tetrachloromethane by *Shewanella putrefaciens* 200. *Appl. Environ. Microbiol.* 59:3763-3770.
- Prytula, M. T., and Pavlostathis, S. G. 1996. Effect of contaminant and organic matter bioavailability on the microbial dehalogenation of sediment-bound chlorobenzenes. *Wat. Res.* 30:2669-2680.
- Roden, E.E. and J.M. Zachara. 1996. Microbial reduction of crystalline iron(III) oxides: Influence of oxide surface area and potential for cell growth. *Environ. Sci. Technol.* 30:1618-1628.
- Scott, D.T., D.M. McKnight, E.L. Blunt-Harris, S.E. Kolesar, and D.R. Lovley. 1998. Quinone moieties act as electron acceptors in the reduction of humic substances by humics-reducing microorganisms. *Environ. Sci. Technol.* 32:2984-2989.
- Seiglemurandi, F., Steiman, R., Benoitguyod, J. L., Muntalif, B., and Sage, L. 1992. Relationship between the biodegradative capability of soil micromycetes for pentachlorophenol and for pentachloronitrobenzene. *Sci. Total Environ.* 123:291-298.
- Steiman, R., Benoitguyod, J. L., Seiglemurandi, F., and Muntalif, B. 1992. Degradation of pentachloronitrobenzene by micromycetes isolated from soil. *Sci. Total Environ.* 123:299-308.
- Straub K.L., M. Benz and B. Schink. 2001. Iron metabolism in anoxic environments at near neutral pH. *FEMS Microbiol. Ecol.* 34:181-186.
- Susarla, S., Masunaga, S., and Yonezawa, Y. 1996. Transformations of chloronitrobenzenes in anaerobic sediment. *Chemosphere* 32:967-977.
- Susarla, S., Yonezawa, Y., and Masunaga, S. 1997. Reductive dehalogenation of chloroanilines in anaerobic estuarine sediment. *Environ. Technol.* 18:75-83.
- Tamura, K., Hasegawa, Y., Kudo, T., and Yamaguchi, I. 1995. Isolation and characterization of PCNB degrading bacterium, *Pseudomonas aeruginosa* strain-I-41. *J. Pestic. Sci.* 20:145-151.
- Travkin, V., B. P. Baskunov, E. L. Golovlev, M. G. Boersma, S. Boeren, J. Vervoort, W. J. H. van Berkel, I. M. C. M. Rietjens, and L. A. Golovleva. 2002. Reductive deamination as a new step in the anaerobic microbial degradation of halogenated anilines. *FEMS Microbiol. Lett.* 209:307-312.
- U.S. Department of Agriculture (USDA). 2002. *Agricultural Chemical Usage – 2000 Nursery and Floriculture Summary*. National Agricultural Statistics Service, Washington, D.C.
- U.S. Department of Agriculture (USDA). 2003. *Agricultural Chemical Usage – 2002 Vegetables Summary*. National Agricultural Statistics Service, Washington, D.C.
- U.S. Environmental Protection Agency (U.S. EPA). 2003. Waste Minimization Priority Chemicals & Chemical Fact Sheets. Office of Solid Waste and Emergency Response, Washington, D.C. (<http://www.epa.gov/epaoswer/hazwaste/minimize/chemlist.htm>).
- van Bodegom, P.M., J.C.M. Scholten and A.J.M. Stams. 2004. Direct inhibition of methanogenesis by ferric iron. *FEMS Microbiol. Ecol.* 49:261-268.
- Wolin, E. A., Wolin, M. J., Wolfe, R. S. 1963. Formation of methane by bacterial extracts. *J. Biol. Chem.* 238:2882-2886.
- Yeh D.H., and S.G. Pavlostathis. 2001. Development of hexachlorobenzene-dechlorinating mixed cultures using Polysorbate surfactants as a carbon source. *Wat. Sci. Technol.* 43(2):43-50.

INFORM: Integrated Forecast and Reservoir Management System for Northern California

Basic Information

Title:	INFORM: Integrated Forecast and Reservoir Management System for Northern California
Project Number:	2004GA100B
Start Date:	7/1/2002
End Date:	6/30/2005
Funding Source:	Other
Congressional District:	5
Research Category:	Climate and Hydrologic Processes
Focus Category:	Hydrology, Management and Planning, Surface Water
Descriptors:	Integrated Forecast-Decision Systems for River Basin Management
Principal Investigators:	Aris P. Georgakakos, Konstantine P. Georgakakos

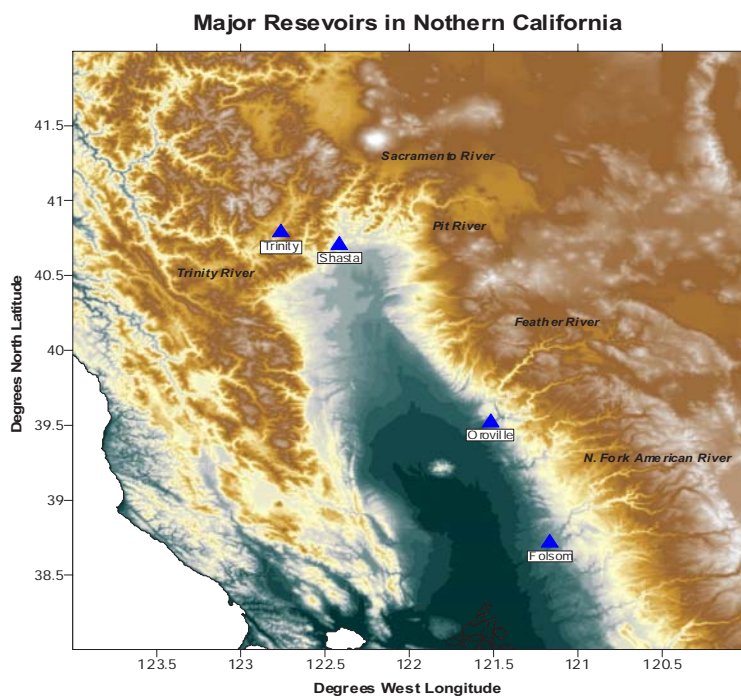
Publication

1. Georgakakos, K.P., Graham, N.H., Carpenter, T.M., Georgakakos, A.P., and H. Yao, Integrating Climate-Hydrology Forecasts and Multi-Objective Reservoir Management for Northern California. EOS, Transactions, American Geophysical Union, Vol. 86, No. 12, March 2005, pages 122-127.
2. Georgakakos, A.P., Decision Support Systems for integrated water resources management with an application to the Nile Basin Keynote Address, Proceedings, International Federation for Automatic Control Workshop on Modeling and Control for Participatory Planning and Managing Water Systems, Venice, Italy, Sep. 29 Oct. 1. Also, in a book entitled Decision Support Systems for Water Resources Management to be published by Elsevier, 2005.
3. Gibson, C.A., J.L. Meyer, N. L. Poff, L.E. Hay, and A. Georgakakos, "Flow Regime Alterations under Changing Climate in Two River Basins: Implications for Freshwater Ecosystems," River Research and Applications, 21: 1-16, 2005.

A DECISION SUPPORT SYSTEM FOR THE RESERVOIRS IN NORTHERN CALIFORNIA

Project INFORM

Interim Technical Report
2004-2005



Aris Georgakakos and Huaming Yao
Georgia Water Resources Institute
School of Civil and Environmental Engineering
Georgia Institute of Technology
Atlanta, Georgia 30332
(404) 894-2240

April 2005

A Decision Support System for the Reservoirs in Northern California

GWRI Progress Report –Year 3 1/2005-04/2005 NOAA Funding Period

The Georgia Water Resources Institute contribution to the INFORM project is to develop and demonstrate the utility of Decision Support Systems (DSS) for reservoir management. The DSS consists of databases, interfaces, and various application programs interlinked to provide meaningful and comprehensive information to decision makers. During the current NOAA funding period, GWRI efforts focused on the following project tasks:

- Expanding the studied system of INFORM DSS to include the San Joaquin River, the Delta, and the Exports to Southern California;
- Developing simulation assessment tool for the expanded system;
- Model testing.

A brief description of the above-mentioned tasks is provided below.

1. The Expanded System

During the last workshop, the GWRI personnel and USBR staff had a discussion on how to better use the INFORM DSS in the operational and planning process in practice. The original INFORM DSS modeled only four major reservoirs in the system independently. The downstream requirements such as minimum flows, delta environmental constraints, water demands were not considered. However, those requirements are the most important factors in the reservoir operation and planning process in practice. Based on the discussion, to make the DSS more useful and realistic, the GWRI team decided to expand the original project system to incorporate all the components downstream of the reservoirs. Specifically, the expanded system includes five major reservoirs (Clair Engle Lake, Shasta, Oroville, Folsom, and New Melones), 10 hydro power plants, the delta of the Sacramento River and the San Joaquin River, and the exports to the southern California (Figure 1). The objectives of the system are water supply, energy generation, minimum river flows, and delta environmental requirements.

2. The Simulation Model

The simulation model is a part of the INFORM comprehensive decision support system. The main goal of the simulation model is to conduct quick assessments under various conditions such as demand changes, hydrological condition changes, and etc. Many system data, constraints, and operation rules used in the simulation model are adopted directly from the existing planning simulation model, a spreadsheet based model provided by the USBR staff. For convenience, the entire system is divided into 6 sub-

systems based on their geological locations and functionalities. The model formulation and assumptions of each sub system are described in Appendix A.

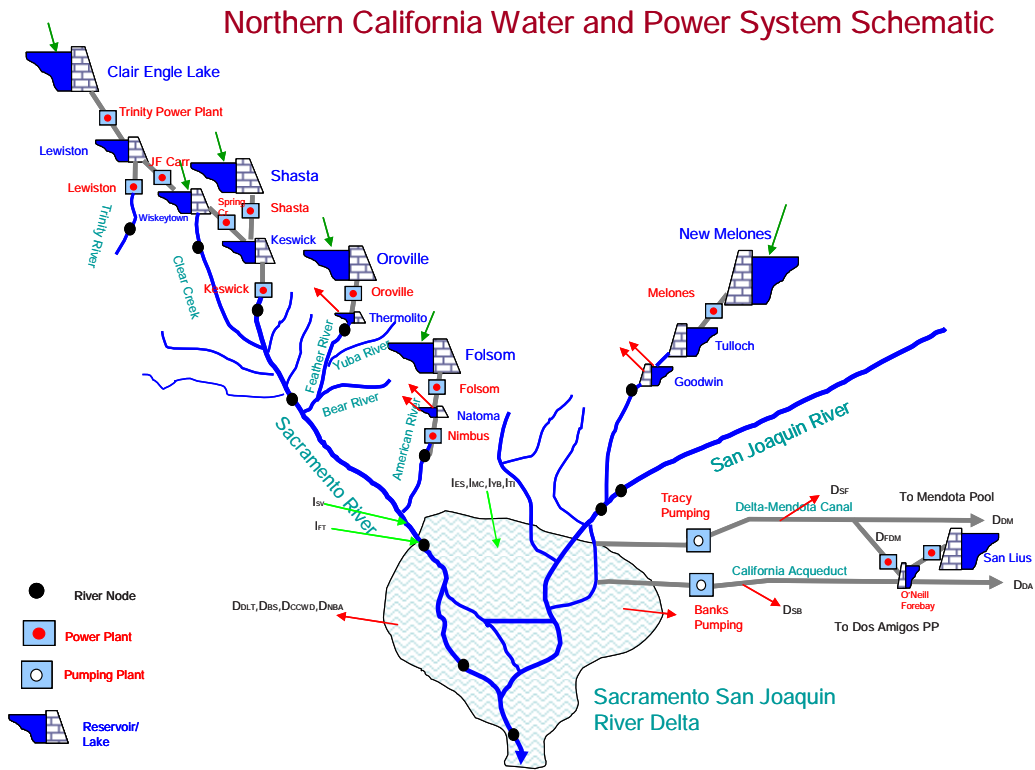


Figure 1: System Schematic

3. Assessment Process Using the Simulation Model

The assessment is done by running the simulation model for a selected historical inflow sequence under various operational conditions. The available historical inflows are from 1968 to 1996 for the four major reservoirs Clair Engle Lake, Shasta, Oroville, and Folsom. Inflows from other tributaries are not available at this moment. The monthly average sequences are used in the sample study. The DSS interface provides easy tools to add new inflow data into the system once they become available. Other operational constraints such as demands, pumping, and minimum and target river requirement, and reservoir target storages are all user definable through the interface.

The simulation starts with the inflow forecasts for all locations. Presently, an imbedded Historical Analog inflow forecasting model is used. The more comprehensive distributed hydrological model will be integrated as it becomes available. At beginning of each month, the forecast model is launched and produces monthly inflow sequences up to one year for all locations. The forecasted inflows, along with the observed inflows up to the current month from the current water year, are used to compute the river index. Based on

the value of river index, the demands and the minimum flow requirements are adjusted according to the user specified rules. Users can also specify the frequency of the demand adjustment, i.e., at which months the demands and the minimum flows are adjusted. The adjusted demands and minimum flows are then used as the planned targets in the simulation.

Assuming that no extra release is required to meet the delta demands and pumping, the reservoir releases are determined simply to meet their local requirements such as target storage and the minimum flows. If the reservoir releases, along with the contributions of delta local streams, can meet the delta requirements, then, the initial assumption is valid and no extra release is required from the reservoirs, the system evolves to the next month using the actual historical inflows of the current month; otherwise, extra release is required and is distributed among the reservoirs according to user specified rules, simulate the system again with the extra release added to the original releases. This process is repeated for every month until the end of the selected historical period. For each month, the simulation model records reservoir storage, demand, deficit, energy generation, and all other quantities of the user's interests. The recorded sequences are used for statistical analysis.

The assessment model generates voluminous results after each run. Selected results from a sample run are presented in Appendix B. The model inputs are described in Appendix C.

4. Outstanding Issues

The assessment model presented here is based on a spreadsheet simulation model provided by the USBR staff. Unfortunately, the spreadsheet model was not fully functional due to conversion problems and did not include full data record required for conducting the long term assessment. With the help of USBR and DWR staff, we were able to get some data from the internet and establish necessary assumptions for making the assessment model workable for demonstration purpose. However, there are still many outstanding issues we would like to address in the upcoming workshop:

- The agreement on the expanded system;
- Functionality and input/output for the DSS models;
- Details of reservoir contributions to meet the delta and export requirements;
- Rules and policies for reduction of demands and minimum flows at various locations;
- Historical unimpaired inflow data at various locations;
- Inflow forecasting models at various locations;
- Information on the power facilities.

References

Yao, H, and A. Georgakakos, 2001. "Assessment of Folsom Lake Response to Historical

- and Potential Future Climate Scenarios," **Journal of Hydrology**, 249, 176-196.
- Georgakakos, A., and H. Yao, 2002, "Implications of Climate Variability and Change for Water Resources Management," **The Climate Report**, 3(4), 9-13.
- Georgakakos, A. P., and H. Yao, "Evaluation of Water Use Scenarios for the Nile Basin," World Bank, ICCON Series Monographs, October 1999, 116p.
- Georgakakos, A. P., "Water Resources Planning and Management for the Lake Victoria Basin," Monograph, FAO Monograph Series, August 2000, 44p.
- Georgakakos, A. P., H. Yao, and Y. Yu, "A Control Model for Hydroelectric Energy Value Optimization," **ASCE J. for Wat. Res. Plan. and Mgt**, 123(1), 30-38, 1997.
- Georgakakos, A. P., H. Yao, and Y. Yu, "Control Models for Hydroelectric Energy Optimization," **Water Resources Research**, 33(10), 2367-2379, 1997.
- Georgakakos, A. P., Yao, H., and Y. Yu, "A Control Model for Dependable Hydropower Capacity Optimization," **Water Resources Research**, 33(10), 2349-2365, 1997.
- Georgakakos, A. P., C. Barrett, and B. Attia, "A Decision Support System for the High Aswan Dam," Proceedings of the Fifth International Workshop on Water Resources Operations Management, sponsored by ASCE, Georgakakos, A.P., and Q.W. Martin Eds., pg. 34-66, Arlington, VA, March 4-6, 1996.
- Georgakakos, A. P., "Operational Tradeoffs in Reservoir Control," **Water Resources Research**, 29(11), 3801-3819, 1993.
- Yao, H., and A. P. Georgakakos, "New Control Concepts for Uncertain Water Resources Systems: 2, Reservoir Management," **Water Resources Research**, 29(6), 1517-1526, 1993.
- Georgakakos, A. P. and H. Yao, "New Control Concepts for Uncertain Water Resources Systems: 1, Theory," **Water Resources Research**, 29(6), 1505-1516, 1993.
- Hooper, E. R., A. P. Georgakakos, and D. P. Lettenmaier, "Optimal Stochastic Operation of the Salt River Project, Arizona," **ASCE Journal of the Water Resources Planning and Management**, Vol. 117, No. 5, pg. 566-587, 1991.
- Georgakakos, A. P., "Computer-Aided Management of the Southeastern U.S. Reservoir System," in "Decision Support Systems," D. P. Loucks, ed., NATO ASI Series, Vol. G 26, pg. 407-428, 1991.
- Georgakakos, A. P., "Extended Linear Quadratic Gaussian Control for the Real-Time Operation of Reservoir Systems," pg. 329—360 in the book entitled "Dynamic Programming for Optimal Water Resources Systems Analysis," A. Esogbue, ed., Prentice Hall Publishing Company, New Jersey, 1989.
- Georgakakos, A. P., "Extended Linear Quadratic Gaussian (ELQG) Control: Further Extensions", **Water Resources Research**, Vol. 25, No. 2, pg. 191 - 201, 1989.
- Georgakakos, A. P., "The Value of Streamflow Forecasting in Reservoir Control", **Water Resources Bulletin**, Vol. 25 No. 4, pg. 789—800, 1989.

Appendix A: Simulation Model Formulation

A.1. Trinity River System

The Trinity River System includes Clair Engle Lake, Trinity Power Plant, Lewiston Lake, Lewiston Plant, JF Carr Plant, Whiskeytown, Clear Creek, and Spring Creek Plant.

The Clair Engle Lake is operated to meet the minimum and the target flow in the Trinity River, and the monthly target storage for Whiskeytown reservoir.

The system dynamics of Clair Engle Lake and Whiskeytown are described by the following water balance equations:

Whiskeytown:

$$S_{WH}(k+1) = S_{WH}(k) + I_{WH}(k) - EVP_{WH}(S_{WH}(k), k) + R_{JF}(k) - R_{CC}(k) - R_{SC}(k)$$

Clair Engle Lake (Trinity):

$$S_{CL}(k+1) = S_{CL}(k) + I_{CL}(k) - EVP_{CL}(S_{CL}(k), k) - R_{CL}(k)$$

$$R_{CL}(k) = R_{LE}(k) + R_{JF}(k)$$

where:

k is the time step in month;

S_{WH} , I_{WH} , EVP_{WH} are the storage, inflow, evaporation loss for Whiskeytown, respectively;

R_{CC} is the minimum river flow requirement for Clear Creek;

R_{SC} is the target flow for Spring Creek plant;

R_{JF} is the flow through JF Carr plant;

R_{LE} is the minimum river flow requirement for Trinity River;

S_{CL} , I_{CL} , EVP_{CL} , R_{CL} are the storage, inflow, evaporation loss, and release for Clair Engle Lake, respectively.

A.2. Shasta Lake System

The Shasta Lake System includes Shasta Lake, Shasta Power Plant, Keswick Lake, Keswick Plant, and the river reach from Keswick to Wilkins.

The Shasta Lake is operated to meet the minimum and the target flow at Wilkins on the Sacramento River and share (if specified) the water supply in the Delta.

The system dynamics of Shasta Lake and flow at Wilkins are described by the following equations:

Shasta Lake:

$$S_{SH}(k+1) = S_{SH}(k) + I_{SH}(k) - EVP_{SH}(S_{SH}(k), k) - R_{SH}(k)$$

$$R_{SH}(k) = R_{KE}(k) - R_{SC}(k) + Q_{DlSH}$$

$$R_{KE}(k) = \max[R_{KE}^{Min}(k), Q_{Wilk}^{min}(k) - R_{CC}(k) - I_{Wilk}(k)]$$

Flow at Wilkins:

$$Q_{Wilk}(k) = R_{CC}(k) + R_{KE}(k) + I_{Wilk}(k)$$

S_{SH} , I_{SH} , EVP_{SH} , R_{SH} are the storage, inflow, evaporation loss, release for Shasta Lake, respectively;

R_{KE} is the release of Keswick reservoir;

R_{KE}^{min} is the minimum Keswick release requirement;

Q_{Wilk}^{min} is the minimum river flow requirement for at Wilkins;

I_{Wilk} is the local inflow between Keswick and Wilkins.

Q_{DlSH} is the share of Shasta for the Delta demand.

A.3. Feather River System

The Feather River System includes Oroville Lake, Oroville plants, Thermolito diversion pond, Yuba River, and Bear River. The inflows from Yuba and Bear are not modeled separately in the simulation model. The flow contributions to the Delta from both rivers are lumped into an aggregated quantity called Sacramento Accretion.

The Oroville Lake is operated to meet the demands from Thermolito, the minimum and target flow requirement on the Feather River, and share (if specified) the water demands in the Delta.

The system dynamics of Oroville Lake and flow downstream of Thermolito on the Feather River are described by the following equations:

Oroville Lake:

$$S_{OR}(k+1) = S_{OR}(k) + I_{OR}(k) - EVP_{OR}(S_{FO}(k), k) - R_{OR}(k)$$

$$R_{OR}(k) = D_{TH}(k) + \max(Q_{TH}^{Min}(k), Q_{TH}^{TGT}(k)) + Q_{DlOR}$$

Flow at Thermolito:

$$Q_{TH}(k) = R_{OR}(k) - D_{TH}(k)$$

where

S_{OR} , I_{OR} , EVP_{OR} , R_{OR} are the storage, inflow, evaporation loss, and release for Oroville Lake, respectively;

D_{TH} is the demand from Thermolito;

Q_{TH}^{min} and Q_{TH}^{TGTn} are the minimum and target flow requirement downstream of Thermolito.

Q_{DIOR} is the share of Oroville for the Delta demand.

A.4. American River System

The American River System includes Folsom Lake, Folsom Plant, Natoma Lake, Nimbus Plant, Natoma Plant, and Natoma diversions.

The Folsom Lake is operated to meet the demands from Natoma reservoir and the minimum and the target flow requirements on the American River, and share (if specified) the water demands in the Delta.

The system dynamics of Folsom Lake and the flow downstream of Nimbus are described by the following equations:

Folsom Lake:

$$S_{FO}(k+1) = S_{FO}(k) + I_{FO}(k) - EVP_{FO}(S_{FO}(k), k) - R_{FO}(k)$$

$$R_{FO}(k) = \max(Q_{NI}^{Min}(k), Q_{NI}^{TGT}(k)) + DPM_{FO}(k) + D_{FS}(k) + Q_{DIFO}$$

where

S_{FO} , I_{FO} , EVP_{FO} , R_{FO} are the storage, inflow, evaporation loss, release for the Folsom Lake, respectively;

DPM_{FO} is the demand from Folsom pumping;

D_{FS} is the demand from Folsom South Canal;

Q_{NI}^{min} and Q_{NI}^{TGT} are the minimum and target flows downstream of Nimbus.

Q_{DIFO} is the share of Folsom Lake for the Delta demand.

A.5. San Joaquin System

The San Joaquin System includes New Melones Lake, New Melones Power Plant, Tulloch Lake, Demands from Goodwin, and the inflows from the main San Joaquin River.

The New Melones is operated to meet the demands at Goodwin and the minimum and the target flow requirement downstream.

The system dynamics of New Melones Lake, Tulloch Lake, and the river flow at Vernalis are described by the following equations:

New Melones:

$$S_{NM}(k+1) = S_{NM}(k) + I_{NM}(k) - EVP_{NM}(S_{NM}(k), k) - R_{NM}(k)$$

Tulloch:

$$S_{TU}(k+1) = S_{TU}(k) + R_{NM}(k) - R_{TU}(k)$$

$$R_{TU}(k) = D_{CUP}(k) + D_{OID/SSJD}(k) + \max(Q_{GO}^{Min}(k), Q_{GO}^{TGT}(k))$$

$$R_{NM}(k) = R_{TU}(k) + (S_{TU}^{TGT}(k+1) - S_{TU}(k))$$

Flow at Vernalis:

$$Q_{VE}(k) = \max(Q_{GO}^{Min}(k), Q_{GO}^{TGT}(k)) + I_{SJR}(k)$$

where

S_{NM} , I_{NM} , EVP_{NM} , R_{NM} are the storage, inflow, evaporation loss, release for the New Melones Lake, respectively;

S_{TU} , R_{TU} are the storage and release for Tulloch, respectively;

D_{CUP} and $D_{OID/SSJD}$ are the demands at Goodwin;

S_{TU}^{TGT} is the target storage for Tulloch Lake;

Q_{GO}^{min} and Q_{GO}^{TGT} are the minimum and target flows downstream of Goodwin;

Q_{VE} is the river flow at Vernalis;

I_{SJR} is the inflow from San Joaquin above Stanilaus junction.

A.6. Delta

The Delta receives inflows from Sacramento, San Joaquin, and several local streams. In addition to the consumptive use inside the Delta and the environmental constraints, the Delta provides storage for exporting water to the south part of California through pumping. Under normal hydrological conditions, the inflows from the Sacramento River, San Joaquin River, and the local stream flows can meet the needs of Delta demands and the water export. However, during dry water years, extra water has to be released from the upper major reservoirs to meet the demands. The required extra water is shared by the large reservoirs in the Sacramento River basin (Clair Engle

Lake, Shasta, Oroville, and Folsom). The shared percentage and operation rules in the simulation are user defined.

A.6.1. Delta Inflows

The local inflows to the Delta include:

- Sacramento Valley Accetion: $I_{SV}(k)$
- Freeport Treatment Plant: $I_{FT}(k)$
- Eastside Stream: $I_{ES}(k)$
- Miscellaneous Creeks Inflow: $I_{MC}(k)$
- Yolo bypass: $I_{YB}(k)$
- Transfer Inflow: $I_{TI}(l)$

Freeport Flow:

$$Q_{FP}(k) = Q_{CC}(k) + Q_{KE}(k) + Q_{NI}(k) + Q_{TH}(k) + I_{SV}(k) + I_{FT}(k)$$

Total Delta Inflow:

$$I_{DE}(k) = Q_{FP}(k) + Q_{VE}(k) + I_{ES}(k) + I_{YB}(k) + I_{TI}(k)$$

A.6.2. Delta Export

The Delta water exports are implemented by the federal agency (USBR) and the State Water Department. The federal export includes:

- CCWD Diversion: D_{CCWD}
- Barker Slough: D_{BS}
- Fed Tracy Pumping: D_{FTPP}
- Fed Banks on-peak D_{FBON}
- Fed Banks off-peak: D_{FBOFF}
- Fed Banks Pumping total: D_{FPPTOT}
- Fed Banks PP CVC: $D_{FBPPCVC}$
- Fed Banks PP Joint: $D_{FBPPJNT}$
- FED Banks PP Transfer: D_{FBPPTR}

The total federal pumped water is:

$$D_{FPPTOT}(k) = D_{FTPP}(k) + D_{DFBON}(k) + D_{DFBOFF}(k) + D_{FBPP}(k) + D_{FBPPCVC}(k) + D_{FBPPJNT}(k) + D_{FBPPTR}(k)$$

The total federal planned export is:

$$D_{FEXTOT}(k) = D_{FPPTOT}(k) + D_{CCWD}(k)$$

The state export includes:

- NBA Diversion: D_{NBA}
- State Banks PP: D_{SBPP}
- State Tracy PP: D_{STPP}

The total state planned export is:

$$D_{SEXTOT}(\mathbf{k}) = D_{NBA}(\mathbf{k}) + D_{SBPP}(\mathbf{k}) + D_{STPP}(\mathbf{k})$$

The total planned export from both federal and state is:

$$D_{EXTOT}(\mathbf{k}) = D_{SEXTOT}(\mathbf{k}) + D_{FEXTOT}(\mathbf{k}) + D_{BS}(\mathbf{k})$$

A.6.3. Delta COA

The Delta COA includes the following definitions:

- Required Delta Outflow: Q_{Dlt}^{\min}
- Delta Consumptive Use: D_{dlt}
- Combined required reservoir release: QRES

$$QRES(\mathbf{k}) = \max(0, D_{Dlt}(\mathbf{k}) + D_{EXTOT}(\mathbf{k}) + Q_{Dlt}^{\min}(\mathbf{k}) - I_{SV}(\mathbf{k}) - Q_{VE}(\mathbf{k}) - I_{FT}(\mathbf{k}) - I_{ES}(\mathbf{k}) - I_{MC}(\mathbf{k}) - I_{YB}(\mathbf{k}))$$

- Total Federal Storage Withdrawal: DS_{FTOT}

$$DS_{FTOT}(\mathbf{k}) = (R_{CC}(\mathbf{k}) - I_{WH}(\mathbf{k})) + (R_{KE}(\mathbf{k}) - I_{SH}(\mathbf{k})) + (R_{FO}(\mathbf{k}) - I_{FO}(\mathbf{k}))$$

- Total State Storage Withdrawal: DS_{STOT}

$$DS_{STOT}(\mathbf{k}) = (R_{OR}(\mathbf{k}) - I_{OR}(\mathbf{k}))$$

- Computed Delta Outflow: Q_{Dlt}

$$Q_{Dlt}(\mathbf{k}) = Q_{FP}(\mathbf{k}) + I_{YB}(\mathbf{k}) + Q_{VE}(\mathbf{k}) + D_{Dlt}(\mathbf{k}) - D_{EXTOT}(\mathbf{k}) + I_{ES}(\mathbf{k}) + I_{MC}(\mathbf{k}) + I_{YB}(\mathbf{k})$$

- Estimated Excess Outflow: Q_{ESTOT}

$$Q_{ESTOT}(\mathbf{k}) = (Q_{Dlt}(\mathbf{k}) - Q_{Dlt}^{\min}(\mathbf{k}))$$

- Un-stored Flow for Export: Q_{UFE}

$$Q_{UFE}(\mathbf{k}) = \begin{cases} D_{EXTOT}(\mathbf{k}) + Q_{ESTOT}(\mathbf{k}) - (DS_{FTOT}(\mathbf{k}) + DS_{STOT}(\mathbf{k})), & \text{if } DS_{FTOT}(\mathbf{k}) + DS_{STOT}(\mathbf{k}) < D_{EXTOT}(\mathbf{k}) \\ 0, & \text{otherwise} \end{cases}$$

- Estimated in-basin use of storage withdrawal: $Q_{inbasin}$

$$Q_{INBSN}(\mathbf{k}) = \max(0, DS_{FTOT}(\mathbf{k}) + DS_{STOT}(\mathbf{k}) - D_{EXTOT}(\mathbf{k}))$$

- USBR Allowable Export: D_{FEXTOT}

$$D_{FEXTOT}^{max}(\mathbf{k}) = \begin{cases} D_{FEXTOT}(\mathbf{k}), & \text{if } Q_{Dlt}(\mathbf{k}) > Q_{Dlt}^{min}(\mathbf{k}), \\ 0.55Q_{UFE}(\mathbf{k}) + DS_{FTOT}(\mathbf{k}), & \text{if } Q_{UFE}(\mathbf{k}) > 0 \\ DS_{FTOT}(\mathbf{k}) - 0.75Q_{INBSN}(\mathbf{k}) \end{cases}$$

- USBR Monthly COA Account: Q_{FCOA}

$$Q_{FCOA}(\mathbf{k}) = \begin{cases} 0, & \text{if } Q_{Dlt}(\mathbf{k}) > Q_{Dlt}^{min}(\mathbf{k}), \\ D_{FEXTOT}^{max} - D_{FEXTOT}(\mathbf{k}), & \text{otherwise} \end{cases}$$

- Accumulated COA(k) S_{SCOA}

$$S_{SCOA}(\mathbf{k} + 1) = S_{SCOA}(\mathbf{k}) + Q_{FCOA}(\mathbf{k})$$

- Adjusted Delta Outflow: Q_{Dlta}

$$Q_{Dlta}(\mathbf{k}) = Q_{FP}(\mathbf{k}) + I_{YB}(\mathbf{k}) + Q_{VE}(\mathbf{k}) + D_{Dlt}(\mathbf{k}) - D_{FEXTOT}^{max}(\mathbf{k}) + I_{ES}(\mathbf{k}) + I_{MC}(\mathbf{k}) + I_{YB}(\mathbf{k})$$

- Adjusted Excess Outflow: Q_{ESTOTA}

$$Q_{ESTOTA}(\mathbf{k}) = (Q_{Dlta}(\mathbf{k}) - Q_{Dlt}^{min}(\mathbf{k}))$$

- Rio Vista Flow: Q_{RV}

$$Q_{RV}(\mathbf{k}) = \begin{cases} 0.87Q_{FP}(\mathbf{k}) - 0.333 * 2632 - 1000, & \text{if } XChannelGate = 1, \\ 0.7Q_{FP}(\mathbf{k}) - 0.333 * 2632 - 2050, & \text{if } XChannelGate = 0, \\ 0.5(0.87Q_{FP}(\mathbf{k}) - 0.333 * 2632 - 1000 + 0.7Q_{FP}(\mathbf{k}) - 0.333 * 2632 - 2050), & \text{otherwise} \end{cases}$$

A.6.4. Delta Environment

- X Channel Gates: XG_{opt}

- Cross Delta Flow: Q_{xdl}

$$Q_{XDLT}(\mathbf{k}) = \begin{cases} 0.133Q_{FP}(\mathbf{k}) + 829, & \text{if } XChannelGate = 1, \\ 0.293Q_{FP}(\mathbf{k}) + 2090, & \text{if } XChannelGate = 0, \\ 0.213Q_{FP}(\mathbf{k}) + 1460, & \text{otherwise} \end{cases}$$

- Antioch Flow: Q_{AN}

$$Q_{AN}(k) = 0.8(Q_{VE}(k) + 2/3D_{DLt}(k) - D_{EXTOT}(k) + Q_{XDIt}(k))$$

- QWEST:

$$Q_{WEST}(k) = Q_{AN}(k) / 0.8 + I_{ES}(k)$$

- Computed Delta/Inflow Ratio (%): $DI\%$

$$DI\%(k) = (Q_{EXTOT}(k) - CCWD) / I_{DE}(k)$$

- X2 Location (km from GG): $X2$

$$X2(k) = 122.2 + 0.3287X2(k-1) - 17.65\text{Log}(Q_{DIt}(k))$$

- Supplemental project water Q_{Sup}

$$Q_{Sup}(k) = DS_{FTOT}(k) + DS_{STOT}(k) - D_{EXTOT}(k)$$

A.6.5. South Delta Formulation:

- Delta Mendota Canal: D_{DM}
- Federal Dos Amigos: D_{FDA}
- Federal ONeil to Dos Amigos: D_{FODS}
- San Felip Demands: D_{SF}
- Cross Valley Demands: D_{CV}
- Federal S EX. In ON: D_{FEXO}
- Federal S EX in SL: D_{FEXSL}
- Federal San Lius P/G: Q_{FSL}

$$Q_{FSL}(k) = D_{DM}(k) + D_{FDA}(k) + D_{FODA}(k) + D_{FPPTOT}(k) - D_{FEXO}(k) - 0.47Evp_{ONeil}$$

- Federal Storage in San Lius: S_{SLF}

$$S_{SLF}(k+1) = S_{SLF}(k) + Q_{FSL}(k) - D_{SF}(k) - 0.47EVP_{ONeil}$$

- South Bay Demand: D_{SB}

➤ State Dos Amigos: D_{SDA}

➤ State San Lius P/G: Q_{SSL}

$$Q_{SSL}(\mathbf{k}) = D_{SEXTOT}(\mathbf{k}) - D_{SB}(\mathbf{k}) - D_{SDA}(\mathbf{k}) - .53Evp_{ONeil}$$

➤ State Storage in San Lius: S_{SLS}

$$S_{SLS}(\mathbf{k}) = S_{SLS}(\mathbf{k}) + D_{SSL}(\mathbf{k}) - 0.53Evp_{ONeil}$$

Appendix B: Simulation Results from the Assessment Model

In the sample run, the historical inflow sequences (Figure B.1) from 1970 to 1995 for Clair Engle Lake, Shasta, Oroville, and Folsom are used. The monthly average values of local inflows for all other tributaries are summarized in Table B.1. The monthly reservoir parameters and constraints (max, min, and target storage, evaporation rates) are listed Table B.2. The minimum river flow requirements are listed in table B.3. The monthly demands from all locations are listed in Table B.4.

The river indices of Sacramento and San Joaquin are computed according to the description posted on the DWR's website. The water year type is classified in to five categories: Critical, Below Normal, Normal, Above Norm, and Wet. The demands and the river flow requirements are adjusted according to the fraction vs. water year type class value relationship, specified by the user. The default relationship is included in Table B.5. It applies to all demand locations. If the water year type is above normal, or wet, then the demand fraction is 1, no reduction is needed. Otherwise, the reduction fraction is 0.6, 0.4, and 0.2 for normal, below normal, and critical, respectively. The program actually allows user to specify different relationships for different locations. In addition, the user can also specify the frequency of the demand adjustment. In the sample run, the demand adjustment is set twice a year, with one in February and one in October. Frequent demand adjustments will reduce the reservoir fluctuations, but also result in large water supply variations.

The selected simulation results are displayed in Figures B.2 to B.7. Figure B.2 shows the elevation sequences of four major reservoirs. All of them experience significant drawdown in year 1978, even with the adjusted demands. The inflow sequences (Figure B.3) indicate that years 1992 and 1993 are dry periods. However, the simulated reservoir elevations were high. The reason for this is that the demands and minimum flow requirements are adjusted accordingly based on the water year indices. The reservoir release sequences are shown in Figure B.4. Figures B.5 and B.6 show the river flow sequences at selected locations. The delta total inflows and outflows are shown in Figure B.7. Figure B.8 shows the comparison of the elevation sequences between the default case and the case with more frequent demand adjustment. The results show that more frequent adjustments can reduce the reservoir fluctuations. Finally, Figure B.9 shows the reservoir elevation sequences corresponding to a run with a fixed demand pattern, where the demands and the minimum flow requirement are independent of the water year types. In this case, the drought periods 1978, 1992, and 1993 were clearly reflected by the significant reservoir drawdown.

Table B.1: Monthly Inflows for Selected Locations (TAF)

Month	Whisktown	Keswick-Wilkens	Sacramento Misc	Eastside Streams	Delta Misc Creeks	New Melones	SJR
Jan	8.	-211.27	-100.	80.67	25.5	76.	133.
Feb	4.	-299.69	-220.	60.44	25.5	43.	31.
Mar	2.	-370.28	-330.	20.72	29.	34.	33.
Apr	1.	-267.47	-175.	21.89	19.	33.	28.
May	1.	-117.56	45.	28.71	11.1	31.	33.
Jun	2.	-125.	-15.	33.2	0.8	30.	71.
Jul	2.	-31.24	121.	30.74	0.9	30.	62.
Aug	4.	564.46	981.	21.52	1.2	30.	63.
Sep	8.	841.7	1465.	21.52	1.8	30.	78.
Oct	12.	1767.58	2482.	40.03	32.3	40.	94.
Nov	45.	1021.	1763.	67.33	17.4	70.	103.
Dec	16.	74.65	328.	146.34	15.4	110.	126.

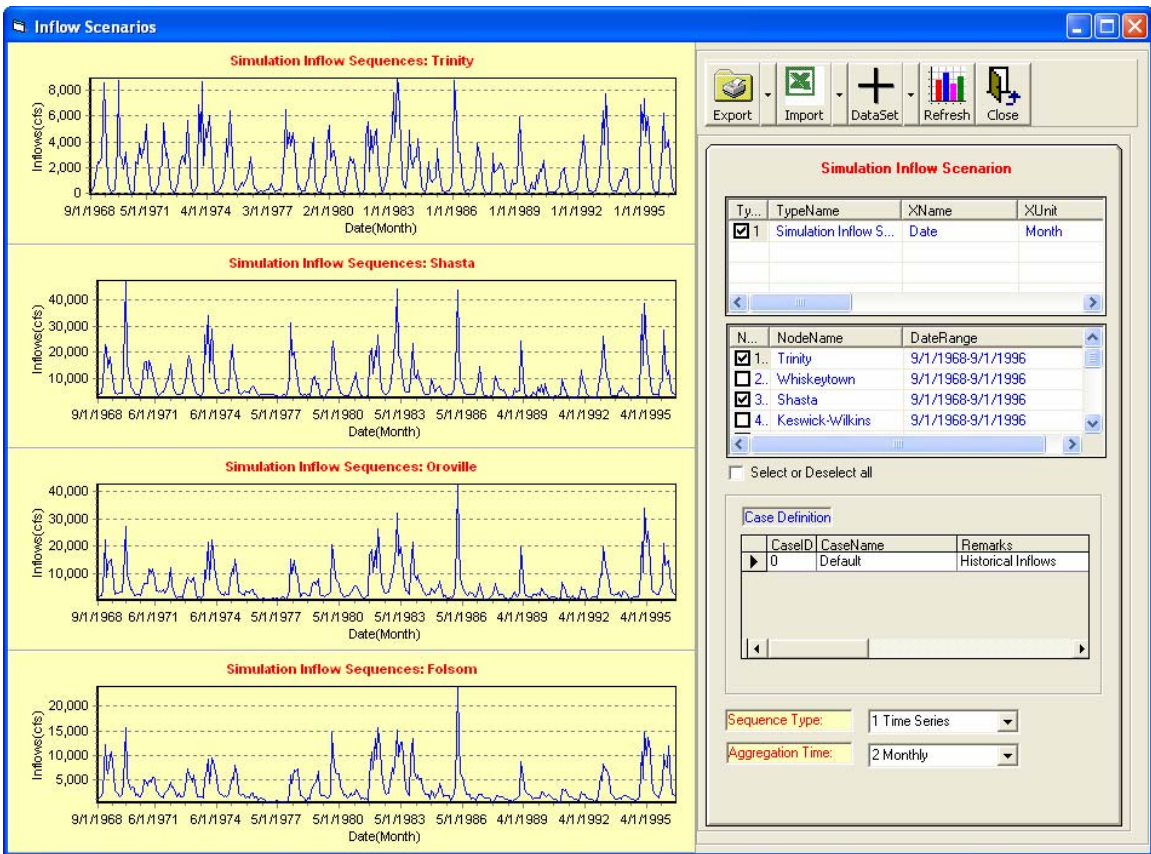


Figure B.1: Historical Monthly Inflow Sequences.

Table B.2: Reservoir Monthly Parameters

Name	Month	Smax (TAF)	Smin (TAF)	Starget (TAF)	Evap Rate (feet)
Clair Engle	Jan	2287.00	312.63	2287.00	0.17
Clair Engle	Feb	2287.00	312.63	2287.00	0.13
Clair Engle	Mar	2287.00	312.63	2287.00	0.20
Clair Engle	Apr	2287.00	312.63	2287.00	0.39
Clair Engle	May	2287.00	312.63	2287.00	0.51
Clair Engle	Jun	2287.00	312.63	2287.00	0.58
Clair Engle	Jul	2287.00	312.63	2287.00	0.76
Clair Engle	Aug	2287.00	312.63	2287.00	0.71
Clair Engle	Sep	2287.00	312.63	2287.00	0.60
Clair Engle	Oct	2287.00	312.63	2287.00	0.30
Clair Engle	Nov	2287.00	312.63	2287.00	0.15
Clair Engle	Dec	2287.00	312.63	2287.00	0.09
WhiskeyTown	Jan	237.90	200.00	205.70	0.17
WhiskeyTown	Feb	237.90	200.00	205.70	0.13
WhiskeyTown	Mar	237.90	200.00	205.70	0.20
WhiskeyTown	Apr	237.90	200.00	237.90	0.39
WhiskeyTown	May	237.90	200.00	237.90	0.51
WhiskeyTown	Jun	237.90	200.00	237.90	0.58
WhiskeyTown	Jul	237.90	200.00	237.90	0.76
WhiskeyTown	Aug	237.90	200.00	237.90	0.71
WhiskeyTown	Sep	237.90	200.00	238.00	0.60
WhiskeyTown	Oct	237.90	200.00	230.00	0.30
WhiskeyTown	Nov	237.90	200.00	205.70	0.15
WhiskeyTown	Dec	237.90	200.00	205.70	0.09
Shasta	Jan	4552	1168	4552	0.17
Shasta	Feb	4552	1168	4552	0.13
Shasta	Mar	4552	1168	4552	0.20
Shasta	Apr	4552	1168	4552	0.39
Shasta	May	4552	1168	4552	0.51
Shasta	Jun	4552	1168	4552	0.58
Shasta	Jul	4552	1168	3882	0.76
Shasta	Aug	4552	1168	3252	0.71
Shasta	Sep	4552	1168	3252	0.60
Shasta	Oct	4552	1168	3872	0.30
Shasta	Nov	4552	1168	4252	0.15
Shasta	Dec	4552	1168	4552	0.09
Oroville	Jan	3538	855	3458	0.17
Oroville	Feb	3538	855	3538	0.13
Oroville	Mar	3538	855	3538	0.20
Oroville	Apr	3538	855	3538	0.39
Oroville	May	3538	855	3538	0.51
Oroville	Jun	3538	855	3343	0.58
Oroville	Jul	3538	855	3163	0.76
Oroville	Aug	3538	855	3163	0.71

Oroville	Sep	3538	855	3163	0.60
Oroville	Oct	3538	855	3163	0.30
Oroville	Nov	3538	855	3163	0.15
Oroville	Dec	3538	855	3163	0.09
Folsom	Jan	975	83	805	0.17
Folsom	Feb	975	83	975	0.13
Folsom	Mar	975	83	975	0.20
Folsom	Apr	975	83	975	0.39
Folsom	May	975	83	975	0.51
Folsom	Jun	975	83	975	0.58
Folsom	Jul	975	83	700	0.76
Folsom	Aug	975	83	575	0.71
Folsom	Sep	975	83	575	0.60
Folsom	Oct	975	83	575	0.30
Folsom	Nov	975	83	575	0.15
Folsom	Dec	975	83	675	0.09
New Melones	Jan	2420	273	2230	0.17
New Melones	Feb	2420	273	2420	0.13
New Melones	Mar	2420	273	2420	0.20
New Melones	Apr	2420	273	2420	0.39
New Melones	May	2420	273	2420	0.51
New Melones	Jun	2420	273	2270	0.58
New Melones	Jul	2420	273	1970	0.76
New Melones	Aug	2420	273	1970	0.71
New Melones	Sep	2420	273	1970	0.60
New Melones	Oct	2420	273	1970	0.30
New Melones	Nov	2420	273	1970	0.15
New Melones	Dec	2420	273	2040	0.09
Tulloch	Jan	67	57	57	0.00
Tulloch	Feb	67	57	57	0.00
Tulloch	Mar	67	57	58	0.00
Tulloch	Apr	67	57	60	0.00
Tulloch	May	67	57	67	0.00
Tulloch	Jun	67	57	67	0.00
Tulloch	Jul	67	57	67	0.00
Tulloch	Aug	67	57	67	0.00
Tulloch	Sep	67	57	62	0.00
Tulloch	Oct	67	57	57	0.00
Tulloch	Nov	67	57	57	0.00
Tulloch	Dec	67	57	57	0.00
San Lius	Jan	2027	450.00	1000.00	0.17
San Lius	Feb	2027	631.60	1464.02	0.13
San Lius	Mar	2027	748.10	1806.84	0.20
San Lius	Apr	2027	835.60	1975.02	0.39
San Lius	May	2027	879.92	1976.43	0.51
San Lius	Jun	2027	694.72	1546.00	0.58
San Lius	Jul	2027	442.12	1062.95	0.76
San Lius	Aug	2027	181.12	642.62	0.71

San Lius	Sep	2027	9.72	352.64	0.60
San Lius	Oct	2027	8.32	312.90	0.30
San Lius	Nov	2027	115.02	354.13	0.15
San Lius	Dec	2027	286.72	514.21	0.09

Table B.3: Monthly Minimum and Target River Flows

Name	Month	Rmin (cfs)	Rtarget (cfs)
Lewiston	Jan	300	300
Lewiston	Feb	300	300
Lewiston	Mar	300	300
Lewiston	Apr	300	300
Lewiston	May	3939	300
Lewiston	Jun	2507	783
Lewiston	Jul	1102	450
Lewiston	Aug	450	450
Lewiston	Sep	450	450
Lewiston	Oct	373	0
Lewiston	Nov	300	300
Lewiston	Dec	300	300
Clear Creek	Jan	150	150
Clear Creek	Feb	200	200
Clear Creek	Mar	200	200
Clear Creek	Apr	200	200
Clear Creek	May	200	200
Clear Creek	Jun	200	200
Clear Creek	Jul	200	200
Clear Creek	Aug	200	200
Clear Creek	Sep	200	200
Clear Creek	Oct	200	200
Clear Creek	Nov	90	90
Clear Creek	Dec	90	90
Spring Creek	Jan	325	325
Spring Creek	Feb	306	306
Spring Creek	Mar	2749	2749
Spring Creek	Apr	252	252
Spring Creek	May	813	813
Spring Creek	Jun	1681	1681
Spring Creek	Jul	2602	2602
Spring Creek	Aug	2114	2114
Spring Creek	Sep	2017	2017
Spring Creek	Oct	1138	1138
Spring Creek	Nov	504	504
Spring Creek	Dec	244	244
Keswick	Jan	3250	3250
Keswick	Feb	3250	3250

Keswick	Mar	3250	3250
Keswick	Apr	8000	8000
Keswick	May	9600	9600
Keswick	Jun	11000	11000
Keswick	Jul	14500	14500
Keswick	Aug	12000	12000
Keswick	Sep	5500	5500
Keswick	Oct	7200	7200
Keswick	Nov	5700	5700
Keswick	Dec	3250	3250
Wilkins	Jan	0	0
Wilkins	Feb	0	0
Wilkins	Mar	0	0
Wilkins	Apr	5000	5000
Wilkins	May	5000	5000
Wilkins	Jun	5000	5000
Wilkins	Jul	5000	5000
Wilkins	Aug	5000	5000
Wilkins	Sep	5000	5000
Wilkins	Oct	5000	5000
Wilkins	Nov	0	0
Wilkins	Dec	0	0
FeatherBelowThermolito	Jan	1250	0
FeatherBelowThermolito	Feb	1250	0
FeatherBelowThermolito	Mar	1250	0
FeatherBelowThermolito	Apr	1250	0
FeatherBelowThermolito	May	2030	0
FeatherBelowThermolito	Jun	0	2706
FeatherBelowThermolito	Jul	0	5692
FeatherBelowThermolito	Aug	5040	5156
FeatherBelowThermolito	Sep	0	4386
FeatherBelowThermolito	Oct	1980	2683
FeatherBelowThermolito	Nov	1750	1815
FeatherBelowThermolito	Dec	1250	0
AmericanRiverbelowNimbus	Jan	800	0
AmericanRiverbelowNimbus	Feb	800	0
AmericanRiverbelowNimbus	Mar	1000	0
AmericanRiverbelowNimbus	Apr	1500	0
AmericanRiverbelowNimbus	May	2300	0
AmericanRiverbelowNimbus	Jun	1800	0
AmericanRiverbelowNimbus	Jul	0	0
AmericanRiverbelowNimbus	Aug	0	0
AmericanRiverbelowNimbus	Sep	0	0
AmericanRiverbelowNimbus	Oct	0	0
AmericanRiverbelowNimbus	Nov	1000	0
AmericanRiverbelowNimbus	Dec	800	0
Goodwin	Jan	175	175
Goodwin	Feb	150	150

Goodwin	Mar	268	268
Goodwin	Apr	760	760
Goodwin	May	800	800
Goodwin	Jun	561	561
Goodwin	Jul	396	396
Goodwin	Aug	352	352
Goodwin	Sep	240	240
Goodwin	Oct	200	200
Goodwin	Nov	200	200
Goodwin	Dec	200	200
DeltaExit	Jan	6001	6001
DeltaExit	Feb	11398	11398
DeltaExit	Mar	11401	11401
DeltaExit	Apr	7848	7848
DeltaExit	May	9319	9319
DeltaExit	Jun	7092	7092
DeltaExit	Jul	6505	6505
DeltaExit	Aug	4261	4261
DeltaExit	Sep	3008	3008
DeltaExit	Oct	4001	4001
DeltaExit	Nov	4655	4655
DeltaExit	Dec	4505	4505

Table B.4: Monthly Demands

Month	Jan	Feb	Mar	Apr	May	Jun	Jul	Aug	Sep	Oct	Nov	Dec
Thermolito	35	0	11	67	189	178	200	178	78	95	104	71
Folsom Pumping	4	4	4	7	8	12	13	12	10	7	5	4
Folsom South Canal	1	1	1	1	2	3	4	4	3	2	1	1
OID/SSJID	0	0	14	60	90	90	95	95	74	14	0	0
CVP Contractors	0	0	0	0	0	0	0	0	0	0	0	0
CCWD	14	17	18	18	14	14	13	13	13	10	11	13
Barker Slough	2	2	1	2	4	5	7	7	6	5	3	3
Federal Tracy PP	258	233	258	250	135	169	270	268	260	258	250	258
Federal Banks On-Peak	0	0	0	0	0	0	28	28	28	0	0	0
State Banks PP	390	355	241	68	108	125	271	278	238	175	193	390
State Tracy PP	0	0	0	0	0	0	0	0	0	0	0	0
Delta Mendota Canal	30	60	100	120	190	220	270	240	180	110	40	30
Federal Dos Amigos	40	50	60	70	110	180	238	178	68	30	30	30
Federal O'Neil to Dos Amigos	0	1	1	1	1	2	2	1	0	0	0	0
San Felipe	6	6	10	15	19	20	21	20	13	11	8	8
South Bay/San Jose	2	2	2	5	5	7	7	8	7	12	8	6
State Dos Amigos	105	127	158	105	348	348	423	388	269	229	196	61
Delta Consumptive Use	-56	-37	-10	63	121	191	268	252	174	118	55	2
Freepport Treatment Plant	14	13	14	12	12	12	12	13	12	12	12	13

Table B.5: System Parameters

Month	X-Channel Gate	O'Neil Loss	X_2	Tracy Pump Cap (cfs)	Banks Pump Cap (cfs)	DI STD (%)
Jan	0.5	0.6	50	4200	6400	0.65
Feb	1	0.8	50	4200	6400	0.35
Mar	1	1.2	50	4200	6400	0.35
Apr	1	1.5	50	4300	6400	0.35
May	1	1.7	50	4300	6400	0.35
Jun	0.3	1.4	50	4300	6400	0.35
Jul	0	1.4	50	4600	6400	0.65
Aug	0	0.9	50	4600	6400	0.65
Sep	0	0.7	50	4500	6400	0.65
Oct	0	0.5	50	4300	6400	0.65
Nov	0	0.5	50	4200	6400	0.65
Dec	0	0.3	50	4200	6400	0.65

Table B.6: Demand Adjustment Fraction vs. River Index Value

River Index Code	River Index Value	Demand Fraction
C	1	0.2
BN	2	0.4
N	3	0.6
AN	4	1
W	5	1

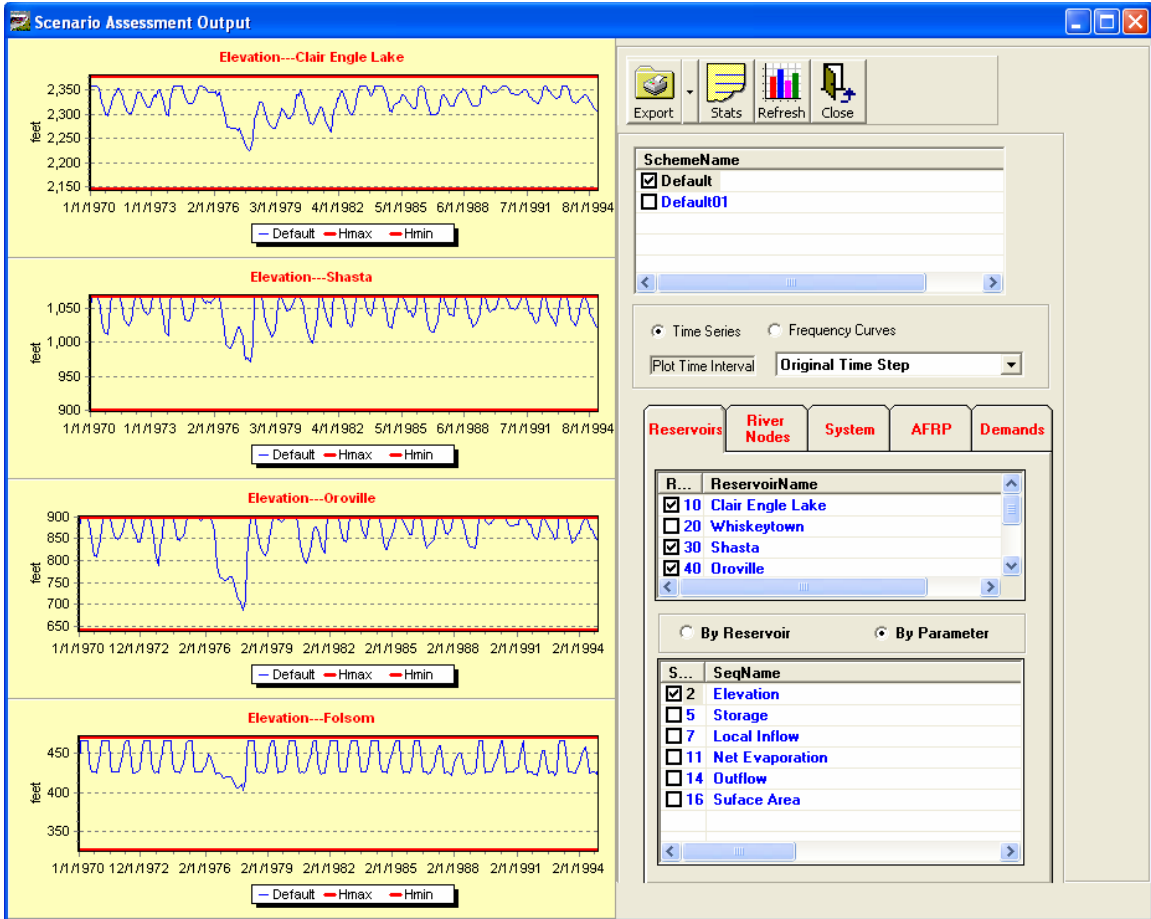


Figure B.2: Reservoir Elevation Sequences

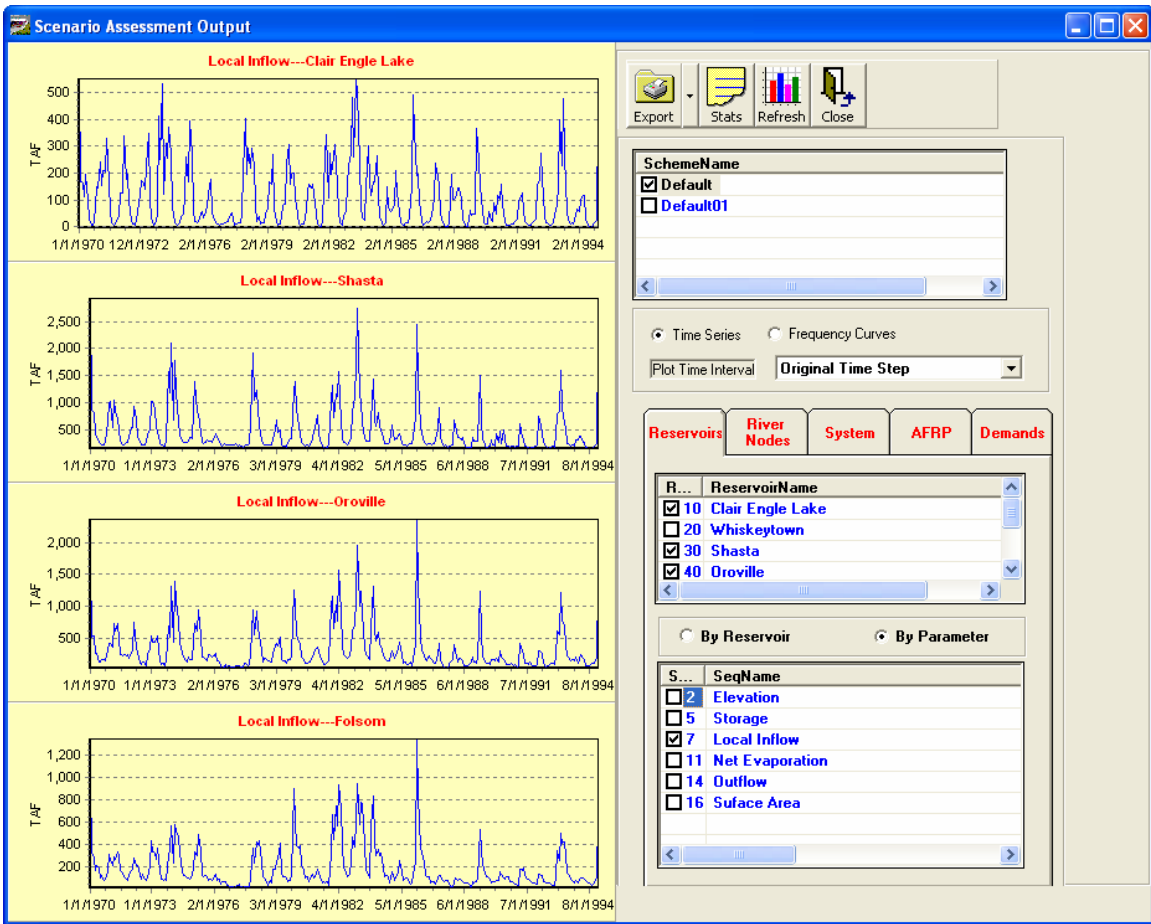


Figure B.3: Reservoir Inflows

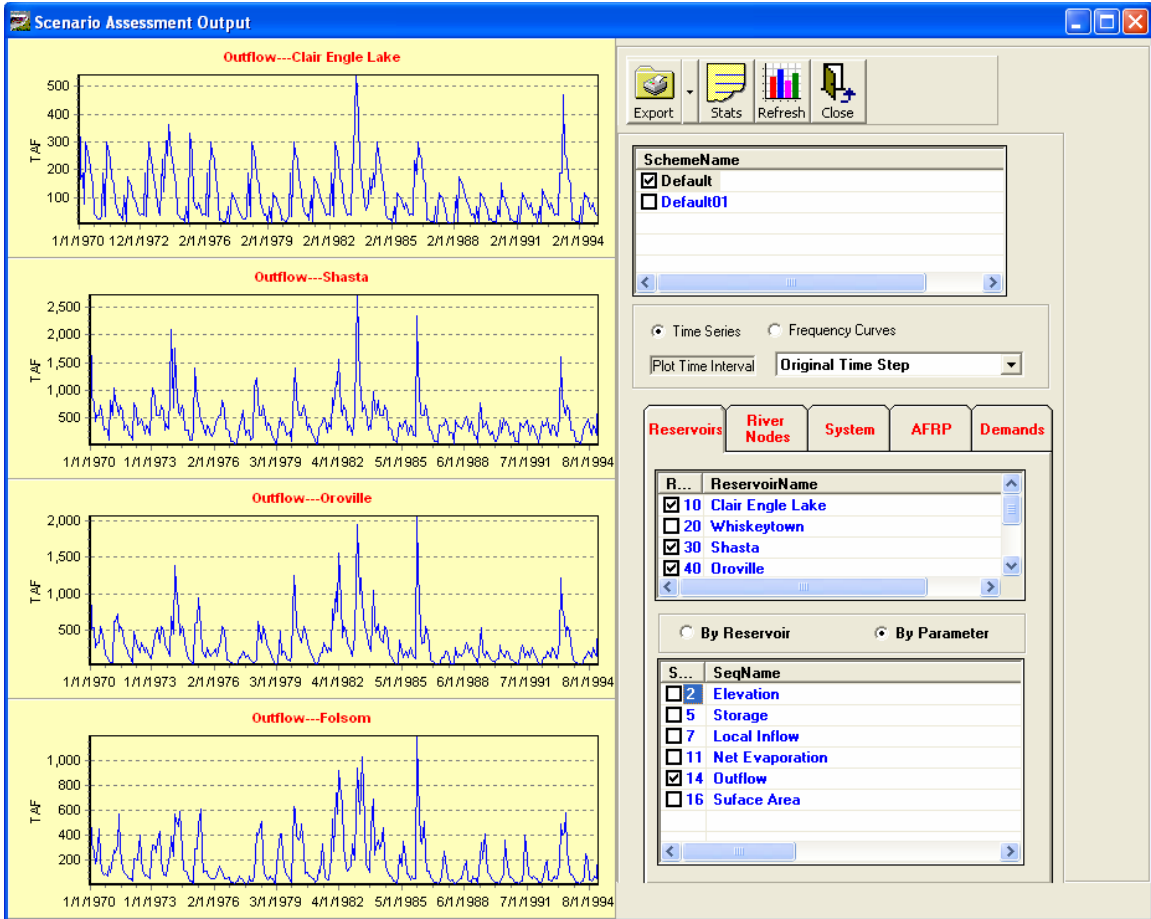


Figure B.4: Reservoir Releases

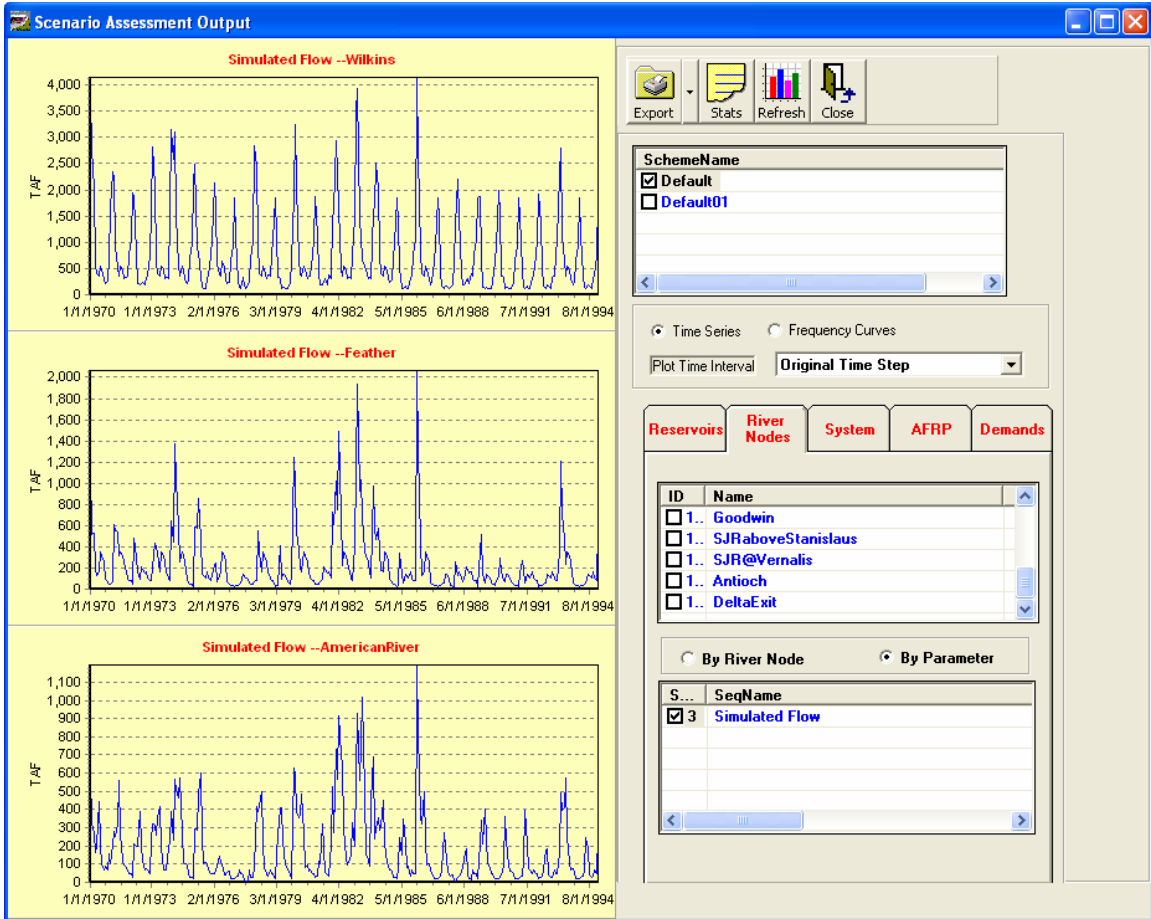


Figure B.5: River Flows at Selected Locations

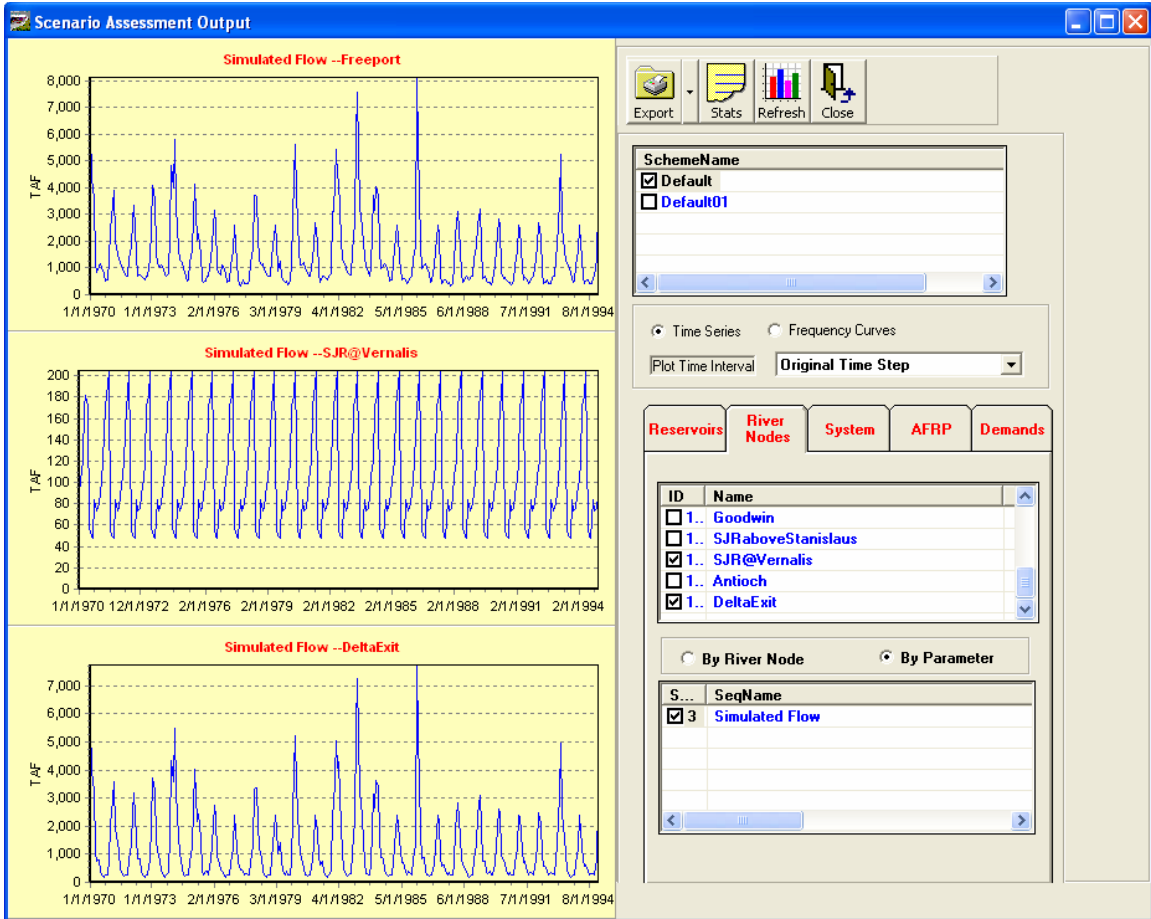


Figure B.6: River Flow at Selected Locations

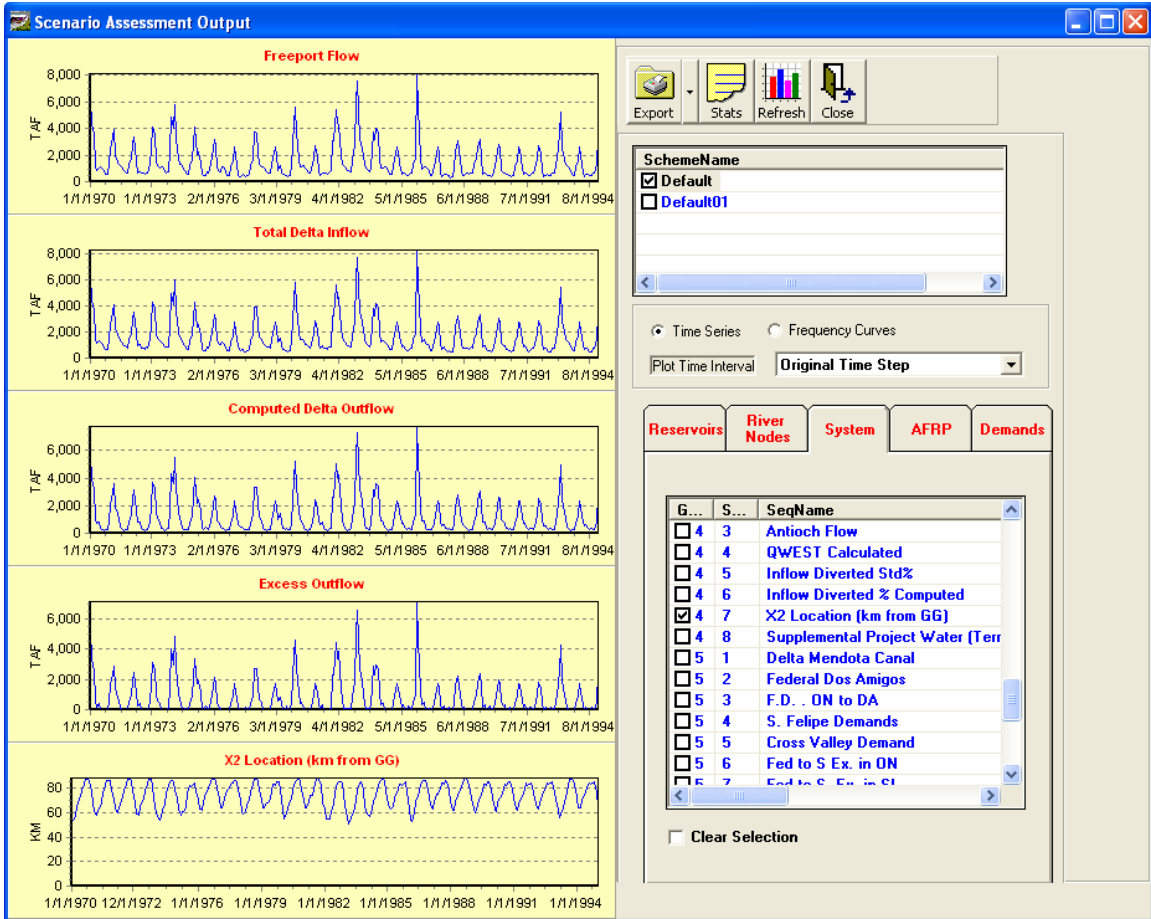


Figure B.7: Selected Delta Sequences

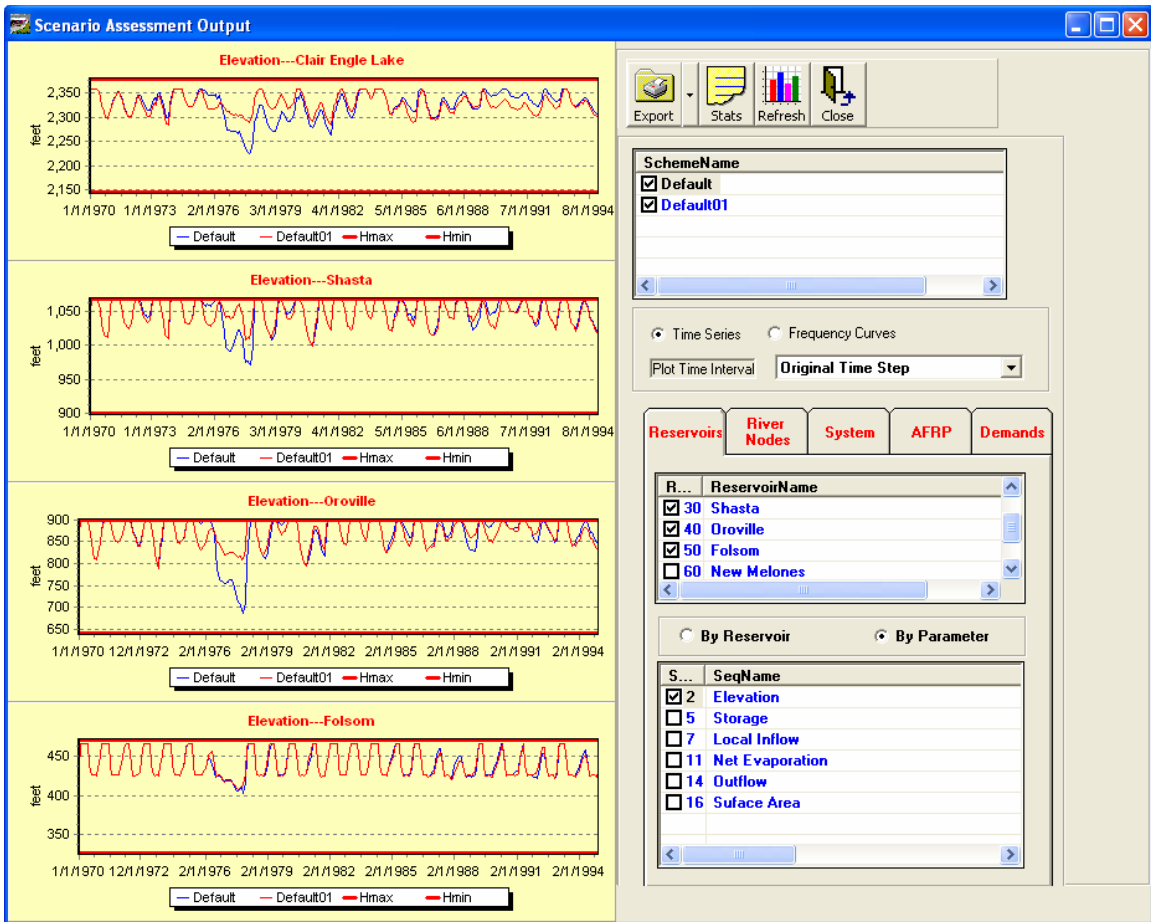


Figure B.8: Reservoir comparisons

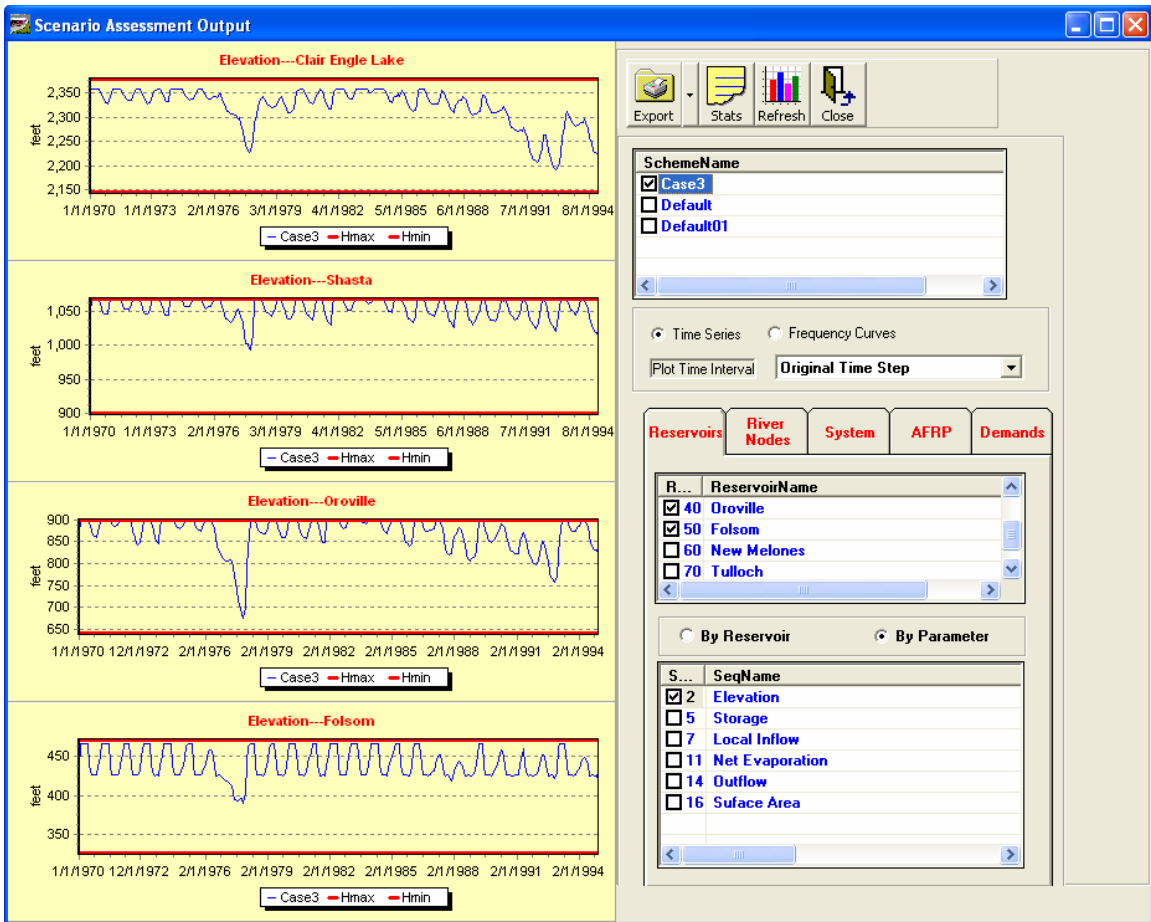
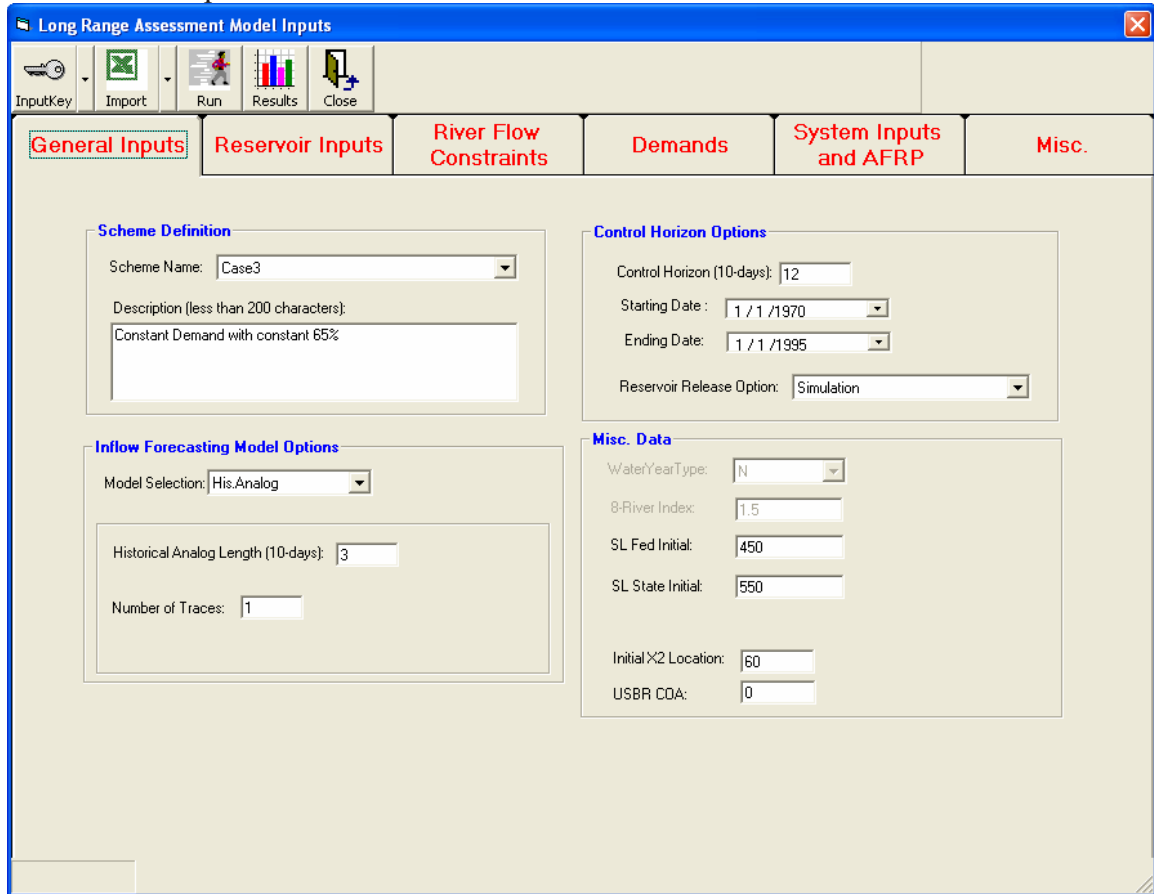


Figure B.9: Reservoir elevation sequences with fixed demand requirement pattern.

Appendix C: Assessment Model Inputs

C.1. General Input



Long Range Assessment Model Inputs

InputKey Import Run Results Close

General Inputs Reservoir Inputs River Flow Constraints Demands System Inputs and AFRP Misc.

Scheme Definition

Scheme Name: Case3

Description (less than 200 characters):
Constant Demand with constant 65%

Control Horizon Options

Control Horizon (10-days): 12

Starting Date: 1 / 1 /1970

Ending Date: 1 / 1 /1995

Reservoir Release Option: Simulation

Inflow Forecasting Model Options

Model Selection: His.Analog

Historical Analog Length (10-days): 3

Number of Traces: 1

Misc. Data

WaterYearType: N

8-River Index: 1.5

SL Fed Initial: 450

SL State Initial: 550

Initial X2 Location: 60

USBR COA: 0

- Scheme definition;
- Control horizon;
- Simulation horizon (starting date, ending date);
- Forecasting model options;
- Initial values for San Luis Storage, X2 Location, and USBR COA.

C.2. Reservoir Data

The screenshot shows the 'Long Range Assessment Model Inputs' application window. The 'Reservoir Inputs' tab is selected, displaying two data tables. The first table, 'Reservoir Time Invariant Parameters', lists reservoir data for various schemes and reservoirs. The second table, 'Reservoir Time Variant Parameters', lists monthly parameters for each reservoir over time.

SchemeName	ReservoirID	ReservoirName	Sini(TAF)
Case3	10	Clair Engle Lake	2226
Case3	20	Whiskeytown	231.8
Case3	30	Shasta	4060
Case3	40	Oroville	3049
Case3	50	Folsom	630
Case3	60	New Melones	1950
Case3	70	Tulloch	60.7
Case3	80	San Luis	1000

SchemeName	ReservoirID	TimeIndex	Smax	Smin	Stgt	Rmin	EvapCoef	Withdrawal
Case3	10	1	2287	312.63	2287	0	0.165	0
Case3	10	2	2287	312.63	2287	0	0.134	0
Case3	10	3	2287	312.63	2287	0	0.199	0
Case3	10	4	2287	312.63	2287	0	0.386	0
Case3	10	5	2287	312.63	2287	0	0.507	0
Case3	10	6	2287	312.63	2287	0	0.581	0
Case3	10	7	2287	312.63	2287	0	0.764	0
Case3	10	8	2287	312.63	2287	0	0.711	0
Case3	10	9	2287	312.63	2287	0	0.595	0
Case3	10	10	2287	312.63	2287	0	0.301	0
Case3	10	11	2287	312.63	2287	0	0.147	0
Case3	10	12	2287	312.63	2287	0	0.092	0
Case3	20	1	237.9	200	205.7	0	0.165	0
Case3	20	2	237.9	200	205.7	0	0.134	0

- Initial storage;
- Monthly values of maximum, minimum, and target Storage;
- Monthly values of downstream flow constraint;
- Monthly values of evaporation coefficients;
- Monthly values of reservoir withdrawal.

C.3. River Flow Constraints

The screenshot shows the 'Long Range Assessment Model Inputs' application window. The 'River Flow Constraints' tab is selected, displaying two data tables. The first table, 'River Flow Requirements', lists parameters for various schemes and time indices. The second table, 'Sliding Rules', lists adjustment fraction coefficients for different water bodies across five cases.

SchemeName	ID	Name	TimeIndex	Rmin	RTgt
Case3	10	Lewiston	1	300	300
Case3	10	Lewiston	2	300	300
Case3	10	Lewiston	3	300	300
Case3	10	Lewiston	4	300	300
Case3	10	Lewiston	5	3939	300
Case3	10	Lewiston	6	2507	783
Case3	10	Lewiston	7	1102	450
Case3	10	Lewiston	8	450	450
Case3	10	Lewiston	9	450	450
Case3	10	Lewiston	10	373	0
Case3	10	Lewiston	11	300	300
Case3	10	Lewiston	12	300	300
Case3	20	JF Carr	1	0	0
Case3	20	JF Carr	2	0	0

SchemeName	Index	Lewiston	JF Carr	Clear Creek	Spring Creek	Keswick	Wilkins	Feather
Case3	1	0.65	0.65	0.65	0.65	0.65	0.65	0.65
Case3	2	0.65	0.65	0.65	0.65	0.65	0.65	0.65
Case3	3	0.65	0.65	0.65	0.65	0.65	0.65	0.65
Case3	4	0.65	0.65	0.65	0.65	0.65	0.65	0.65
Case3	5	0.65	0.65	0.65	0.65	0.65	0.65	0.65

- Monthly values of minimum and target flows;
- Adjustment Fraction Coefficients of Minimum and Target Flow vs. Water Year Index relationship.

C.4. Demands

Water Demands

Scheme	Time Index	Thermit	Folsom P	Folsom S	OID/SSJ	CVP Con	CCWD	Barker S	Federal T	Federal B	Federal B	Federal B	Federal B	Federal B	Federal B
Case3	1	35	4	0.96	0	0	14	2	258	0	0	0	0	0	0
Case3	2	0	4	0.96	0	0	16.8	1.5	233	0	0	0	0	0	0
Case3	3	11	4	1.2	14	0	18.4	1.4	258	0	0	0	0	0	0
Case3	4	67	7	1.44	60	0	18.3	1.9	249.921	0	0	0	0	0	0
Case3	5	189	8	2.16	90	0	14	3.9	134.7986	0	0	0	0	0	0
Case3	6	178	12	2.88	90	0	14	5.2	169	0	0	0	0	0	0
Case3	7	200	13	3.6	95	0	12.7	6.6	270	28	0	0	0	0	0
Case3	8	178	12	3.6	95	0	12.7	6.9	268	28	0	0	0	0	0
Case3	9	78	10	2.88	74	0	12.7	5.5	260	28	0	0	0	0	0
Case3	10	95	7	1.92	14	0	9.8	4.6	258	0	0	0	0	0	0
Case3	11	104	5	1.44	0	0	11.1	3.1	250	0	0	0	0	0	0
Case3	12	71	4	0.96	0	0	12.7	2.9	258	0	0	0	0	0	0

Sliding Rules:

Scheme	Index	Thermit	Folsom P	Folsom S	OID/SSJ	CVP Con	CCWD	Barker S	Federal T	Federal B	Federal B	Federal B	Federal B	Federal B	Federal B
Case3	1	0.65	0.65	0.65	0.65	0.65	0.65	0.65	0.65	0.65	0.65	0.65	0.65	0.65	0.65
Case3	2	0.65	0.65	0.65	0.65	0.65	0.65	0.65	0.65	0.65	0.65	0.65	0.65	0.65	0.65
Case3	3	0.65	0.65	0.65	0.65	0.65	0.65	0.65	0.65	0.65	0.65	0.65	0.65	0.65	0.65
Case3	4	0.65	0.65	0.65	0.65	0.65	0.65	0.65	0.65	0.65	0.65	0.65	0.65	0.65	0.65
Case3	5	0.65	0.65	0.65	0.65	0.65	0.65	0.65	0.65	0.65	0.65	0.65	0.65	0.65	0.65

- Monthly values of demands;
- Demand Adjustment Fraction vs. Water Year Index relationship.

C.5. System Inputs and AFRP

The screenshot shows the 'Long Range Assessment Model Inputs' application window. The 'System Inputs and AFRP' tab is selected, displaying two data tables.

System Inputs Table:

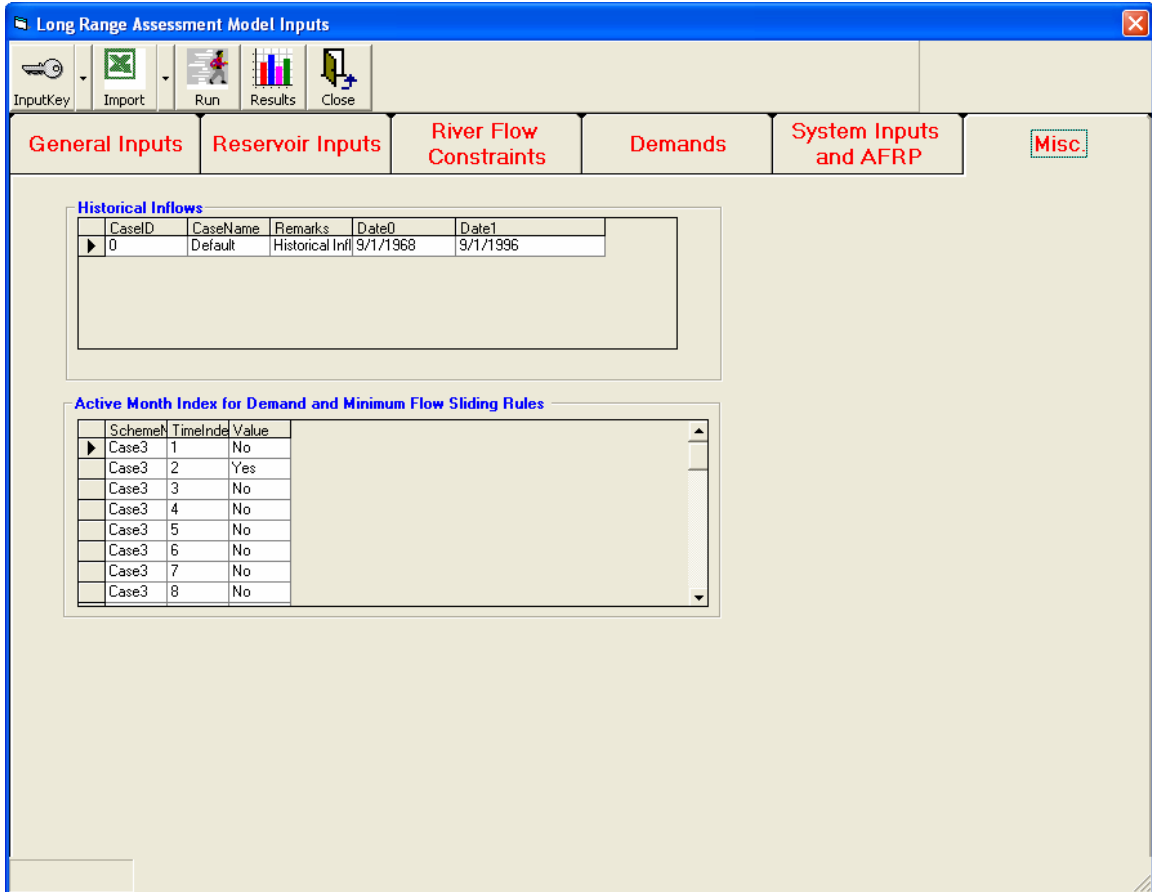
SchemeName	TimeIndex	X-Channel Gate	O'Neil Loss	X2	Max Tracy Pum	Max Banks Pum	DI%ST
Case3	1	0.5	0.6	50	4200	6400	0.65
Case3	2	1	0.8	50	4200	6400	0.35
Case3	3	1	1.2	50	4200	6400	0.35
Case3	4	1	1.5	50	4300	6400	0.35
Case3	5	1	1.7	50	4300	6400	0.35
Case3	6	0.3	1.4	50	4300	6400	0.35
Case3	7	0	1.4	50	4600	6400	0.65
Case3	8	0	0.9	50	4600	6400	0.65
Case3	9	0	0.7	50	4500	6400	0.65
Case3	10	0	0.5	50	4300	6400	0.65
Case3	11	0	0.5	50	4200	6400	0.65

AFRP Constraints Table:

Name	ID	Storage	JAN	FEB	MAR	APR	MAY	JUN	JUL
Clear Creek	1	0	100	100	100	100	100	100	
Clear Creek	1	700	100	100	100	100	100	100	
Clear Creek	1	750	100	100	100	100	100	100	
Clear Creek	1	800	100	100	100	100	100	100	
Clear Creek	1	850	150	100	100	100	100	100	
Clear Creek	1	900	150	150	100	100	100	100	
Clear Creek	1	1000	150	150	150	100	100	100	
Clear Creek	1	1100	150	150	150	100	100	150	
Clear Creek	1	1150	200	150	150	100	100	150	
Clear Creek	1	1200	200	150	150	150	150	150	
Clear Creek	1	1300	200	200	150	150	150	150	

- Monthly values of for X-Channel Gate, O'Neil Evaporation Loss, Coefficients, Max Tracy Pumping Capacity, Maximum Banks Pumping Capacity, and Export to Inflow Ratio Constraints;
- AFRP constraints for each month.

C.6. Miscellaneous



- Historical inflow dataset selection;
- Demand and minimum flow adjustment frequency.

Appendix D: Simulation Model Acronyms

- Central Valley Project (CVP)
- State Water Projects (SWP)
- Stockton East Water District (SEWD)
- Central San Joaquin Irrigation District (CSJID)
- Oakdale/South San Joaquin Irrigation District (OSSJID)
- Microsiemens/cm (EC)
- Delta Mendota Canal (DMC)
- Agreement of Coordinated Operation (COA)

Appendix E: Descriptions and Definitions of Water Year Type and River Index from DWR's website(<http://cdec.water.ca.gov/cgi-progs/iodir/wsi>)

- The Sacramento valley 40-30-30 index for water year types; Wet, Above Normal, Below Normal, Dry, and Critical, is used to determine year types for Delta outflow criteria and Sacramento system requirements.
- The San Joaquin Valley 60-20-20 Index is used to determine year types for flow requirements at Vernalis.
- The Sacramento River Index (SRI), is used to trigger relaxation criteria related to May-June Net Delta Outflow(NDO) requirements. The SRI refers to the sum of the unimpaired runoff in the water year as published in the DWR Bulletin 120 for the Sacramento River at Bed Bridge, Feature River inflow to Oroville, Yuba River at Smartville and American River inflow to Folsom reservoir.
- The Eight River Index is used to trigger criteria related to January Net Delta Outflow, February to June X2 standards and February export restrictions. The eight river index refers to the unimpaired runoff for the four locations mentioned under SRI plus Stanislaus River inflow to New Melones Reservoir, Tuolumne River inflow to Don Pedro Reservoir, Merced River inflow to Exchequer Reservoir and San Joaquin River inflow to Millerton Lake.
- Sacramento River Runoff is the sum of unimpaired flow in million acre-feet at:
 - Sacramento River above Bend Bridge
 - Feather River at Oroville (aka inflow to Lake Oroville)
 - Yuba River near Smartville
 - American River below Folsom Lake

Also known as the "Sacramento River Index", this index was previously used to determine year type classifications under SWRCB Decision 1485.

Also previously referred to as the "4 River Index" or "4 Basin Index".

$$\begin{aligned} \text{Index} = & 0.4 * \text{Current Apr-Jul Runoff} \quad (1) \\ & + 0.3 * \text{Current Oct-Mar Runoff} \quad (1) \\ & + 0.3 * \text{Previous Year's Index} \quad (2) \end{aligned}$$

Notes:

- (1) Runoff is the sum of unimpaired flow in million acre-feet at:
Sacramento River above Bend Bridge
Feather River at Oroville (aka inflow to Lake Oroville)
Yuba River near Smartville
American River below Folsom Lake

- (2) Maximum 10.0 for previous year index term

Year Type Classification: Index based on flow in million acre-feet:

Wet	Equal to or greater than 9.2
Above Normal	Greater than 7.8, and less than 9.2
Below Normal	Greater than 6.5, and equal to or less than 7.8
Dry	Greater than 5.4, and equal to or less than 6.5
Critical	Equal to or less than 5.4

This index, originally specified in the 1995 SWRCB Water Quality Control Plan, is used to determine the Sacramento Valley water year type as implemented in SWRCB D-1641. Year types are set by first of month forecasts beginning in February. Final determination is based on the May 1 50% exceedence forecast.

➤ San Joaquin Valley Water Year Type Index (60-20-20)

Water Year Index based on flow in million acre feet

$$\begin{aligned} \text{Index} = & 0.6 * \text{Current Apr-Jul Runoff} \quad (1) \\ & + 0.2 * \text{Current Oct-Mar Runoff} \quad (1) \\ & + 0.2 * \text{Previous Year's Index} \quad (2) \end{aligned}$$

Notes:

- (1) Runoff is the sum of unimpaired flow in million acre-feet at:
Stanislaus River below Goodwin Reservoir (aka inflow to New Melones Res.)
Tuolumne River below La Grange (aka inflow to New Don Pedro Reservoir)
Merced River below Merced Falls (aka inflow to Lake McClure)
San Joaquin River inflow to Millerton Lake
- (2) Maximum 4.5 for previous year index term

Year Type Classification: Index based on flow in million acre-feet:

Wet	Equal to or greater than 3.8
-----	------------------------------

Above Normal	Greater than 3.1, and less than 3.8
Below Normal	Greater than 2.5, and equal to or less than 3.1
Dry	Greater than 2.1, and equal to or less than 2.5
Critical	Equal to or less than 2.1

This index, originally specified in the 1995 SWRCB Water Quality Control Plan, is used to determine the San Joaquin Valley water year type as implemented in SWRCB D-1641. Year types are set by first of month forecasts beginning in February. Final determination for San Joaquin River flow objectives is based on the May 1 75% exceedance forecast.

➤ Sacramento Valley and San Joaquin 8 River Index

This index is the sum of the previous month's unimpaired runoff for the 8 rivers that are included in the above Sacramento River Unimpaired Runoff and San Joaquin Valley Water Year Type Index. A listing of reconstructed indices based on historical observed runoff is posted at http://cdec.water.ca.gov/water_supply.html . The official year types are based on May 1st's forecasts, not the observed runoff.

Remote Sensing of Precipitation Combining Geostationary and TRMM

Basic Information

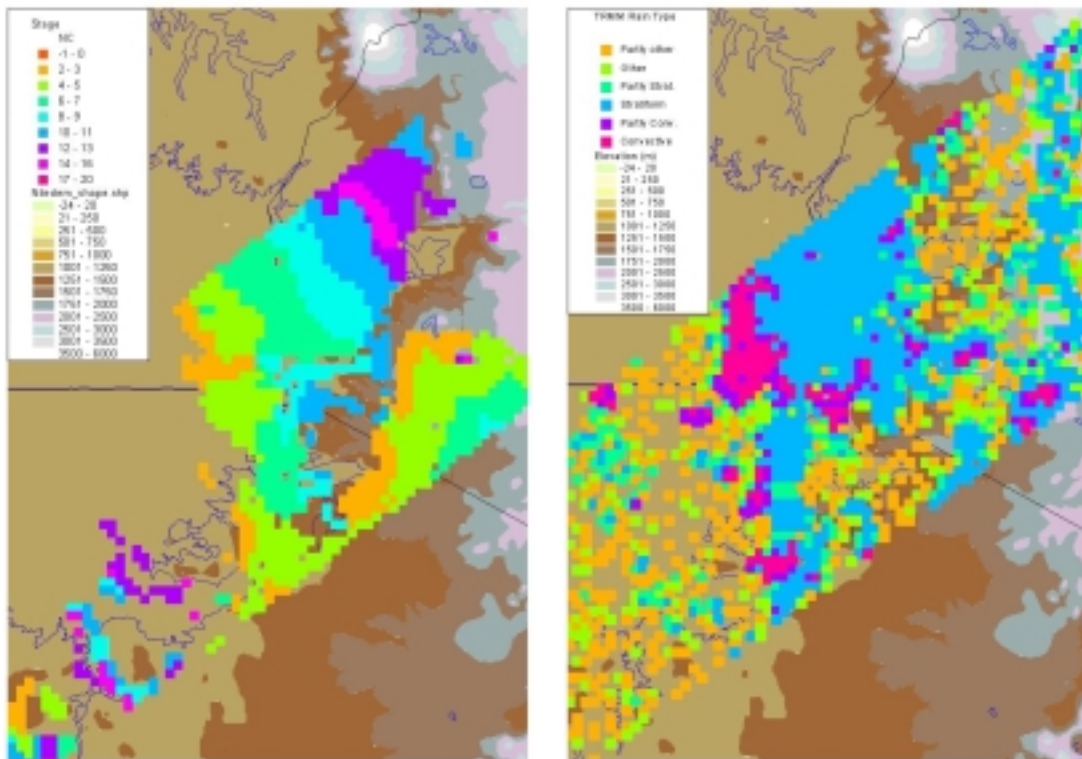
Title:	Remote Sensing of Precipitation Combining Geostationary and TRMM
Project Number:	2004GA101O
Start Date:	7/1/2004
End Date:	6/30/2005
Funding Source:	Other
Congressional District:	5
Research Category:	Climate and Hydrologic Processes
Focus Category:	None, None, None
Descriptors:	Remote Sensing
Principal Investigators:	Aris P. Georgakakos

Publication

Remote Sensing of Precipitation Combining Geostationary and TRMM Satellite Data

First Year Technical Report for Project NRA-02-ES-05,

“The Impact of Precipitation Measurement Missions on Hydrologic and Water Resource Predictions”



Aris Georgakakos and Carlo DeMarchi
Georgia Water Resources Institute
School of Civil and Environmental Engineering
Georgia Institute of Technology
Atlanta, Georgia 30332
(404) 894-2240

May 2005

Contents

1	<i>Introduction</i>	1
2	<i>Characteristics of the Estimation Methodology</i>	3
2.1	General structure	3
2.2	The IR/VIS-precipitation relation	5
2.3	Uncertainty characterization	6
3	<i>Rain-gage and Satellite Data</i>	11
3.1	Meteosat images	11
3.1.1	Characteristics of Meteosat images	11
3.1.2	Meteosat data processing	13
3.2	TRMM images	16
3.2.1	Characteristics of TRMM images	16
3.2.2	TRMM data processing	18
3.3	Rain-gage data	21
3.3.1	Characteristics of rain-gage data	21
3.3.2	Rain-gage data processing	21
4	<i>Identification of Convective Storms</i>	23
4.1	Detecting convective-storm occurrence at the pixel level	24
4.1.1	The training and verification data sets	28
4.1.2	Calibration and validation of artificial neural networks	31
4.2	Relation between IR, stage, and precipitation	33
5	<i>Single Pixel Analysis</i>	39
5.1	Characteristics of the single pixel estimation process	39
5.2	Estimation model performance	44
5.2.1	Model calibration (1996-1998)	44
5.2.2	Model validation (1996-1997)	45
5.2.3	Comparison with Adjusted GPI (TRMM product 3B42).	46
5.2.4	Discussion	47
5.3	Estimation incorporating precipitation autocorrelation	50
5.3.1	Autocorrelated model calibration (1996-1998)	54
5.3.2	Autocorrelated model validation (1996-1997)	56
5.3.3	Discussion	57
6	<i>Multi-pixel Analysis</i>	63
7	<i>Conclusions</i>	64
8	<i>References</i>	66

1 Introduction

Since its launch in late 1997, the Tropical Rainfall Monitoring Mission (TRMM) satellite has provided a variety of high quality data that have spurred several advances in hydrological and meteorological studies. The most innovative TRMM sensor, the Precipitation Radar (PR), routinely produces highly-reliable and detailed three-dimensional representations of rain fields that have offered new insights on the physics of precipitation phenomena (**Hirose and Najkamura, 2004; De Angelis et al., 2004**). On the other hand, these high-quality instantaneous precipitation measurements have found limited direct operational use due to the low PR sampling frequency (7-8 passages per month at the equator).

To overcome this limitation, TRMM information could be combined with information provided by other satellite systems with more frequent but less reliable data. **Greco and Anagnostou, 2001**, for example, proposed to use PR data for improving passive microwave precipitation retrieval algorithms, while **Bellerby et al., 2000**, used PR data for calibrating a precipitation estimation algorithm based on infrared and visible (IR/VIS) images from geostationary satellites. However, such efforts are sparse, and no definitive methodology has been established yet.

The research described herein proposes and evaluates a robust methodology for operational assessment of precipitation using TRMM PR data and half-hour IR/VIS data from geostationary satellites. The study recognizes that precipitation estimates based on satellite images are affected by substantial uncertainty that satellite sensor and methodology improvements may reduce, but not completely eliminate. Furthermore, estimation uncertainty varies with time and spatial resolution, respectively ranging from less than an hour to days and months, and from a few to hundreds of square kilometers. Thus, a goal of the proposed methodology is to explicitly quantify the uncertainty associated with precipitation estimation.

The proposed methodology is applied and tested in the Lake Victoria basin (Equatorial Africa). Comparisons with conventional rain gage data from 100 rain gages over a two-year period (1996-1998) indicate that the method exhibits high estimation reliability.

This report is structured in seven chapters. Chapter 2 illustrates the framework of the estimation methodology. Chapter 3 describes the data used for calibration and testing. Chapter 4 investigates a new procedure for identifying convective storms at the pixel level. Chapter 5 discusses the estimation approach and quantifies its performance at the pixel level. Chapter 6 outlines the steps required to aggregate the single pixel estimates over larger regions in a statistically consistent manner. Finally, Chapter 7 summarizes the research results and outlines the future project plan.

The research described herein has been funded by several sources including the Food and Agriculture Organization of the United Nations (FAO/UN) under the Nile Decision Support Program, the United States Geological Survey under the State Water Resources Program, and NASA (Goddard Space Flight Center, GSFC) under Project NRA-02-ES-05 entitled “The Impact of Precipitation Measurement Missions on Hydrologic and Water Resource Predictions.” The last project is a collaborative effort between NASA’s GSFC (with lead PIs **Dr. C. Peters-Liddard** and **Dr. J.M. Sheppard**) and the Georgia Water Resources Institute (GWRI) at Georgia Tech (with lead PI **Dr. A. Georgakakos**). This document serves as the GWRI first year Interim Project Report.

2 Characteristics of the Estimation Methodology

2.1 General Structure

Precipitation estimation methodologies using satellite images can be subdivided into three broad categories:

- Procedures based on IR/VIS images, mainly from geostationary satellites;
- Procedures based on microwave images from low earth orbiting (LEO) satellites;
- Procedures combining IR/VIS images from geostationary satellites with microwave images from LEO satellites.

Procedures based on IR/VIS images from geostationary satellites

Satellite IR/VIS sensors convey information on cloud presence, type, extent, and evolution history. Subsequently, IR/VIS procedures transform this information, more or less empirically, into precipitation estimates. The advantage of these techniques is that IR/VIS images from geostationary meteorological satellites are available every 15 to 30 minutes with a spatial resolution of 1 to 8 km, allowing a continuous monitoring of the cloud evolution. Their disadvantage is that this information is only indirectly related to precipitation and that this relation is subject to considerable variations in time and space (Arkin and Xie, 1994). Because of this, dense networks of rain gages are needed to optimize this relation in space and time (for example Todd et al., 1995; Georgakakos et al., 2001).

Procedures based on microwave images from LEO satellites

The relation of precipitation rate and microwave radiation is more reliable than infrared or visible radiation. For this reason, microwave sensors provide better estimates of instantaneous rain (Ebert et al., 1996; Todd et al., 2001). However, microwave image sensors are presently available only aboard LEO satellites, and this information is only available every 3 to 6 hours. This low temporal frequency does not provide good precipitation estimates at the daily-dekad temporal resolution (Ebert et al, 1996).

Furthermore, microwave images are available only since 1987, limiting their use for hydrological applications where longer records are needed.

Procedures combining images from geostationary and LEO satellites

The underlying concept of these methodologies is to use the instantaneous precipitation rate maps produced by microwave sensors to update/optimize in space and time the relation between IR/VIS images and precipitation rate. This relation is then applied to the continuous flow of IR/VIS images from geostationary satellites (**Adler et al., 1993; Hsu et al., 1997**). Typically, the relation IR/VIS-precipitation is derived from coincident microwave and IR/VIS images during the month preceding the estimation over a $1^{\circ} \times 1^{\circ}$ area. The major advantage of this approach is that it does not rely on extensive ground data for calibration. The major drawback is that it requires online information from multiple sources. Further, these methods often do not have “memory” in the sense that they are based on just the most recent fraction of available data.

The methodology presented herein belongs to the third category in that precipitation estimation is based on IR/VIS images from geostationary satellites with the IR/VIS-precipitation rate relationship obtained from contemporaneous TRMM-PR and geostationary satellite images. The proposed methodology differs from other techniques in the same category in that it uses

- TRMM PR data rather than passive microwave radiation images;
- all available coincident TRMM PR and IR/VIS images to build the IR/VIS-precipitation rate relationship, not just data of the previous month;
- coincident PR and IR/VIS data from a $6^{\circ} \times 7^{\circ}$ area, but distinguishes them according to orography features (lake/land and elevation).

TRMM PR estimates of instantaneous precipitation are much more reliable than passive microwave precipitation estimates, but they are approximately 33% of the images supplied by the TRMM Microwave Imager. However, using **all** available coincident TRMM and IR/VIS images to build the IR/VIS-precipitation relation as opposed to

monthly data partly corrects this deficit. Furthermore, the use of large data sets provides a more robust assessment of precipitation average spatial distribution and variability. This is essential for characterizing estimation uncertainty and for applying the procedure to periods for which microwave data are not available. Also, larger data sets allow for regionalizing the IR/VIS-precipitation relationship based on orography features rather than on latitude/longitude, leading to better precipitation estimates in heterogeneous terrains.

2.2 *The IR/VIS-precipitation relation*

In the last 30 years several algorithms have been proposed for estimating precipitation from IR/VIS satellite images. Some of the most commonly used approaches are summarized below:

- IR threshold for rain/no rain and single precipitation rate;
 - fixed in time and space (GPI, **Richards and Arkin**, 1981; **Arkin and Meisner**, 1987);
 - spatially and temporally varying (Adjusted GPI, **Adler et al.**, 1993; **Todd et al.**, 1995; Universally Adjusted GPI, **Xu et al.**, 1999);
- Discrimination between convective and stratiform rain (CST, **Negri and Adler**, 1988; **Negri and Adler**, 2002);
- IR/Rain rate probability matching (3B41RT, **Huffman et al.**, 2003; MIRA, **Todd et al.**, 2001);
- IR Texture – IR, $\mu\text{IR}_{3\times 3}$, $\sigma\text{IR}_{3\times 3}$, $\mu\text{IR}_{5\times 5}$, $\sigma\text{IR}_{5\times 5}$ – (PERSIANN, **Hsu et al.**, 1997);
- Indicator of cloud growth – $P(t)=F(\text{IR}(t))$ if $\text{IR}(t)-\text{IR}(t-1)=0$, 0 otherwise – (NESDIS Autoestimator, **Vincente et al.**, 1998);
- Lookup tables for rain-rate indexed by IR and VIS (**King et al.**, 1995) or IR_{11} , $\text{IR}_{11}-\text{IR}_{12}$, and $\text{IR}_{11}-\text{WV}$ (**Kurino**, 1997);
- Bivariate VIS-IR frequency (**Tsonis et al.**, 1996; **Georgakakos et al.**, 2001);
- IR, VIS Texture (PERSIANN, **Hsu et al.**, 1999; **Bellerby et al.**, 2000);

The methodology of this work utilizes a “lookup table” approach similar to those of **King et al.** (1995) and **Kurino** (1997). The approach of these investigators is to develop a matrix relating rain-rates to satellite IR-VIS pairs. Each element of this matrix represents the average hourly precipitation rate over an 8 km X 8 km area corresponding to a satellite observed IR-VIS pair. The average precipitation rates were obtained from six months of coincident radar and satellite observations. At nighttime, the precipitation rate is derived as function of the IR alone. This procedure performs better than approaches that only use IR information (First Algorithm Intercomparison Project, **Arkin and Xie**, 1994) because the visible data help discriminate raining cumulonimbi from the similarly cold, but semitransparent, non-raining cirri, and identify precipitation from thick versus shallow clouds. Since then several other algorithms have added the visible data to the IR for precipitation estimation (**Tsonis et al.**, 1996; **Hsu et al.**, 1999; **Bellerby et al.**, 2000). **Kurino** (1997) used the same general approach, but the rain-rate matrixes were indexed by triplets, IR₁₁, IR₁₁-IR₁₂, and IR₁₁-WV, where the IR₁₁ is the infrared radiation at 11 μm (indicated as IR in the rest of the report), IR₁₂ the infrared radiation at 12 μm, and WV is the infrared radiation at 6.7 μm, also known as water vapor (WV) channel. The value of IR₁₁-IR₁₂ is used to discriminate cirri, while IR₁₁-WV is useful for deep convection detection. **Bellerby et al.** (2000) and **Georgakakos et al.** (2001) have also used WV for precipitation estimation.

The look-up table used in this research is indexed by orography, IR, VIS during daytime or IR-WV during nighttime, storm stage, and month. At each half-hour time slot, the precipitation over a pixel is determined as function of the satellite observed IR/VIS/WV radiation in the pixel, orography, and season.

2.3 Uncertainty characterization

As mentioned in the introduction, one of the main research goals is to provide a complete characterization of the uncertainty inherent in precipitation estimates. This implies that half-hour precipitation should be treated as a random variable, the distribution of which

needs to be defined. The observed IR/VIS/WV values are expected to condition the mean, variability, and the general shape of this distribution.

A way to characterize the precipitation probability distribution is by assuming a probabilistic model and fitting it to experimental data. **Bell (1987)** modeled ocean precipitation as a temporally and spatially homogeneous and isotropic random process. He also assumed that there is an average probability $f > 0$ of rain and that the intensity of rainy events is distributed lognormally. Further, he modeled the correlation of the precipitation at different points as a decreasing function of the distance d between the points. This model was used to assess the ability of microwave LEO sensors to reconstruct monthly average precipitation over a large and homogeneous area. As such, there is no dependence between precipitation rate and observed IR/VIS/WV characteristics.

Fiorucci et al. (2001) also model precipitation as a log-normal random process, and conditioned the precipitation mean and variance at a pixel (i,j) and time t on the observed IR radiation at the same location:

$$\mu_{i,j,t} = L\left(\frac{IR_{i,j,t} - C}{M} + 1\right) \exp\left(-\frac{\mu_{i,j,t} - C}{M}\right) \quad \sigma_{i,j,t} = CV \cdot \mu_{i,j,t} \quad \rho_{(i,j),(k,l)} = \exp\left(-\frac{d_{(i,j),(k,l)}}{\gamma}\right)$$

Spatial autocorrelation of precipitation is modeled as exponentially decreasing with distance, but the authors do not consider temporal autocorrelation.

The distribution of the average precipitation over a period/region could be analytically derived using the appropriate summation formulas.

An alternative strategy is the ensemble technique, a procedure convenient when analytical forms of the probability density function are too difficult to derive. In this case, an ensemble of equally likely values is derived by randomly sampling a distribution of observed/simulated values. For example, **Georgakakos, 1989**, used ensembles of past observed flow sequences with initial values similar to the flows observed at time t and $t-1$

for predicting the range of possible flows at time $t+1$, $t+2$, etc. **Walser et al., 2004**, assessed the prediction capabilities of mesoscale numerical weather prediction (NWP) models by randomly perturbing the NWP initial conditions and observing the variability of the NWP output.

This study adopts the ensemble approach by associating each combination of input variables with the entire distribution of TRMM PR rain rates observed over a long period of time. Specifically, at each timeslot, an ensemble of equally likely precipitation values are obtained by randomly sampling the distribution of PR rates corresponding to particular combination of IR, VIS, WV, storm stage, orography, and month. This approach is not limited by a particular probability model over the sample data. Further, it is easy to update and is relatively robust since outliers do not influence the entire distribution, but only a small number of cases. The disadvantages of this approach is that it requires keeping in random computer memory a lot of data and using a Monte Carlo approach to derive the distribution of precipitation over a region/period. The estimation procedure for the precipitation over a single pixel can be delineated as follows:

- 1 The daily Meteosat IR time series (consisting of half-hour values) for a given pixel is processed by a neural network to determine the presence and evolution (storm stage) of convective storms (Figure 2.3.1 A).
- 2 At each timeslot t , the corresponding $IR(t)$ and $storm\ stage(t)$, defined in Step 1, identify a distribution of PR samples (Figure 2.3.1 B).
- 3 One estimate of daily precipitation is generated by randomly sampling the precipitation rates corresponding to the IR-stage combinations during the day and summing the resulting half-hour precipitation rates (Figure 2.3.1 C). The process is repeated N times resulting in N daily precipitation estimates (Figure 2.3.1 B).
- 4 To assess the accuracy and statistical consistency of the approach, the probabilistic position of the gage record with respect to the ensemble distribution is recorded (Figure 2.3.1 D). This value is used to determine various statistics such as the inter-quartile compliance rate, 95% compliance rate, Kolmogorof-Smirnov compliance statistic, among others.

- 5 The same approach is used to produce 10-day (dekad) and monthly precipitation estimates by extending the number of half-hour time series from 48 to 480, or to 48 times the number of days in the desired interval.
- 6 More sophisticated estimation procedures can be obtained by adding VIS(t)/WV(t), orography, and the calendar month in the set of indexing variables. A PR distribution similar to that of Figure 2.3.1 B will be identified by the appropriate combination of the input values in each time slot. Namely, for each member X of the ensemble:

$$\text{Precip}(t) = f[\text{IR}(t), \text{VIS}(t)/\text{WV}(t), \text{stage}(t), \text{orography}, \text{month}, \varepsilon],$$

where

Precip(t)= precipitation rate at time t for element X;

IR(t)= infrared radiation at time t;

VIS(t)= visible radiation at time t;

WV(t)= water vapor radiation at time t;

ε = random error.

To extend this approach over a region, the random errors used for sampling the rain-rate distributions must be generated in a way that maintains the precipitation spatial correlation observed in the region. This topic is taken up in Chapter 6.

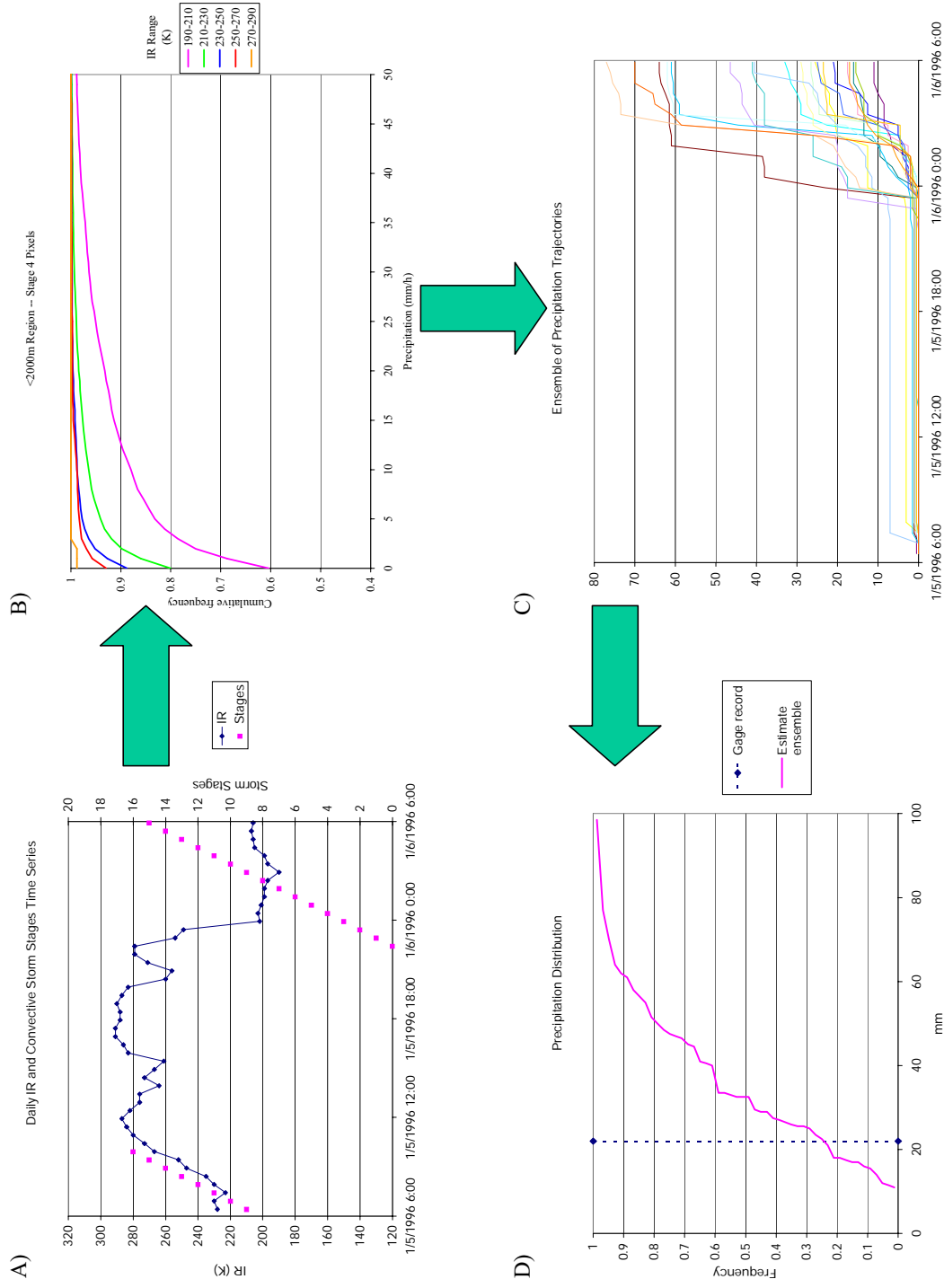


Figure 2.3.1: Schematic of the ensemble estimation of daily precipitation at the pixel level

3 Rain-gage and Satellite Data

The proposed precipitation estimation methodology has been evaluated in an area surrounding Lake Victoria. More specifically, this area is depicted in (Figure 3.1.1 and Figure 3.3.1) and extends from 29°E to 36°E and from 5°S to 3°N. Lake Victoria covers roughly the central 10% of this region. This region is flanked by high mountains, with Mount Elgon (4155 m) in the east side and Mount Ruwenzori (5109 m) in the west. The climate of the region is equatorial, but elevation and lake influence contribute to moderate temperatures all year round. The lowlands in the southern side of the area are considerably drier than the rest of the basin.

Precipitation is driven mainly by the migration of the Inter Tropical Convergence Zone with the related northeast and southeast monsoons. Lake Victoria is large enough to partly modify the general circulation by creating a permanent pressure low attracting moisture from the Congo rainforest in the west. Further, it creates local precipitation patterns similar to those created by land-sea interaction. The high mountains in the basin also influence the climate by creating windward and leeward regions.

This section illustrates the satellite and rain-gage data available to this project as well as data available for future modeling developments. Data processing for quality control is also described.

3.1 *Meteosat images*

3.1.1 Characteristics of Meteosat images

Meteosat is a family of geostationary meteorological satellites located above the point 0°E, 0°N that monitor the weather evolution over the region shown in Figure 3.1.1. Meteosat's main sensor, the VISSR imaging radiometer, produces a digital image of the full earth disk every 30 minutes in the three channels described in Table 3.1.1. The size

of the image elements (pixels) is approximately equal to that indicated in Table 3.1.1 at the sub-satellite point, but increases moving towards the periphery of the view.

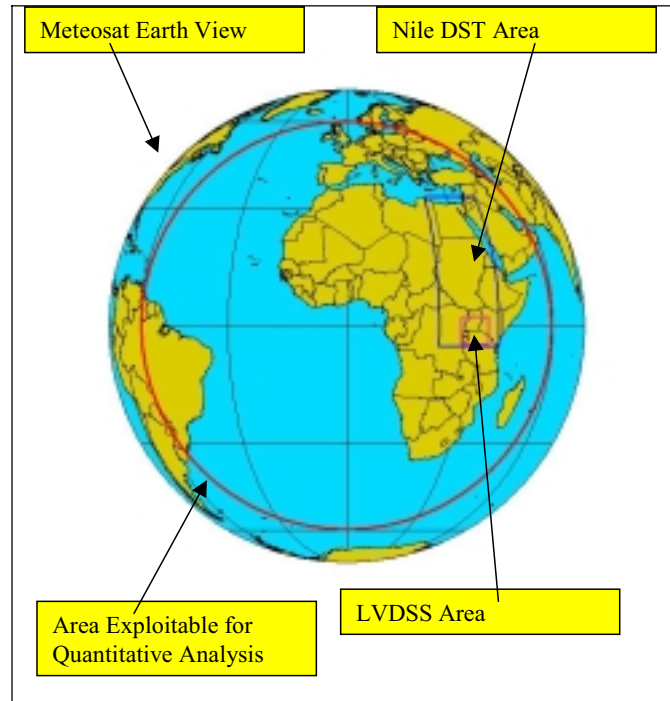


Figure 3.1.1: Full Disk View of the Meteosat Satellites

Table 3.1.1: Characteristics of the VISSR imaging radiometer (Eumetsat, 2000)

Channel	Electromagnetic band (μm)	Sub-satellite spatial resolution (km)	Direct and indirect meteorological information provided
VIS	0.5 – 0.9	2.5 x 2.5 (5.0 x 5.0)	Albedo (daytime) – Thickness of clouds.
WV	5.7 – 7.1	5.0 x 5.0	Water vapor in the middle troposphere -- Thickness of clouds/Overshooting
IR	10.5 – 12.5	5.0 x 5.0	Thermal infrared temperature – Surface temperature and cloud top's elevation

Only two channels at a time are normally broadcasted due to restrictions on the receiving hardware and software. Typically, these two channels are the thermal infrared (IR) channel and either the visible (VIS) or the water vapor (WV) channel, according to a predefined schedule. VIS images are available between 5:30 GMT and 22:00 GMT,

while the WV images are available between 22:30 GMT and 5:00 GMT. Further, the VIS channel is transmitted at half its nominal spatial resolution, by sub-sampling the full resolution image. At 11:30 GMT Meteosat images are available only for the Mediterranean basin.

Four different Meteosat satellites, Meteosat-4 through Meteosat-7, have provided digital images over the period 1992-2003. While the general characteristics of images have remained those described in Table 3.1.1, each satellite's sensors require specific digital count – radiance relations. Further, the performance of the sensors vary during their operational life because of sensor degradation and environmental influences, requiring a continuous recalibration of the count-radiance relationship. The satellite-specific sensor count-radiance relation and the calibration coefficients can be retrieved from the Eumetsat web site (www.eumetsat.de). Some calibration coefficients are also embedded in the satellite broadcasted digital images as auxiliary parameters. The quality of the image (i.e., the noise level) is also different from satellite to satellite.

3.1.2 Meteosat data processing

Meteosat digital images were available to this project in three different formats, namely B.U.R.S.L. Autosat 3.1 (FAO/UN – Egypt images before December 1996), B.U.R.S.L. Autosat Block 5 (FAO/UN – Egypt images after December 1996 and FAO/UN – Uganda images), and Eumetsat OpenMTP. All three formats hold much more information than needed for this study, dramatically increasing storage requirements. Further, extracting the data from these files is a cumbersome process that easily fails if the digital files are corrupted. It also requires merging data files in different formats for producing a continuous sequence of images. For these reasons the digital images have been re-sampled over a regular rectangular grid with $0.05^{\circ} \times 0.05^{\circ}$ resolution and transformed into a nimbler intermediate format called NileDST Grid Format. (NileDST stands for the Nile Decision Support System that has been developed by the Georgia Water Resources Institute at Georgia Tech, **Georgakakos**, 2004.) The translation process included the following steps:

1. Elimination of missing and noisy lines;
2. Conversion of digital counts into blackbody temperatures (IR and WV channels) and albedo (VIS channel) with correction of the solar-angle effect for the latter.
3. Filtering of clearly invalid values;
4. Filtering of pixels outside the range $AVG_{5 \times 5} - 3 \times STDEV_{5 \times 5} < \text{pixel value} < AVG_{5 \times 5} + 3 \times STDEV_{5 \times 5}$, where $AVG_{5 \times 5}$ is the channel average over a five pixels by five pixels square centered on the pixel of interest, and $STDEV_{5 \times 5}$ is its standard deviation;
5. Detection and elimination of corrupted, spatially or temporally displaced, and duplicated images;
6. Correction of the displacement error.

Table 3.1.2: Available Meteosat data

Period	Spatial and temporal coverage of images	Source
06/1992-12/1994	South of 22N	FAO – Egypt
01/1995-12/1995	South of 22N – 96%	FAO – Egypt + Eumetsat
01/1996-12/1996	South of 22N – 98%	FAO – Egypt + Eumetsat
01/1997-12/1997	Nile Basin – 98%	FAO – Egypt + Eumetsat
01/1998-09/17/1998	Nile Basin - Complete	Eumetsat
09/18/1998-12/1998	South of 10N – Complete	FAO Entebbe + Eumetsat
01/1999	South of 5N– Complete	Eumetsat
02/1999-25/05/1999	Nile Basin - Complete	Eumetsat
06/05/1999-04/2000	Nile Basin – 88% coverage	FAO – Egypt
05/2000-07/2000	None	
08/2000-14/09/2001	Nile Basin – 83%	FAO – Entebbe
15/09/2001-12/29/2002	Nile Basin – 83%	FAO – Entebbe

Satellite digital images in 1996-1997 were frequently affected by one or more lines of noise like the one shown in Figure 3.1.2. Quality of the remaining files range from good to optimal in the case of the OpenMTP files.

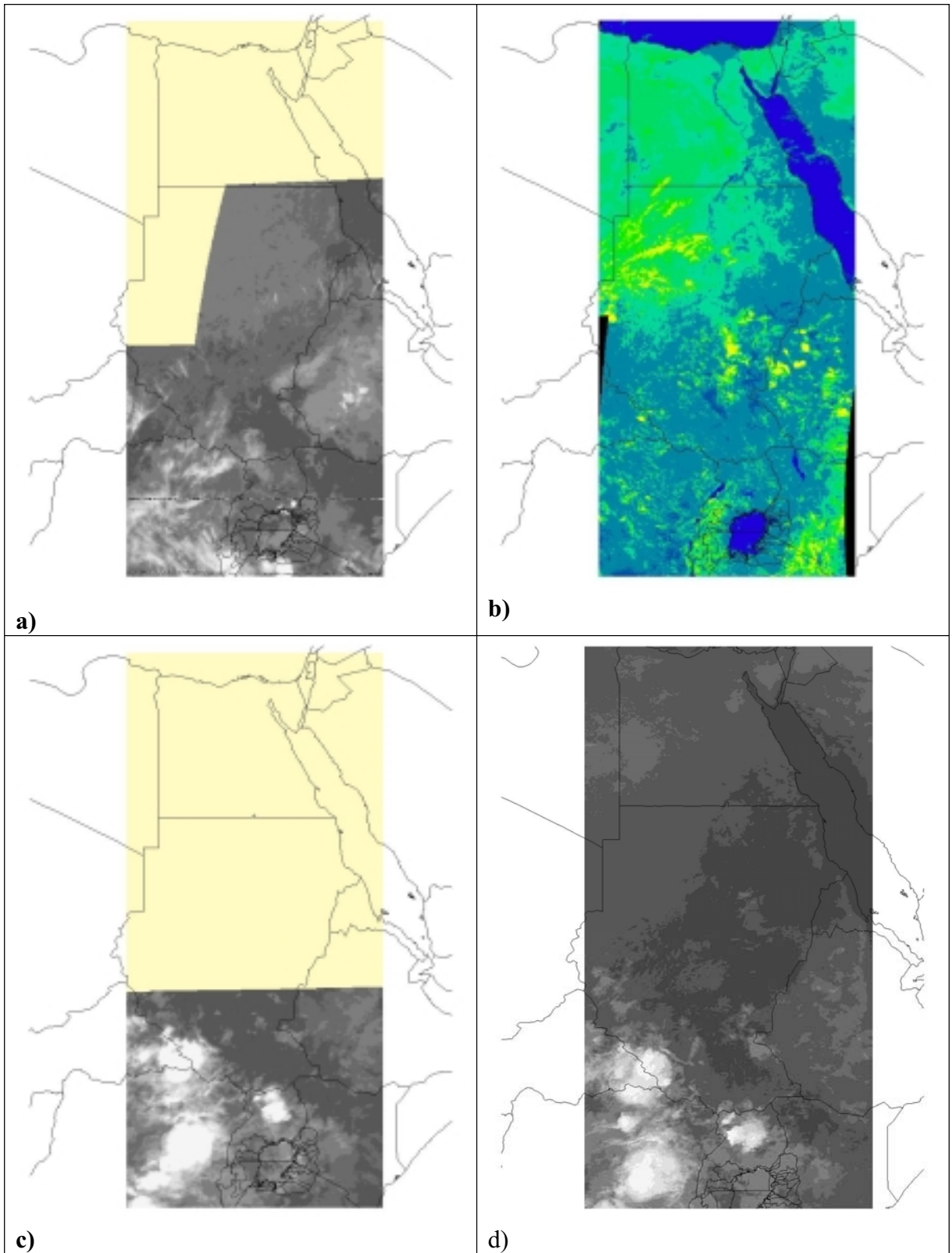


Figure 3.1.2: a) Example of FAO-Egypt IR Image until 1996. A line of noise slightly North of Lake Victoria is maintained for illustrative purposes. b) Example of FAO-Egypt

VIS Image after 1996. c). Example of FAO-Entebbe IR Image in 1998. d) Example of Eumetsat IR Image.

3.2 *TRMM images*

3.2.1 Characteristics of TRMM images

The Tropical Rainfall Measuring Mission (TRMM) is a joint mission between the National Aeronautics and Space Administration and the National Space Development Agency (NASDA) of Japan aimed at providing the first detailed and comprehensive dataset on the four dimensional distribution of rainfall and latent heating over under-sampled oceanic and tropical continental regimes.

The TRMM satellite is placed on an orbit inclined of 35° with respect to the equator at an altitude of 350-500 km. This orbit allows TRMM to monitor the tropical areas with higher temporal frequency and to distribute its passages above the same point uniformly over the entire twenty-four hour period. This TRMM characteristic is essential for the proper sampling of precipitation over the tropics given the strong diurnal cycle affecting rainfall in this area (Li et al., 1996). For the same reason it is essential also for using precipitation measurements for calibrating estimation procedures based on infrared images from geostationary satellites (Morrissey and Janowiak, 1996).

This work uses only two of the five TRMM sensors, the Precipitation Radar (PR) and the TRMM Microwave Imager (TMI). PR is a 2m x 2m phased array antenna operating at the frequency of 13.8 GHz that provides the vertical distribution of instantaneous reflectivity along its swath. From this information, the presence and type of rain is assessed and the rain rate estimated. The beam is electronically scanned cross track $\pm 17^\circ$ with respect to nadir in 0.6 s. The swath is subdivided in 49 angle bins each with a near-surface horizontal diameter of a little more than 4 km. Each angle bin is subdivided in 80 range bins distributed every 250 m from just above the earth ellipsoid to the altitude of 20 km. An effective signal-to-noise ratio of 4 dB is obtained for rain as low as 0.7 mm h^{-1} (Kummerow et al., 1998, 2000).

The short-term drifts in PR performance due to the variation in the solar illumination of the satellite during its orbits and consequent change in the instrumentation temperature are contained within 1 dB. An Active Radar Calibrator located in Japan monitors Long-term changes in the PR performance allowing for timely adjustments in the algorithms used for deriving precipitation rates. Differences in rainfall reflectivity measures with ground and airborne radar in Florida and Japan were on average limited within 1 dB (Kummerow et al., 2000).

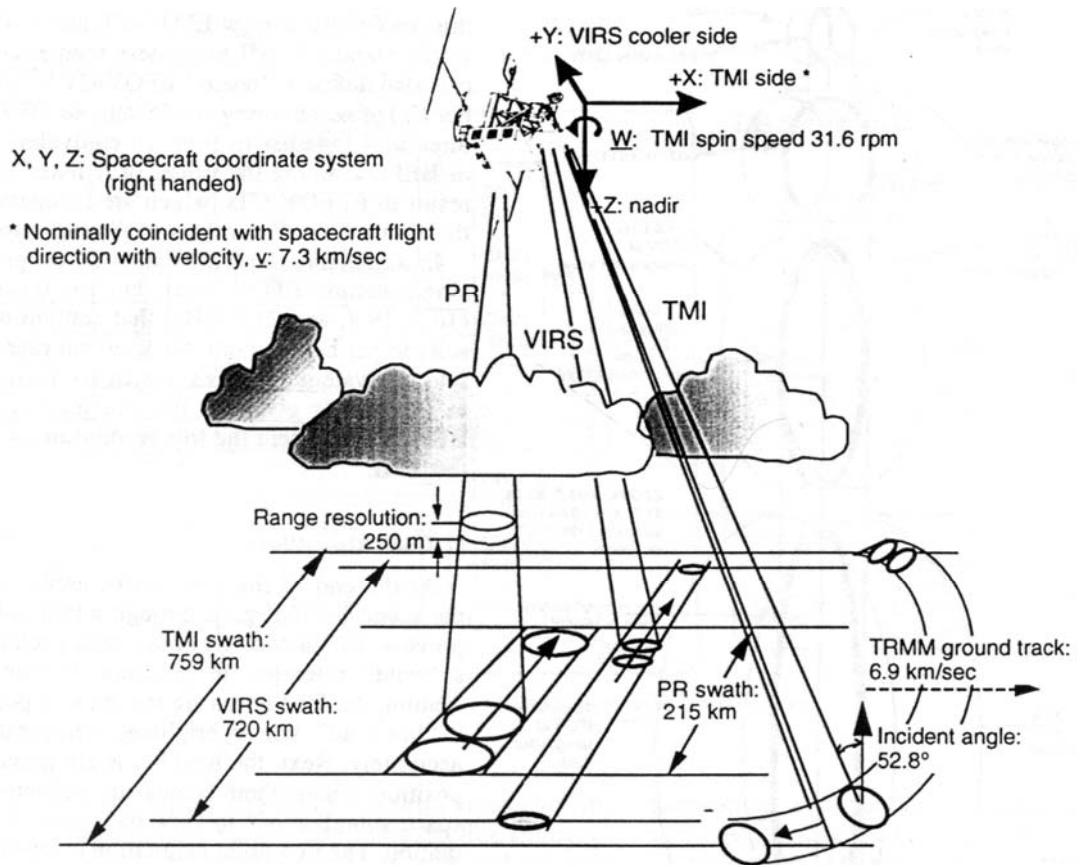


Figure 3.2.1: Schematic view of the scan geometries of the three primary rainfall sensors: TMI, PR, and VIRS(after Kummerow et al., 1998)

TMI is a nine-channel microwave radiometer with architecture similar to the Special Sensor Microwave/Imager (SSM/I). The main differences are the addition of two 10.7 GHz vertical and horizontal polarization channels, the shift of the frequency of the water vapor channel from 22.325 to 21.3 GHz, and the higher spatial resolution due to the

lower orbit altitude. TMI's swath is an arc 758.5 km wide (Figure 3.2.1) with a spatial resolution varying from 63x37 km at 10.65 GHz to 7x5 km at 85.5 GHz (Kummerow et al., 1998).

PR and TMI are used alone or in combination to produce several types of products, varying in complexity from the basic reflectivity to monthly precipitation estimates.

3.2.2 TRMM data processing

This project is currently using products "2A23 – PR Qualitative" and "2A25 – PR Profile" data. The former product first determines whether each range bin is above or below the ground surface and if the corresponding radar reflectivity is reliable. Then, the presence of rain is assessed as "possible" (the return power is larger than the 90%-tile noise) or "certain" (the return power exceeds the "possible" noise level by more than three times the noise standard deviation).

PR assesses the rain type by merging the results of two different methods for classifying rain type: the H-method based on the horizontal reflectivity distribution (Steiner et al., 1995) and the V-method based on the reflectivity vertical profile. The final precipitation classification is obtained by merging the outcomes of the H-Method and V-Method with other information in the bright band (BB), resulting in a complex categorization of the rain type. The project, however, retained only the major precipitation classes (stratiform, convective, and "other") by using the following scheme (TSDIS, 2004)

(merged) rainType[i] / 100 = 1: stratiform;
2: convective;
3: other.

Smearing of BB near the antenna scan edges seriously affects the BB detection, which is about 80% for antenna scan angles in the interval $\pm 7^\circ$ from nadir, but only about 20% at the swath edges. Further, the rain/no-rain discrimination seems also to be dependent on

the angle-bin. To alleviate the impact of side-lobe clutter, the project does not use the first and last two pixels of each PR swath.

TRMM data have been re-sampled along the 0.05°x0.05° NileDST grid for matching with contemporaneous Meteosat data. When two or more TRMM pixels fall within the same NileDST pixel the resulting rain is classified as “entirely convective”, “entirely stratiform”, “entirely mixed”, or “no-rain” if the original TRMM data were of the same type. If they were of different types, the resulting NileDST pixel is classified as “partially convective”, “partially stratiform”, or “partially mixed” (Figure 3.2.2).

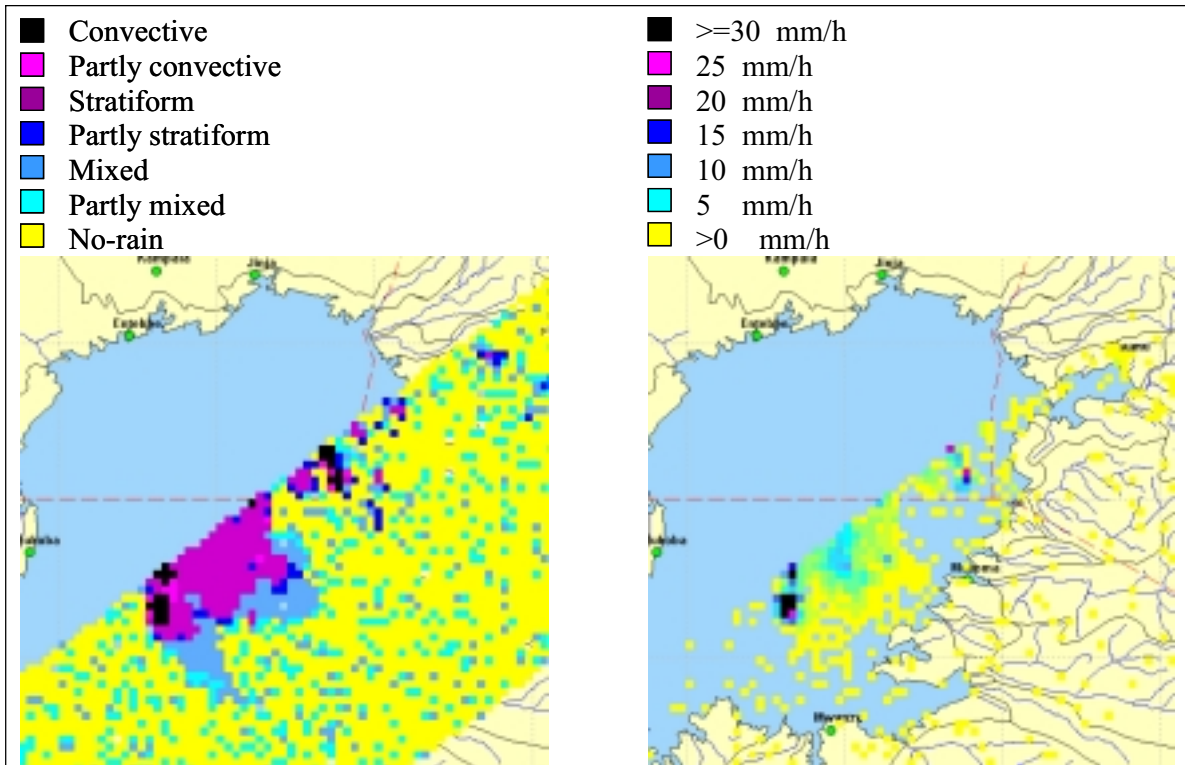


Figure 3.2.2: Example of rain type and near surface rain-rate information provided by TRMM

Product “2A25 – PR Profile” reports the precipitation rate as well as its reliability for each beam of the PR swath over 80 vertical levels. It also includes additional information relevant to the precipitation rate retrieval procedure.

It was not possible to use precipitation rates at a predetermined elevation or the average rain between 2 and 4 kilometers, two TRMM products that are frequently used for precipitation estimates, because of the large variation in elevation in the Lake Victoria basin makes them either applicable only to a limited portion of the area or too far from the surface. Near surface rain, on the other hand, is available for all pixels of the basin, thus allowing a complete coverage of all elevation bands. It also accounts for precipitation evaporation along raindrop trajectories, an issue that may be relevant in the drier parts of the basin. On the other hand, near surface rain is likely to be noisier than precipitation rates averaged over several vertical levels and more strongly affected by ground clutter. A basin-wide comparison between precipitation rates near the surface and at 2 kilometers altitude suggested that near surface rates below 0.7 mm/hr are very likely to be noise and were thus eliminated.

As with the rain type product, 2A25 pixels have been re-sampled to fit the 0.05°x0.05° NileDST grid by averaging the precipitation of multiple TRMM pixels falling within the same NileDST pixel.

Table 3.2.1: Available TRMM data

Period	Spatial and temporal coverage of images	Source
01/1996-12/1996	None	
01/1997-12/1997	None	
01/1998-12/1999	-5N÷5N, 28E÷38E 816 valid TRMM passages	University of Connecticut
12/1997-Present	Nile Basin Acquisition in process	NASA

3.3 *Rain-gage data*

3.3.1 Characteristics of rain-gage data

The precipitation estimation procedure has been evaluated using the December 2002 version of the FAO Nile Data Base (NBD-Dec02-2) and some additional data from the Kenya Ministry of Water, Tanzania Ministry of Water, and the Egyptian Nile Forecast Center. This data were available to GWRI/Georgia Tech as part of the development of the Nile DST and other projects.

3.3.2 Rain-gage data processing

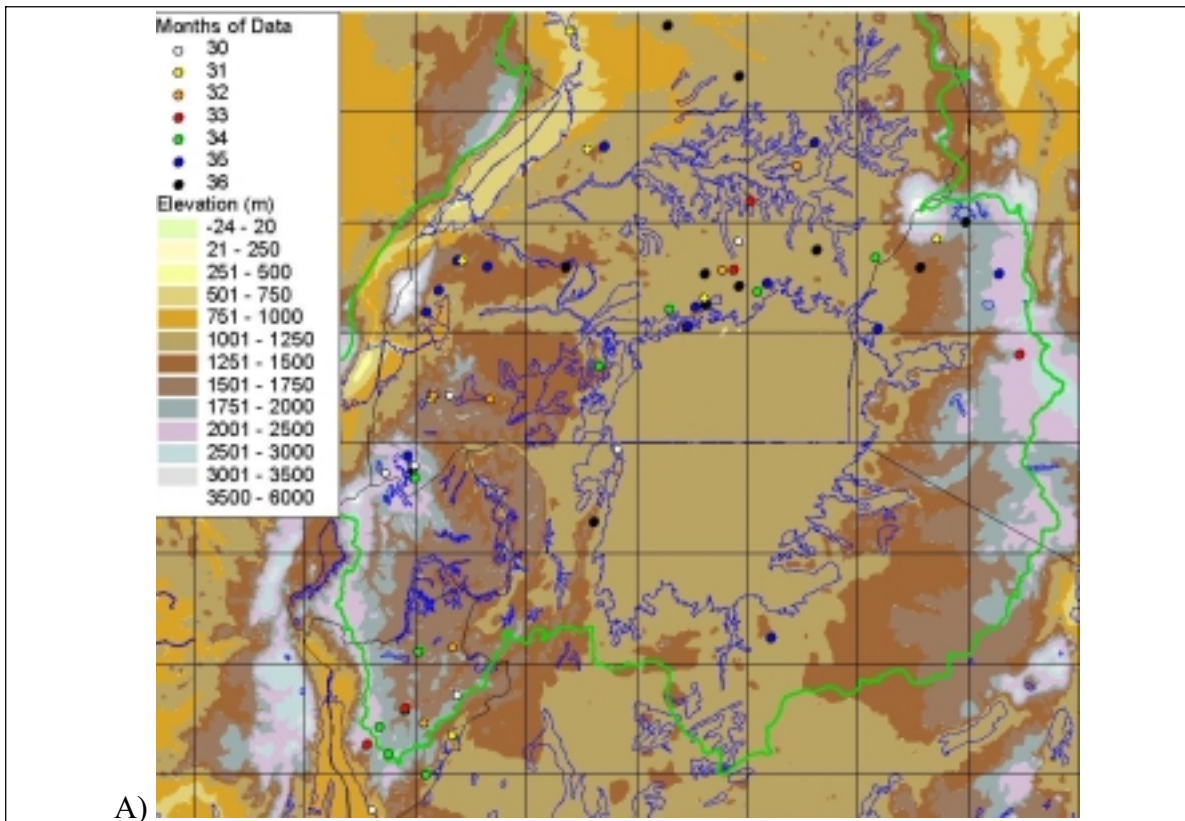
Rain gage data have undergone extensive examination to ensure the quality of the records. The main quality control steps were as follows:

- 1 Rain gage coordinates have been verified against GIS maps and WMO or national identification codes;
- 2 Duplicate and ambiguous precipitation records have been eliminated;
- 3 Monthly sequences of daily precipitation with less than 90% records have been dismissed;
- 4 For each rain-gage, the average precipitation during each month of 1996, 1997, and 1998 has been compared against the 15-year average precipitation. Months with precipitation outside the normal range or months with insufficient records were compared against measurement at neighboring stations;
- 5 Correlation in 10-day precipitation between neighboring stations was checked;
- 6 Only stations featuring at least 30 months of valid precipitation records in the 1996-1998 or 20 months of valid precipitation records in the 1996-1997 periods were retained;
- 7 Differences in the correlation between daily precipitation and satellite estimates at neighboring stations were investigated;

The resulting data records that passed the previous tests are reported in Table 3.3.1 and in Figure 3.3.1. The rain gage density in the basin fluctuates significantly making the examination of the gage records particularly difficult. Therefore, it is likely that despite all quality control efforts, rain gage data still suffer from a higher percentage of error than similar data from other parts of the world.

Table 3.3.1: Available rain gage data in the Lake Victoria region

Period	Stations with temporal coverage of at least 83%	Source
01/1996-12/1997	Lake Victoria basin - 98	FAO
01/1996-12/1998	Lake Victoria basin - 61	FAO
01/1998-12/1998	Lake Victoria basin - 48	FAO



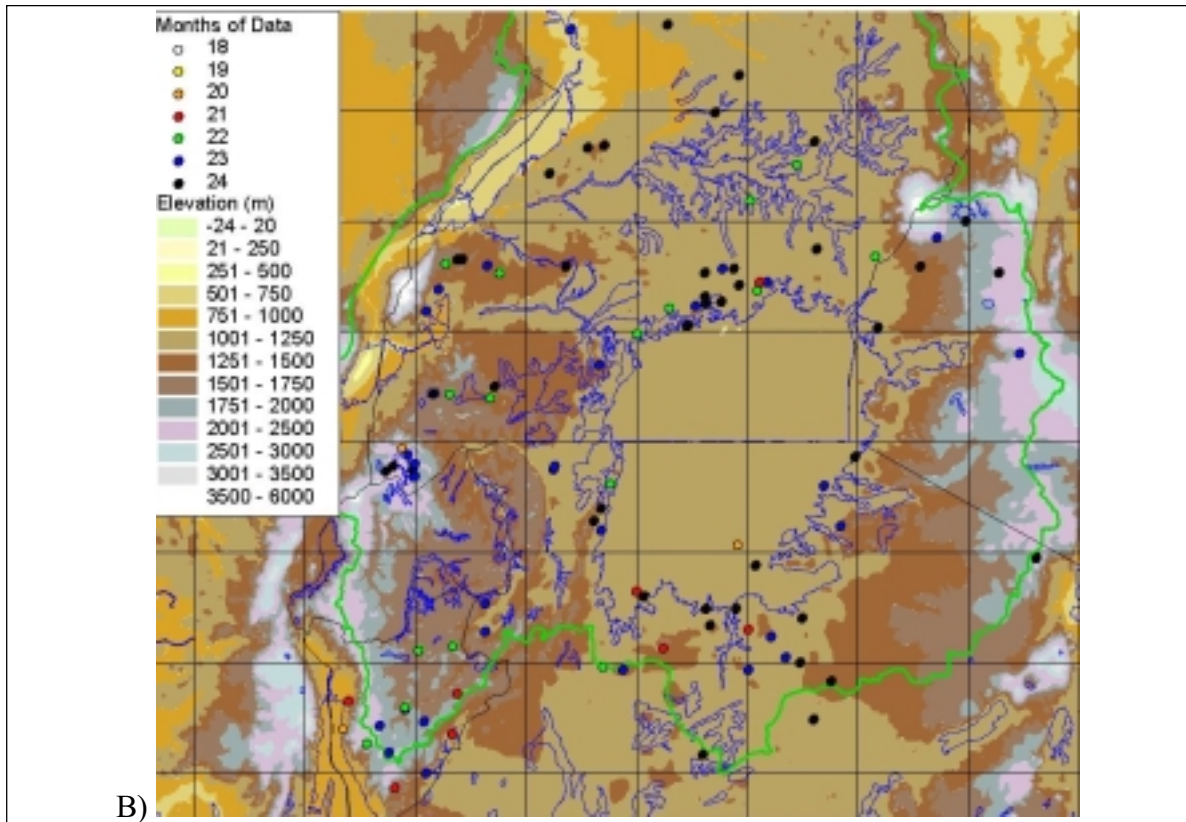


Figure 3.3.1: Available rain gages with (A) at least 30 months of valid data in the period 1996-1998 (B) at least 20 months of valid data in the period 1996-1997

4 Identification of Convective Storms

Most procedures using infrared and visible images from geostationary satellites for estimating precipitation have an “instantaneous” nature in the sense that the estimation of the precipitation at a certain time is based only on the satellite images taken at that particular time. Some procedures recognize the importance of the temporal change of cloud characteristics and base their estimates on pairs of consecutive satellite images (Vincente et al., 1998; Bellerby et al., 2000). On the other hand, it is generally recognized that convective storms feature three distinct phases—developing, mature, and dissipating—each with a distinct rain regime. Using specific relations between cloud characteristics and precipitation for these different phases of the convective storm and for different types of storms should yield better precipitation estimates. Such an approach to precipitation estimation involves two steps:

1. Detecting the onset of the convective storm and its termination;

2. Determining the relation between precipitation and cloud characteristics for different parts of the storm.

4.1 Detecting convective-storm occurrence at the pixel level

Detecting the occurrence of a convective storm over a pixel means identifying the presence of a pattern that can be associated with this phenomenon, such as that in Figure 4.1.1, in the time series of satellite infrared and visible data for that pixel. This task is made more complex by the fact that high variable factors, such as storm duration, intensity, and antecedent condition, confer a large variability to these “signatures”.

Georgakakos et al. (2000) tested several methods for identifying the presence of such typical patterns. The best results in terms of effectiveness and computing requirements were obtained by adopting a Multilayer Feed-Forward Neural Network (MFFNN) specifically trained to recognize a catalog of 6-hour long IR and VIS patterns associated with typical convective patterns. The convective patterns were selected by determining storm centers, or cores, where numerous adjacent patterns are identical and similar to that of Figure 4.1.1. Further away from these storm cores, patterns were identified as non-core, or transitional, when they began to lose that typical convective shape. As a consequence of this approach, the number and variety of patterns used for training were limited.

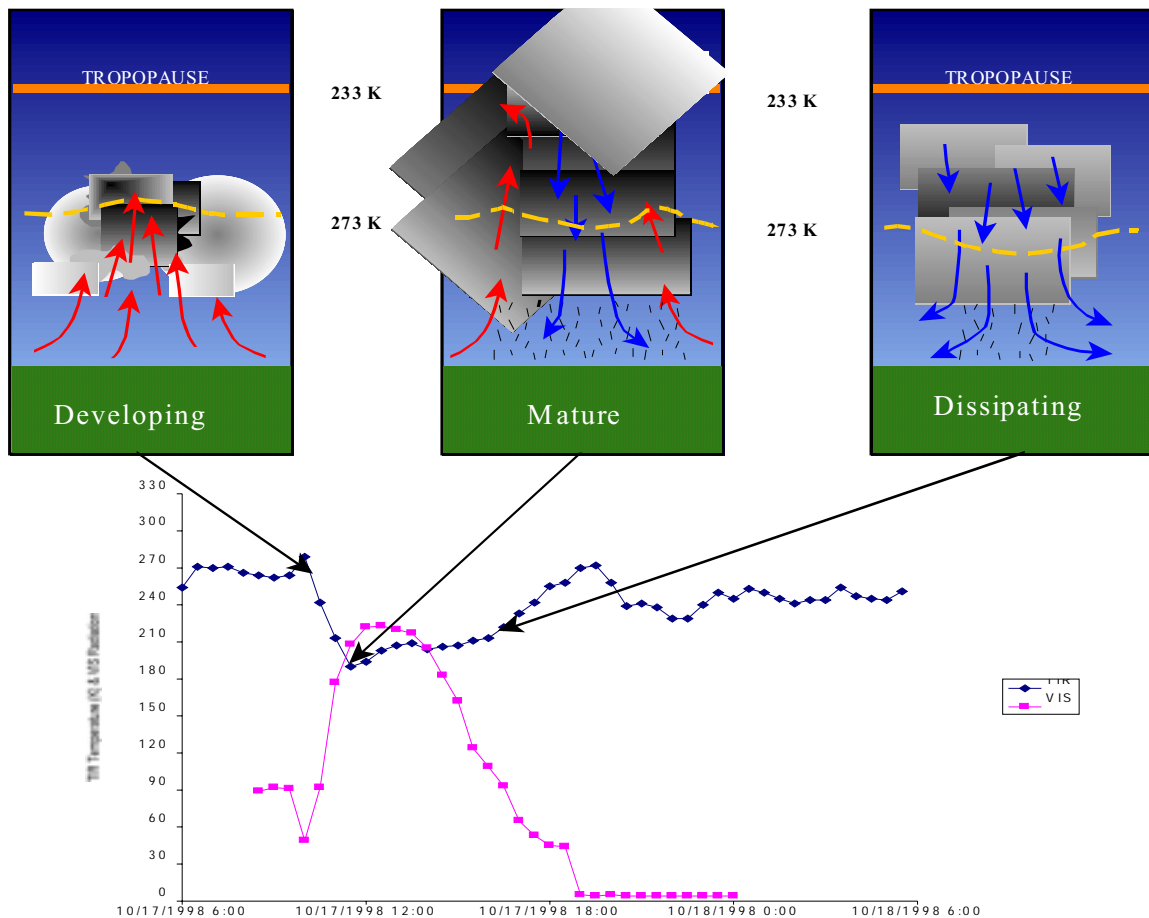


Figure 4.1.1: Infrared and Visible pattern during a typical convective storm

This work improves the approach of **Georgakakos et al. (2000)** in the following aspects:

1. The IR patterns selected for training the MFFNN are not chosen according to their resemblance to an idealized model, but because they correspond to pixels categorized as convective in a contemporaneous TRMM PR swath. The non-convective patterns are chosen among the patterns corresponding to pixels categorized as non-convective by TRMM.
2. TRMM PR rain type information is also used for validating the MFFNN ability to discriminate between convective and non-convective patterns.
3. The neural network is trained to recognize only IR patterns, since the daily variation of the VIS signal, especially that transmitted by Meteosat satellites, makes long sequences of VIS data difficult to use.

4. The IR patterns are composed of between five and eight IR values around the onset of the developing phase of the storm. Shorter IR patterns limit the computation time, reduce the effect of missing slots, and are less sensitive to storm duration variability.
5. The explored MFFNNs architectures include both three-layer and four-layer MFFNNs with several combinations of nodes.

Artificial Neural Networks (ANN) are mathematical devices designed to mimic the information-processing patterns of the biological neural networks in the brain. A description of ANN is outside the scope of this report, but a good and concise description of the neural network properties and applications in hydrology can be found in ASCE, 2000a and 2000b. However, some neural network features for convective pattern recognition may be of interest:

- Three or four-layer MFFNN with sigmoidal activation functions;
- Number n of input values varying between five and eight;
- Number of nodes in the first hidden layer (the one closer to the input layer) set to n , $2*n$, $3*n$, $4*n$, or $5*n$;
- Number of nodes in the second hidden layer (if present) set to n ;
- Output value close to one if a convective pattern is present in the input sequence, close to zero otherwise.

ANN training is done offline and does not interfere with operational convective storm identification. Namely, for each pixel (i,j) and time slot t the ANN determines if a convective pattern is present in the sequence $IR(i,j,t), \dots, IR(i,j,t+n)$ (Figure 4.1.2).

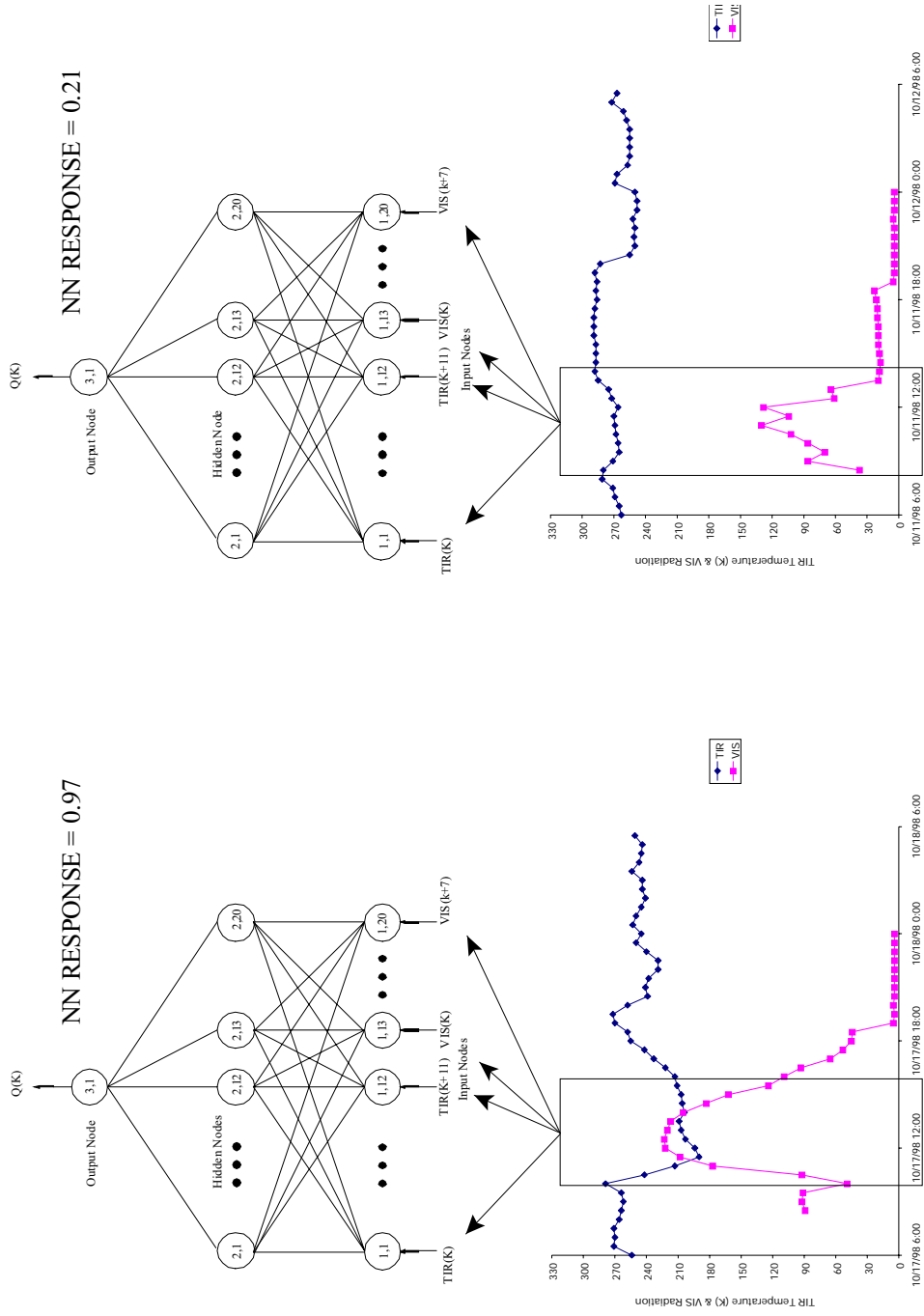


Figure 4.1.2: Schematic of MFNN application for convective storm identification

4.1.1 The training and verification data sets

As mentioned in the previous section, the MFNN is trained to recognize a set of convective and non-convective IR patterns (training set). A key issue in this process is identifying when to stop the training. If a neural network is under-trained, it will only be able to identify the dominant features of the patterns, resulting in large errors. On the other hand, if over-trained, the network essentially memorizes the specific patterns in the training set, but cannot identify other similar signals. In view of this, the approach adopted herein was to train the network on a first data set, and to determine when to stop training based on its predictive performance over a second data set (verification data set).

Selecting the convective patterns for the training/verification sets

TRMM PR rain type data from the first ten days of each month of 1998 for a total of 1081 patterns were used to select the convective pattern candidates for the MFNN training and verification sets. However, past work with TRMM data in the Lake Victoria region suggested that the IR patterns associated with convective storms could be clustered into three clearly distinct shapes (Figure 4.1.3):

Deep and steep convection

The IR traces belonging to this class (Figure 4.1.3 A) are characterized by a strong and rapid IR dip (minimum IR below 230 K; dIR/dt of at least -26 K hr^{-1}). In Figure 4.1.3 A, the solid purple line marks the borderline with shallow convection, while the green and triangle line marks the borderline with deep, but slowly building, convection. This class accounts for 70.2% of patterns and features an average rain rate of 27 mm hr^{-1} .

Shallow convection

The IR traces belonging to this class (Figure 4.1.3 B) are characterized by a shallow convection (minimum IR above 230 K) and are frequently found over mountainous areas. This category accounts for 14.2% of patterns and features an average rain rate of 17.4 mm hr^{-1} .

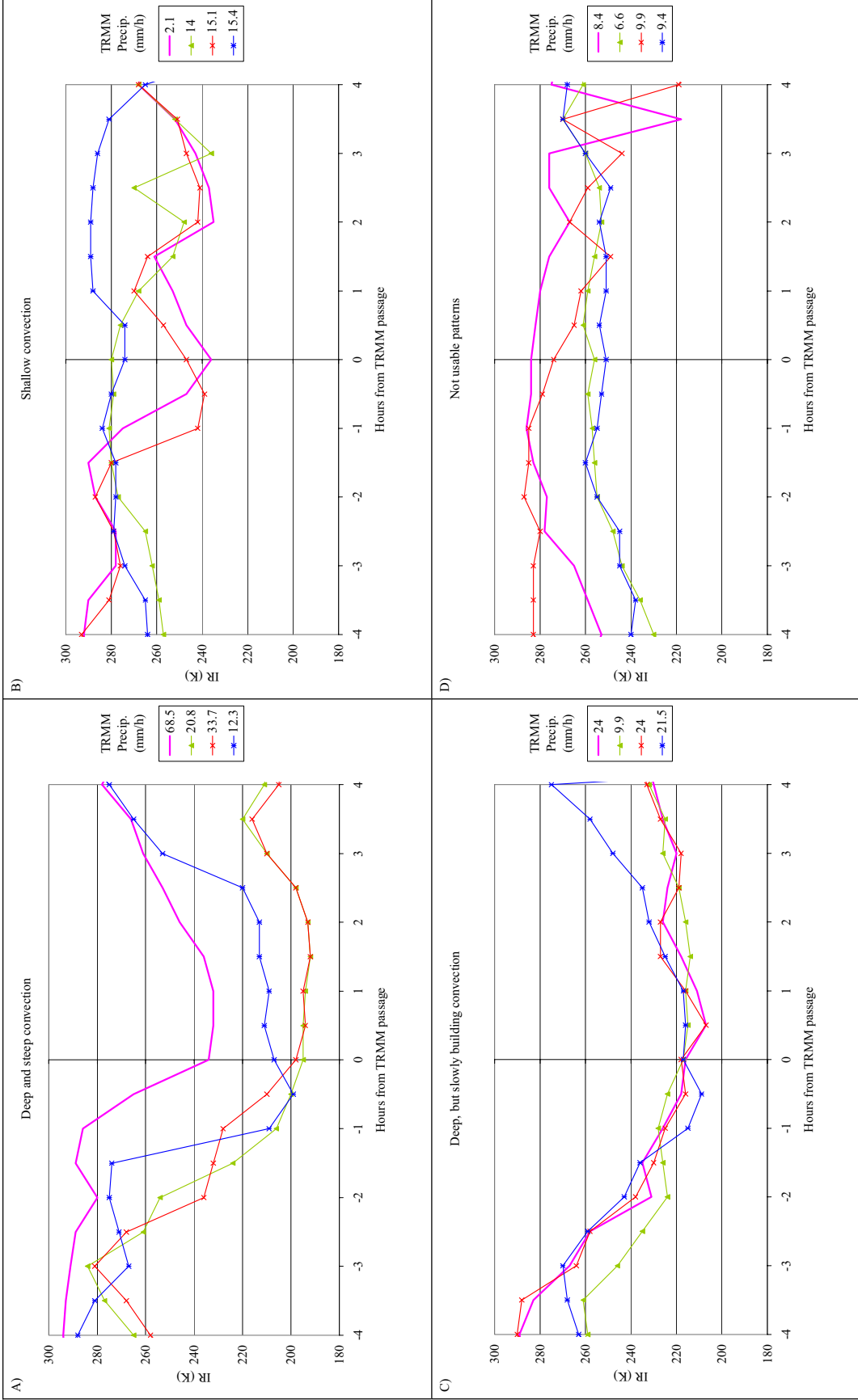


Figure 4.1.3: Convective pattern classification

Deep, but slowly building convection

These IR traces (Figure 4.1.3 C) display strong, but gradual, IR dips (minimum IR below 230 K; dIR/dt of less than -20 K hr^{-1}) and are frequently found over the lake surface.

This class accounts for 13.4% of all patterns and has an average PR surface rain of 22.8 mm hr^{-1} .

A small fraction of patterns (2.2%) does not fall in any of these three categories nor does it show an alternative common behavior (Figure 4.1.3 D).

Mixing these distinct patterns in the same training/verification sets would have diminished the sharpness of the ANN. Since the large majority of the convective patterns fall in the first category that features the largest average rain rate, it was decided to train the neural network to recognize only this type of convective patterns. Further, the convective patterns were aligned around the time at which the IR dip reaches $IR=240 \text{ K}$ to emphasize the common pattern (Figure 4.1.5).

Selecting the non-convective patterns for the training/verification sets

A set of patterns corresponding to non-convective patterns must be included in the training set. These patterns (Figure 4.1.4) include clear sky (solid purple line) and shallow convective patterns (green line with triangles). Since the purpose of the neural network is to mark the onset of a convective storm, the set also incorporates IR traces corresponding to the period antecedent to the storm (red line with x), its mature stage (blue line with asterisks), and its dissipating phase (dashed dark blue line).

TRMM PR Rain Type maps from the first ten days of each month of 1998 were used to (1) identify non-convective pixels that were at a distance of at least one or two pixels from the nearest convective pixel, and (2) to determine the direction in which storms were moving for selecting pixels at their antecedent, mature, and dissipating phases. With these additions, the training and verification sets consisted of 379 convective and 379 non-convective patterns each, listed alternating elements of the two types to achieve a balance between convective and non-convective patterns.

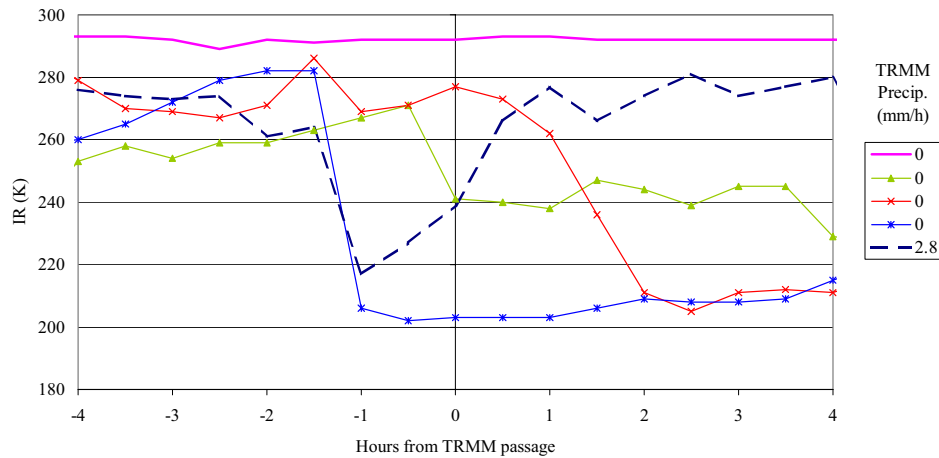


Figure 4.1.4: IR traces for non convective patterns

4.1.2 Calibration and validation of artificial neural networks

The performance of the ANN architectures described in section 4.1.1 were evaluated using the following indicators:

$$AWES = 1 - POD + FAR$$

$$POD = \frac{C_c}{C_c + N_c}$$

$$FAR = \frac{C_n}{N_n + C_n}$$

where

AWES = Area-Weighted classification Error Score (Todd et al., 1995);

POD = Probability of Detection;

FAR = False Alarm Rate;

C_c = number of convective patterns detected as convective by the MFFNN;

C_n = number of non-convective patterns detected as convective by the MFFNN;

N_c = number of convective patterns detected as non-convective by the MFFNN;

N_n = number of non-convective patterns detected as non-convective by the MFFNN.

The verification set was developed independently of the set used to calibrate the MFFNN, but it also consisted of the same type of convective and non-convective patterns. This set was also used to determine model biases and weights. Thus, to assess model

performance, it became necessary to use a third set of patterns completely independent from the training and verification sets. The third set will be referred to as the validation set and was developed from all IR patterns coincident with a TRMM PR convective pixel during the last 20 days of each month of 1998. It also included all non-convective patterns associated with non-convective TRMM PR pixels at a distance of three or more pixels from any fully or partially convective pixel during the same period.

Verification POD was above 0.98 and FAR below 2% in all configurations, but shorter input traces featured higher POD and AWES, probably because reduced input lengths are less affected by the variability in storm duration and evolution. However, this trend stopped or even reversed at the 5-value input configuration. The Verification FAR did not seem to depend significantly on the length of the input. There was no apparent relation between the number of ANN layers and nodes and its performance over the verification set, other than the observation that the two layer MFFNNs with many nodes in the first hidden layer performed somewhat worse than the rest of the ANNs.

Validation statistics were also impressive given that they were derived from a completely independent set of data: POD is in the 78-81% range, a high value considering that the validation set included also isolated fully convective pixels and percentages of “shallow convection”, “deep, but slowly building convection”, and “Not usable” patterns likely similar to the training/verification period. The validation FAR is in the 3-5% range, also notably low. Similarly to verification, validation POD and FAR decreased with the number of input values.

The best results were obtained with 6-value inputs (Figure 4.1.5) followed by 5-value inputs. This is positive because a reduced input set is less computationally demanding and less affected by missing values. It also reduces the delay in providing real-time precipitation estimates. Among all ANN architectures with 6 input values, the best was the one with two hidden layers of six nodes each. Its validation performance is as follows:

$POD_{\text{valid}} = 0.81$; $FAR_{\text{valid}} = 0.04$; $AWES_{\text{valid}} = 0.23$

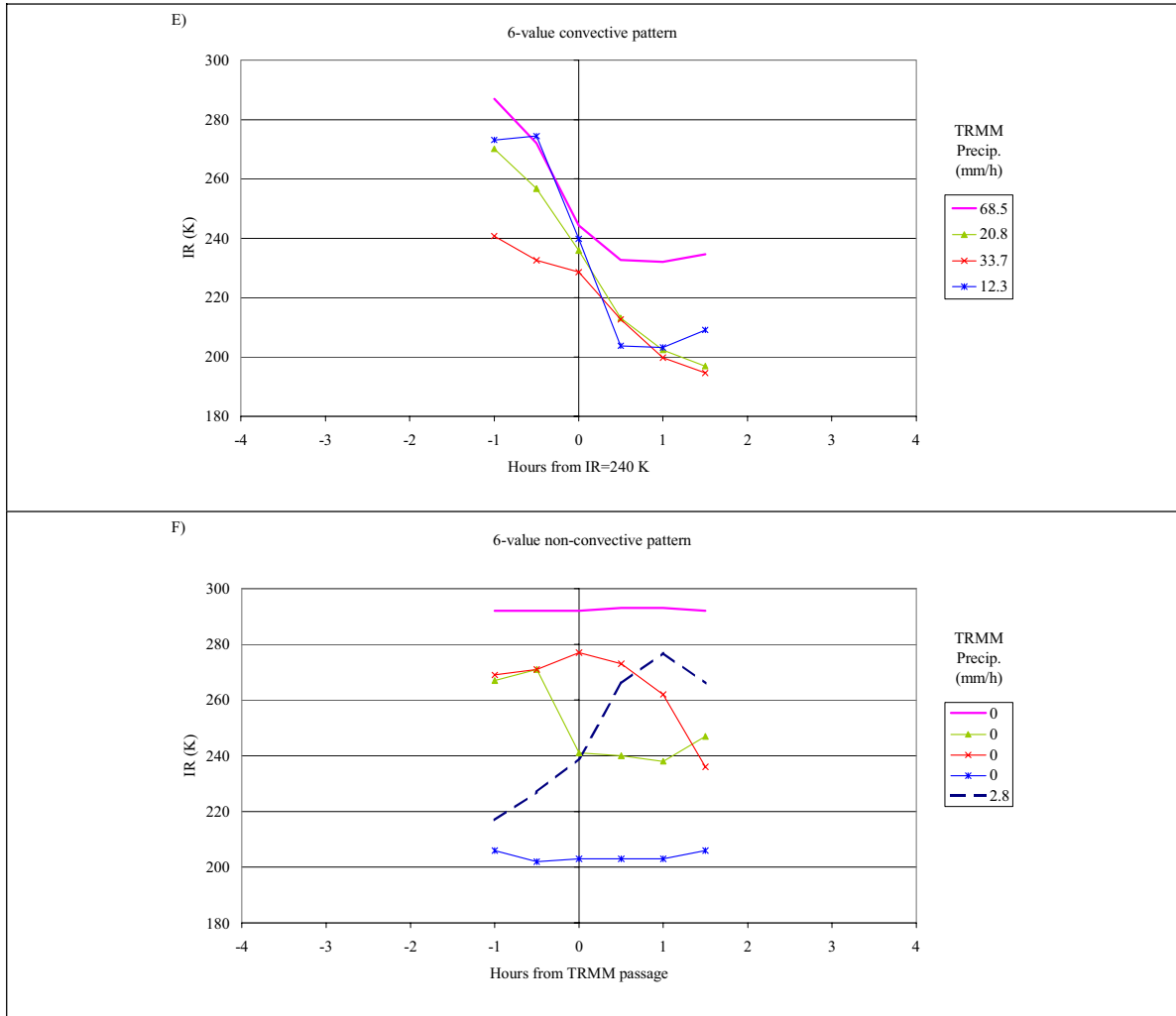


Figure 4.1.5: Convective and non-convective traces used for training six-value neural networks

4.2 Relation between IR, stage, and precipitation

The frequency of TRMM measurement of precipitation at any given location around the equator varies between once a day for TMI to once every three to four days for PR. Consequently, TRMM images provide a spatial distribution of precipitation, but cannot directly provide its temporal distribution. On the other hand, when properly

synchronized, the geostationary IR signals in pixels belonging to the same storm show a strong similarity (Figure 4.2.1). It can be argued that, at any given time, neighboring pixels are experiencing different temporal phases of the same storm evolution. Therefore, the TRMM snapshot of precipitation can be also viewed as an image of the rain-rates associated with different temporal stages of the storm. A proper synchronization of the TRMM samples according to the storm stage instead of the measurement time allows for reconstructing the temporal distribution of precipitation for the storm from the TRMM image (Figure 4.2.1).

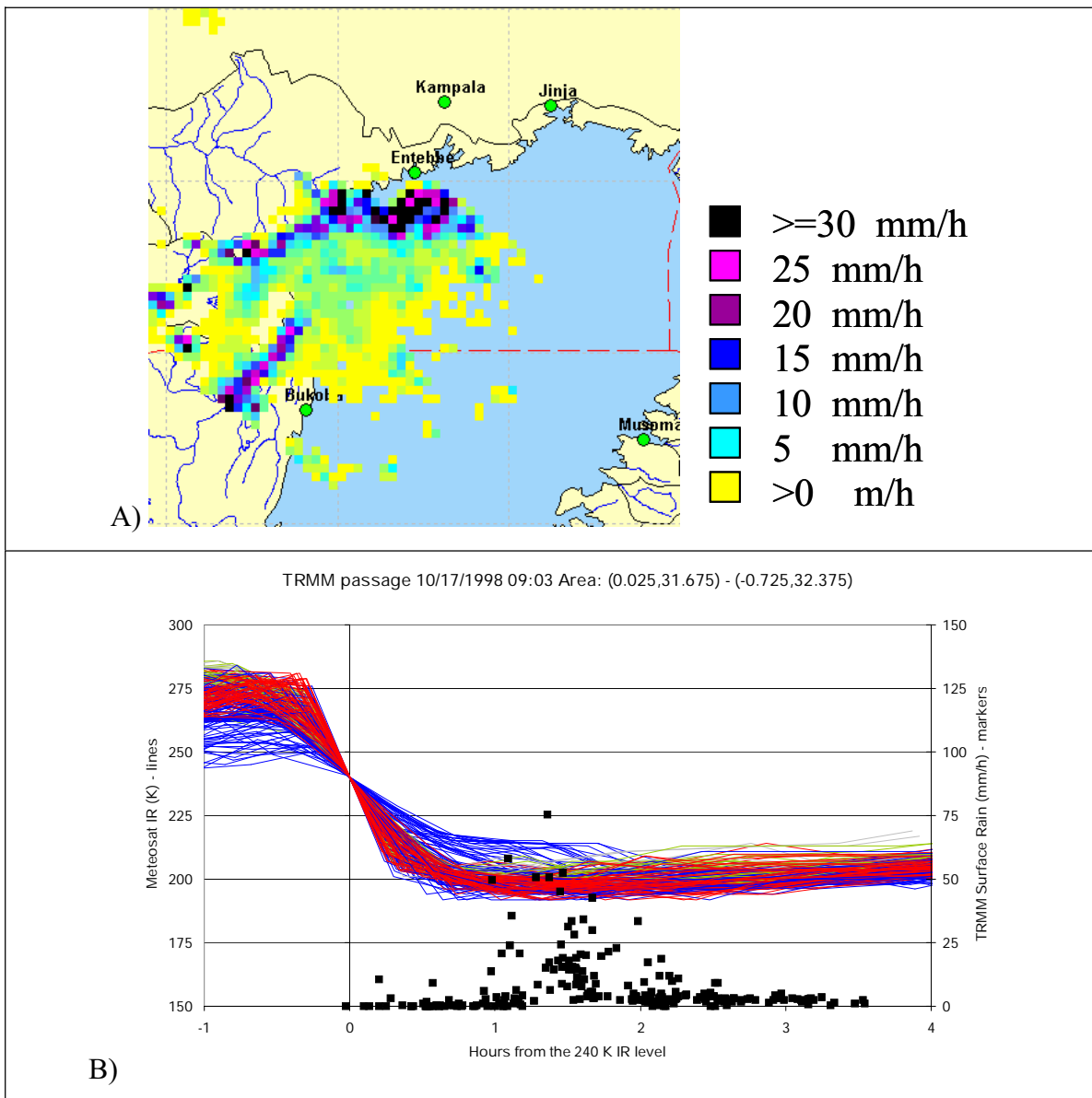


Figure 4.2.1: A) TRMM PR spatial rain distribution; B) Temporal precipitation distribution derived from synchronizing the corresponding IR patterns around the IR=240 K point

A good point for synchronizing the storm IR traces appears to be the time when IR reaches 240 K during the IR dip, which is characteristic of the developing phase of the convective cell (Figure 4.2.1). Since the traces used for training the neural network for recognizing the onset of a convective storm were synchronized around this temperature, the time when the neural network peaks can also be used as a synchronizing point. In this case, the neural network not only identifies the presence of a convective storm over a pixel, but also defines its stage evolution index by the number of half-hour timeslots from the neural network peak.

It is assumed that the storm ceases to affect a pixel when the pixel IR temperature returns to 253 K or higher. Further, the storm stage index varies from one (30 minutes before the Neural Network indicates the convective event) to twenty (ten hours later). The precipitation rate at the twentieth time slot after the neural network peak (NN+20) is used for the rare cases when the storm lasts more than ten hours.

Figure 4.2.2 and Figure 4.2.3 show the average precipitation rate derived from 1998-1999 TRMM PR surface rain data as function of IR and storm stage respectively for Lake Victoria pixels and land pixels between 2000m and 3000m elevation. The “All Pix” curves include all available pixels without distinction of storm stage. The “Non-CI” curves represent the precipitation rate of pixels not identified by the neural network as belonging to a convective storm.

Chart A shows that the convective storm classification captures the large majority of intense-rain pixels since the “Non-CI” precipitation is mostly lower than the average precipitation. The second slot after the neural network peak corresponds to more or less the middle of the IR decrease during the development phase and shows high precipitation intensity over the entire IR range, with increased strength in the lower IR.

The following slots (Chart B) have precipitation curves of similar shape, but intensity decreasing with the distance from the neural network peak. Remarkably, precipitation intensity for the same IR varies considerably with stage number confirming the assumption that precipitation rate depends on storm stage. Also, the shapes of the precipitation curves vary considerably with orography. Rain intensity at low IR is higher over the lake than over the land, while the reverse is true for IR above 230 K.

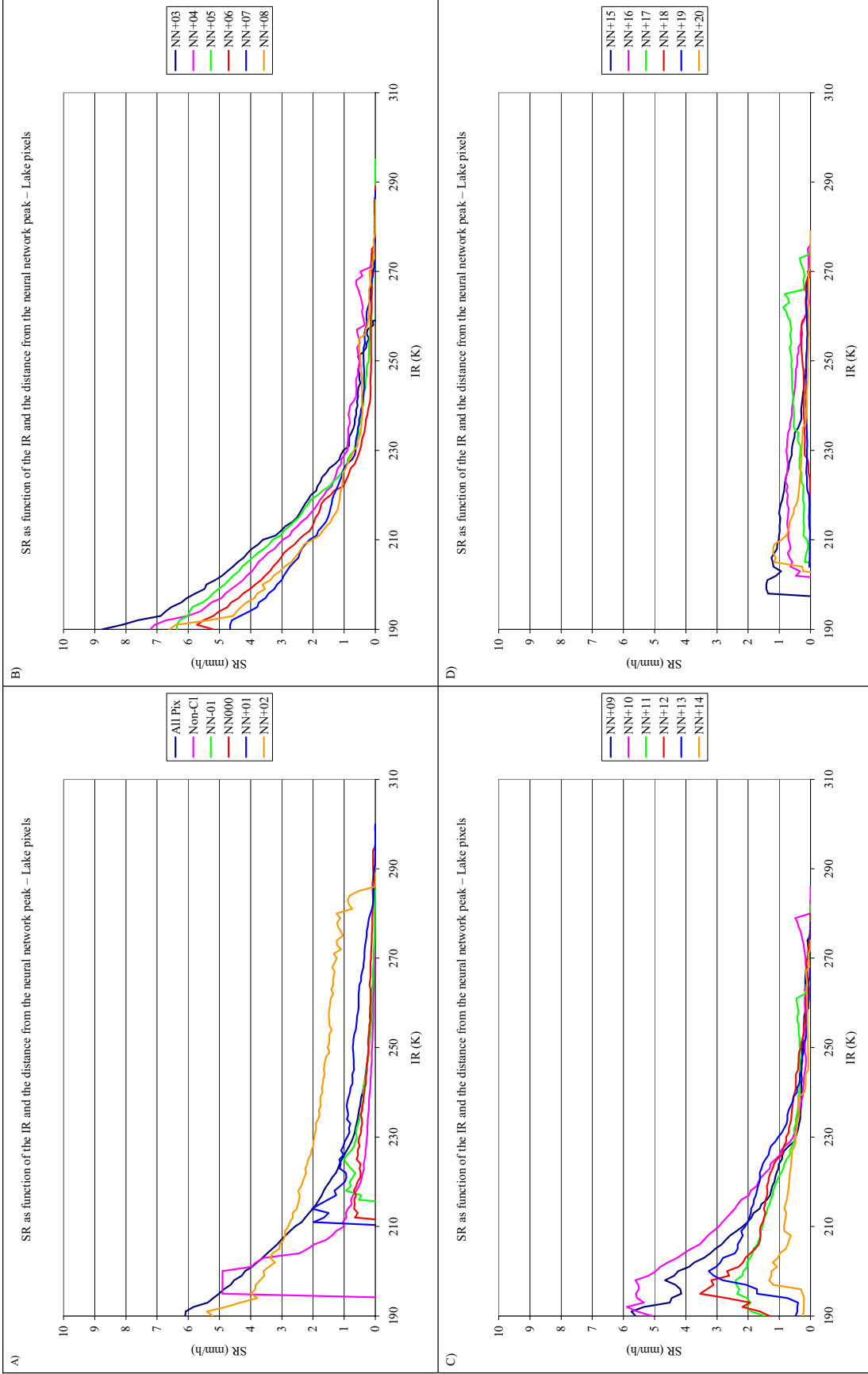


Figure 4.2.2: TRMM PR surface rain distribution as function of IR and distance from the neural network peak (stage) for Lake pixels

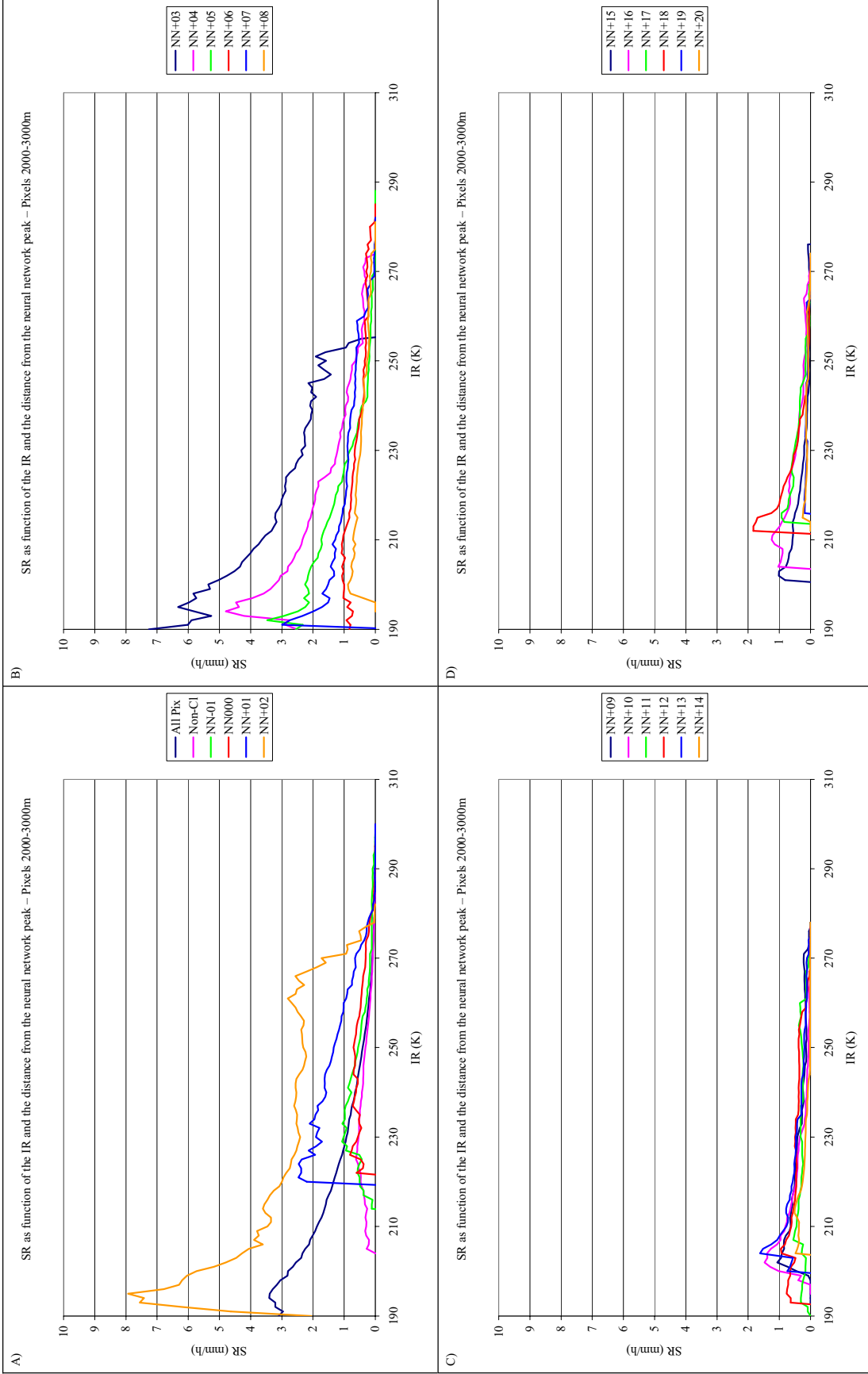


Figure 4.2.3: TRMM PR surface rain distribution as function of IR and distance from neural network peak for 2000-3000 m pixels

5 Single Pixel Analysis

5.1 Characteristics of the single pixel estimation process

Precipitation estimation at the pixel level is obtained by integrating the identification and temporal evolution of convective storms described in Chapter 4 with the estimation structure described in Chapter 2. Some implementation details of the estimation process are noted next:

Determination of the rain-rate distributions

The rain-rate distribution as function of IR, VIS/WV, storm stage, orography, and month have been derived from 816 TRMM passages over the Lake Victoria area during 1998-1999. This data base consists of more than 1.9 million points.

Number of traces in the precipitation ensemble

Increasing the size of the ensemble reduces the uncertainty in the ensemble statistics introduced by the random selection of the half-hour precipitation rates composing the ensemble. By contrast, increasing the size of the ensemble also linearly increases the computation time. Table 5.1.1 shows that a minimum of 200 ensemble elements is required for having stable simulation results.

Table 5.1.1: Variation of precipitation estimation statistics using the median of the ensemble for different ensemble sizes

	Entire period	Daily			Dekad			Month		
Ensemble elements	Bias/Gage	Corr	MAE/Gage	95%C	Corr	MAE/Gage	95%C	Corr	MAE/Gage	95%C
50	0.033	0.439	1.102	0.904	0.646	0.553	0.801	0.741	0.387	0.753
100	0.034	0.442	1.100	0.911	0.648	0.552	0.807	0.744	0.385	0.759
200	0.035	0.443	1.098	0.905	0.649	0.551	0.795	0.743	0.386	0.739
400	0.035	0.445	1.098	0.907	0.648	0.551	0.797	0.744	0.385	0.741

Orography

Figure 4.2.2 and Figure 4.2.3 show that there are deep differences in the precipitation distribution over different geographical areas. Incorporating these differences in the

estimation procedure translates into better precipitation estimates. Among several different partitions of the TRMM data according to orography, the one reported in Table 5.1.2 has proved to be most robust.

Table 5.1.2: Partitioning scheme of the TRMM pixels according to the pixel orography

Region of application	Lake	0-1000m		1000-2000m		2000-3000m	
TRMM SR pixels for precipitation distribution		min	max	min	max	min	max
	Lake	0	1250	750	2250	1750	3250

This partitioning scheme subdivides the testing area into four regions: the Lake Victoria, and the land pixels below 1000 m, between 1000 and 2000 m, and between 2000 and 3000 m. Since there are no rain-gages above 3000 m, this area is not considered here. In an operational use of the procedure, a fifth region considering these pixels must be added. Only SR data from the Lake Victoria pixels are used for deriving the rain-rate distribution used over the Lake region. The rain-rate distributions for the three elevation bands of the land pixels are derived using SR data from pixels up to 250 m above and below the elevation band boundaries. This extension is necessary to include enough data to yield sufficiently detailed precipitation distributions even when several input variables are considered. The amount of TRMM data in 1998-1999 is not sufficient for designing a more detailed partitioning scheme.

Monthly distributions

There are several reasons why it is useful to include a certain degree of seasonality in the choice of the rain-rate distribution:

- In certain periods of the year cold, but non-rainy, clouds like the cirri may be more common than the cold, but rainy clouds like the cumuli or nimbo-cumuli;
- Availability of humidity in the air may affect the precipitation generated from similar type of clouds. This is especially true during the monsoon and the dry seasons.
- Albedo has a seasonal pattern that is only partially corrected by the solar angle correction.

The approach taken in this research is to generate a different rain-rate distribution for each month. However, given the limited amount of data available, using truly monthly distribution causes a decrease in the detail of the relation between rain-rate and IR/VIS or IR/WV, resulting in better statistics at the monthly level, but worse at the daily. As a compromise, the “monthly” precipitation distributions are therefore generated using TRMM data from the specific month and from the month before and after.

IR and VIS screening

Meteosat images are affected by thermal noise and sometimes from slight changes in the satellite position and inclination that cause geometric error in the images. Further, several Meteosat images were missing and were substituted with data obtained from linearly interpolating the closer available images. TRMM PR surface rain data are also affected by thermal noise and may be affected by spurious echoes, especially over mountains. The resampling of the Meteosat and TRMM images to a regular grid introduces a further source of error. Finally, and likely most importantly, TRMM and Meteosat images are not always coincident, but may be spaced up to 15 minutes apart. All these errors cause precipitation rates to be wrongly attributed to high IR and low VIS, thus increasing the estimation bias and decreasing its correlation. To decrease the impact of this phenomenon, precipitation rates corresponding to $IR > 258K$ and $VIS < 40\%$ have been screened out.

Statistics for evaluating the precipitation estimate ensemble approach

To assess the effectiveness of the proposed precipitation estimation approach, two aspects must be considered at the same time:

- The ability of the ensemble average to track the behavior of the gage records;
- The capability of the ensemble to represent in a statistically meaningful way the uncertainty of the precipitation patterns.

The first aspect is quantified by commonly used statistics:

Bias (Bias): For a single gage it is the difference over the simulation period between the total gage precipitation and the average of the ensemble total precipitation. This value is given as percentage of the total gage precipitation given the large variation in the precipitation patterns around the basin. When applied to a group of gages, this statistic is the average of the single rain-gage relative biases.

Absolute Bias (Abias): it is used only when considering a group of rain-gages. It is the average of the absolute value of the single rain-gage relative biases. It gives a measure of the spread of the biases.

Correlation (Corr): For a single gage it is the correlation coefficient between the ensemble average and the corresponding rain-gage record over the same estimation period (day, dekad, or month). When applied to a group of gages, this statistic is the average of single rain-gage correlation.

Rank correlation (Rcorr): For a single gage it is the correlation coefficient between the rank of the ensemble average and the rank of the corresponding rain gage record over the same estimation period (day, dekad, or month). When applied to a group of gages, this statistic is the average of single rain-gage rank correlation.

Mean Absolute Error (MAE): For a single gage it is the average of the absolute difference between the gage record and the ensemble average over the same estimation period (day, dekad, or month). This value is given as percentage of the average gage precipitation. When applied to group of gages, this statistic is the average of the single rain-gage MAE.

The capability of the ensemble to represent in a statistically meaningful way the precipitation variability at the gage is quantified by the following statistics:

Average ensemble 95% width (95%R): For a single gage, it is the average of the differences between the 2.5-percentile and the 97.5-percentile of the estimate ensemble. When applied to a group of gages, it is the average of the single rain-gage 95% widths.

Ensemble 95% compliance (95%C): For a single gage, it is the frequency at which the gage records fall between the 2.5-percentile and the 97.5-percentile of the ensemble. When applied to a group of gages, it is the average of the single rain-gage 95% compliances.

Lower end 95% error (95%L): For a single gage, it is the frequency at which the gage records are less than the ensemble 2.5-percentile. When applied to a group of gages, it is the average of the single rain-gage lower end 95% error.

KS-statistics (KS): For a single gage, it is the maximum of the absolute difference between the distribution of the ensemble-percentiles corresponding to the gage readings and the 0-1 uniform distribution. The rationale behind this index is that the ensemble represents the variability of precipitation in a statistically meaningful way if the gage position with respect to the ensemble is uniformly distributed over the entire range. When applied to a region, it is the average of the single rain-gage KS statistics.

90% KS acceptance (KS₁₀): For a single gage, it is the difference between the gage KS statistic and the threshold below which rejecting the hypothesis that the percentile distribution is 0-1 uniform implies a 10% error probability. For groups of rain-gages, it is the number of gages that have a KS statistic below the critical threshold.

99% KS acceptance (KS₀₁): For a single gage, it is the difference between the gage KS statistic and the threshold below which rejecting the hypothesis that the percentile distribution is 0-1 uniform implies a 1% error probability. For groups of rain-gages, it is the number of gages that have a KS statistic below the critical threshold.

5.2 Estimation model performance

5.2.1 Model calibration (1996-1998)

The calibration dataset is composed of 61 gages distributed over the elevation range 630-2300 m and located mostly in the northern and western sides of the basin (Figure 3.3.1 A). Before the presentation of the results, it is noted that some parameters of the estimation procedure described earlier (i.e., IR and VIS thresholds, number and limits of the orographic bands, use of tri-monthly precipitation distribution, among others) were selected to optimize the results over 1996-1998. In selecting these parameters, however, care was exercised to ensure that this selection was not too specific to the calibration dataset. For example, better results could have been obtained if the elevation bands used for regionalizing the rain-rate distributions were 0-1100, 1100-2000, and 2000-3000 meters instead of the more regular 0-1000, 1000-2000, 2000-3000 m actually adopted. Furthermore, slightly better results would have been obtained if VIS screening was performed at 41% instead of 40%. However, such improvements would be minor and would not add to the general applicability of the method.

Table 5.2.1 reports the performance of the single-pixel estimation procedure (IVWU_NN) compared against the performance of the single-pixel adaptation of the GPI technique. According to the later, the rain-rate equals 3 mm h^{-1} if IR is below 235 K, and zero otherwise. Results show that the proposed model has a much better bias than the GPI over the period 1996-1998 and also much better correlation, especially at the daily level.

Table 5.2.1: IVWU_NN and GPI performance for the calibration period (1996-1998)

Day											
Method	Bias/ Gage	Abias /Gage	Corr	RCorr	MAE/ Gage	95%R	95%C	95%L	KS	KS ₁₀	KS ₀₁
GPI	0.77	0.77	0.38	0.51	1.58						
IVWU_NN	0.03	0.13	0.44	0.56	1.10	14.5	0.90	0.03	0.36	0	0
Dekad											
Method	Bias/ Gage	Abias /Gage	Corr	RCorr	MAE/ Gage	95%R	95%C	95%L	KS	KS ₁₀	KS ₀₁

GPI	0.77	0.77	0.60	0.68	0.97						
IVWU_NN	0.03	0.13	0.65	0.72	0.55	63.5	0.80	0.12	0.21	31	39
Month											
Method	Bias/ Gage	Abias /Gage	Corr	RCorr	MAE/ Gage	95%R	95%C	95%L	KS	KS ₁₀	KS ₀₁
GPI	0.77	0.77	0.71	0.73	0.85						
IVWU_NN	0.03	0.13	0.74	0.76	0.39	119.5	0.74	0.14	0.24	27	44

On the other hand, the 95% compliance rate could be acceptable at the monthly level, but is low especially at the dekad and monthly level.

5.2.2 Model validation (1996-1997)

The validation dataset is composed of 42 gages that were not included in the calibration dataset. These gages are distributed over the elevation range 816-2400 m and are located mostly in the southern and eastern sides of the basin, with three gages situated on islands (Figure 3.3.1 A and B).

Table 5.2.2 shows that the proposed model (IVWU_NN) has a bias slightly higher than the bias of the calibration set, but is clearly lower than the GPI bias. The correlation is also higher, reaching almost 0.80 at the monthly level, and continues to be better than GPI's correlation, especially at the dekad level. The 95% compliance rate is a little lower than for the calibration case. Overall, the validation statistics are very similar to the calibration statistics, supporting the hypothesis that the estimation procedure is generally valid, independently of the calibration data set.

Table 5.2.2: IVWU_NN and GPI performance for the validation period (1996-1997)

Day											
Method	Bias/ Gage	Abias /Gage	Corr	RCorr	MAE/ Gage	95%R	95%C	95%L	KS	KS ₁₀	KS ₀₁
GPI	0.87	0.89	0.41	0.50	1.69						
IVWU_NN	0.06	0.17	0.46	0.54	1.14	12.8	0.91	0.03	0.43	0	0
Dekad											
Method	Bias/ Gage	Abias /Gage	Corr	RCorr	MAE/ Gage	95%R	95%C	95%L	KS	KS ₁₀	KS ₀₁
GPI	0.87	0.89	0.63	0.72	1.10						

IVWU_NN	0.06	0.17	0.70	0.76	0.59	58.5	0.77	0.14	0.25	19	26
Month											
Method	Bias/ Gage	Abias /Gage	Corr	RCorr	MAE/ Gage	95%R	95%C	95%L	KS	KS ₁₀	KS ₀₁
GPI	0.87	0.89	0.75	0.77	0.98						
IVWU_NN	0.06	0.17	0.79	0.81	0.42	110.3	0.69	0.20	0.26	20	33

5.2.3 Comparison with Adjusted GPI (TRMM product 3B42).

The GPI method uses a fixed IR threshold at 235 °K to separate rainy pixels from non-rainy pixels and applies a fixed precipitation rate of 3 mm hr⁻¹. The Adjusted GPI (TRMM product 3B42) also uses a fixed IR threshold of 235 °K to discriminate rainy pixels from non-rainy ones, but the rain-rate is calibrated by month and by 1°x1° region. The optimal rain-rate is determined so that the method applied to coincident IR and TRMM TMI images over each area reproduces the total observed monthly TMI precipitation. In

Table 5.2.3 the Adjusted GPI has been derived by applying the appropriate adjusted rain-rate and 235 K threshold to the single-pixel IR sequence. Unfortunately, this product is available since January 1998 only.

Table 5.2.3: Partitioning scheme of the TRMM pixels according to the pixel orography

Day											
Method	Bias/ Gage	Abias /Gage	Corr	RCorr	MAE/ Gage	95%R	95%C	95%L	KS	KS ₁₀	KS ₀₁
GPI	0.67	0.67	0.42	0.53	1.51						
3B42	0.48	0.48	0.41	0.52	1.41						
IVWU_NN	0.04	0.17	0.45	0.58	1.11	13.3	0.91	0.02	0.40	0	0
Dekad											
Method	Bias/ Gage	Bias/ Gage	Corr	RCorr	MAE/ Gage	95%R	95%C	95%L	KS	KS ₁₀	KS ₀₁
GPI	0.67	0.67	0.65	0.70	0.89						
3B42	0.48	0.48	0.63	0.68	0.79						
IVWU_NN	0.04	0.17	0.64	0.71	0.57	59.7	0.79	0.12	0.31	22	36
Month											
Method	Bias/ Gage	Bias/ Gage	Corr	RCorr	MAE/ Gage	95%R	95%C	95%L	KS	KS ₁₀	KS ₀₁

	Gage	Gage			Gage						
GPI	0.67	0.67	0.75	0.75	0.77						
3B42	0.48	0.48	0.72	0.70	0.64						
IVWU_NN	0.04	0.17	0.74	0.73	0.41	112.5	0.72	0.15	0.28	35	44

The 1998 dataset is composed of 48 rain-gages with at least 10 months of valid precipitation data. All gages belong also to the calibration data set.

The 3B42 product bias is substantially lower than the GPI bias, but is still much higher than the IVWU_NN bias. In terms of correlation, IVWU_NN performs better than the other two estimators at the daily level, but is slightly worse than the GPI at the dekad and monthly level. However, it should be noted that monthly correlation with each gage is here computed with only 10-12 samples.

The fact that the IVWU_NN performance over a fraction of the calibration period is very similar to the performance over the entire calibration period indicates that the model performs consistently.

5.2.4 Discussion

The correlation between IVWU_NN and rain gages at the daily level (0.45) seems low, but the following factors should be considered:

1. The single station correlation varies between 0.29 and 0.61.
2. There is a relevant difference in the spatial scale of the gage ($< 1 \text{ m}^2$) and satellite ($>25 \text{ km}^2$) measured precipitation. The shorter the temporal resolution of the precipitation estimate, the higher is expected to be the impact of this difference. This is especially true for the tropics, where precipitation is highly variable.
3. In several parts of the basin, geographical features (mountains, ridges, valleys, and shorelines) strongly influence precipitation patterns even at the sub-pixel level;
4. Daily rain gage data were often of poor quality. It is very likely that quality control has eliminated the most problematic gages, but it is also almost certain that errors still affect several gages, limiting model performance.

Figure 5.2.1 may help to better appreciate the daily correlation between rain-gage and satellite-based precipitation estimates. Gages 10046 and 1000419 are the only two instances in the dataset for which the closest neighboring gage is located within the same pixel. The correlations of these two stations with IVWU_NN are 0.54 and 0.51 respectively, while the correlations of the gages with their closest neighbor are 0.64 and 0.77 respectively.

Overall, IVWU_NN average estimation tracks gage data better than GPI and 3B42, both in terms of bias and in terms of correlation. The performance of the average estimation show good consistency over the entire calibration set (1996-1998), a subset of it (1998), and the validation set (1996-1997), indicating that the method is sufficiently robust. This is especially notable considering that (1) no TRMM data is available for 1996-1997, (2) the visible data were derived according to two different methodologies in 1996-1997 and 1998-1999 (Eumetsat, 2004; Rigolier et al., 2002), and (3) Meteosat changed satellite platform in 1996 and 1998. Further, there is a good potential for improving the estimator performance using more TRMM data.

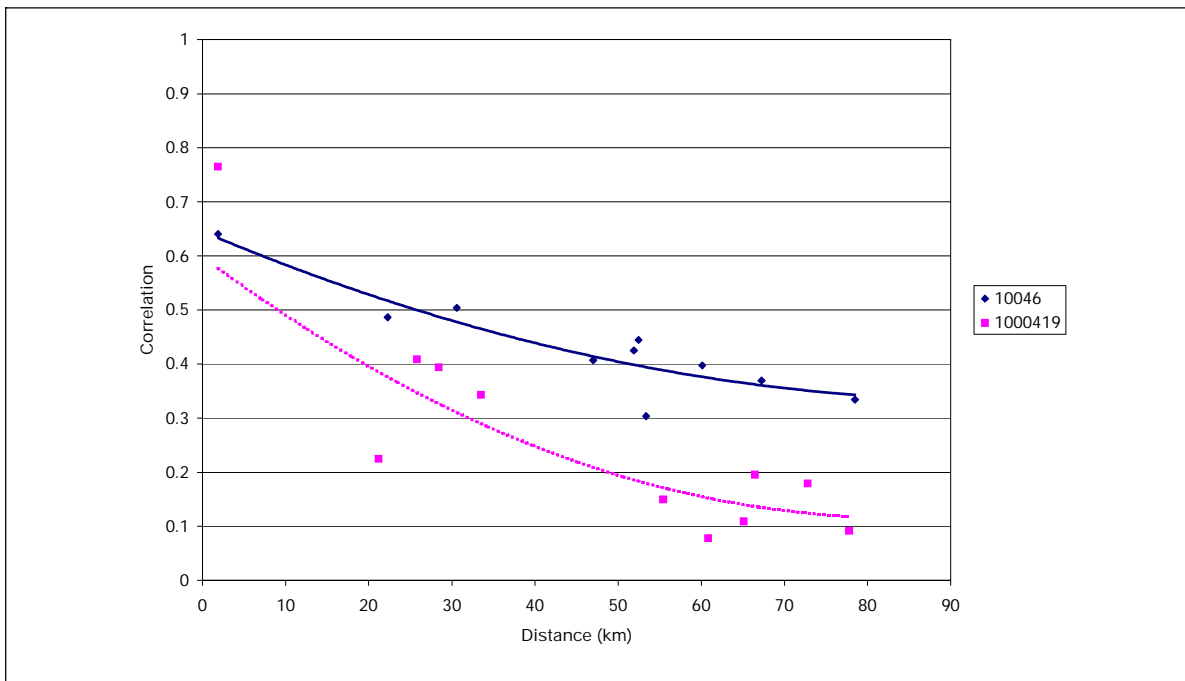


Figure 5.2.1: Rain-gage daily precipitation correlation of as function of gage distance (correlation IVWU_NN-10046 =0.54, IVWU_NN-1000419=0.51)

By contrast, the representation of precipitation variability is not satisfying. The 95% compliance rate can be considered acceptable at the daily level (91%), but not at the dekad (79%) and monthly resolutions (72%).

After extensive investigation, the reason that the model is able to track the precipitation average well, but it is not able to account for the full extent of precipitation variability was attributed to the fact that precipitation rates at consecutive timeslots are chosen independently, ignoring the temporal autocorrelation that may be present. TRMM images do not directly provide a measure of the precipitation temporal autocorrelation. Thus, to test this hypothesis, the precipitation temporal autocorrelation was derived from the spatial TRMM images considering the precipitation correlation in adjacent pixels at stage t and $t-1$ as determined by the neural network (Figure 5.2.2).

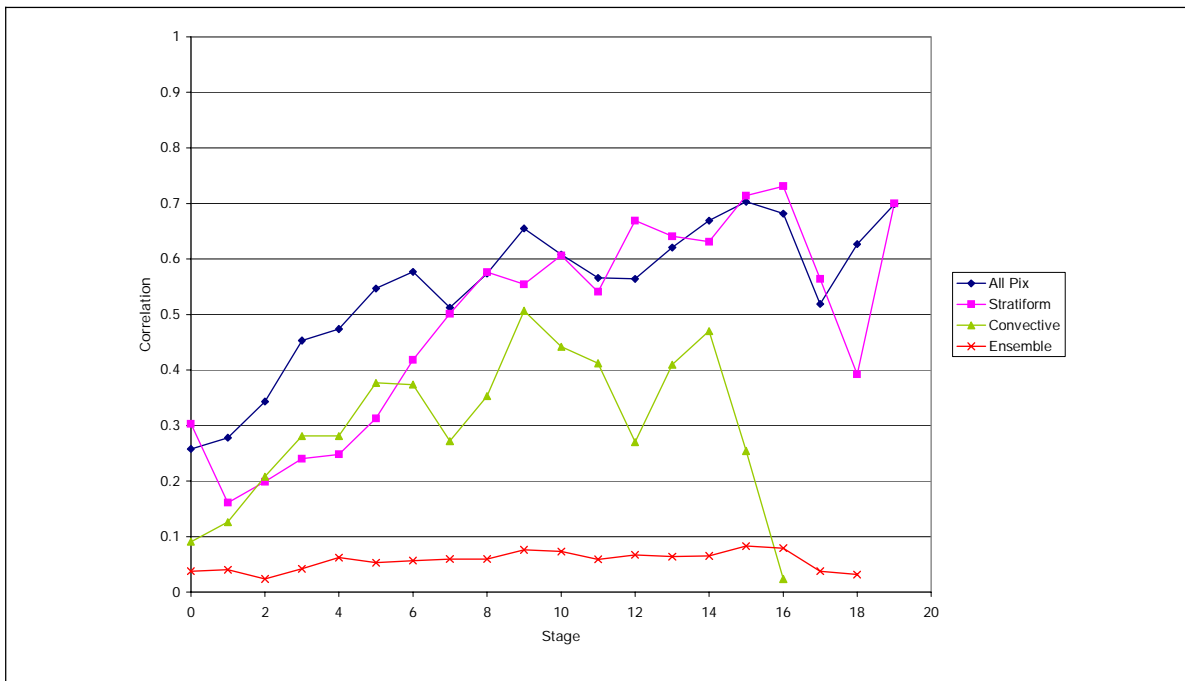


Figure 5.2.2: Lag 1 stage autocorrelation of 1998-1999 TRMM-SR data in the Lake Victoria basin and in the IVWU_NN model.

The precipitation temporal autocorrelation is very significant especially at the later stages, where stratiform or mixed precipitation is dominant. It is also much stronger than

the autocorrelation in the precipitation produced by the IVWU_NN model (the “Ensemble” series of Figure 5.2.2).

5.3 Estimation incorporating precipitation autocorrelation

The one-step autocorrelation of single-pixel precipitation is implemented by conditioning the rain-rate distribution on precipitation at time t-1 in addition to IR, VIS/WV, stage, orography, and month. That is, for each member X of the ensemble:

$$\text{precip}(t) = \begin{cases} f[\text{IR}(t), \text{VIS}(t)/\text{WV}(t), \text{stage}(t), \text{precip}(t-1), \text{orography}, \text{month}, \varepsilon] & \text{stage}(t) \geq 0 \\ f[\text{IR}(t), \text{VIS}(t)/\text{WV}(t), \text{stage}(t), \text{orography}, \text{month}, \varepsilon] & \text{stage}(t) < 0 \end{cases}$$

where

precip(t): precipitation rate at time t for element X;

precip(t-1): precipitation rate at time t-1 for element X;

IR(t): IR at time t;

VIS(t): VIS at time t;

WV(t): WV at time t;

ε : random error;

The derivation of the temporal precipitation relation from TRMM data is possible only for the timeslots belonging to a convective storm. The precipitation over pixels not belonging to a convective storm event (identified by the ANN) is presumed to be temporally uncorrelated.

The rationale of this approach is that the new input variable (precip(t-1)) restricts the pool of available precipitation rates that can be used to build the rain-rate distributions for time t, thus establishing a relation between precipitation at time t and at time t-1. At the same time, an entire set of possible precipitation rates is associated with precip(t-1), thus

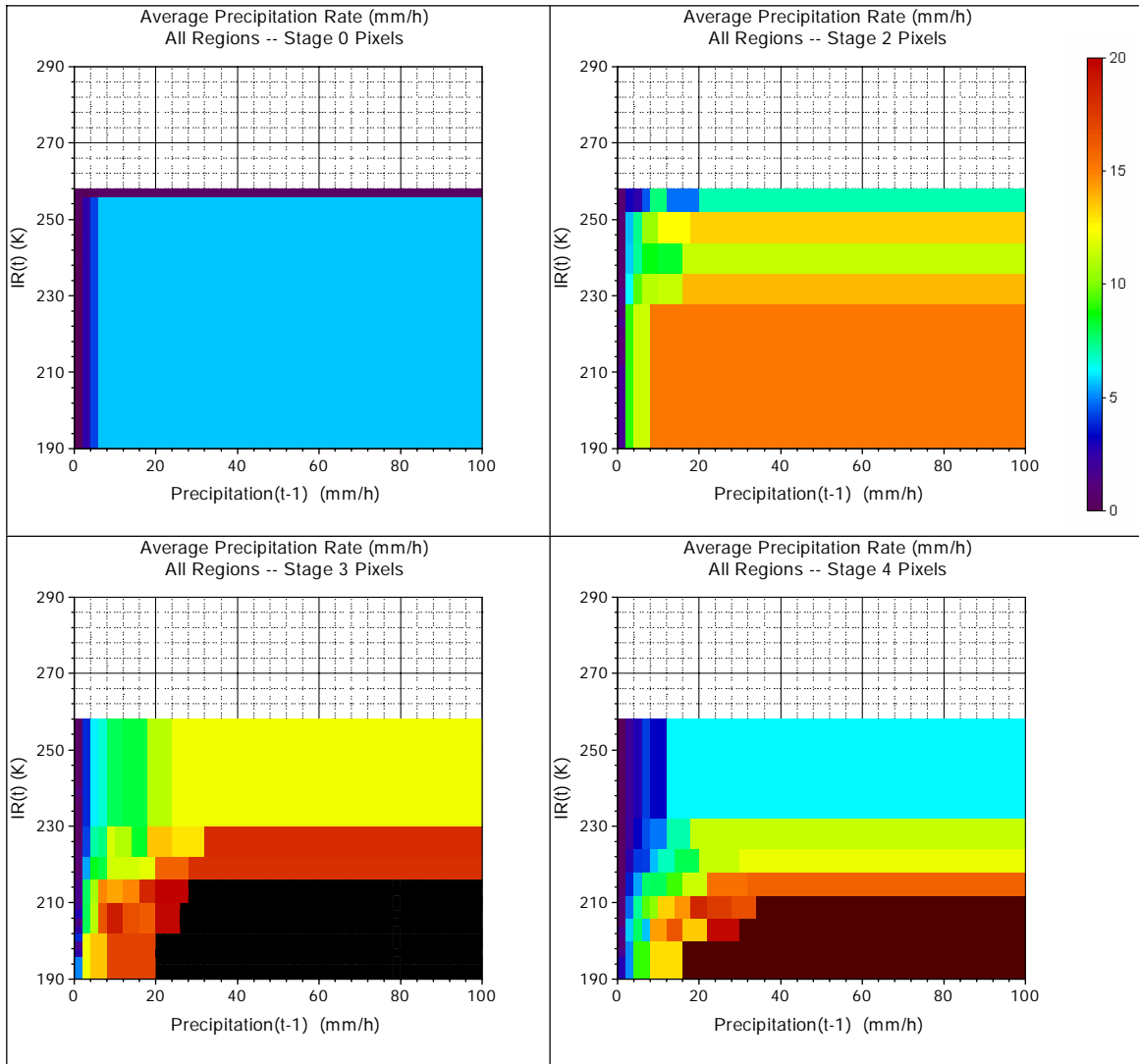
directly accounting for the random component of this relation. An important aspect of this approach is that it is not based on any hypothesis on the probabilistic distribution of the instantaneous rain-rates, something that is very suitable to the markedly skewed distribution of TRMM SR data.

Adding precip(t-1) to the input variable set further fragments the data available for building the rain-rate distributions and prevents the use of VIS(t)/WV(t) and month information during convective storms . Consequently, the precipitation at time t is determined according to the following formula:

$$\text{precip}(t) = \begin{cases} f[\text{IR}(t), \text{stage}(t), \text{precip}(t-1), \text{orography}, \epsilon] & \text{stage}(t) \geq 0 \\ f[\text{IR}(t), \text{VIS}(t)/\text{WV}(t), \text{stage}(t), \text{orography}, \text{month}, \epsilon] & \text{stage}(t) < 0 \end{cases}$$

The average of the precipitation distributions used to determine precip(t) (Figure 5.3.1 and Figure 5.3.2) behaves as expected: the average rate increases with decreasing IR and with increasing precip(t-1). Further, the average rain rate peaks between stages 3 and 7. The segmentation of the IR(t)/precip(t-1) space looks very rough for stage(t)=0, but this is actually due to the fact that most of the precip(t-1) data in this case is zero. The following stages are characterized by a larger variety of precip(t-1), so that the resulting rain-rate map is more finely detailed.

Figure 5.3.2 shows the effect that the subdivision of TRMM PR data according to the orography may have on the average rain-rate mapping and, consequently, on the rain-rate distributions: the lake pixels are barely enough to guarantee an acceptably detailed mapping of the precipitation. For example, precipitation maps for stage 0 to stage 1 and precip(t-1)>0 are insensitive to IR. The future availability of more TRMM PR under this project would enable a more accurate estimation of these relationships.



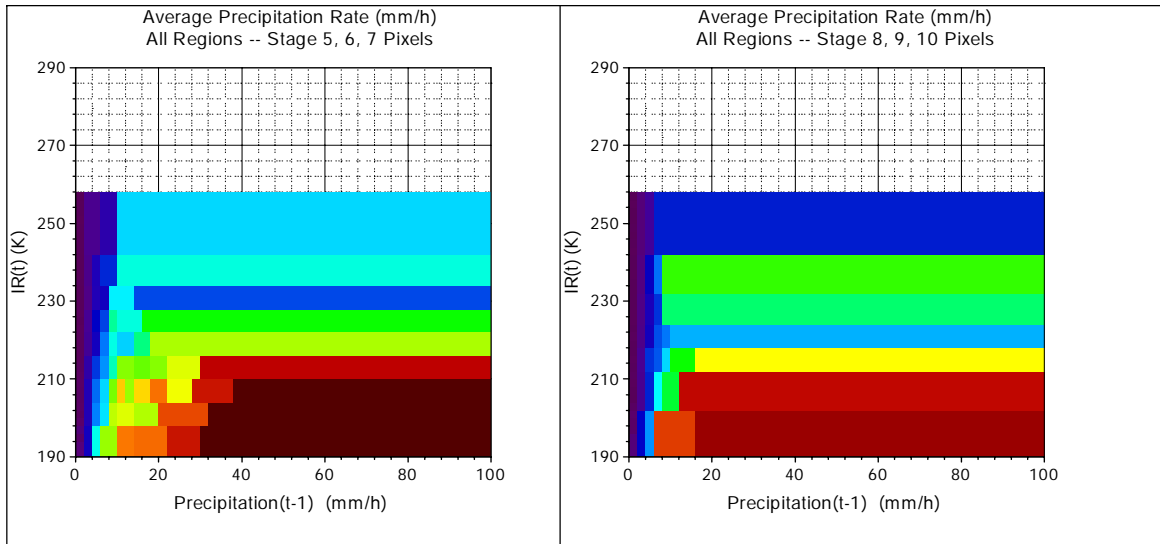
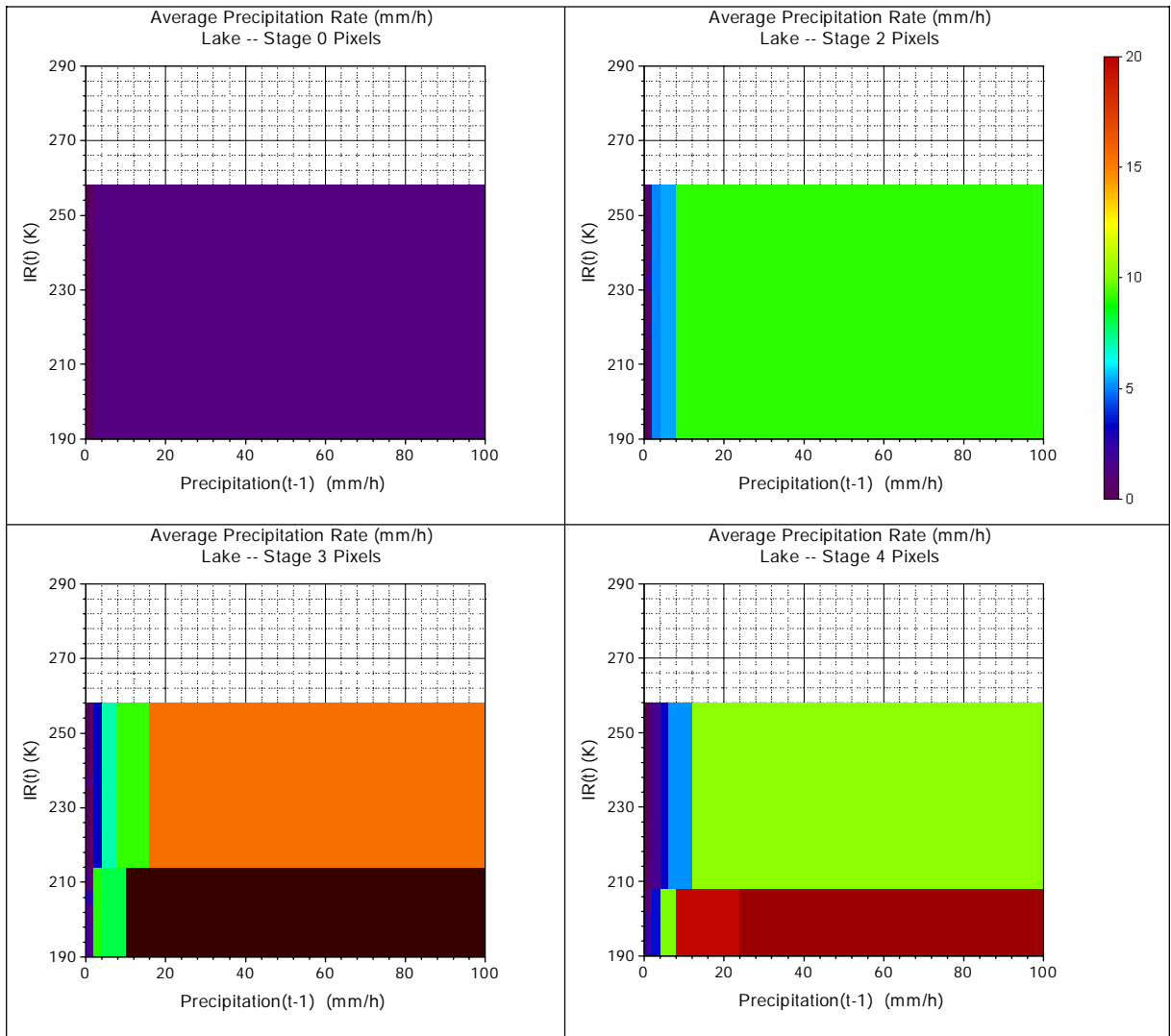


Figure 5.3.1: Average precipitation rate as function of IR and precip(t-1) for all regions and at least 75 TRMM data per bin



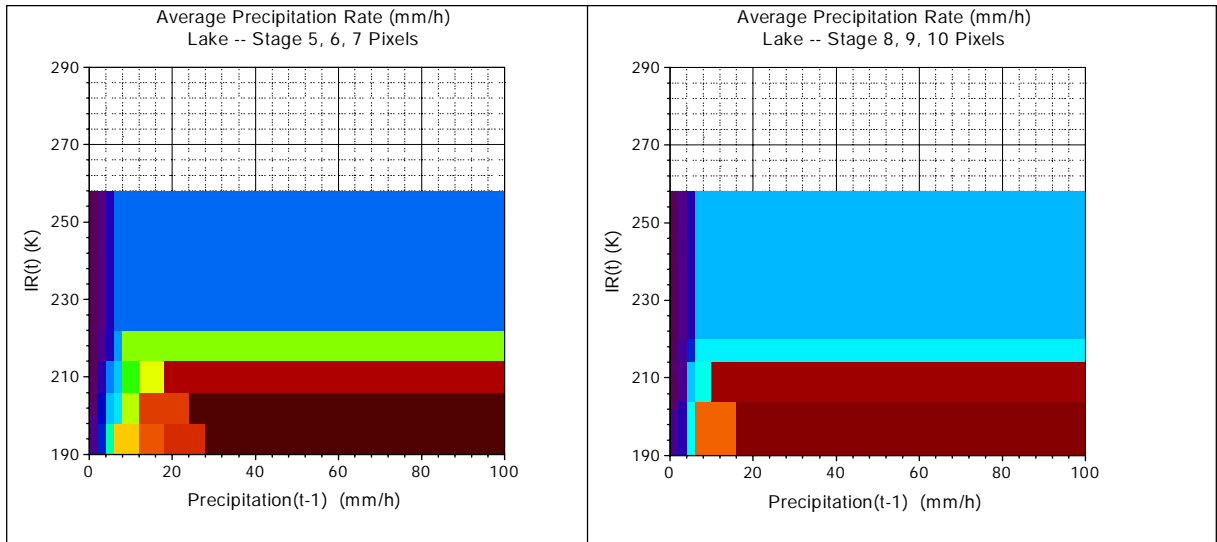


Figure 5.3.2: Average precipitation rate as function of IR and precip(t-1) for lake pixels and at least 75 TRMM data per bin

5.3.1 Autocorrelated model calibration (1996-1998)

Table 5.3.1 reveals that the autocorrelated estimator (IVWA_NN) has a bias similar in magnitude to that of the uncorrelated estimator (IVWU_NN), but a slightly lower absolute bias. On the other hand, its correlation with rain-gage data is lower than that of the IVWU_NN, especially at the monthly level. This is the effect of not including VIS/WV and month in the variable used to identify the precipitation distribution to be used during storm events.

Table 5.3.1: IVWU_NN and IVWA_NN performance for the calibration period (1996-1998)

Day											
Method	Bias/ Gage	Abias /Gage	Corr	RCorr	MAE/ Gage	95%R	95%C	95%L	KS	KS ₁₀	KS ₀₁
IVWU_NN	0.03	0.13	0.44	0.56	1.10	14.5	0.90	0.03	0.36	0	0
IVWA_NN	-0.02	0.12	0.43	0.55	1.09	20.4	0.94	0.00	0.37	0	0
Dekad											
Method	Bias/ Gage	Abias /Gage	Corr	RCorr	MAE/ Gage	95%R	95%C	95%L	KS	KS ₁₀	KS ₀₁
IVWU_NN	0.03	0.13	0.65	0.72	0.55	63.5	0.80	0.12	0.21	31	39
IVWA_NN	-0.02	0.12	0.63	0.71	0.56	91.5	0.92	0.04	0.18	33	45
Month											

Method	Bias/ Gage	Abias /Gage	Corr	RCorr	MAE/ Gage	95%R	95%C	95%L	KS	KS ₁₀	KS ₀₁
IVWU_NN	0.03	0.13	0.74	0.76	0.39	119.5	0.74	0.14	0.24	27	44
IVWA_NN	-0.02	0.12	0.71	0.73	0.40	176.3	0.89	0.05	0.18	43	51

On the other hand, the 95%C and KS indexes improve **substantially** at all levels. The 95%C reaches 94%, 90.4%, and 86.9% at the daily, dekad, and monthly resolutions. The number of stations passing the KS test at the dekad and monthly level increases, especially at the 10% significance level. Despite all these improvements in the representation of the precipitation variability, the KS test at the daily level still indicates that no station has a gage percentile distribution close to the uniform distribution. The most likely explanation of this behavior is that the distribution of daily precipitation is not continuous, but presents a discrete probability for precipitation equal to zero, posing a problem on how to compute the associated percentile. The definition used here, as suggested in several sources, is:

$$\text{Percentile}(\text{gage}) = \text{Prob}(\text{satellite} < \text{gage})$$

where gage = precipitation recorded at the gage;

satellite = precipitation estimate (ensemble).

If the weather is warm and clear during an entire day, it is most likely that all elements of the daily precipitation ensemble are zero. If it happens that the gage records no rain, the associated percentile is 0.995 for a 200-member ensemble. In the continuous distribution case, for which the KS test is formally applicable, this percentile is associated with the event that gage precipitation is higher than all ensemble elements, a completely different situation. The number of such events in this region is much higher than 0.5% as in certain parts of the basin no rain is recorded for three to four months. In the dekad and monthly distributions, on the other hand, such a high discrete probability is not present, making these cases more suitable for the KS test.

Given that the uncorrelated dekad and monthly performances improved when “monthly” precipitation distributions were used, there is a good chance that these performances will further improve when additional TRMM PR data are used.

Figure 5.3.3 shows that adding precip(t-1) to the criteria used for selecting precip(t) successfully increases the autocorrelation of the ensemble sequences to a level closer to that determined from the TRMM images.

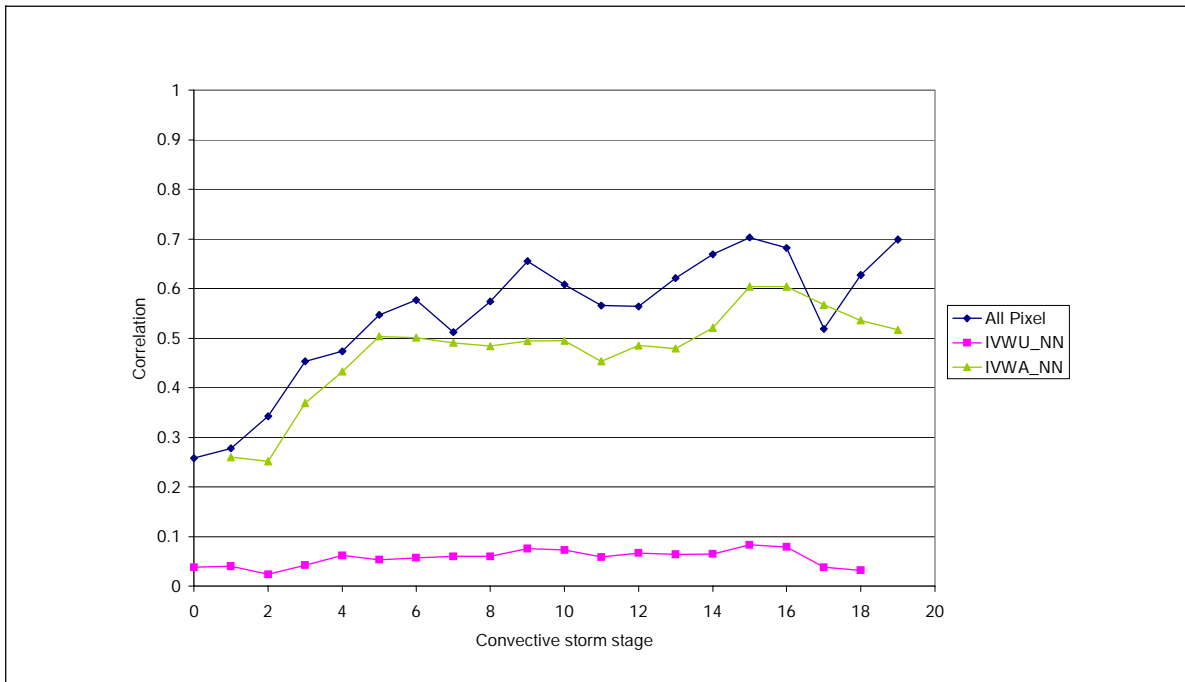


Figure 5.3.3: One-step autocorrelation of convective storm precipitation determined directly from the TRMM data (All Pixel) and as reproduced by the IVWU_NN and IVWA_NN models.

5.3.2 Autocorrelated model validation (1996-1997)

The IVWA_NN model performance for the validation data set is similar to that for the calibration set. As with IVWU_NN, the bias is slightly higher, most likely because the southern part of the basin, which was practically absent from the calibration set, is less rainy. IVWA_NN correlation is also higher than in the calibration dataset, similar to IVWU_NN. The 95% compliance rate is a couple of points lower than in calibration, probably because of the bias increase.

Overall, the absolute model performance is very similar to that of the calibration set and the relative differences with IVWU_NN are also exhibited.

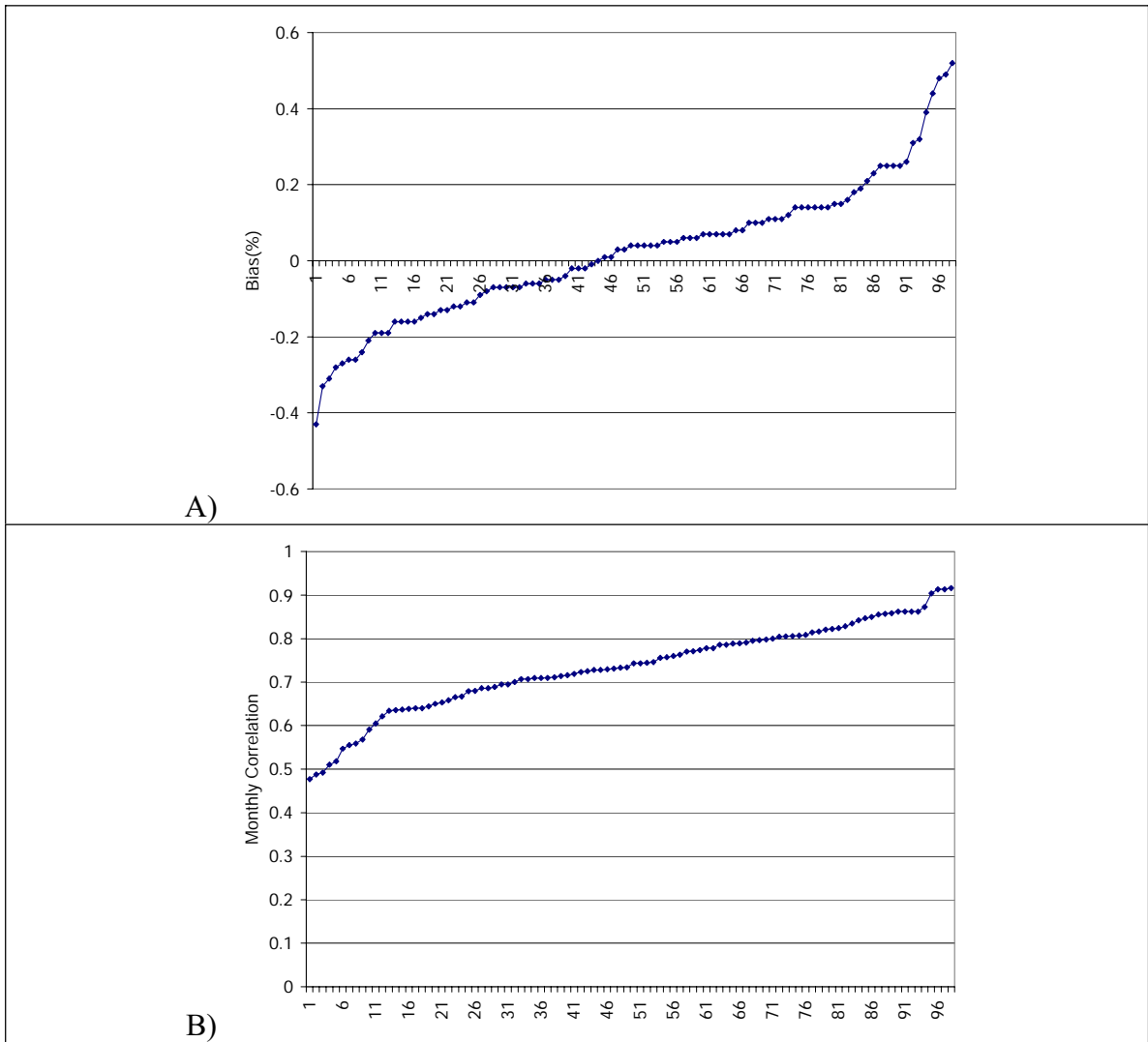
Table 5.3.2: IVWU_NN and IVWA_NN performance for the validation period (1996-1997)

Day											
Method	Bias/ Gage	Abias /Gage	Corr	RCorr	MAE/ Gage	95%R	95%C	95%L	KS	KS ₁₀	KS ₀₁
IVWU_NN	0.06	0.17	0.46	0.54	1.14	12.8	0.91	0.03	0.43	0	0
IVWA_NN	0.03	0.16	0.44	0.53	1.14	18.6	0.95	0.00	0.42	0	0
Dekad											
Method	Bias/ Gage	Abias /Gage	Corr	RCorr	MAE/ Gage	95%R	95%C	95%L	KS	KS ₁₀	KS ₀₁
IVWU_NN	0.06	0.17	0.70	0.76	0.59	58.5	0.77	0.14	0.25	19	26
IVWA_NN	0.03	0.16	0.66	0.75	0.60	87.7	0.89	0.05	0.23	21	29
Month											
Method	Bias/ Gage	Abias /Gage	Corr	RCorr	MAE/ Gage	95%R	95%C	95%L	KS	KS ₁₀	KS ₀₁
IVWU_NN	0.06	0.17	0.79	0.81	0.42	110.3	0.69	0.20	0.26	20	33
IVWA_NN	0.03	0.16	0.76	0.79	0.44	166.6	0.87	0.07	0.19	33	39

5.3.3 Discussion

The previous sections showed that IVWA_NN has a very small average bias both with respect to the calibration and verification data sets. To fully understand the model capability, however, it is necessary to observe the distribution of model performance across the gage stations. Thus, the IVWA_NN performance for the entire 1996-1997 dataset is now considered, using all 98 gages to better represent the precipitation distribution over the region. Figure 5.3.4 A shows that the absolute value of the relative bias is above 50% for only 1% of all stations and below 20% for 77% of gages. Figure 5.3.4 B shows that the monthly correlation is below 0.5 in only 3% of cases and above 0.7 in 68% of cases. Figure 5.3.4 C shows that the monthly 95% compliance rate is below 0.8 in only 18% of the stations. Further, assuming that the three gages with the lowest compliance rate are outliers, the average compliance rate increases to 89%.

Figure 5.3.5 sorts the gages West to East and South to North, so that it is very likely that adjacent gages are relatively close. Figure 5.3.5 A shows that there is not a clear relation between bias and elevation. By contrast, monthly correlation reveals two areas in the western mountains where correlations are distinctly lower. This, however, does not seem to be a direct consequence of elevation, since there are gages at high elevation where correlation is good, but most likely a consequence of a complex orography.



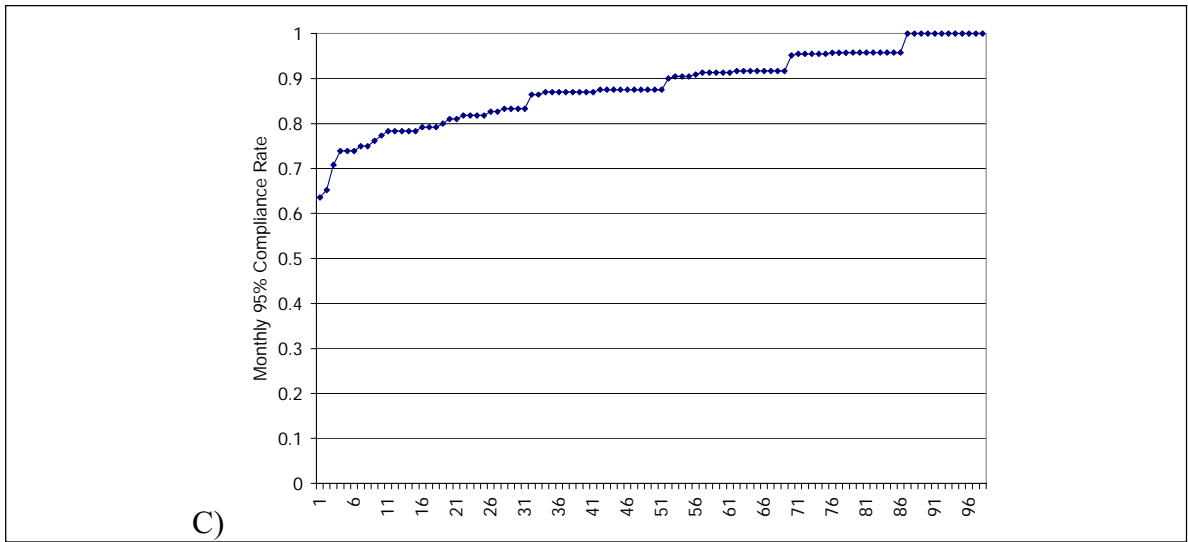
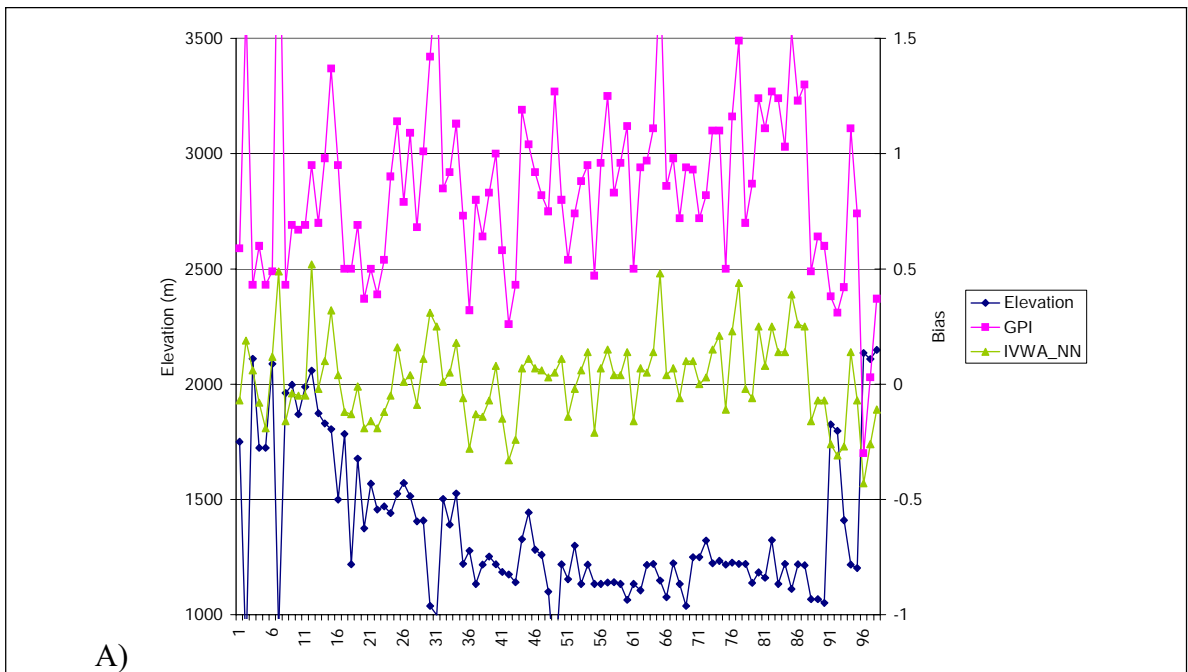


Figure 5.3.4: IVWA_NN relative bias, monthly correlation, and monthly 95% compliance rate distribution for the entire 1996-1997 dataset



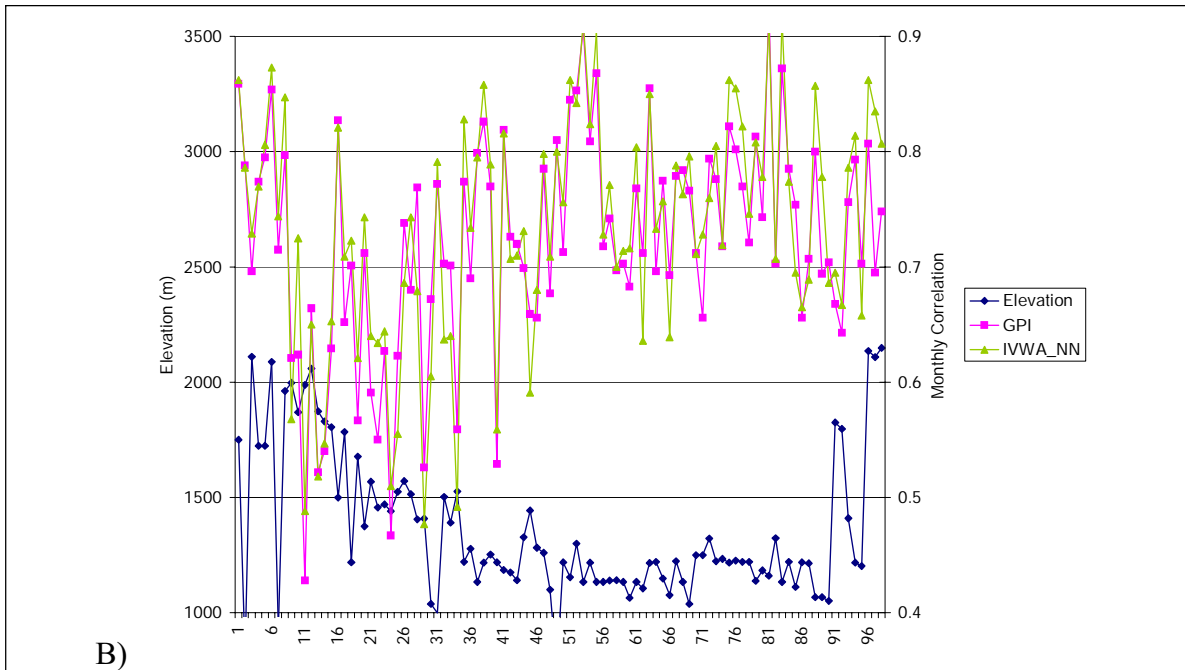


Figure 5.3.5: Relative bias and monthly correlation of the GPI and IVWA_NN models as function of the gage elevation for the entire 1996-1997 dataset

Figure 5.3.6 A shows that four of the gages for which IVWA_NN overestimates precipitation are situated in the Rift Valley, a deep and dry valley surrounded by very high mountains in the western side of the region.

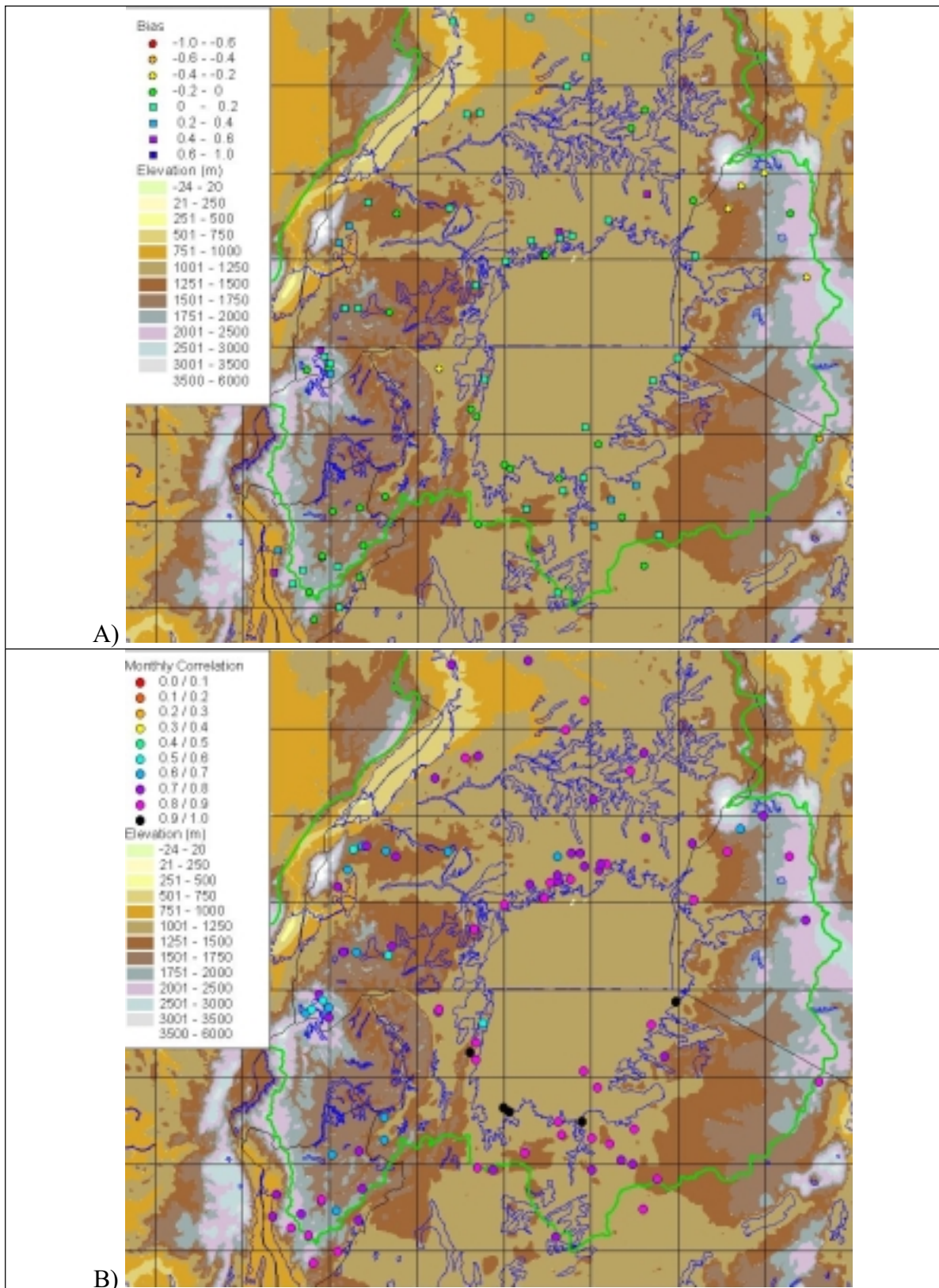


Figure 5.3.6: Relative bias and monthly correlation of the IVWA_NN estimator for the entire 1996-1997 dataset

Two other gages where IVWA_NN overestimates precipitation are located in the very orographically complex region of Mbarara in the western side of the basin. IVWA_NN seems also to overestimate precipitation in some areas shortly inland of the Lake Victoria shoreline. A possible explanation of this phenomenon, is that clouds carried by the lake breeze lose most of their humidity when they come over the shore because of convergence and are relatively dry when they move inland. IVWA_NN somewhat underestimates precipitation on the eastern mountains, probably due to a higher contribution of shallow precipitation of orographic origin in this area.

Figure 5.3.6 B shows that the gages with poor correlation are concentrated around some orographically complex regions in the western side of the basin and on a location along the western shore of Lake Victoria. These observations, however, have to be re-evaluated after eliminating the possibility of questionable rain gage data quality.

6 Multi-pixel Analysis

Most hydrological applications of remotely sensed precipitation interest areas larger than a single 5x5 km pixel requiring the aggregation of the precipitation over several pixels. As shown in Figure 6.1, instantaneous precipitation is strongly spatially correlated. Ignoring this correlation when randomly selecting the rain-rates for the single pixels would still probably yield good estimates of mean areal precipitation over a larger area, but it would underestimate its variability much like the effect of temporal autocorrelation.

Therefore, the correct characterization of the statistical properties of precipitation for multiple pixels requires generating a random precipitation field at each time step and for each member of the ensemble. The precipitation random field must be generated consistently with the spatial correlation structure derived from the TRMM images (Figure 6.1) and the single pixel probability densities associated with the observed IR, VIS/WV, and stage conditions. One possible approach that this may be accomplished in the Turning Bands Method of **Mantoglou and Wilson, 1982**. The multi-pixel analysis will be addressed in the next phase of this work.

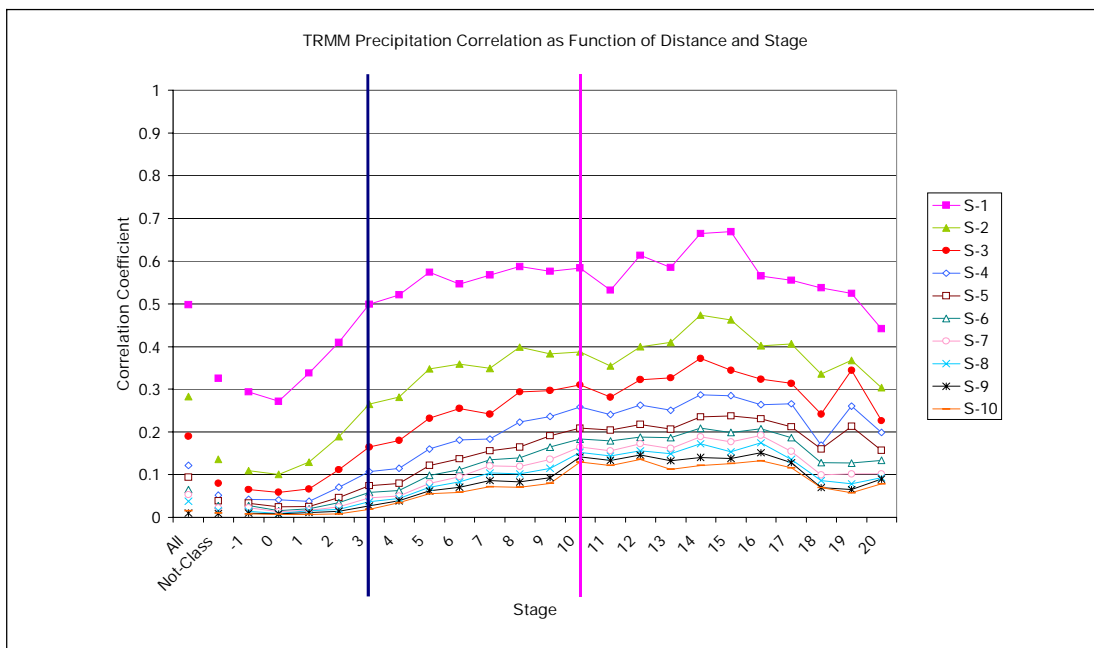


Figure 6.1: Precipitation spatial correlation in the Lake Victoria region as function of the storm stage and distance in pixels (s-1, s-2, etc.)

7 Conclusions

A precipitation estimation methodology using TRMM PR and geostationary satellite images has been developed. The methodology exploits infrared and visible images, geography, and seasonality, and uses a neural network for identifying major storms at the pixel level and for reconstructing their temporal evolution. In addition, the methodology provides a full characterization of estimation uncertainty.

The methodology has been tested at the pixel level over a three-year period on a complex environment showing better average performances than GPI and 3B42. Further, estimation variability is consistent with gage precipitation variability.

The procedure is robust and performs consistently also for years for which TRMM data are not available. The method is constrained by the limited number of data (two years) used for building the relation between IR/VIS/WV and precipitation. It is expected that model performance will improve if more TRMM data become available.

A strategy for estimating precipitation over larger areas in a statistically consistent way has been devised and is currently being implemented.

Acknowledgements

The research described herein has been funded by several sources including the Food and Agriculture Organization of the United Nations (FAO/UN) under the Nile Decision Support Program, the United States Geological Survey under the State Water Resources Program, and NASA (Goddard Space Flight Center, GSFC) under Project NRA-02-ES-05 entitled “The Impact of Precipitation Measurement Missions on Hydrologic and Water Resource Predictions.” The last project is a collaborative effort between NASA’s GSFC (with lead PIs **Dr. C. Peters-Liddard** and **Dr. J.M. Sheppard**) and the Georgia Water Resources Institute (GWRI) at Georgia Tech (with lead PI **Dr. A. Georgakakos**). The authors are very grateful to the above-mentioned sponsoring agencies and collaborators.

References

- Arkin, P.A. and P. Xie (1994). The global precipitation climatology project: First Algorithm Intercomparison Project. **Bull. Amer. Meteor. Soc.** 75: 401-419.
- Arkin, P.A. and B.N. Meisner (1987). The relationship between large-scale convective rainfall and cold cloud over the western hemisphere during 1982-84. **Mon. Wea. Rev.** 115: 51-74
- Adler, R.F., J.A. Negri, P.R. Keehn, and I.M. Hakkarinen (1993). Estimation of monthly rainfall over Japan and surrounding waters from a combination of low-orbit microwave and geosynchronous IR data. **J. Appl. Meteor.** 32: 335-356.
- ASCE Task Committee on Application of Artificial Neural Networks in Hydrology (2000a). Artificial neural networks in hydrology. I: preliminary concepts. **Journal Of Hydrologic Engineering**, 5(2), 115-123.
- ASCE Task Committee on Application of Artificial Neural Networks in Hydrology (2000b). Artificial neural networks in hydrology. II: hydrologic applications. **Journal Of Hydrologic Engineering**, 5(2), 124-137.
- Bell, T.L. (1987). A space-time stochastic model of rainfall for satellite remote-sensing studies. **J. Geophys. Res.** 92(D8), 9631-9643.
- Bellerby, T., M. Todd, D. Kniveton, and C. Kidd (2000). Rainfall estimation from a combination of TRMM Precipitation Radar and GOES multispectral satellite imagery through the use of an Artificial Neural Network. **J. Appl. Meteor.** 39: 2115 – 2128.
- De Angelis, C.F., G.R. McGregor, and C. Kidd (2004). A 3 year climatology of rainfall characteristics over tropical and subtropical South America based on Tropical Rainfall Measurement Mission precipitation radar data. **Int. J. of Climatology** 24(3): 385-399.
- Ebert, E.E., M.J. Manton, P.A. Arkin, R.J. Allam, G.E. Holpin, and A. Gruber. Results from the GPCP Algorithm Intercomparison Programme. **Bull. Am. Met. Soc.** 77(12): 2875-2887.
- Eumetsat (2004). Meteosat VIS channel calibration information. http://www.eumetsat.de/en/dps/mpef/calibration/vis_calibration.html accessed on 5/12/2004.
- Eumetsat (2000). **The Meteosat System, Revision 4**. Eumetsat Technical Report EUM TD 05, pp. 66. Darmstadt, Germany.
- Fiorucci, P., P. LA Barbera, L.G. Lanza, and R. Minciardi (2001). A geostatistical approach to multisensor rain field reconstruction and downscaling. **Hydrol. Earth Sys. Sci.** 5(2): 201-213.
- Georgakakos, A.P., (2004). Decision Support Systems for integrated water resources management with an application to the Nile Basin. **Key note Address, Proceedings**, International Federation for Automatic Control Workshop on Modeling and Control for Participatory Planning and Managing Water Systems, Venice, Italy, Sep. 29 – Oct. 1.
- Georgakakos, A.P., H. Yao, K. Brumbellow, C. De Marchi, S. Bourne, and M. Mullusky (2000). **Lake Victoria Decision Support System**. Technical Report GWRI-2000-1. Georgia Water Resources Institute, Atlanta, GA.

- Georgakakos, A.P (1989). The value of streamflow forecasting in reservoir operation. **Water Resour. Bull.** 25(4): 789-800.
- Georgakakos, K.P., D. Tsintikidis, B. Attia, and J. Roskar (2001). Estimation of pixel-scale daily rainfall over the Nile River catchments using multi-spectral METEOSAT data. In **Remote Sensing and Hydrology 2000**. IAHS Publ. No 267, Wallingford, U.K.
- Greco, M. and E.N. Anagnostou (2001). Overland precipitation estimation from TRMM passive microwave observations. **J. Appl. Meteor.** 40(8): 1367-1380.
- Hirose, M. and K. Nakamura (2004). Spatiotemporal variation of the vertical gradient of rainfall rate observed by the TRMM precipitation radar. **J. Clim.** 17(17): 3378-3397.
- Huffman, G.J., R.F. Adler, E.F. Stocker, D.T. Bolvin, and E.J. Nelkin (2003). Analysis of TRMM 3-hourly multi-satellite precipitation estimates computed in both real and post-real time. In **Proc. 12th Conf. Satellites, Meteorology and Oceanography**, Long Beach, CA, Feb. 9-13, 2003.
- Hsu, K., X. Gao, S. Sorooshian, and H.V. Gupta (1997). Precipitation estimation from remotely sensed information using artificial neural networks, **J. Appl. Meteor.** 36,: 1176-1190.
- Hsu, K., H.V. Gupta, X. Gao, and S. Sorooshian (1999). Estimation of physical variables from multi-channel remotely sensed imagery using a neural network: application to rainfall estimation. **Water Resources Research** 35(5): 1605-1618.
- King, P.W.S., W.D. Hogg, and P.A. Arkin (1995). The role of visible data in improving satellite rain-rate estimates. **J. Appl. Meteor.** 34: 1608-1621.
- Kummerow, C., J. Simpson, O. Thiele, W. Barnes, A.T.C. Chang, E. Stocker, R.F. Adler, A. Hou, R. Kakar, F. Wentz, P. Ashcroft, T. Kozu, Y. Hong, K. Okamoto, T. Iguchi, H. Kuroiwa, E. Im, Z. Haddad, G. Huffman, B. Ferrier, W.S. Holson, E. Zipser, E.A. Smith, T.T. Wilheit, G. North, T. Krishnamurti, and K. Nakamura (2000). The status of the Tropical Rainfall Measuring Mission (TRMM) after two years in orbit. **J. Appl. Meteor.** 39: 1965-192.
- Kummerow, C., W. Barnes, T. Kozu, J. Shiue, and J. Simpson (1998). The Tropical Rainfall Measuring Mission (TRMM) sensor package. **J. Atmos. Oceanic Technol.** 15: 809-817.
- Kurino, T. (1997) A satellite infrared technique for estimating “deep/shallow” precipitation. **Adv. Space Res.** 19(3): 511-514.
- Li, Q., R. L. Bras, and D. Veneziano (1996). Analysis of Darwin rainfall data: Implications on sampling strategies. **J. Appl. Meteor.** 35: 372-385.
- Mantoglou, A., and J.L. Wilson (1982). The turning bands method for simulation of random fields using line generation by a spectral method. **Water Resour. Res.** 18(5): 1379-1394.
- Morrissey, M.L. and J.E. Janowiak (1996). Sampling-induced conditional biases in satellite climate-scale rainfall estimates. **J. Appl. Meteor.** 35: 541 – 548.
- Negri, A.J. and R.F. Adler (2002). A TRMM-calibrated rainfall algorithm applied over Brazil. **J. Geophys. Res.** 107(D20), 8048-8062.
- Negri, A.J. and R.F. Adler (1988). A satellite infrared technique to estimate tropical convective and stratiform rainfall. **J. Climate Appl. Meteor.** 27: 30-51.

- Richards, F. and P. Arkin (1981). On the relationship between satellite-observed cloud cover and precipitation. **Mon. Wea. Rev.** 109: 1080-1093.
- Rigollier, C., M. Lefèvre, Ph. Blanc, and L. Wald (2002). The operational calibration of images taken in the visible channel of the Meteosat-series of satellites. **J. Atmos. Oceanic Technology** 19(9): 1285-1293
- Sorooshian, S., K-L Hsu, X. Gao, H.V. Gupta, B. Imam, and D. Braithwaite (2000). Evaluation of PERSIANN system satellite-based estimates of tropical rainfall. **Bull. Am. Met. Soc.** 81: 2035-2046.
- Steiner, M., R.A. Houze, Jr., and S.E. Yuter (1995): "Climatological characterization of three-dimensional storm structure from operational radar and rain gauge data", **J. Appl. Meteor.** 34: pp.1978-2007.
- Todd, M.C., C.K. Kidd, D.R. Kniveton, and T.J. Bellerby (2001). A combined satellite infrared and passive microwave technique for estimation of small scale rainfall over the global tropics and sub-tropics. **J. Atmos. Oceanic Technology** 18: 742-755
- Todd, M.C., E.C. Barrett, M.J. Beaumont, and J. Green (1995). Satellite identification of rainy days over the upper Nile River basin using an optimum infrared rain/no rain threshold temperature model. **J. Appl. Meteor.**, 34, 2600-2611.
- TSDIS (2004) **Interface Control Specification Between the Tropical Rainfall Measuring Mission Science Data and Information System (TSDIS) and the TSDIS Science User (TSU): File Specifications for TRMM Products - Level 2 and Level 3.** TSDIS-P907, Volume 4. Greenbelt, Maryland
- Tsonis, A.A., G.N. Triantafyllou, and K.P. Georgakakos (1996). Hydrological applications of satellite data. 1. rainfall estimation. **J. Geophys. Res.** 101(D21), 26517-26525.
- Vincente, G.A., R.A. Scofield, and W.P. Menzel (1998). The operational GOES infrared rainfall estimation technique. **Bull. Am. Met. Soc.** 79: 1883-1898.
- Walser, A., D. Lüthi, and C. Schär (2004). Predictability of precipitation in a cloud-resolving model. **Mon. Wea. Rev.** 132: 560-577.
- World Meteorological Organization (1974). **Hydrometeorological survey of the catchments of lakes Victoria, Kyoga, and Albert: Burundi, Egypt, Kenya, Rwanda, Sudan, United Republic of Tanzania and Uganda. V. 1, PT. 1-2: Meteorology and Hydrology of the basin.** Report WMO-RAF—66-025; WMO-TR—1. Geneva, Switzerland.
- Xu, L., X. Gao, S. Sorooshian, P.A. Arkin, and B. Imam (1999). A microwave infrared threshold technique to improve the GOES precipitation index. **J. Appl. Meteor.** 38: 569-579.

Information Transfer Program

Hydrologic Engineering for Dam Design

Basic Information

Title:	Hydrologic Engineering for Dam Design
Project Number:	2004GA98O
Start Date:	10/11/2004
End Date:	10/13/2004
Funding Source:	Other
Congressional District:	5
Research Category:	Engineering
Focus Category:	Hydrology, Floods, Water Supply
Descriptors:	Continuing Education Course
Principal Investigators:	Bert Holler

Publication

Georgia Water Resources Conference, April 2005

Basic Information

Title:	Georgia Water Resources Conference, April 2005
Project Number:	2004GA99B
Start Date:	7/1/2004
End Date:	6/30/2005
Funding Source:	104B
Congressional District:	11
Research Category:	Not Applicable
Focus Category:	Water Quantity, Water Quality, Management and Planning
Descriptors:	Biennial statewide conference
Principal Investigators:	

Publication

Proceedings of the

2005

Georgia Water Resources Conference

April 25, 26 and 27, 2005
Athens, Georgia

Sponsored by:
U.S. Geological Survey
Georgia Department of Natural Resources
Natural Resources Conservation Service
The University of Georgia
Georgia Institute of Technology

Editor
Kathryn J. Hatcher

Institute of Ecology
The University of Georgia
Athens, Georgia U.S.A.

Georgia Water Resources Conference Steering Committee

Nap Caldwell, Georgia DNR Environmental Protection Division
Carol Couch, Georgia DNR Environmental Protection Division
Robert R. Pierce, U.S. Geological Survey
Kathryn J. Hatcher, Institute of Ecology, The University of Georgia
Jimmy Bramblett, USDA Natural Resources Conservation Service
Aris Georgakakos, Georgia Water Research Institute and School of
Civil Engineering, Georgia Institute of Technology

Conference Co-Sponsors

American Society of Civil Engineers, Georgia Section
American Water Resources Association, Georgia Section
American Water Works Association, Georgia Section
Association County Commissioners of Georgia
Georgia Soil and Water Conservation Commission
Georgia Water & Pollution Control Association
Georgia Ground Water Association
Georgia Lake Society
Georgia Municipal Association
Georgia Water Wise Council
National Weather Service, Southeast River Forecast Center
Natural Resources Conservation Service (SCS)
Soil and Water Conservation Society
Soil Science Society of Georgia
Water Environment Federation, Georgia
The Georgia Conservancy
Upper Chattahoochee River Keeper
U.S. Army Corps of Engineers: South Atlantic Division
U.S. Army Corps of Engineers, Mobile District
U.S. Army Corps of Engineers, Savannah District
U.S. Environmental Protection Agency, Region IV
U.S. Environmental Protection Agency, Environmental Research Lab
U.S. Fish and Wildlife Service

**Each article in the proceedings may be viewed
by clicking on the hyperlinked page number
in the Table of Contents below.**

Website <http://ga.water.usgs.gov/gwrc>

Related Publications:

Hatcher, Kathryn J. (editor):

Proceedings of the 1989 Georgia Water Resources Conference

May 16 and 17, 1989

ISBN: 0-935835-01-6 LOC# 89-84386 (245 pages)

Proceedings of the 1991 Georgia Water Resources Conference

March 19 and 20, 1991

ISBN: 0-935835-02-4 LOC# 91-70247 (356 pages)

Proceedings of the 1993 Georgia Water Resources Conference

April 20 and 21, 1993

ISBN: 0-935835-03-2 LOC# 92-76060 (412 pages)

Proceedings of the 1995 Georgia Water Resources Conference

April 11 and 12, 1995

ISBN: 0-935835-04-0 LOC# 95-68015 (412 pages)

Proceedings of the 1997 Georgia Water Resources Conference

March 20, 21 and 22, 1997

ISBN: 0-935835-05-9 LOC# 97-71355 (550 pages)

Proceedings of the 1999 Georgia Water Resources Conference

March 30 and 31, 1999

ISBN: 0-935835-06-7 LOC# 99-61857 (604 pages)

Proceedings of the 2001 Georgia Water Resources Conference

March 26 and 27, 2001

ISBN: 0-935835-07-5 LOC# 2001087837 (793 pages)

Proceedings of the 2003 Georgia Water Resources Conference

April 23 and 24, 2003

ISBN: 0-935835-09-1 LOC# 2003104494 (900 pages)

Hatcher, Kathryn J. (editor). 1950 -

Proceedings of the 2005 Georgia Water Resources Conference

2005

Library of Congress Control Number: 2005926249

ISBN 0-935835-09-1

Printed in United States of America.

This book was published by the Institute of Ecology, The University of Georgia, Athens, Georgia 30602-2202. The views and statements advanced in this publication are solely those of the authors and do not represent official views or policies of The University of Georgia, the U.S. Geological Survey, the Georgia Water Research Institute as authorized by the Water Research Institutes Authorization Act of 1990 (P.L. 101-397) or the other conference sponsors.

TABLE OF CONTENTS

KEYNOTE SPEAKERS

Monday Luncheon:

Conference Keynote Address on Georgia Water Resources.....*	
Governor Sonny Perdue, Governor of Georgia	

Tuesday Luncheon:

Georgia Water Resources: Where Are We; How Did We Get Here; and Where Are We Going? 1	
James E. Kundell, Vinson Institute of Government, University of Georgia	

Monday Dinner at Flinchum=s Phoenix:

Pictures of Four Georgia Rivers: Stories, Images, and Observations.....*	
Ben Emanuel, Georgia River Survey	

TRACK I. STATE WATER PLAN AND POLICY

Water Allocation Legal Issues

Moderator: Robert S. Bomar, Deputy Attorney General, Georgia Department of Law

Water Reallocation in Georgia: If Not a Market, Then What? 6	
Wilson G. Barmeyer, Georgia Law Review, University of Georgia	

Rebutting Regulated Riparian 10	
John R. Wodraska, PBS&J	

Interbasin Transfer and Basin of Origin Protection in Georgia..... 13	
Stephen Draper, The Draper Group	

Georgia Code and the Model Water Code: A Comparison of Rules for Surface Water Withdrawals 17	
Michael Wald, School of Public and International Affairs, University of Georgia	

Regional Water Plans

Moderator and Organizer: Robin McDowell, Georgia DNR Environmental Protection Division

Sound Science Studies in Coastal Georgia and Comprehensive Statewide Water Management Planning 19	
Napoleon Caldwell, Georgia DNR Environmental Protection Division	

Middle Chattahoochee Watershed Stewardship Program: A BluePrint for Successful Communities Project.....*	
Dorothy Rodrigue McDaniel, The Georgia Conservancy	

The Next Wave of Regional Water Planning: Case Study on the Northwest Georgia Regional Water Resources Partnership 21	
Jerry Jennings, Trish Reifenberger, Brown & Caldwell	

Status of the Flint River Regional Water Development and Conservation Plan 25	
Rob McDowell, Georgia Environmental Protection Division	

Plenary Session

Moderator: Robert R. Pierce, U.S. Geological Survey

Creating Georgia's Sustainable Water Future - The Road Forward*	
Carol Couch, Director, Georgia Environmental Protection Division	

Panel: Perspectives on State Water Plan Process

Moderator: Rick Brownlow, Atlanta Regional Commission

Organizer: Julie Mayfield, The Georgia Conservancy and Georgia Water Coalition

The Process for Developing the Initial Edition of Georgia=s Comprehensive Statewide Water Management Plan 29	
Napoleon Caldwell, Georgia Environmental Protection Division	

Views on Developing Georgia=s First Comprehensive Statewide Water Management Plan 31	
--	--

- Nap Caldwell, Georgia EPD
- Bob Scanlon, City of Savannah
- Kevin Green, Metropolitan Atlanta Chamber of Commerce
- Julie Mayfield, The Georgia Conservancy
- Rob McDowell, Georgia EPD

Panel: Water Allocation/Reallocation Policy

Moderator: Michael Wald, School of Public and International Affairs, University of Georgia

Assistant Moderator: Sarah Gaines, Ecology, University of Georgia

Organizer: Kathryn Hatcher, University of Georgia

State Water Policy Alternatives for Water Allocation and Reallocation (post)	37
- Kevin Farrell, Georgia Environmental Protection Division	
- Bob Bomar, Deputy Attorney General, Georgia Department of Law	
- Cianatt Howett, Southern Environmental Law Center	
- Joel Cowan, Board of Metro North Georgia Water Planning District	
- David Newman, School of Forest Resources, University of Georgia	

Low Impact Development

Moderator: Bruce Ferguson, School of Environmental Design, University of Georgia

Evaluating Alternatives for Coastal Development	44
Patricia McIntosh, Georgia Conservancy; Jill Huntington, Georgia Coastal Management Program: One Conservation Way; Nancy Cofer-Shabica and Amanda Rutherford, Perot Systems Government Services (PSGS) onsite contractor at NOAA Coastal Services Center	
Growth Readiness for Georgia: Water Quality Matters	47
Randy Hartmann, GA Dept of Community Affairs; and Joel Haden, Sustainable Development Project Manager, Tennessee Valley Authority	
The Water Resources Component of the Ecological Footprint of a Federal Research Laboratory in Athens, Georgia	50
Stephen R. Kraemer, US EPA National Exposure Research Laboratory, Athens	
New Directions in Low Impact Development - Implications for Urban Redevelopment	54
Neil Weinstein, Low Impact Development, Inc.	

Integrated Water Resources Planning

Moderator: Ade Oke, Georgia DNR Environmental Protection Division

Developing Statewide Water Plans: Needs and Challenges	58
Pat Gleason, Dan Rodrigo, and Paul Brown, Camp, Dresser &McKee	
South Carolina Water Plan C Second Edition	63
Bud Badr, South Carolina DNR, Land-Water Conservation; Andrew Wachob and Joseph A Gellici, Hydrologist, South Carolina DNR	
The Yellow River Law: A Framework for Integrated River Basin Management	66
George F. McMahon, ARCADIS	
Tennessee Valley Authority (TVA) Reservoir Operations Study and Programmatic EIS B Alternatives Analysis and Balancing in Water Management	*
Paul Leonard, ENTRIX, Inc.	

Legislative Update and Water Policy

Moderator: Stephen Draper, Draper Group

Environmental Issues in the 2005 Georgia Legislature	76
Sally Bethea, Upper Chattahoochee Riverkeeper	
Georgia Water Law: How to Go Forward Now?	78
Joseph Dellapenna, Villanova University	

Panel: Indicators for Sustainability

Moderator and Organizer: PJ Newcomb, GaDNR-Pollution Prevention Assistance Division

Panel Discussion: Indicators for Sustainable Water Resources in Georgia [90](#)
PJ Newcomb, Georgia DNR Pollution Prevention Assistance Division

Speakers:

- Nap Caldwell, Georgia Environmental Protection Division
- Michael Chang, Earth & Atmospheric Science, Georgia Institute of Technology
- Gary Hawkins, Biological and Agricultural Engineering, University of Georgia
- Zaneta Ivery, Georgia Department of Community Affairs

Conflict Resolution

Developing Consensus among Stakeholders in Water Resources Planning [93](#)

Dan Rodrigo and Paul Brown, CDM Inc.

A New Framework for Water Conflict Resolution [98](#)

George McMahon, ARCADIS G&M, Inc.

Modeling for Conflict Resolution Using Parameterization of Operations and Strong Stakeholder Initiatives [105](#)

Wei Zeng and David E. Hawkins, GaDNR-EPD; George F. McMahon, ARCADIS Inc.

Agency Tech Assistance & Funds for Local Water Resources Planning- Management, I and II

Moderator and Organizer: Donata Renfrow, US Army Corps of Engineers, Mobile District

- Nap Caldwell - GA EPD Senior Planning and Policy Advisor for Water
- Ben Dickerson, GA DOT, Ecologist, Office of Environment and Location
- Mark Bartlett - Federal Highway Administration, Asst. Division Administrator
- Jimmy Bramblett, USDA Natural Resources Conservation Service (invited)
- Wallace Brittain, National Park Service, Division Chief for the Recreation and Conservation Division
- David Horning, US Fish and Wildlife Service-- Representative to the SE Natural Resources Leaders Group
- Larry Prather, US Army Corps of Engineers, HQ, Asst. Director of Civil Works, Legislation and Planning
- Hudson Slay, US EPA, Region IV, Watershed Branch
- Jeff Hughes, USEPA Region IV, Environmental Finance Center

Workshop: Adopt-A-Stream Monitoring

Georgia Adopt-A-Stream: Field Demonstrations [113](#)

Harold Harbert and Kimberly Morris-Zarneke, Adopt-A-Stream Program, Georgia Environmental Protection Division

TRACK II. ATLANTA AREA WATER ISSUES

Public Education and Awareness

Moderator and Organizer: Kelley O'Brien, Atlanta Regional Commission

Sponsor: Atlanta Regional Commission

Making a Splash: The Clean Water Campaign from Grassroots to Mass Media..... [115](#)

Kelley O'Brien, Atlanta Regional Commission

Georgia Adopt-A-Stream Program and Georgia Project Wet: Tools for an Urban Watershed [119](#)

Harold L. Harbert, Kimberly Morris-Zarneke, and Mary Martin Giroux,

GA DNR-EPD, Georgia Adopt-A-Stream

Utilizing Existing Resources to Broaden Reach of Residents *

Ann Kirk, Keep Smyrna Beautiful, Smyrna City Hall

Remembering the Community in Community Outreach - Why LanCool is Cool! [121](#)

Marci Hawk Davis, Brown&Caldwell

Atlanta Area Stream Quality

Moderator: Mark N. Landers, U.S. Geological Survey

Characterization of Anthropogenic Organic Compounds in the Source Water and Finished Water for the City of Atlanta, October 2002--September 2004	125
Elizabeth A. Frick and Melinda Dalton, US Geological Survey	
Some Initial Sediment-associated Trace Element Results from the City of Atlanta, Georgia, Water-quality Monitoring Network.....	132
Arthur J. Horowitz, Kent J. Elrick, and James J. Smith, US Geological Survey	
Preliminary Analysis of the Water Quality Variability of Urban Streams, Atlanta, Georgia, May 2003 - October 2004	136
Norman E. (Jake) Peters, USGS	
Evaluation of the Long-term Impacts of Urbanization on a Piedmont Headwater Stream: A Comparison of Physical, Biological, and Chemical Indicators of Response	140
Robert Bourne and Ted Mikalsen, Cobb Co. Water System; and Steve Shelton, GA EPD	
The Effects of Development on Conductivity Levels In Urban Streams	147
Ted Mikalsen, GaEPD	
Planning for the Future: Development of the Metro District Water Management Plans Moderator and Organizer: Pat Stevens, Atlanta Regional Commission Sponsor: Metropolitan North Georgia Water Planning District From Creation to Plans: The Metropolitan North Georgia Water Planning District and the First Integrated Water Resources Plans	148
Pat Stevens, Atlanta Regional Commission; and Rob Bocarro, MACTEC Engineering, Inc.	
Creating an Integrated Plan for Long-term Wastewater Management for 16 Metropolitan Counties: Ground-breaking Collaboration among Utilities	151
Pamela Burnett, Metcalf&Eddie, Inc.	
Preparing the Water Supply and Water Conservation Management Plan for Metro North Georgia: Process and Results	154
David M. Ashley, Jordan, Jones & Goulding, Inc.	
Watershed Management Planning for the Metropolitan North Georgia Water Planning District	157
Doug Baughman, Heather Dyke, Betsy Massie, and Avinash Patwardhan, CH2M HILL	
Launching Plans into Action: Implementation of the Metro District Water Plans Moderator and Organizer: Rick Brownlow, Atlanta Regional Commission Sponsor: Metropolitan North Georgia Water Planning District The Water District Plans - One Year Later: Implementation and Ongoing Planning	161
Rick Brownlow, Atlanta Regional Commission	
Implementation of Watershed Management Requirements and Model Ordinances	164
Steve Haubner, Atlanta Regional Commission	
Implementation of the Metropolitan North Georgia Water Planning District=s Water Conservation Measures	168
Cindy Daniel, Atlanta Regional Commission	
Panel: ACF Basin Federal Water Requirements Moderator and Organizer: George William (Jerry) Sherk, Colorado School of Mines The Corps' Conundrum: Reconciling Conflicting Statutory Requirements in the ACF River Basin	171
George William Sherk, Colorado School of Mines	
Growing Water Demand and Inevitable Litigation: The Missouri and ACF River Basins.....	174
Don Blankenau, Attorney, Fennemore Craig P.C.	
Quantifying the Federal Requirement: Water for Fish and Wildlife in the Apalachicola-Chattahoochee-Flint River Basin	187
Jerry Ziewitz, US FWS	
Water Quality and Minimum Instream Flow	*
Howard Marshall, USEPA (retired)	
An Appraisal of Consumptive Demand Limit for the Upper Chattahoochee Basin	181
Steve Leitman, Damayan Water Project, Quincy FL	
ACF River Allocation Issues Moderator: Aris Georgakakos, Georgia Water Resources Institute, Georgia Institute of Technology	

The State of the Chattahoochee River -- A Call to Action	<u>184</u>
Mark Crisp, Guernsey&Co; and Dick Timmerberg, West Point Lake Coalition	
Reflections on the ACF and ACT Basin Compacts	<u>189</u>
Harold D. Melton, Governor's Office, and R. Todd Silliman, McKenna Long & Aldridge LLP	
The Utton Center=s Model Compacts Project	<u>193</u>
George William Sherk, Colorado School of Mines	
Sustainable Utilities Management, Lanier Reuse	
Moderator: Pamela Burnett, Metcalf & Eddy, Inc.	
Sponsor: Georgia Water & Pollution Control Association	
Sustainable Water Resources Management by Georgia Utilities: Clayton County Water Authority	<u>196</u>
Mike Thomas, Clayton County Water Authority	
Water Reuse - A Water Supply Option in the Metropolitan Atlanta Area?	<u>200</u>
Paula Feldman Yari, Jordan, Jones & Goulding, Inc.	
Sustainable Water Resources for Gwinnett County, Georgia.....	<u>204</u>
James Scarbrough, Gwinnett County Department of Public Utilities	
Atlanta Water Supply Issues	
Moderator: Trish Reifenberger, Brown & Caldwell, Inc.	
Integrated Water Resources Management in North Georgia - Implications of Wastewater Management Policy.....	<u>207</u>
David J. Sample and Robert A. Bocarro, MACTEC Engineering Inc	
Decentralized Wastewater Treatment: Planning, Alternatives, Management	<u>212</u>
Linda MacGregor, McKenzie MacGregor Incorporated	
Hickory Log Creek Reservoir: A New Approach to Sustainable Water Management	<u>217</u>
George McMahon, ARCADIS G&M, Inc., and A. Roy Fowler, Cobb County-Marietta Water Authority	
Alternative to Federal Appropriations Federal Hydropower Rehab in the Southeast	<u>222</u>
Al Pless, Southeastern Power Administration	
Sewage Overflow and Infrastructure	
Moderator: Dieter Franz, Brown & Caldwell, Inc.	
Development of an SSO Mitigation Plan: What We Can Learn from the Field	<u>225</u>
David Sample, Robert A. Bocarro, Margaret Tanner, and Monique Latalladi, MACTEC Engineering and Consulting, Inc.	
Implementing a Cost Effective Inflow and Infiltration Program and the Benefits for Watershed Management	<u>229</u>
Rob Bocarro, MACTEC Engineering and Consulting	
Identifying Sewage Failures in Urban Environments: Examples from Athens, GA	<u>218</u>
Denise Carroll and Todd Rasmussen, University Of Georgia, School of Forest Resources	
Asset Management for Water Resources Infrastructure	<u>232</u>
Ron Cagle, Jordan, Jones & Goulding, Inc.	

TRACK III. INSTREAM FLOW AND RESTORATION

Instream Flow Guidelines for Georgia	
Moderator and Organizer: Mary Davis, The Nature Conservancy	
Legal Issues Surrounding Stream Flow in Georgia	<u>240</u>
Ciannat Howett and Gilbert B. Rogers, Southern Environmental Law Center	
Some "Pros and Cons" of Alternative Methods of Defining Instream Flow Requirements	<u>243</u>
Mary Freeman, US Geological Survey	
Instream Flow Guidelines and Protection of Georgia=s Aquatic Habitats	<u>247</u>
Mary M. Davis, The Nature Conservancy	

Instream Flow Studies in Georgia

Moderator and Organizer: Erik Dilts, Entrix, Inc.	
The Evolution of Georgia=s Instream Flow Policy	252
Nap Caldwell, Georgia Environmental Protection Division	
Effects of Surface Water Withdrawals and Reservoirs on Stream Fishes in the Georgia Piedmont.....	255
Mary Freeman, US Geological Survey	
Time-Series Stream Temperature And Dissolved Oxygen Modeling In The Lower Flint River Basin	258
Guoyuan Li and C. Rhett Jackson, University of Georgia, School of Forest Resources	
Development of an Integrated Flow Regime Recommendation for the Cheoah River, N.C.	262
Erik Dilts and Paul Leonard, ENTRIX, Inc.; and Donley Hill, U.S. Forest Service	
Essential Decisions for an Instream Flow Policy	266
Andrew G. Keeler, School of Public Policy and Management, Ohio State University; and Todd Rasmussen, School of Forest Resources, University of Georgia	

Panel: Instream/Downstream Flow Protection Policy

Moderator: Alan Covich, Institute of Ecology, University of Georgia	
Assistant Moderator: Ryan Eaves, MPA Program, University of Georgia	
Organizer: Kathryn Hatcher, Institute of Ecology, University of Georgia	
State Water Policy Alternatives for Instream and Downstream Flow Protection (post)	270
- John Biagi, Georgia DNR Wildlife Resources Division	
- Jerry Ziewitz, US Fish & Wildlife Service	
- Brian Richter, The Nature Conservancy	
- Bob Scanlon, GMA representative	
- Billy Turner, Columbus Water Works	

Streamflow and Fish Distribution

Moderator: Becky Champion, Columbus State University	
Biodiversity in the Chattahoochee Headwaters--Rare Fishes Found in Recent Study	279
Darcie Holcomb, Upper Chattahoochee Riverkeeper	
Buried Alive: Potential Consequences of Burying Headwater Streams in Drainage Pipes	283
Judy Meyer and Krista L. Jones, Institute of Ecology, University of Georgia; and Geoffrey C. Poole, Eco-metrics, Inc.	
Waters to the Sea: The Chattahoochee River CD	*
Becky Champion, Columbus State University	

Aquatic Ecosystems

Moderator: William Tietjen, Georgia Southwestern University	
Wood Debris Recruitment from Differing Riparian Landforms in a Gulf Coastal Plain Stream:	
The Role of Floods	287
Stephen Golladay and Juliann Battle, Joseph W. Jones Ecological Research Center	
Microhabitat Preferences by Aquatic Invertebrates Influence Bioassessment Metrics in	
Piedmont Streams of Georgia and Alabama	291
M. Brian Gregory, U. S. Geological Survey	
Comparison of Bioassessment Methods of Ecological Condition Using Aquatic Macroinvertebrate	
Assemblages in Southwest Georgia Headwater Streams	297
Rebecca T. Winn, International Paper; Thomas L. Crisman, University of Florida; and Stephen W. Golladay, J. W. Jones Ecological Research Center at Ichauway	
Foodweb Modeling for P.C.B. in the Twelvemile Creek Arm of Lake Hartwell, GA/SC.....	301
Brenda Rashleigh and M. Craig Barber, U.S. Environmental Protection Agency, Athens, GA; and David M. Walters, U.S. Environmental Protection Agency, Cincinnati, OH	
Evaluating Management Needs of Lake Blackshear, Georgia	305
Martin Lebo, Weyerhaeuser Company; H. E. Cofer, Dept. of Geology; W. L. Tietjen and P. Y. Williams, Dept of Biology, Georgia Southwestern State University; and D. Partridge, GA Department of Natural Resources	

Imperiled Aquatic Species

Moderator: Sandra Tucker, U.S. Fish and Wildlife Service	
--	--

Current Status of Endemic Mussels in the Lower Ocmulgee and Altamaha Rivers	309
Jason Wisniewski, Greg Krakow, and Brett Albanese, Georgia DNR Natural Heritage Program	
The Swamp Eel, <i>Monopterus Sp. Cf. M. Albus</i> , in the Chattahoochee River System, Fulton County, Georgia.....	313
Carrie A. Straight and Thomas R. Reinert and Byron J. Freeman, Institute of Ecology, UGA; and Jay Shelton, School of Forest Resources, University of Georgia	
Spring Creek Watershed Partnership in Southwest Georgia	317
Sandra Abbott, US Fish & Wildlife Service	
Design of an Environmental Monitoring Program for the Lake Allatoona/Upper Etowah River Watershed.....	319
James B. (Sam) Stribling and Steven R. Davie, TetraTech Inc.	
Etowah Habitat Conservation Plan	
Moderator: Sandra Tucker, US Fish and Wildlife Service	
Etowah Habitat Conservation Plan	*
Sandy Tucker, US FWS, and Laurie Fowler, University of Georgia, Institute of Ecology	
Developing Measures of Success for the Etowah River Basin	323
Candace Stoughton and Mary Davis, The Nature Conservancy, Etowah River Office	
Prioritizing River Restoration Sites in the Etowah River, Georgia	326
Will Duncan and Robin Goodloe, U.S. Fish and Wildlife Service; Mark C. Leao and Eric Prowell, School of Forest Resources, University of Georgia	
The Etowah Habitat Conservation Plan Outreach Program: A Social Networks Based Approach to Public Participation and Stakeholder Involvement	329
Curt Gervich, University of Georgia, Institute of Ecology	
Stream Restoration	
Moderator: Jamie Higgins, US Army Corps of Engineers, South Atlantic Division	
Implementation of Natural Channel Design on Two Georgia Power Stream Restoration Projects	332
Steve Jones, Environmental Services, Inc.; Jim Candler, Georgia Power Company	
Butler Creek Aquatic Ecosystem Restoration Project	335
Dean Trawick, Matthew Lang, Inez Bergerson, and Maria Chin, US Army Corps of Engineers, Mobile AL	
Restoration of Peters Creek, Spartanburg, South Carolina	338
J. Mark Ballard and Dan Rice, Jordan, Jones & Goulding, Inc.; and Roger Rhodes, Spartanburg Water System, Spartanburg, SC	
Chattahoochee River Restoration: Removal of City Mills and Eagle and Phenix Dams	342
Michael J. Eubanks and James O. Buckalew, U.S. Army Corps of Engineers	
Ecosystem Restoration	
Moderator: Jamie Higgins, US Army Corps of Engineers, South Atlantic Division	
Considerations for Developing a Model for Measuring Aquatic Ecosystem Improvement from Restoration of Urban Development	346
E. Aylin Lewallen and Paul M. Leonard, ENTRIX, Inc.	
Restoration of the Wormsloe Plantation Salt Marsh in Savannah, Georgia	350
Dan Rice, Jordan, Jones & Goulding, Inc.; Susan Knudson and Lisa Westberry, GA DOT	
Construction of an Offshore Bird Nesting Island at Savannah Harbor	354
William Bailey, US Army Corps of Engineers, Savannah District	
Case Studies of Phytoremediation of Petrochemicals and Chlorinated Solvents in Soil and Groundwater	358
Valentine Nzengung, Department of Geology	

TRACK IV. FLOODPLAIN MAPPING, CONSERVATION

Floodplain GIS Mapping

Moderator and Organizer: Kimberly Zimmerman Shorter, City of Roswell	
Sponsor: Georgia Chapter of American Water Resources Association	
Floodplain Modeling Applications for Emergency Management and Stakeholder Involvement	
A Case Study: New Braunfels, Texas	360
Emily Holtzclaw, Betty Leite, and Rick Myrick, CH2M HILL Inc.	
Pilot Application of Automated Floodplain Generator Tool For Priority Area 3 of Cobb County, Georgia	
Darren Baird, Steve Jencen and Elizabeth Krousel, AMEC Earth and Environmental	e362
Innovative Floodplain Management	
David Briglio, P.E., Jordan, Jones & Goulding, Inc.	363
GIS Applications for Water Resources	
Moderator and Organizer: Scott Bales, Georgia Environmental Protection Division	
Georgia's Map Modernization Scoping Effort	
Nolton G. Johnson and Michael DePue, Georgia EPD	367
Riverine Flood Hazard Modeling in HAZUS-MH: Overview of Model Implementation	
Subrahmanyam Muthukumar, Center for GIS, Georgia Institute of Technology	371
Comprehensive Water Resources Management Through Geographic Information Systems.....	
Bruce B. Taylor, Clayton County Water Authority	375
Practical Applications of GIS for Water Resources- Gwinnett County Case Study	
Sam Crampton, Dewberry; and Sam Fleming, Gwinnett County Dept. of Public Utilities	377
Georgia River Forecasting and Climatology	
Moderator and Organizer: Mark Fuchs, Southeast River Forecast Center, NWS	
A Climatological Assessment of Flood Events in Georgia	
Jeffrey C. Dobur and James Noel, National Weather Service Forecast Office	381
Communication of Critical Hydrometeorological Information during the 2004 Tropical Storm Season	
in Georgia.....	386
Mark Fuchs, Southeast River Forecast Center	
Using The National Weather Service AHPS Web Site.....	
Jack Bushong, Southeast River Forecast Center (SERFC) National Weather Service	389
Panel: Effectiveness of NWS Products during 2004 Tropical Season	
Moderator: Mark Fuchs, Southeast River Forecast Center, National Weather Service	
- John Feldt, Hydrologist-in-Charge, SERFC/NWS	
- Brian McCallum, Assistant District Chief, Georgia District, US Geological Survey	
- Joel Galt, Georgia Power, Southern Company Generation and Marketing	
- Brock Long, FEMA Hurricane Program Specialist, Atlanta	
- Dan Brown, GEMA Chief of Communications, Atlanta	
- Memphis Vaughan, US Army Corps of Engineers, Mobile District	
- Ed Fiegle, Georgia DNR Safe Dams Program.	
Watershed Assessment	
Developing and Implementing a Source Water Protection Plan for Macon	
Water Authority=s Drinking Water Sources	391
Mark Wyzalek, Manager, Macon Water Authority	
The Use of In-house Resources by a Municipality to Conduct a Watershed Assessment	
Bob Bourne, Cobb County Water System	*
Water Quality Implications of Bio-Fuels Development in Georgia	
Sara Barczak, Southern Alliance for Clean Energy; Keshav Das, Faculty of	395
Engineering, UGA; Rita Kilpatrick, Southern Alliance for Clean Energy	
Multi-Year Research on the Use of Constructed Wetlands for Advanced Wastewater Treatment	
Gene W. Eidson, Southeastern Natural Sciences Academy	399
Designing Constructed Wetlands for Mitigating Risks from Flue Gas Desulfurization Wastewater	
George M. Huddleston III, Cynthia Murray-Gulde, and F. Douglas Mooney,	404
Entrix, Inc.; John H. Rodgers, Jr., Clemson University	

Georgia Sustainability Initiative

Moderator and Organizer: Robert Donaghue, Georgia Pollution Prevention Assistance Division

Water Conservation at Delta Air Line: Significant Water and Wastewater Reduction	408
Chris Shannon and Paul Dellinger, Delta Air Lines; Adrienne Thorpe, DNR Pollution Prevention Assistance Division	
City of Atlanta Partners with P ² AD To Help Water Customers Save Money	411
Judy Adler, Pollution Prevention Assistance Division; Ben Taube City of Atlanta; PJ Newcomb and Adrienne Thorpe, Pollution Prevention Assistance Division	
Industry Taking Action - Case Study of a Water Use Efficiency Program in Coca-Cola Plants	414
Pranav Padhiar, Coca-Cola Enterprises, and Patricia Anderson, Nalco Alliance	
Local Utility and Industries Partner to Achieve Phosphorus Reduction	417
John C. Allen, GaDNR Pollution Prevention Assistance Division	
Visions of a Sustainable Georgia	*
Robert Donaghue, GaDNR Pollution Prevention Assistance Division	

Water Conservation in Landscape

Moderator: Rose Mary Seymour, Biological and Agric. Engineering Dept., University of Georgia

Sponsor: Georgia Water Wise Council and GWPCA

A Community Approach to Water Conservation.....	420
Andrew Pearson, Athens Clarke County Water Conservation, and Paul A. Thomas, UGA	
Capturing Rain Water to Replace Irrigation Water for Landscapes: Rain Harvesting and Rain Gardens	423
Rose Mary Seymour, University of Georgia- Griffin Campus	
Water-Wise Demonstration Landscape: A Case Study in Water Conservation.....	427
Gary Wade, UGA Horticulture	
A Case Study: The Implementation of a Water Conservation Plan by Georgia Golf Course Superintendents.....	431
Clint Waltz and R. N. Carrow, Crop and Soil Sciences, UGA; Mark Esoda, Atlanta Golf Club; and F. T. Siple, Lanier Golf Club	
Development of a Water Conservation Educational Program for Turfgrass Professionals.....	435
F. Clint Waltz and R. N. Carrow, Crop and Soil Sciences, University of Georgia	
New Guide for Green Industries on Water Conservation Best Management Practices	438
Rose Mary Seymour, Clint Waltz, Gil Landry, Gary Wade, Bob Westerfield, and David Berle, University of Georgia (poster)	

Water Conservation

Moderator: Kevin Green, Metropolitan Atlanta Chamber of Commerce

Economic Feasibility of Recycling Chiller Water in Poultry Processing Plants by Ultrafiltration.....	440
Horacio Saravia and Jack E. Houston, UGA Agric. & Applied Economics; Romeo Toledo and Heather M. Nelson, UGA Dept. of Food Science and Technology	
Water Conservation Opportunities Through Energy Efficiency in Georgia	444
Sara Barcza and Rita Kilpatrickk, Southern Alliance for Clean Energy	
Using Dynamic Utility Systems Models for Water Use Accountability and Planning in Georgia	448
Joe Volpe and Charlie Voss, Golder Associates Inc.	
Building a State of Water Conservation: GA EPD Strengthens Water Conservation in Policy and Planning.....	451
Alice Miller Keyes, Georgia DNR Environmental Protection Division	

Potable Water Reuse

Moderator and Organizer: Alice Cook and Dieter Franz, Brown & Caldwell Inc.

Sponsor: Georgia Water & Pollution Control Association

Potable Water Reuse: Health Considerations	*
Christine Moe, Public Health Emory Univ.	
Impacts of Water Re-use on Drinking Water Treatment Plant Practices	e454
R. Wayne Jackson, Cobb County - Marietta Water Authority	

Lake Lanier Water Quality	455
Val M. Perry, Lake Lanier Association	
Panel: Public Perception of Water Potable Reuse - Science, Risk, and Necessity.....	457
Moderator: Frank Stephens, Gwinnett Co. Public Utilities	
- Christine Moe, Emory University	
- Wayne Jackson, Cobb County/Marietta Water Authority	
- Mike Leonard, Brown&Caldwell	
Panel: Water Conservation/Efficiency and Reuse Policy	
Moderator: Gail Cowie, Vinson Institute of Government, University of Georgia	
Organizer: Kathryn Hatcher, Institute of Ecology, University of Georgia	
Assistant Moderator: Lauren Burch and Julia Beckhusen, University of Georgia	
State Water Policy Alternatives for Water Conservation/Efficiency and Reuse (post)	459
- Alice Miller Keyes, Georgia EPD	
- Cindy Daniel, Atlanta Regional Commission	
- Shana Udvardy, The Georgia Conservancy	
- Brian Skeens, Georgia Water & Pollution Control Assoc.	
- David Bennett, Georgia Soil & Water Conservation Comm.	

TRACK V. WATERSHED PROTECTION

Stream Riparian Buffers	
Moderator: Judy Meyer, Institute of Ecology, University of Georgia	
Potential Trout Population Response to Reduced Riparian Buffer Widths for North Georgia.....	469
Krista L. Jones, Geoffrey C. Poole, Judy L. Meyer, William Bumback, and Elizabeth Kramer, Institute of Ecology, University of Georgia	
Developing Riparian Guidelines on Forest Service Land in the Southern Appalachians	470
Jack Holcomb, USDA Forest Service Southern Region	
A Statewide Analysis of Riparian Vegetation Change, from 1974 to 1998.....	474
Elizabeth Kramer and Bill Bumback, Institute of Ecology, University of Georgia	
Runoff Impacts to Stream Quality	
Moderator: David Radcliffe, Crop and Soil Sciences Dept., University of Georgia	
Using the Georgia P-Index to Identify High Risk Management of Poultry Litter	478
Julia Gaskin, Keith Harris, and Mark Risee, UGA Biological & Agricultural Engineering Dept.; Miguel Cabrera, UGA Crop and Soil Science	
Hydrologic and Water Quality Implications of Management of Tall Fescue Pastures in a Southern Piedmont Environment.....	482
Dinku Endale, A. J. Franzluebbbers, J. A. Stuedemann, and D. H. Franklin, USDA-ARS; and N. S. Hill, University of Georgia, Crop and Soil Science	
Land Use Effects on Suspended Sediment Yield in Six Small Georgia Watersheds.....	486
Ken Bradshaw, David Radcliffe, Karin Lichtenstein, UGA Crop and Soil Sciences; Mark Risse and Mark Bakker, UGA Biological and Agricultural Engineering; C. Rhett Jackson and Daniel Markewitz, UGA School of Forest Resources	
Evaluation of Total Phosphorus in the Ocmulgee-Oconee-Altamaha River Basin of Georgia.....	490
Josh Romeis and Rhett Jackson, University of Georgia- Forest Resources	
Stream Quality Studies	
Moderator: Brenda Rashleigh, U.S. EPA, Environmental Research Laboratory, Athens	
Phosphorus, Sediment, and E.coli Loads in Unfenced Streams in the Georgia Piedmont	494
H. L. Byers, Monte K. Matthews, Miguel L. Cabrera, John G. Andrae, David E. Radcliffe, Carl S. Hoveland, Department of Crop and Soil Sciences, UGA; Dorcas H. Franklin,	

USDA-ARS, JPCS-NRCC; Mark A. McCann, Department of Animal and Dairy Science, University of Georgia; Holli A. Kuykendall, Grazingland Water Quality Specialist, USDA-NRCS; Vaughn H. Calvert II, Central Research and Education Center, Eatonton, GA (poster)	
Survival And Regrowth of Fecal Enterococci in Desiccated and Rewetted Sediments	499
Peter G. Hartel, Karen Rodgers, and Jared A. Fisher, UGA Dept. of Crop & Soil Sciences; Jennifer L. McDonald, and Lisa C. Gentit, UGA Marine Extension Service; Ernesto Otero and Yaritza Rivera-Torres, UGA Dept of Marine Sciences; Tamara L. Bryant and Stephen H. Jones, University of New Hampshire, Natural Resources Department	
Diel Turbidity Fluctuations in Streams, Gwinnett County, Georgia.....	503
Stephanie Gillain, U. S. Geological Survey	
Effects of Tropical Depressions Ivan and Jeanne on Water Quality of the Upper Oconee River Basin: Results from a Watershed Group Monitoring Program	509
Sue Eggert, UGA Department of Entomology; David Wenner, UGA Dept of Geology; Deanna Conners, UGA Institute of Ecology; Elizabeth Little, UGA Dept of Plant Pathology; Melanie Ruhlman, U.S.D.A- Natural Resources Conservation Service; and Lina Wayo, University of Georgia	
Watershed Group Monitoring Programs: An Investigation of Nitrate Contamination at the State Botanical Gardens of Georgia	513
David B. Wenner, UGA Department of Geology; Sue Eggert, UGA Dept of Entomology; and Elizabeth Little, UGA Dept of Plant Pathology	
Stream Data for TMDL Models	
Moderator: Josh Romeis, School of Forest Resources, University of Georgia	
Reconnaissance of Baseflow Water Quality in Georgia	516
S. Jack Alhadeff and Mark N. Landers, U S Geological Survey	
Dissolved Oxygen Characteristics of Georgia Streams	520
Thomas R. Dyar and S. Jack Alhadeff, U. S. Geological Survey	
The Use of Hydroacoustic Current Meters to Measure the Flow of Georgia Streams.....	522
Anthony J. Gotvald, U. S. Geological Survey	
Improving Stream Solute Load Estimation by Using the Composite Method: A Comparative Analysis Using Data from the Panola Mountain Research Watershed	524
Brent T. Aulenbach, U S Geological Survey, and Richard P. Hooper, CUASHI	
Organic Waste Contamination Indicators in Small Georgia Piedmont Streams	529
Roger Burke and Jon Molinero, USEPA	
Watershed Alliances and Education	
The Upper Flint River Watershed Alliance: Finding Solutions to Common Goals	533
Leigh Askew and Corinne Blencoe, Office of Environmental Management, Georgia Department of Community Affairs	
Achieving the WaterFirst Designation - Highlights of Five Communities	536
Leigh Askew, Environmental Management, Georgia Dept of Community Affairs	
Water Education Tools For Specific Audiences	540
Joe Krewer, Georgia Department of Community Affairs	
FLOW: Forging Leadership in our Watershed, Garden Club of GA.....*	
Becky Champion, Columbus State University	
Initiative for Watershed Excellence.....	543
William L. Cox and Mark Nuhfer, U..S Environmental Protection Agency, Region IV	
Watershed Management: Working Toward Results	
Moderator: Hudson Slay, EPA Region 4 Watershed Management Office	
EPA=s Watershed Management Office: Organizing for Results	545
William L. Cox, Director Watershed Management Office, US EPA-Region 4	
Georgia Environmental Protection Division TMDL Based Wasteload Allocations	547

Vince Williams, Georgia EPD
 The TMDL Process... What Happens Next? The Practical Experience Implementing TMDL
 Plans in the Suwannee Basin..... [549](#)
 Emily Perry, South Georgia Regional Development Center
 Implementing Water Quality Improvements Strategies in the Coosawatee River/Carter=s Lake Watershed [553](#)
 Karl Kreis, North Georgia Regional Development Center

Water Quality Permit Trading
 Moderator: Curt Fehn, US Environmental Protection Agency-Region IV
 Assistant Moderator: Justin Welch, Institute of Ecology, University of Georgia
 An Evaluation of Water Quality Trading in Georgia Watersheds [555](#)
 Kristin Rowles, Georgia State University, Policy Studies
 Pollutant Trading: Estimating Costs of Phosphorus Removal in Wastewater Treatment Facilities [559](#)
 Feng Jiang and M B Beck, UGA School of Forest Resources; K Rowles and
 R G Cummings, Georgia State University
 Water Quality Trading in Georgia: Addressing Two Potential Impediments to Success..... [564](#)
 Nanette Nelson, UGA Institute of Ecology; Andrew Keeler, School of Public
 Policy & Management, Ohio State University

Panel: TMDL Allocation/Reallocation Policy
 Moderator: Emily Perry, South Georgia Regional Development Center
 Assistant Moderator: Candace Connell, MPA program, University of Georgia
 State Water Policy Alternatives for TMDL Allocation and Reallocation ([post](#))..... [567](#)
 - Vince Williams, Georgia Environmental Protection Division
 - Curry Jones, US Environmental Protection Agency, Region4
 - Bill White, Ga Soil and Water Conservation Commission
 - Shana Udvardy, Georgia Water Coalition
 - Matt Harper, Atlanta Regional Commission

TMDL Plans Development
 Moderator: Curry Jones, U.S. Environmental Protection Agency, Region IV
 Organizer: Gail Mitchell, U.S. Environmental Protection Agency, Region IV
 Site Specific Water Quality Criteria in TMDL Development..... *
 James Greenfield, US Environmental Protection Agency, Region IV
 TMDL Development Process for Nutrients in Coosa Basin *
 Elizabeth Booth, Georgia EPD
 The Success and Challenges of Implementing Sediment and Pathogen TMDL=s in Stekoa Creek..... [576](#)
 Dick L. Fowler, US Forest Service; and Jeff Duvall, Developer

TRACK VI. STORMWATER, SAVANNAH RIVER

Stream Channel Restoration
 Moderator: Justin Ellis, Institute of Ecology, University of Georgia
 Conducting Rapid Fluvial Geomorphic Assessments Based on the Channel Evolution Model:
 A Case Study in Griffin, Georgia..... [578](#)
 Nick Jokay and Brian Watson, Tetra Tech Inc.
 Implementation of Natural Channel Design on an Urban Stream Restoration Project on a Confined
 Stream Channel in Fulton Co., Georgia..... *
 Ron Spears and Steve Jones, Environmental Services, Inc.
 Clayton County Water Authority=s Gateway Stream Restoration Project [583](#)
 Phillip Sacco and Emily Holtzclaw, CH2M HILL; Kim Zimmerman and Mike Thomas,
 Clayton County Water Authority

Adequacy of NPDES Stormwater Regulations Moderator: Doug Baughman, CH2M HILL	
Controlling Construction Stormwater Runoff.....	586
Alice Champagne, Upper Chattahoochee Riverkeeper	
Regulating Industrial Stormwater.....	590
Elizabeth Nicholas, General Counsel, Upper Chattahoochee Riverkeeper	
Implementation of Georgia's New NPDES Industrial Storm Water Requirements	593
Martin Hamann, LFR Levine Fricke	
Employing Certification to Safeguard Water Supplies	597
Terence Centner, University of Georgia, Agricultural and Applied Economics	
Agricultural Environmental Management Systems to Protect Water Quality.....	601
Carrie Lynn Presley Fowler and Terence J. Centner, UGA Agric.&Applied Economics; and L. Mark Risse, University of Georgia, Biological and Agricultural Engineering	
Panel: Erosion and Sediment Control	605
Sponsor: Georgia Section ASCE Environmental Tech Group	
Moderator: Jo Ann Macrina, Manhard Inc	
.Panel of Speakers:	
- Ray Wilke: Effective Erosion and Sediment Control	
- Steve McCutcheon: Application of BMPs and Technology	
- Terry Sturm: Instream Sediment Sources in Peachtree Creek	
- David Bennett: HB 285 & Mandatory Education Program for Erosion and Sediment Control in Georgia	
BMPs for Runoff Control	
Moderator: David Sample, MACTEC Inc.	
Sponsor: Georgia Section of ASCE, Environmental Technical Group	
Using Impervious Surface Limits to Protect Imperiled Fish Species.....	*
Seth Wenger, UGA Institute of Ecology	
Results and Evaluations: A City of Griffin TEA-21 Highway Corridor @ Griffin, Georgia	607
Brant Keller and Courtney Nolan, Griffin Public Works & Utilities	
Use of Green Roofs for Ultra-Urban Stream Restoration in the Georgia Piedmont(USA).....	612
Timothy Carter, UGA Institute of Ecology; and Todd Rasmussen, School of Forest Resources, University of Georgia	
Greenscapes and Greenbuilding: Integrating A Engineered Soils@ as a Stormwater Best Management Practice in Sustainable Landscape Construction	617
Wayne King., EARTH Products LLC	
Field Evaluation of Compost and Mulches for Erosion Control.....	621
Mark Risse and Julia W. Gaskin, UGA Biol.&Agric. Engineering, L. Britt Faucette, Filtrex Inc., Carl F. Jordan, UGA Institute of Ecology; Miguel Cabrera and Larry T. West, UGA Crop and Soil Sciences	
Gwinnett County Stormwater Management I	
Moderator: Janet Vick, Gwinnett County Department of Public Utilities	
Organizer: David Chastant, Gwinnett County Department of Public Utilities	
Implementing Storm Water Development Regulations B Experiences in Gwinnett County, Georgia	626
David Chastant, Gwinnett County, Storm Water Management Division	
Watershed Improvement Planning Gwinnett County, Georgia	630
Pete Wright, Engineer, Storm Water Management, Gwinnett County Public Utilities	
Dotting Your i's: Remedying iDiCs B at the Local Level	634
Steve Leo, Gwinnett County Dept. of Public Utilities	
Stormwater Utility Implementation Using GIS	638
Bridget Lawlor and Eric Rothstein, CH2M HILL; and Alex Mohajer, Stormwater Programs, DeKalb County Roads and Drainage	

Storm Water Management Program Implementation-
Experiences in Gwinnett County, Georgia - II
Moderator: David Chastant, Gwinnett County Dept. of Public Utilities
Storm Water Infrastructure B Lessons Learned Gwinnett County, Georgia [642](#)
Janet P. Vick, Gwinnett County Public Utilities, Storm Water Management
Implementation of a Natural Resources Conservation Service Watershed Dam Program B Gwinnett County [645](#)
Sam Fleming, Gwinnett County Department of Public Utilities
Upgrading the NRCS Y-14 Dam in Gwinnett County [649](#)
Gregg W. Hudock and Richard W. Humphries, Golder Associates Inc., Sam Fleming
and Terry West, Gwinnett County Department of Public Utilities
Seasonality and Trends in Stream Water Quality in Gwinnett County, Georgia, 1996-2003..... [653](#)
Mark N. Landers, U.S. Geological Survey

Savannah River Basin Analysis I and II

Moderator: William Bailey, US Army Corps of Engineers, Savannah District
Organizer: Leroy Crosby, US Army Corps of Engineers, Savannah District
Savannah River Basin Comprehensive Study: Overview and Assessment/Feasibility *
Leroy Crosby, US Army Corps of Engineers - Savannah District
Updating the Savannah River Drought Plan *
William Lynch, US Army Corps of Engineers - Savannah District
RES-SIM Model of Savannah River..... *
Stan Simpson and Jason Ward, US Army Corps of Engineers -Savannah District
Ecosystem Flows for Savannah River *
Amanda Wrona, The Nature Conservancy

Panel: Planning for Water Uses in Savannah Basin *

- Moderator: Leroy Crosby, US Army Corps of Engineers - Savannah District
- Freddy Vang, SC DNR Land-Water-Conservation Division
 - Sen. Bob Waldrep, Savannah River Basin Coalition
 - Frank Carl, Savannah River Keeper
 - Max Hicks, City of Augusta, Public Utilities
 - Mike Massey, Lake Volunteer Organizations
 - Mike Grey, Hartwell Lake Chamber Coalition
 - William Lynch, US Army Corps of Engineers

TRACK VII. GROUND WATER AND COASTAL

Conservation Tillage's Importance in the State Water Plan
Moderator: Gary Hawkins, Biological and Agric. Engineering, University of Georgia
Sponsor: Soil and Water Conservation Society, GA Chapter
Organizer: Wayne Reeves ARS, and Gary Hawkins UGA
Benefits of Conservation Tillage on Rainfall and Water Management [658](#)
Francisco J. Arriaga and Kip Balkcom, National Soil Dynamics Laboratory, USDA-ARS
Conservation Tillage to Manage Water and Supplemental Irrigation in Georgia [661](#)
C.C. Truman, USDA-ARS Southeast Watershed Research Lab, D.L. Rowland,
USDA-ARS, National Peanut Research Lab;
Conservation Tillage in Georgia: Economics and Water Resources [665](#)
D. W. Reeves, D.A. Abrahamson, H.H. Schomberg, USDA-ARS Natural Resource
Conservation Center; M.L. Norfleet, USDA-NRCS RIAD; H. Causarano, Auburn University;
G.L. Hawkins, Biological and Environmental Engineering, University of Georgia
Continuous No-tillB How It Pays Everyone from the Farm to the City [669](#)
Dan Towery, Ag Conservation Solutions [paper only]

Piedmont Ground Water Supply I	
Session Organizer: Lester J. Williams, Hydrologist, USGS	
Moderator: John Costello, Georgia Geologic Survey	
Common Types of Water-bearing Features in Bedrock, Rockdale County, Georgia	671
Lester Williams and William C. Burton, U.S. Geological Survey	
Joint Systems and Their Potential Influence on Groundwater in the Lithonia-Conyers Area, Georgia	678
Donna D. Tucker and Lester J. Williams, U.S. Geological Survey	
Ground Water Exploration and Development in Igneous and Metamorphic Rocks of the Southern Piedmont/Blue Ridge	680
Thomas J. Crawford and Randy L. Kath, University of West Georgia	
Surface Water and Ground Water Exploration and Development in the Georgia Piedmont: Carroll County, an On-Going Case Study	*
Jim Baxley, Carroll County Water Authority	
Establishment of a Groundwater and Surface-Water Monitoring Network to Assess the Potential Effects of Groundwater Development in an Igneous and Metamorphic Rock Aquifer, and Preliminary Data, Lawrenceville, Georgia, 2003- 2004	685
Phillip N. Albertson, US Geological Survey	
Piedmont Ground Water Supply II	
Session Organizer: Lester J. Williams, Hydrologist, USGS	
Moderator: John Costello, Georgia Geologic Survey	
Hydraulic Logging Methods--a Summary of Field Methods Used in Fractured Bedrock Systems	693
Carole Johnson and John H. Williams and Lester J. Williams, U.S. Geological Survey	
Transient Changes in Fracture Aperture During Hydraulic Well Tests in Fractured Gneiss	699
Todd Schweisinger, E. Svenson, L.C. Murdoch, Clemson University, Geological Sciences	
Air-Slug Low-Pressure Straddle-Packers System to Facilitate Characterization of Fractured BedRock	703
Erik Svenson, T. Schweisinger, L.C. Murdoch, Clemson University, Geological Sciences	
The Identification and Mapping of Ground-Water Bearing Crystalline Bedrock Fractures Within The Georgia Piedmont Using the Electrical Resistivity Technique	*
H. Dan Harman, Jr., P. G., Ground-Water Services, Inc.	
Education for Private Well Owners I and II	
Moderator: Leticia Sonon, University of Georgia	
Organizers: Tina Pagan and Dr. Paul Vendrell, University of Georgia; Debbie Warner, USGS	
A Closer Look at SouthEast Regional Drinking Water Wells: Identifying Problems Using a Down Well Camera	707
Paul Vendrell, Feed and Environmental Water Lab, University of Georgia; Tina Pagan, University of Georgia Cooperative Extension Service; Mark Risse, Department of Biological and Agricultural Engineering, University of Georgia; William Thom, University of Kentucky, Department of Agronomy	
Chemical Contamination Of Individual Water Wells: 1993 - 2003	*
Jane M. Perry, Director, Chemical Hazards Program, Environmental Health and Injury Prevention Branch, Georgia Division of Public Health	
Water Quality in Georgia's Private Drinking Water Wells	713
Dr. Leticia Sonon, Paul Vendrell, and Rick Hitchcock, Agricultural and Environmental Services Laboratories, University of Georgia (poster)	
Coweta County's Well Ordinance: A Proactive Approach to Protect the Drinking Water and Health of Well Owners	717
Patricia Gammans, GA Dept. of Public Health, Newnan GA	
Well Protection Solution: New Tools for Educating Individuals on Wellhead Management	718
Tina Pagan, University of Georgia Cooperative Extension Service; Paul Vendrell, Feed and Environmental Water Lab, University of Georgia; Mark Risse, Department of Biological and Agricultural Engineering, University of Georgia	
Educational Circulars and Private Well Owner Resources:	
Providing Drinking Water Information to the Public	721
Jorge H. Atilas, Department of Family and Consumer Sciences, University of Georgia	

A Georgia County Agent=s Perspective: Delivering an Effective County Program to Private Wells Owners	723
J. Keith Fielder, Putnam County Extension Service	
Southwest Georgia - Albany Health District's Abandoned Well Program	725
Melvin F. Jones, Georgia Public Health, Southwest Georgia Health District	
PANEL: Private Wells and Groundwater Protection	*
Thomas J. Crawford, University of West Georgia	
Irrigation Water Use I and II	
Moderator: Jim Hook, University of Georgia	
Estimating the Value of Irrigation Water in Georgia	728
Kyle C. Spurgeon, Jeffrey D. Mullen, Agricultural and Applied Economics Department, University of Georgia	
Irrigation Management Strategies in Georgia	731
Yingzhuo Yu, Jeffrey D. Mullen, Agricultural and Applied Economics, University of Georgia; Gerrit Hoogenboom, Biological and Agricultural Engineering, University of Georgia	
Status of Georgia's Irrigation Infrastructure	735
Kerry A. Harrison, James E. Hook, University of Georgia at Tifton	
Real-time Monitoring of Water Withdrawals Used for Farm Irrigation	*
Dr. James E. Hook, University of Georgia, National Environmentally Sound Production Agriculture Laboratory	
The Potential of a Decision Support System to Simulate for Irrigation Scheduling in Southwest Georgia	740
Axel Garcia y Garcia, Larry C. Guerra, and Gerrit Hoogenboom, Biological and Agricultural Engineering, University of Georgia; James E. Hook, Crop and Soil Sciences, University of Georgia at Tifton; Kerry A. Harrison, Biological and Agricultural Engineering, University of Georgia at Tifton	
Flint River Basin Models	
Moderator: Rob McDowell, Georgia EPD	
Two-dimensional Flood-Inundation Model of the Flint River at Albany, Georgia	744
Jonathan Musser and Thomas R. Dyar, U. S. Geological Survey	
Constructing a Hydrologic Model of the Ichawaynochaway Creek Watershed	748
Wei Zeng and Menghong Wen, GaDNR Environmental Protection Division	
Watershed Modeling and Calibration for Spring Creek Sub-basin in Flint Basin of Georgia Using EPA BASINS/HSPF Modeling Tool	752
Yi Zhang and Menghong Wen, Basin Analysis Program, Georgia DNR Environmental Protection Division	
Automatic Calibration and Predictive Uncertainty Analysis of a Semi-distributed Watershed Model	756
Zhulu Lin and David Radcliffe, UGA Department of Crop and Soil Sciences	
Surface and Ground Water Interactions	
Ground Water Conditions in Georgia 2003	760
David Leeth, U. S. Geological Survey	
Using Stream Gage Data to Quantify Surface Water/Ground Water Exchanges Between the Upper Floridan Aquifer and the Lower Flint River, Georgia, USA, 1989-2003	764
S. P. Opsahl, Scott E. Chapal, and Christopher C. Wheeler, J.W. Jones Ecological Research Center	
The Framework of GIS-based Decision Support Systems (DSS) for Water Resources Management at the Flint River Basin	769
Yi Zhang, David Hawkins, Wei Zeng and Menghong Wen, Georgia DNR EPD	
The Surface/Vadose Package for Computing Runoff, Evapotranspiration, and Net Recharge in MODFLOW	773
Greg Council, GeoTrans, Inc.	
Coastal Ground Water Levels	
Moderator: Greg Cherry, U.S. Geological Survey	
Impact of a Major Industrial Shutdown of Groundwater Flow and Quality in the St. Marys Area, Southeastern Georgia and Northeastern Florida, 2001-2003	778

Michael F. Peck, Keith W. McFadden, and David C. Leeth, U. S. Geological Survey Modeling the Freshwater Lens Below Barrier Islands with the Sea Water Intrusion (SWI) Package	782
Mark Bakker and Deborah J. Borden, UGA Biological & Agricultural Engineering Computation of Leakance of the Middle Semiconfining Unit, Floridan Aquifer System, Berwick Plantation, Chatham County, Georgia.....	785
Robert E. Faye, Robert E. Faye & Assoc., Inc.; Harold E. Gill, Carter & Sloope, Inc. Georgia Coastal Sound Science Initiative 2005 - What Have We Learned?	789
John Clarke and Dorothy F. Payne, U S Geological Survey, Atlanta, GA; and William F. Falls, U S Geological Survey, Columbia, SC	

Panel: Minimum Ground Water Level Policy ([post](#)).....*

- Moderator: Rick Krause, US Geological Survey (retired)
Assistant Moderator: Amber Alfonso, University of Georgia
- Bill McLemore, Georgia Geologic Survey, GaDNR-EPD
- John Clarke, US Geological Survey
- Ed Urheim, Georgia Rural Water Association repr.
- David Kyler, Center for a Sustainable Coast
- Gary Black, Georgia Agribusiness Council

Savannah Harbor Project- Ground Water Effects Assessment of Saltwater Migration Through The Upper Floridan Confining Unit in The Savannah Harbor Area	792
H. Cardwell Smith and Margaret G. McIntosh, U.S. Army Corps of Engineers, Savannah District	
Saltwater Intrusion Modeling of the Savannah Harbor Expansion Project	796
Mark Maimone and R. Paul Hossain, Camp Dresser & McKee	
Identifying Impacts to Estuarine Wetlands from the Savannah Harbor Expansion Project	800
William Bailey, US Army Corps of Engineers	

Ground Water Contamination Moderator: Nate Toll, School of Forest Resources, University of Georgia	
Strontium Isotope Systematics of Stream Base Flow within the Georgia Piedmont Province	803
Seth Rose, Department of Geology, Georgia State University; and Paul D. Fullagar, Geological Sciences, University of North Carolina-Chapel Hill	
Estimating Time to Achieve Groundwater Protection Standards using Exponential Decline Plots	807
John Raymer, Jordan Jones & Goulding	
Analysis of Groundwater Flow Paths and Potential for Interstate Migration of Contaminants in the Vicinity of the Savannah River Site, Georgia and South Carolina, 2002B 2020	810
Gregory S. Cherry, U S Geological Survey	

POSTER AND EXHIBIT SESSION

Ecological Surveys of Four River Corridors in Georgia	812
B. N. Emanuel, R. Dean Hardy, Richard A. Milligan, Jr., and Bryan L. Nuse, Georgia River Survey	
Coastal Region Training Center for the Georgia Adopt A Stream Program at Savannah State University	816
Joseph P. Richardson, Marine Sciences Program, Savannah State University	
Using Adopt-A-Stream in the Coastal Plain: A Look at the Macroinvertebrate Index	819
Tara K. Muenz, Joseph W. Jones Ecological Research Center and UGA Institute of Ecology; Stephen W. Golladay, Joseph W. Jones Ecological Research Center; and George Vellidis, University of Georgia, Tifton Campus, Tifton, GA	
Restoration Status of the Robust Redhorse	823
William Bailey, US Army Corps of Engineers, Savannah District	
Distribution of Unionid Mussels in Tributaries of the Lower Flint River, Southwestern Georgia: An Examination of Current and Historical Trends	828

Charlotte A. Chastain, Stephen W. Golladay, and Tara K. Muenz, Joseph W. Jones Ecological Research Center	
Watershed Monitoring Group Programs: Impact and Assessment of Oil and Sewage Spills in Hunnicutt Creek; Athens, Georgia	<u>832</u>
Lina Wayo, David Wenner, and Valentine Nzengung, UGA Geology; and Mark McConnell, Board Member, Upper Oconee Watershed Network	
Community Partners for Healthy Streams: A Pollution Prevention Strategy	<u>836</u>
Jennifer McCoy, Cobb County Water System, Adopt-A-Stream Coordinator	
Salamander Predation on Aquatic Macroinvertebrates	<u>838</u>
Richard D. Schulthies and Darold P. Batzer, UGA Department of Entomology	
Macroinvertebrates in Headwater Streams of the Piedmont	<u>842</u>
Melissa Churchel and D. P. Batzer, UGA Entomology; and C. Rhett Jackson, University of Georgia, School of Forest Resources	
Efficacy of Four Different Sampling Methods of Wetland Macroinvertebrates	<u>845</u>
Jennifer.A. Henke and D.P. Batzer, University of Georgia, Entomology	
Biomat Effects on Wastewater Infiltration from On-Site System Dispersal Trenches	<u>848</u>
Shelby D. Finch, Larry T. West, and Elizabeth V. Hufstetler, UGA Crop and Soil Sciences	
Evaluation of Permeability Estimates for Soils in the Southern Piedmont in Georgia	<u>852</u>
M.E. Abreu and Larry T. Test, University of Georgia, Soil and Crop Sciences	
Utilizing Instrumentation to Measure Acoustic Reflectance as a Surrogate for Suspended Sediment Concentrations along a Piedmont River in Rockdale County, Georgia	<u>856</u>
Daniel Stephens, U.S. Geological Survey	
Effects of Forestry Practices on Hydrology and Sediment Transport Behavior of Headwater Streams in Southwest Georgia	<u>858</u>
William. B. Summer and C. Rhett Jackson, UGA Warnell School of Forest Resources; D. Jones and S. W. Golladay, International Paper; and M. Miwa, J W Jones Ecological Research Center	
Evaluation of Phosphate, and Escherichia Coli Concentra-tions during a Spring Storm in the North Oconee River, Athens, Georgia	<u>862</u>
Elizabeth Purvis and David Wenner, University of Georgia, Geology	
Stormwater Methods and Trends for "First Flush" Treatment in Georgia	<u>866</u>
Larry Weidmann, Watermann Water Quality	
Trends in Agricultural Sources of Nitrogen in the Altamaha River Watershed	<u>869</u>
Sylvia C. Schaefer, UGA Institute of Ecology; and Merryl Alber, University of Georgia, Marine Sciences	
Effects of Hurricanes Frances, Ivan and Jeanne on Georgia Irrigators	<u>873</u>
Julia Beckhusen and Joseph B. Goodenbery, University of Georgia, Dept. of Agricultural and Applied Economics; Gerrit Hoogenboom, Dept. of Biological and Agricultural Engineering, University of Georgia, Griffin, Georgia; Jeffrey D. Mullen, Dept. of Agricultural and Applied Economics, UGA	
The Impact of Local Weather Variability on Irrigation Water Use in Georgia	<u>876</u>
Larry C. Guerra, Axel Garcia y Garcia, and Gerrit Hoogenboom, Biological and Agricultural Engineering, UGA; James E. Hook, National Environmentally Sound Production Agriculture Laboratory and Crop and Soil Sciences Department, UGA, Tifton, GA; Kerry A. Harrison, Cooperative Extension Service, UGA, Tifton, GA and Vijendra K. Boken, The University of Mississippi Geoinformatics Center, Department of Geology and Geological Engineering	

Development of Water Use Projections for Ground Water Flow Models in the Coastal Plain of Georgia and South Carolina, 2000--2035	<u>880</u>
Julia Fanning and Gregory S. Cherry, U. S. Geological Survey	
Broiler Water Demand: Forecasting with Structural and Time Series Models	<u>882</u>
Jack E. Houston, UGA Department of Agricultural & Applied Economics; Murali Adhikari, Alabama A&M University, Department of Ag Business; and Laxmi Paudel, UGA Department of Agricultural and Applied Economics	
Operate a Wastewater Treatment Plant from the Palm of Your Hand	<u>886</u>
James Hall and William C. Harrington, PARSONS	
Volatile Organic Compounds in Streams near Wastewater Outfalls, Rockdale County, Georgia, 2002-2004	<u>890</u>
Jolene Jones, U. S. Geological Survey	
Interpretation of Anthropogenic Enrichment of Metal Concentrations in Sediments from a Savannah Harbor Boat Slip	<u>896</u>
Patrick Graham, Applied Technology & Management, Inc.	
Comparing Transport Times Through Salinity Zones in the Ogeechee and Altamaha River Estuaries Using Squeezebox	<u>900</u>
Joan E. Sheldon And Merryl Alber, UGA Dept. of Marine Sciences	
Water Quality Conditions near Cumberland Island, Georgia	<u>904</u>
Merryl Alber and Janice Flory, UGA Marine Sciences; and Karen Payne, University of Georgia, Marine Extension Service, Spatial Technology Center	
Combining Targeted Sampling and Bacterial Source Tracking(BST) During Calm Versus Windy or Stormy Beach Conditions	<u>909</u>
Jennifer McDonald, Lisa C. Gentit, Keith W. Gates, Katy L. Austin, and Carolyn N. Belcher, University of Georgia Marine Extension Service; Peter G. Hartel, Karen Rodgers, Jared A. Fisher, and Sarah N. J. Hemmings, UGA Department of Crop and Soil Sciences; and Karen A. Payne, UGA Marine Extension Service, Savannah, GA	
Detailed Geologic Mapping of Aquifer Recharge Areas in the Upper Coastal Plain of SW Georgia	<u>913</u>
Mark D. Cocker, Georgia Geologic Survey	
Potential Effects of GroundWater Development in Eastern Camden County, Georgia, on Ground Water Resources of Cumberland Island National Seashore	<u>917</u>
Sherlyn Priest and John S. Clarke, U.S. Geological Survey, Peachtree Business Center	
Uranium, Radium, and Radon in Well Water in South Carolina: Distribution and Problems	<u>921</u>
Peter A. Stone, Robert J. Devlin, Bruce Crawford, and David G. Baize, SC Dept. Health And Environmental Control	
Well and Spring Vulnerability to Contamination in the Mountains and Inner Piedmont of South Carolina: A Tritium Survey Testing Local Recharging	<u>924</u>
Peter A. Stone, H. Lee Mitchell, and R. Todd Adams, SC Dept. Health and EnvironmentalControl	
Saltwater Contamination Due to Well Construction ProblemsCA Case Study from Vernonburg, Georgia	<u>927</u>
Mark E. Hall and Michael F. Peck, USGS	
Preliminary Chlorofluorocarbon Ages for Groundwater Samples from Production Wells in the Lawrenceville area, Georgia	<u>929</u>
Nicole Vermillion, Georgia State University, and Lester Williams, USGS	

2004 Advanced Technical Seminar: Seepage for Earthen Dams

Basic Information

Title:	2004 Advanced Technical Seminar: Seepage for Earthen Dams
Project Number:	2004GA103B
Start Date:	11/2/2004
End Date:	11/4/2004
Funding Source:	Other
Congressional District:	5
Research Category:	Not Applicable
Focus Category:	None, None, None
Descriptors:	Professional Education Seminar
Principal Investigators:	

Publication

Savannah River Workshop

Basic Information

Title:	Savannah River Workshop
Project Number:	2004GA104B
Start Date:	11/18/2004
End Date:	11/19/2004
Funding Source:	104B
Congressional District:	5
Research Category:	Not Applicable
Focus Category:	Management and Planning, Water Quality, Water Quantity
Descriptors:	Regional Workshop
Principal Investigators:	

Publication

Savannah River Workshop

(November 18th-19th, 2004, Savannah, GA)

Organized by
The South Carolina Water Resources Center
The Georgia Water Resources Institute

Tentative Agenda

Thursday, November 18, 2004

6:30 PM: Reception and informal discussions

Friday, November 19, 2004

9:00 AM: Welcoming remarks and workshop objectives

9:15 – 10:45 AM: State Overview Presentations on the Savannah River
South Carolina (SCDHEC, SCDNR)
Georgia (Ga EPD, Ga DNR)

10:30-10:45 AM: Break

10:45 – 12:00 N: Federal Agency Panel
US Army Corps of Engineers
US Geological Survey
US Environmental Protection Agency

12:00 – 1:15 PM: Lunch
Speaker: “Legal Framework for Water Sharing Compacts;
Southeast US Experience”

1:15 - 2:45 PM: University and Stakeholder Panel

2:45 – 3:00 PM: Break

3:00 – 3:45 PM: Break out sessions on Information Needs

3:45 – 4:00 PM: Plenary summary reports

4:00 – 4:45 PM: Break out sessions on Partnerships

4:45 – 5:00 PM: Plenary summary reports

5:00 – 5:30 PM: Workshop Recommendations

5:30 PM: Adjourn

Student Support

Student Support					
Category	Section 104 Base Grant	Section 104 RCGP Award	NIWR-USGS Internship	Supplemental Awards	Total
Undergraduate	1	0	0	1	2
Masters	0	0	0	3	3
Ph.D.	4	0	0	3	7
Post-Doc.	0	0	0	1	1
Total	5	0	0	8	13

Notable Awards and Achievements

Publications from Prior Projects

None